



THE HONG KONG
POLYTECHNIC UNIVERSITY

香港理工大學

Pao Yue-kong Library

包玉剛圖書館

Copyright Undertaking

This thesis is protected by copyright, with all rights reserved.

By reading and using the thesis, the reader understands and agrees to the following terms:

1. The reader will abide by the rules and legal ordinances governing copyright regarding the use of the thesis.
2. The reader will use the thesis for the purpose of research or private study only and not for distribution or further reproduction or any other purpose.
3. The reader agrees to indemnify and hold the University harmless from and against any loss, damage, cost, liability or expenses arising from copyright infringement or unauthorized usage.

If you have reasons to believe that any materials in this thesis are deemed not suitable to be distributed in this form, or a copyright owner having difficulty with the material being included in our database, please contact lbsys@polyu.edu.hk providing details. The Library will look into your claim and consider taking remedial action upon receipt of the written requests.

The Hong Kong Polytechnic University

Department of Applied Biology and Chemical Technology

**Synthesis, Characterization and
Application of
Smart Magnetic Core-Shell Polymeric
Particles**

Ho Kin Man Edmond

A thesis submitted in partial fulfillment of
the requirements for the Degree of Doctor of Philosophy

(March 2007)



Pao Yue-kong Library
PolyU • Hong Kong

CERTIFICATE OF ORIGINALITY

I hereby declare that this thesis is my own work and that, to the best of my knowledge and belief, it reproduces no material previously published or written, nor material that has been accepted for the award of any other degree or diploma, except where due acknowledgement has been made in the text.

Ho Kin Man Edmond

March 2007

ABSTRACT

There has been increasing interest in the design and fabrication of magnetic core-shell (MCS) polymeric particles, due to their magnetic-responsive properties. Such core-shell particles have been successfully synthesized through various approaches, such as suspension-crosslinking, layer-by-layer (LBL), and other polymerization techniques. Nevertheless, there are still some drawbacks including, leaching and dissolution problem of magnetic nanoparticles under an acidic environment, ill-defined core-shell nanostructure, incomplete encapsulation of magnetic nanoparticles, tedious synthetic procedures, and the use of large amounts of emulsifiers and surfactants. In addition, the particles produced through these approaches have limited amount of functional groups on their particle surface. The work presented in this thesis aims to develop a simple, convenient, inexpensive, and surfactant/emulsifier-free approach to prepare MCS particles, and the use of MCS particles for electromagnetic interference (EMI) shielding application has also been explored. The MCS particles containing γ -Fe₂O₃ nanoparticles inside the polymer cores were prepared via a two-step synthesis: 1) preparation of vinyl-coated magnetic nanoparticles (MPS-Fe₂O₃); 2) synthesis of magnetic core-shell (MCS) particles via hydroperoxide-induced graft copolymerization of methyl methacrylate (MMA) from

chitosan in the presence of MPS-Fe₂O₃ nanoparticles.

Part I – Synthesis of vinyl-coated magnetic nanoparticles

MPS-Fe₂O₃ nanoparticles were prepared via co-precipitation of aqueous solutions of Fe²⁺ and Fe³⁺ salts in a NH₄OH solution, followed by coating them with trisodium citrate to generate citrate-coated iron oxide (c-Fe₂O₃) nanoparticles (~ 10 nm). These nanoparticles were then modified via hydrolysis and condensation of tetraethyl orthosilicate (TEOS) and 3-(trimethoxysilyl)propyl methacrylate (MPS) to generate MPS-Fe₂O₃ nanoparticles (Chapter 4). Properties of these nanoparticles including particle size, surface charge density, composition and magnetic responsiveness were characterized with dynamic light scattering, zeta-potential, FT-IR spectroscopy, thermogravimetry analysis (TGA) and vibrating sample magnetometer (VSM), respectively.

Part II – Synthesis of magnetic core-shell (MCS) particles

MCS particles were synthesized via hydroperoxide-induced graft copolymerization of methyl methacrylate (MMA) from chitosan in the presence of the MPS-Fe₂O₃ nanoparticles (Chapter 5). The MCS particles were produced in high

yield. Transmission electron microscopy (TEM) images of the MCS particles clearly revealed a well-defined core-shell nanostructure, where the poly(methyl methacrylate) cores containing γ -Fe₂O₃ nanoparticles were coated with chitosan shells. The presence of chitosan shell was confirmed with a ζ -potential measurement. Particle size measurement determined that the MCS particles had sizes around 200 nm with narrow size distribution. Magnetization measurement of the particles using vibrating sample magnetometer (VSM) showed that the core-shell particles possessed a good magnetic responsiveness with superparamagnetic property.

Part III –Multi-functional core-shell nanocomposites as a water-based coating for electromagnetic interference (EMI) shielding applications

Electromagnetic interference (EMI) is a well-known problem in electronic circuits. Electromagnetic radiation particularly at high frequencies not only interferes with electronics, but may also have potential hazard to human being. Thus, there is a critical need in developing versatile and effective EMI shielding materials. In the last part of this thesis, a novel magnetic and conducting nanocomposite as a water-based multi-functional coating for EMI shielding applications is described (Chapter 6). Formation of these nanocomposites was achieved by simply mixing the MCS particles with purified single-walled carbon nanotubes (SWNTs). TEM images of the

nanocomposites showed that the SWNTs formed a bridge between MCS particles. Furthermore, the presence of MCS particles can significantly avoid the formation of large SWNTs bundles, which is a major challenge in using the SWNTs. Atomic force microscopy (AFM) images of the nanocomposites showed that these nanocomposites formed a continuous film on a glass substrate, indicating that they possessed a good film forming ability. Exploration of the MCS particles-SWNTs nanocomposites for electromagnetic interference (EMI) shielding will be attempted. Thus, this novel material could have great potential for EMI shielding applications.

LIST OF PUBLICATIONS AND PATENTS

RELATED TO MY THESIS

1. Ho, K. M.; LI, P. Design and Synthesis of Novel Magnetic Polymeric Particles. Polymer Materials: Science & Engineering. Vol. 91, 416 (2004).
2. Ho, K. M.; LI, P. Preparation of Magnetic-Responsive Particles and their Current Applications”. Journal of Magnetism and Magnetic Materials. (2007) (In preparation).
3. Ho, K. M.; LI, P. Synthesis and Characterization of Magnetic Core-Shell Particles.: *Tert*-hydroperoxide-Induced Graft Copolymerization of MMA from Chitosan in the Presence of Vinyl-Coated Iron Oxide Nanoparticles. Chemistry of Materials. (2007) (In preparation).
4. Ho, K. M.; LI, P. Hydrogen Peroxide-Induced Graft Copolymerization of MMA from Chitosan in the Presence of Vinyl-Coated Iron Oxide Nanoparticles. Chemistry of Materials. (2007) (In preparation).
5. Ho, K. M.; LI, P. Multi-functional Core-Shell Nanocomposites as a Water-Based Coating for Electromagnetic Interference (EMI) Shielding Applications. Nano Letters. (2007) (In preparation).
6. Ho, K. M.; LI, P. Multi-functional Core-Shell Nanocomposites as a Water-Based Coating for Electromagnetic Interference (EMI) Shielding Applications. US.

Patent (2007) (In preparation).

List of Publications for Other Work

1. ZHU, J.M.; TANG, A.; LAW, L.P.; FENG, M.; HO, K.M.; LEE, D.K.L.; HARRIS, F.W.; LI, P. Amphiphilic Core-Shell Nanoparticles with Poly(ethylenimine) Shells as Potential Gene Delivery Carriers. Bioconjugate Chemistry. Vol. 16, pp. 139–146 (2005).
2. SUNINTABOON, P.; HO, K. M.; LI, P.; CHENG, S. Z. D.; HARRIS, F. W. Formation of Nanostructured Materials via Coalescence Amphiphilic Hollow Particles. Journal of the American Chemical Society. Vol. 128, pp. 2168–2169 (2006).
3. HO, K. M.; MAO, X. P.; GU, L. Q.; LI, P. Novel Route to Enzyme Immobilization: Core-Shell Nanoenzyme Consisting of Well-defined Poly(methyl methacrylate) Cores and Cellulase Shells. Bioconjugate chemistry (2007) (In preparation).

List of Publications and Awards in Conferences

1. HO, K.M. and LI, P. Novel Preparation of Magnetic Amphiphilic Core-Shell Polymeric Particles. The Tenth Symposium on Chemistry Postgraduate Research in Hong Kong, The Hong Kong Baptist University, Hong Kong, pp. O-33, 22 Mar 2003.
2. HO, K.M. and LI, P. Design and Synthesis of Magnetic Polymeric Particles. The Eleventh Symposium on Chemistry Postgraduate Research in Hong Kong, The Hong Kong Polytechnic University, Hong Kong, pp. Oral-6, 17 Apr 2004.
3. HO, K.M. and LI, P. Design and Synthesis of Novel Magnetic Polymeric Particles. 228th American Chemical Society National Meeting, Philadelphia, PA, USA, pp. 22-26, PMSE-233, 22–26 Aug 2004.
4. HO, K.M. and LI, P. Design and Synthesis of Magnetic Amphiphilic Core-Shell Polymeric Particles. The Twelfth Symposium on Chemistry Postgraduate Research in Hong Kong, City University of Hong Kong, Hong Kong, pp. O-87, 23 Apr 2005.
5. HO, K.M. and LI, P. Synthesis and Characterization of Novel Biocompatible Core-Shell Polymer Particles Containing Magnetic Nanoparticles in the Cores. PACIFICHEM 2005, Hawaii, USA, PS-36, 15–20 Dec 2005.

6. HO, K.M.; LI, P. SUNINTABOON, P.; LI, P.; CHENG, S. Z. D.; HARRIS, F. W.

Formation of Nanostructured Materials via Coalescence Amphiphilic Hollow

Particles. The Thirteen Symposium on Chemistry Postgraduate Research in Hong

Kong, The Hong Kong University of Science and Technology, Hong Kong, pp.

O-97, 22 April 2006.

ACKNOWLEDGEMENTS

I wish to express my deepest gratitude to my supervisors Dr. Li Pei, for her intelligent and insightful suggestions, encouragement and professional mentoring throughout the course of my work, and for her valuable comments and revisions on the drafts of this thesis. Her novel ideas on my research project and devoted attitude in science made my study a rewarding experience.

A special thank to the all the colleagues in the research group of Dr. Li Pei for their helpful discussions, continual support and encouragement. They are Dr. Leung Man Fei, Lei Wei Ying, Lee Cheng Hao Samuel, Dr. Chen Cheng, Dr. Wu Ai-Hua, Dr. Zhang Xia Hua, Hetti-Mimi, and Fan Chi Ho.

I would like to acknowledge Dr. Pang K. H. Geoffery of Department of Physics for teaching me the operation of transmission electron microscopy (TEM) and X-ray diffraction (XRD). I would like to thank Mr. Yeung, M. L. of Materials Research Center for providing the atomic force microscopy (AFM) service. I also wish to thank Mr. Lo of Department of Physics for providing the field-emission scanning electron microscopy (FE-SEM) service. Finally, I am grateful to the staff, especially the

technical staff and the general supporting of Department of Applied Biology and Chemical Technology, who have helped me in various ways.

TABLE OF CONTENT

CERTIFICATE OF ORIGINALITY	ii
ABSTRACT	iii
LIST OF PUBLICATIONS	vii
ACKNOWLEDGMENTS	xi
TABLE OF CONTENT	xiii
ABBREVIATIONS AND SYMBOLS	xxi
Chapter 1 General Background to Magnetism	1
1.1. Magnetism	1
1.1.1. Important Terminologies	2
1.1.2. Types of Magnetism	4
1.1.2.1. Diamagnetism	5
1.1.2.2. Paramagnetism	5
1.1.2.3. Ferromagnetism	6
1.1.2.4. Antiferromagnetism	7
1.1.2.5. Ferrimagnetism	7
1.2. Magnetic Behavior of Ferromagnetism and Ferrimagnetism	8

1.2.1. Hysteresis	8
1.3. Magnetic Behavior of Superparamagnetic Nanoparticles and Their Important Features	10
1.4. Variety of Magnetic Particles	12
1.4.1. <i>Bulk</i> Iron Oxides: Magnetite and Maghemite	13
1.4.1.1. Crystal Structure and Magnetic Properties	14
1.4.1.2. Surface Properties and Chemistry	16
Chapter 2 Applications of Magnetic Iron Oxide Particles	19
2.1. Magnetic-Assisted Cell Separation and Immunoassays	19
2.2. Drug Delivery	21
2.3. Magnetic Mediated Hyperthermia (MMH)	24
2.4. Magnetic Resonance Imaging (MRI)	25
2.5. Electromagnetic Interference (EMI) Shielding	27
2.6. Ferrofluids	28
Chapter 3 Magnetic-Responsive Particles: Literature Methods and Our Approach	29
3.1 Synthesis of Surface-Modified Magnetic Iron Oxide Nanoparticles and Their Applications	29
3.1.1 Co-precipitations from Bulk Solution and Their Surface Modifications	29
3.1.2 Co-precipitations in the Presence of Polymers	34

3.1.3	Water-in-Oil (W/O) Microemulsions	37
3.1.4	High-Temperature Decomposition of Organic Precursors	40
3.2	Synthesis of Magnetic Polymeric Particles and Their Applications	43
3.2.1	Suspension Cross-linking Approach	44
3.2.2	Layer-by-Layer (LBL) Approach	45
3.2.3	Seed Precipitation Polymerization	46
3.2.4	Emulsion/Inverse Microemulsion Polymerization	50
3.2.5	Miniemulsion/inverse Miniemulsion Polymerization	51
3.3	Our Approach to Novel Magnetic Core-Shell (MCS) Particles	55
3.3.1	Research Aims	56
3.3.2	Design Rationale of MCS Particles	56
3.3.3	Our Strategies to MCS Particles	58
3.3.4	Specific Objectives	60
Chapter 4	Synthesis of Surface-Modified Magnetic Nanoparticles	61
4.1.	Introduction	61
4.2.	Experimental	62
4.2.1.	Materials	62
4.2.2.	Synthesis of <i>Organic-Based</i> γ -Fe ₂ O ₃ Nanoparticles: Oleate-Coated γ -Fe ₂ O ₃ (o-Fe ₂ O ₃)	62
4.2.3.	Synthesis of <i>Aqueous-Based</i> γ -Fe ₂ O ₃ Nanoparticles:	63
4.2.3.1.	γ -Fe ₂ O ₃	63
4.2.3.2.	Citrate-Coated γ -Fe ₂ O ₃ (c-Fe ₂ O ₃)	64
4.2.3.3.	Vinyl-Coated γ -Fe ₂ O ₃ (MPS-Fe ₂ O ₃)	65

4.2.4. Measurement and Characterization	67
4.3. Results and Discussion	70
4.3.1. Synthesis of α - Fe_2O_3 Nanoparticles	70
4.3.2. Synthesis of Aqueous-Based γ - Fe_2O_3 Nanoparticles	76
4.3.2.1. γ - Fe_2O_3	76
4.3.2.2. α - Fe_2O_3	82
● Effect of HNO_3 Surface Treatment	83
4.3.2.3. MPS- Fe_2O_3	90
● Effect of TEOS Addition	96
● Effect of Reaction Temperature	97
4.4. Conclusions	101
Chapter 5 Synthesis of Magnetic Core-Shell (MCS) Particles	103
5.1. Hydroperoxide-Induced Graft Copolymerization of Vinyl Monomer from Water-Soluble Polymer Containing Amino Groups	104
5.1.1. Mechanism of the Graft Copolymerization	104
5.1.2. Important Features	105
5.2. Experimental	107
5.2.1. Materials	107
5.2.2. Graft Copolymerization of MMA from Chitosan in the Presence of Surface-Modified Magnetic Nanoparticles	108
5.2.2.1. α - Fe_2O_3	108
5.2.2.2. α - Fe_2O_3	110
5.2.3. Graft Copolymerization of Methyl Methacrylate (MMA) from Chitosan in the Presence of MPS- Fe_2O_3	111

Nanoparticles Initiated with <i>tert</i> -Butyl Hydroperoxide (TBHP) or Hydrogen Peroxide (H ₂ O ₂)	
5.2.4. Measurement and Characterization	113
5.3. Results and Discussion	117
5.3.1. Graft Copolymerization of MMA from Chitosan in the Presence of Surface-Modified Magnetic Nanoparticles	117
5.3.1.1. α -Fe ₂ O ₃	117
5.3.1.2. γ -Fe ₂ O ₃	120
5.3.2. Graft Copolymerization of MMA from Chitosan in the Presence of MPS-Fe ₂ O ₃ Nanoparticles	123
5.3.2.1. Preparation of MCS Particles Using TBHP as an Initiator	127
● Effect of Chitosan, MMA and MPS-Fe ₂ O ₃ Weight Ratio	127
● Effect of Solid Content	132
● Effect of TBHP	133
● Effect of MPS-Fe ₂ O ₃ Content	137
● Effect of Other Water-Soluble Polymer Containing Amino Groups	140
● Compositions of MCS Particles, and Magnetic Graft Copolymers	150
● Particle Size and Size Distribution of MCS particles	155
● Morphology of MCS Particles	156
● Characterization of MCS Particle Surface Charges	158

● Colloidal Stability and Critical Coagulation Concentration (CCC) of MCS particles	159
● Magnetization Measurement of MCS Particles	162
● Proposed Reaction Mechanism for MCS Particle Formation	163
● Summary	165
5.3.2.2. Preparation of MCS particles using H ₂ O ₂ as an initiator	167
● Effect of Reaction Temperature	169
● Effect of H ₂ O ₂ Concentration	171
● Effect of MPS-Fe ₂ O ₃ Content	178
● Effect of MMA Content	181
● Scope of Other Vinyl Monomers	183
● Compositions of MCS Particles, and Magnetic Graft Copolymers	191
● Particle size and size distribution of MCS particles	196
● Morphologies of MCS Particles	197
● Characterization of MCS Particle Surface	198
● Colloidal Stability and Critical Coagulation Concentration (CCC) of MCS Particles	200
● Magnetization Measurement of MCS Particles	203
5.4 Conclusions	204

Chapter 6	Multi-Functional Core-Shell Nanocomposites as a Water-Based Coating for Electromagnetic Interference (EMI) Shielding Applications	206
6.1	Introduction	207
6.1.1	Mechanism of EMI Shielding	207
6.1.2	Types of EMI Shielding Materials	211
6.1.3	Carbon Nanotube/Polymer Composites for EMI Application	212
6.1.4	Limitations of Current Technologies	214
6.1.5	Design Rationale of Novel EMI Shielding Coating Materials	217
6.1.6	Desirable Properties for MCS Particles-SWNTs Nanocomposites	218
6.2	Experimental	220
6.2.1	Materials	220
6.2.2	Experimental Procedures	221
6.2.2.1	Synthesis of Magnetic Core-Shell (MCS) Particles	221
6.2.2.2	Purification of As-Prepared Single-Walled Carbon Nanotubes (<i>AP</i> -SWNTs)	223
6.2.2.3	Preparation of MCS Particles-SWNTs Nanocomposites	223
6.2.2.4	Measurement and Characterization	225
6.3	Results and Discussion	229
6.3.1	Synthesis of MCS Particles	229

6.3.2	Purification of <i>AP</i> -SWNTs	232
6.3.3	Formation of MCS Particles-SWNTs Nanocomposites	238
6.3.3.1	Effect of Weight ratio of MCS Particles to Acid-Treated SWNTs	239
6.3.3.2	Effect of pH	239
6.3.4	Morphologies of MCS Particles-SWNTs Nanocomposites	241
6.3.5	Film-Forming Ability of MCS Particles and MCS Particles-SWNTs Nanocomposites	243
6.3.6	Magnetic Properties of MCS Particles-SWNTs Nanocomposites	250
6.4	Conclusions	251
Chapter 7	Conclusions and Recommendations for Future Study	253
Appendix		256
References		277

ABBREVIATIONS AND SYMBOLS

Symbol	Description
T_B	Blocking temperature
c- Fe_2O_3	Citrate-coated iron oxide nanoparticles
Conv. %	Monomer Conversion
CTS	Chitosan
CTS% graft	Percentage of chitosan grafted on MCS particle surface
D_v	Volume-average hydrodynamic diameter
D_n	Number-average hydrodynamic diameter
D_v/D_n	Polydispersity index of the particle size distribution
DLS	Dynamic light scattering
DSC	Differential scanning calorimetry
EMI	Electromagnetic interference
Encap. %	Encapsulation efficiency
FE-SEM	Field-emission scanning electron microscopy
FT-IR	Fourier-Transform Infrared Spectroscopy
Fe_3O_4	Magnetite
HR-TEM	High resolution-transmission electron microscopy

H ₂ O ₂	Hydrogen peroxide
ICDD	International Center for Diffraction Data
IEP	Isoelectric point
MPS-Fe ₂ O ₃	Vinyl-coated γ -Fe ₂ O ₃
MRI	Magnetic Resonance Imaging
M _s	Saturation magnetization
o-Fe ₂ O ₃	Oleate-coated iron oxide nanoparticles
γ -Fe ₂ O ₃	Maghemite
γ -Fe ₂ O ₃ %	γ -Fe ₂ O ₃ percentage
TGA	Thermogravimetry Analysis
T _b	Blocking temperature
TBHP	<i>tert</i> -butyl hydroperoxide
SC. %	Solid content
TEM	Transmission Electron Microscopy
XRD	X-Ray Diffraction
UV-VIS	Ultraviolet-visible spectrophotometer
VSM	Vibrating sample magnetometer
ζ -potential	Zeta-potential

Chapter 1

General background to magnetism

This chapter will cover the fundamental concepts and properties of magnetic materials, especially those unique properties of magnetic nano-materials and their deviations from respective bulk properties.

1.1 Magnetism

Magnetism originates from the movement of electrons, which include the spin and orbital motions of an electron. Regarding the spin motion of an electron, the electron is considered as a spinning ball of charge. When it rotates, a magnetic dipole moment or a magnetic field is generated around the *spin*, where the spin direction is quantized, either “up” (\uparrow) or “down” (\downarrow).¹ Regarding the orbital motion of an electron, since an electron circulates around the *nucleus of an atom*, this creates a flow of charge on the atom.² This flow of charge as a circular current loop produces magnetic lines of force known as a magnetic dipole. Summation of these magnetic dipoles in molecular orbitals creates current loops around the atom, thus generating a net magnetic field. Therefore, all materials inherently possess magnetic fields, where their magnetic properties are governed by the spin or orbital motions of their electrons.

1.1.1 Important terminologies

1.1.1.1 Magnetization (M)

When a substance is placed in an external magnetic field (H), magnetic dipoles in this substance are magnetized. The intensity of the substance being magnetized (i.e. magnetic moment) per unit volume is called '*magnetization*', symbolized as M. The density (or flux) of the magnetic lines of force exerted on a substance under the influence of a magnetic field (H) is termed the magnetic induction, B, and is given by the Equation 1.1.

$$B = H + 4\pi M \quad (1.1)$$

Where the 4π factor originates from the unit field created by a unit pole on the surface of a sphere of 1 cm radius, which enclose the pole with a surface area of $4\pi r^2$.

1.1.1.2 Magnetic susceptibility (κ or χ or χ_M)

The magnetic susceptibility (κ) is a measure of the effectiveness of magnetic moments being induced in a material under an external magnetic field (Equation 1.2). It can be expressed in terms of volume, as κ ($\text{emu cm}^{-3}\text{Oe}^{-1}$) or mass, χ ($\text{emu g}^{-1}\text{Oe}^{-1}$), or mole, χ_M ($\text{emu mol}^{-1}\text{Oe}^{-1}$).

$$M = \kappa H \text{ or } M = \chi H$$

$$\kappa = \frac{M}{H} \quad (1.2)$$

1.1.1.3 Magnetic permeability (μ)

Magnetic permeability (μ) is the tendency of the magnetic lines of force to pass through a medium, which is defined in Equation 1.3. Combining Equation (1.1), (1.2) and (1.3), magnetic permeability is expressed in terms of magnetic susceptibility (Equation 1.4).

$$\mu = \frac{B}{H} \quad (1.3)$$

$$\mu = 1 + 4\pi\kappa \quad (1.4)$$

1.1.1.4 Magnetization units

There are different unit systems that are currently used in magnetization measurement. They include cgs or Gaussian system, and SI units (SI-1, SI-2 and SI-3). In the cgs (centimeters, grams, seconds) system, magnetization (M) is reported as electromagnetic units per volume (emu/cm^3) or mass (emu/g). Magnetic field strength (H) is measured in Oersted (Oe) and the magnetic permeability in an vacuum is given the value of unity. In the SI (system international) units, magnetization (M) is reported as Telsa (T), and magnetic field strength (H) is measured in amperemeters (A/m). Detailed unit conversion table is given in Appendix, Table A-1.

1.1.2 Types of magnetism

Magnetism of materials is governed by different arrangements of magnetic moments and their responses to an external magnetic field. Five basic types of magnetism are observed in nature, as illustrated in Figure 1.1. They include diamagnetism, paramagnetism, ferromagnetism, antiferromagnetism, and ferrimagnetism. Figure 1.1 illustrates the different forms of magnetism.

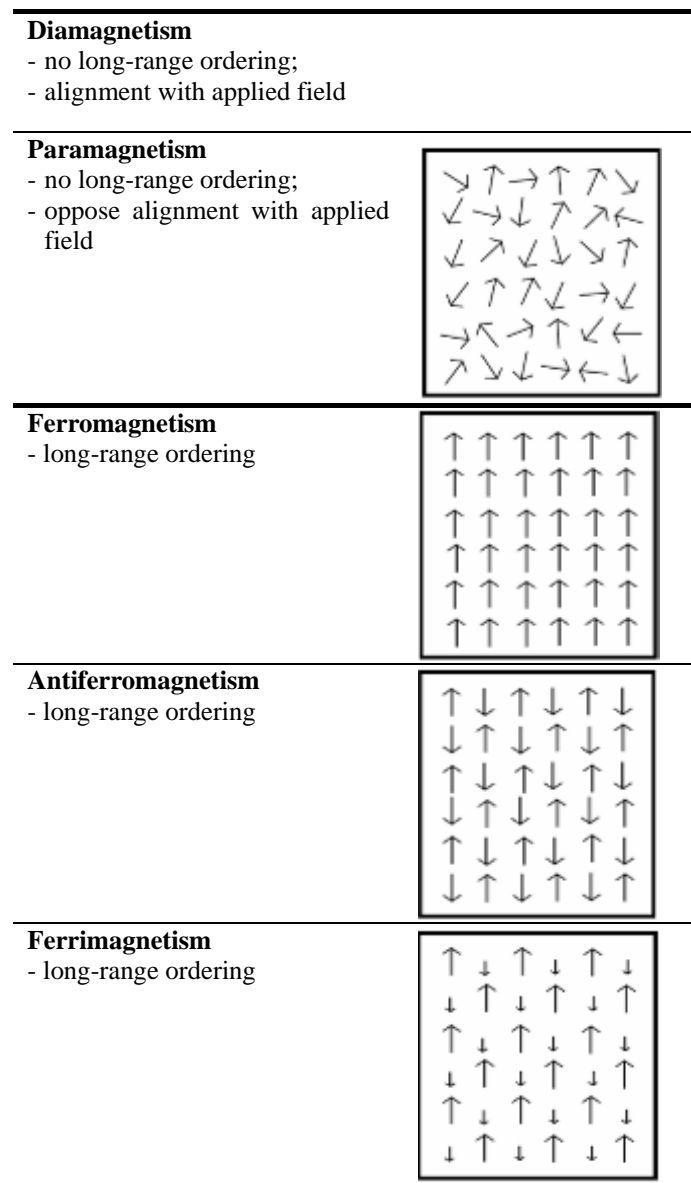


Figure 1.1. Schematic diagram of different forms of magnetism.

1.1.2.1 Diamagnetism

Diamagnetism is found in elements with *full-filled* electronic sub-shells. It means that two electrons are fully occupied in the subshells where they are aligned in antiparallel direction (i.e. pair-up). Due to this spin orientation, magnetic moments cancel out each other, resulting in a zero net magnetic moment. Diamagnetic substances involve a slight repulsion ($\chi < 0 \text{ emu g}^{-1}\text{Oe}^{-1}$) when an external magnetic field is applied. The magnetic susceptibility of diamagnetic substances is very small ($10^{-6} \text{ emu g}^{-1}\text{Oe}^{-1}$) with negative magnitude, and temperature-independent. Hence, diamagnetic materials are usually considered as ‘non-magnetic’ substances. The magnetic susceptibility of a diamagnetic substance such as water is $\chi = -9.05 \times 10^{-6} \text{ emu g}^{-1}\text{Oe}^{-1}$.

1.1.2.2 Paramagnetism

Paramagnetism observed in materials is attributed to unpaired electrons in atomic subshells (often in the 3d or 4f shells of each atom), in which atomic magnetic moments are uncoupled with each other and randomly aligned (Figure 1.1). Therefore, paramagnetic materials result in a zero magnetic moment and no long-range order. When the substances are placed in an applied magnetic field, their magnetic moments result in partial alignment because the alignment is restricted by the random thermal motion of electron spins in an atom. When the applied magnetic field is removed, thermal fluctuations make the magnetic moments flip back to their original position, turning magnetic moments to zero.

1.1.2.3 Ferromagnetism

Ferromagnetic substances also possess unpaired electrons in electronic subshells. Atomic magnetic moments align parallel in direction with equal magnitude in which they have direct coupling interactions with each other, resulting in long-range ordering (Figure 1.1). Therefore, these aligned moments in *ferromagnetic* materials have a spontaneous magnetization even without an applied magnetic field. Hence, they are referred to as permanent magnets. The magnetic susceptibility of *ferromagnetic* materials is large ($0.01\text{--}10^6 \text{ emu g}^{-1}\text{Oe}^{-1}$) with positive magnitude, and temperature-dependent. Increasing temperature results in a dramatic decrease in magnetic susceptibility, because thermal fluctuations disrupt the long-range ordering of the magnetic moments. Further increasing temperature to the Curie temperature (T_C) causes ferromagnetic materials to display paramagnetic behavior. In this case, thermal energy is sufficient to overcome the long-range ordering of the magnetic moments.

1.1.2.4 Antiferromagnetism

Antiferromagnetism materials have atomic magnetic moments arranged in an anti-parallel fashion of an equal magnitude (Figure 1.1). Furthermore, the moments couple with each other,³ thus leaving a zero magnetic moment. In the presence of an external magnetic field, *antiferromagnetic* materials only exhibit small magnetic susceptibility ($0\text{--}0.1 \text{ emu g}^{-1}\text{Oe}^{-1}$). However, increasing temperature dramatically increases magnetic susceptibility of the material because thermal energy is sufficient to cause the equal and oppositely aligned magnetic moments to fluctuate randomly (i.e. disrupting the antiparallel ordering). When increasing temperature to the Néel temperature (T_N), it leads to a disappearance of the long-range ordering. At that temperature, *antiferromagnetic* substances exhibit *paramagnetism* behavior.

1.1.2.5 Ferrimagnetism

Ferrimagnetic materials consist of antiparallel alignment of magnetic moments, which is similar to antiferromagnetic substances (Figure 1.1). However, the magnetic moments in *ferrimagnetic* materials are of unequal magnitude, thus resulting in the spontaneous magnetization. These unequal magnitudes of magnetic moments in *ferrimagnetic* substances are inherent from the presence of two or more interpenetrating sublattices. A detailed explanation will be provided in the Section 1.4.1.1. The magnetic behavior of *ferrimagnetic* materials is similar to that of *ferromagnetic* materials.

1.2 Magnetic behavior of ferromagnetism and ferrimagnetism

As mentioned in Section 1.1.2.3 and 1.1.2.5, *ferromagnetic* and *ferrimagnetic* materials possess a *spontaneous* magnetization. However, most of them are *unmagnetized* initially, because most of their magnetic domains are randomly oriented. On the other hand, when a sufficient large magnetic field is applied to cause full alignment of all magnetic domains, a strong magnetization can be achieved. Once the materials become magnetized, they remain magnetized for a long time even if an applied magnetic field is removed. Thus, they are referred to as permanent magnets.

1.2.1 Hysteresis

Figure 1.2 shows the magnetic behavior of *bulk* ferromagnetic or ferrimagnetic materials. At $M = 0$, they are unmagnetized (i.e. zero magnetization) in which magnetic domains are randomly oriented within the materials. When they are placed in an increasing applied magnetic field, magnetic domain walls start to rotate initially. As the field increases to the extent at which it is sufficiently large enough to cause all magnetic domains align in the same direction, the materials become saturated in magnetization (M_s).

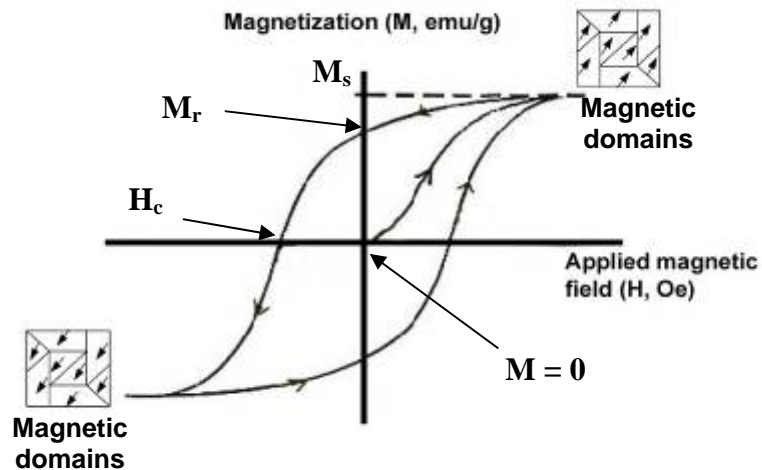


Figure 1.2. A plot of magnetization (M) against an applied magnetic field (H), M-H curve of ferromagnetic or ferrimagnetic materials. (M_s is the saturation magnetization, M_r is the remnant magnetization, and coercivity, H_c is the magnitude of the reverse field required to demagnetization)

As the field is removed, because high energy is required to disrupt the long range coupling of magnetic moments in the domains, it is difficult to return their moments to the original position, thus causing the magnetization to be retained in the material (i.e. remnant magnetization, M_r). To bring the magnetic moments back to their original position, a demagnetization force (H_c) is required. Hysteresis is the lack of retraceability of the magnetization curve during magnetization/demagnetization process, which is related to the re-orientation of magnetic domains within the material. Hence, *bulk* ferro- or ferri-magnetic materials always possess hysteresis.

1.3 Magnetic behavior of superparamagnetic particles and their important features

As the particle size of ferro- or ferri-magnetic materials decreases, the number of magnetic domains per particle decreases. When the size decreases down to the limit where the domain wall is energetically unfavorable to exist, the size reaches a single-domain size.⁴ As the particle size of the materials further decreases to nano-scale (i.e. < 30 nm), the energy associated with the alignment of magnetic moments in this material (i.e. magnetic anisotropy) decreases. When this energy decreases to the extent which is comparable to the thermal energy, the magnetic moments within the particle are free to fluctuate, as paramagnetic materials (i.e. no spin-spin coupling). Compared with paramagnetic materials, these nano-scale particles have much higher susceptibility value than that for paramagnetic materials since these particles contain 10^5 paramagnetic atomic moments. Hence, this phenomenon is called “superparamagnetism”.

Because of the free fluctuation of magnetic moments at room temperature, the magnetic behavior of superparamagnetic particles is different from that of *bulk ferro- or ferri-magnetic* particles, as shown in Figure 1.3. During the magnetization/demagnetization process, superparamagnetic particles show no magnetic *remanence* (M_r) or *coercive force* (H_c). Furthermore, they have higher magnetic susceptibility than *bulk* particles, which means that they can reach saturation magnetization at lower applied magnetic field strength (1–2 K Oe).

Another important feature is their very fast flipping of the net moments during the demagnetization process (i.e. 10^{-11} – 10^{-12} s). Fast flipping of net magnetic moment in superparamagnetic particles is attributed to the fact that thermal energy is sufficient to overcome the anisotropy barrier of orientation of a single particle. Thus, the magnetic moments are free to fluctuate and align with the applied magnetic field.

The free motion of magnetic moments is dependent on temperature. When temperature decreases below a critical temperature (i.e. blocking temperature, T_B), the thermal energy is not sufficient to overcome the energy barrier of magnetization orientation in a single particle; therefore, the anisotropy of the particle blocks the free motion of magnetic moments.^{3,5-6} Hence, a remnant magnetization (i.e. hysteresis loop) are able to be observed in superparamagnetic materials at blocking temperature (T_B).

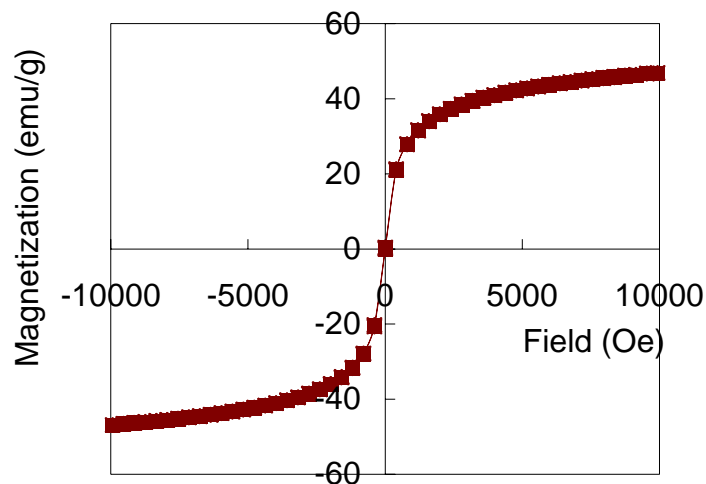


Figure 1.3. Magnetic behavior of superparamagnetic particles at room temperature.

1.4 Variety of magnetic particles

Pure metal particles (e.g. Ni, Co, Fe) are classified as ferromagnetic materials, while ferrite oxides particles (i.e. $MO \cdot Fe_2O_3$, where $M = Fe, Mn, Co, Ni, Cu$) are classified as ferrimagnetic materials. Therefore, metal particles usually have higher saturation magnetization (M_s) than metal oxide particles (Table 1.1). However, these metal particles are highly toxic in nature and are susceptible to oxidation.

Table 1.1. Magnetic properties of *bulk* metals and metal oxides.

Substances	Magnetism	Saturation magnetization (M_s , emu/cm ³)	Curie Temperature (K)
Ni		485	631
Co (cubic)	Ferromagnetism	1400–1422	1404
Fe (Cubic)		1700–1714	1043
γ - Fe_2O_3		394	820–986
$FeO \cdot Fe_2O_3$	Ferrimagnetism	480–500	858
$MnO \cdot Fe_2O_3$		410	573
$CoO \cdot Fe_2O_3$		400	793
$NiO \cdot Fe_2O_3$		270	858
$CuO \cdot Fe_2O_3$		135	728

Ni, Co and Fe are easily oxidized to form *antiferromagnetic* metal oxides (NiO, CoO and FeO) at an ambient temperature, which means that their magnetic responsiveness rapidly decreases with time. Although some synthetic and physical methods are developed to protect such metal particles against oxidation,^{7,8} the problem of oxidation is still of concern during storage and usage. Compared with metal particles, ferrites are less toxic. Ferrites are iron oxides with a common crystalline structure of $MOFe_2O_3$, where M is generally Fe, Ni, or Mn. For

example, maghemite ($\gamma\text{-Fe}_2\text{O}_3$), magnetite (Fe_3O_4) and cobalt ferrites (CoFe_2O_4) (Table 1.1). They all exhibit *ferrimagnetism* in *bulk* phase, and *superparamagnetism* when their sizes are less than a critical size causing thermal energy to be sufficient to overcome the anisotropy barrier of a single particle.⁹ Among them, magnetite (Fe_3O_4) and maghemite ($\gamma\text{-Fe}_2\text{O}_3$) are more suitable for biomedical applications because their biocompatibility has already been proven.¹⁰ Therefore, they have been used in various biomedical applications including cell separation, immunoassay, clinical diagnosis, enzyme and cell immobilization, drug delivery, and hyperthermia.

1.4.1 Bulk Iron oxides: magnetite and maghemite

Iron oxides, the generic name for iron oxides, hydroxides, oxyhydroxides, and other related compounds, are common minerals that are widespread in nature (Table 1.2). Among them, only magnetite (Fe_3O_4) and maghemite ($\gamma\text{-Fe}_2\text{O}_3$) display ferrimagnetism, which is due to their both having a cubic crystalline structure.

Table 1.2. Iron oxyhydroxide and iron oxide species.¹¹

Minerals	Crystallographic system	Formula	Magnetism
Goethite	Orthorhombic	$\alpha\text{-FeOOH}$	Antiferromagnetic
Akaganéite	Monoclinic	$\beta\text{-FeOOH}$	Antiferromagnetic
Lepidocrocite	Orthorhombic	$\gamma\text{-FeOOH}$	Antiferromagnetic
Feroxyhyte	Hexagonal	$\delta'\text{-FeOOH}$	Ferrimagnetic
Ferrihydrite	Hexagonal	$\text{Fe}_5\text{HO}_8 \cdot 4\text{H}_2\text{O}$	Antiferromagnetic
Hematite	Hexagonal	$\alpha\text{-Fe}_2\text{O}_3$	Weakly ferromagnetic
Maghemite	Cubic	$\gamma\text{-Fe}_2\text{O}_3$	Ferrimagnetic
Magnetite	Cubic	Fe_3O_4	Ferrimagnetic

Table 1.3 shows the physical properties of *bulk* magnetite and maghemite. They both have similar physical properties, except for their color and saturation magnetization. Magnetite has slightly higher saturation magnetization (M_s) than maghemite. Such a difference is due to the difference in Fe atom distributions in two sub-lattices between magnetite and maghemite, which will be discussed in the next section.

Table 1.3. Physical properties of maghemite and magnetite.¹¹

	Crystal system	Unit cell dimension (nm)	Density (g/cm ³)	Color	Saturation magnetization (emu/g)
Magnetite (Fe ₃ O ₄)	Cubic	a ₀ = 0.839	5.26	Black	90–98
Maghemite (γ-Fe ₂ O ₃)	Cubic	a ₀ = 0.834	4.87	Reddish-brown	76–81

1.4.1.1 Crystal structure and magnetic properties

Both magnetite and maghemite have an inverse spinel crystal structure with a face-centered cubic unit cell (Figure 1.4). The *fcc* unit cell is made up of cubic close packing (*ccp*)^b of array of oxide (O²⁻) ions, where Fe cations are distributed into two sub-lattices: octahedral (sixfold coordination) and tetrahedral (four coordination) interstices. For the unit cell of magnetite, Fe²⁺ occupies octahedral sites (*o-sites*), while Fe³⁺ occupies tetrahedral (*t-sites*) and octahedral sites (*o-sites*), giving a chemical formula of Fe³⁺₈[Fe²⁺₈Fe³⁺₈]O₃₂. The electron spins of Fe²⁺ and Fe³⁺ in *o-sites* are antiparallel with respect of Fe³⁺ in *t-sites*, giving an inverse spinel arrangement (Figure 1.5). In addition, the spins of Fe²⁺

^b where the sheets are ABCABC...

and Fe^{3+} have unequal magnitudes, thus creating a net magnetic moment within the two sub-lattices and giving rise to the observed ferrimagnetism.

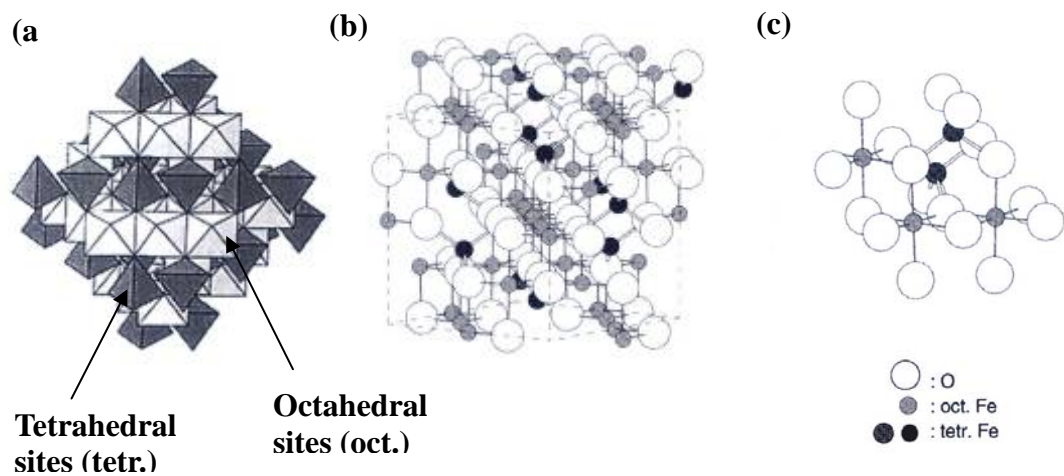


Figure 1.4. Structure of magnetite.¹¹ (a) Polyhedral model with alternating octahedral and tetrahedral sites; (b) ball-and-stick model of unit cell; (c) ball-and-stick model of octahedral (oct.) and tetrahedral sites (tetr.).

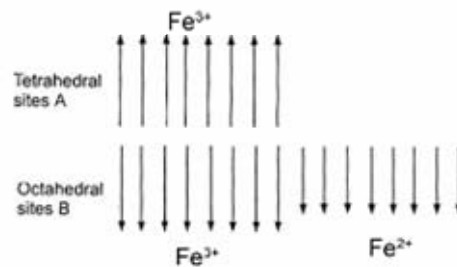


Figure 1.5. Spin arrangements in magnetite.

Maghemite has a structure similar to that of magnetite, only differing in that all Fe cations are in the trivalent state. Cation vacancies compensate for the oxidation of Fe(II) cations. Therefore, maghemite is considered a Fe(II)-deficient magnetite in which Fe^{3+} cations are distributed over the 8 *t-sites* and 16 *o-sites*, while the vacancies (\square) are only confined to the *o-sites*, giving a formula of

$\text{Fe}^{3+}_8[\text{Fe}^{3+}_{5.3}\square_{2.7}\text{Fe}^{3+}_8]_6\text{O}_{32}$. Ferrimagnetism observed in maghemite is due to the net magnetic moment created by the spin distribution and the unequal spin magnitude difference. Due to the deficiency of Fe^{2+} in maghemite, maghemite has slightly lower magnetic susceptibility than magnetite (Table 1.3).

1.4.1.2 Surface properties and chemistry

When magnetite or maghemite nanoparticles are dispersed in aqueous solution, they tend to form aggregates at neutral pH, and subsequently lose their unique properties: superparamagnetism and high surface area. Understanding of the surface properties and chemistry of the nanoparticles are crucial to avoid particle aggregation and prevent loss of their important properties. As mentioned earlier (Section 1.4.1.1), magnetite and maghemite have an inverse spinel crystal structure with a face-centered cubic unit cell where Fe atoms occupy the octahedral and tetrahedral sites formed by the layer sheets of oxides.

In this unit cell, the Fe atoms are not fully coordinated with oxides. Therefore, Fe atoms at the surface of iron oxides act as Lewis acids providing coordination sites for molecules with lone pair electrons (i.e. Lewis bases). When iron oxide nanoparticles are dispersed in water, the Fe atoms that are near the particle surface can readily coordinate with water, leaving the surface with hydroxyl-functionalized groups (Figure 1.6). Such surface hydroxyl groups are amphoteric and are able to react with either acids or bases.¹⁰ Thus, the nanoparticle surfaces can be either positive or negative, depending on the pH of the dispersion.

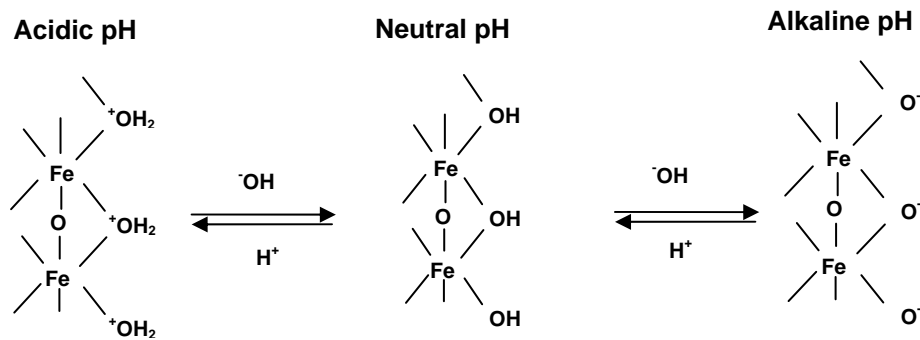


Figure 1.6. Amphoteric nature of magnetite or maghemite.¹¹

This amphoteric surface causes the nanoparticles to form aggregates at neutral pH (i.e. isoelectric point) because electrical charges are not sufficient to overcome the *van der Waals* attractive force between particles. In addition, as the nanoparticles tend to form clusters, magnetic dipole-dipole attractions between particles become significant, thus resulting in an irreversible particle agglomeration. Although the colloidal stability of the nanoparticles can be gained by simply adjusting solution pH away from flocculation range (pH 6–10), as is shown in Figure 1.7, their stability is strongly affected by the presence of highly charged cations (Ca^{2+}) or strong polarizing ions (Na^+ , NH_4^+).¹²

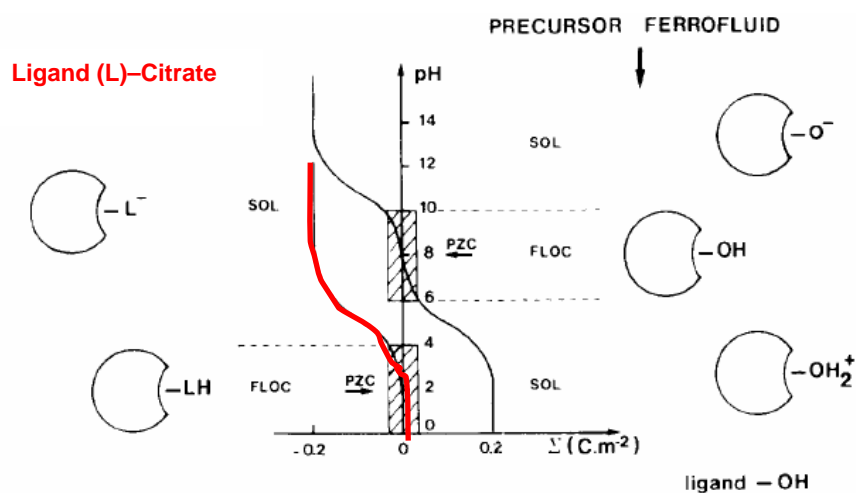


Figure 1.7. pH stability of iron oxide nanoparticles [Adapted from Bacri *et al.* 1990].¹³

To obtain a stable magnetic dispersion, magnetic nanoparticles can be coated with citrate ligand to generate them with negative surface charges (Figure 1.7).¹⁴ This coating is achieved via either (1) chemisorption of the carboxylate group of a citrate molecule onto Fe atoms at the surface of iron oxide nanoparticles (Figure 1.8), or (2) reacting the carboxylate groups with the Fe-OH bonds via an acid-base reaction, giving a Fe-O-C linkage with the elimination of H₂O.¹⁵ Because the carboxyl groups bring the ISE point of the nanoparticles to pH 2, the coated nanoparticles are peptizable for a wide range of pHs.^{13,16} More stabilization methods such as electrostatic stabilization or steric stabilization for magnetic nanoparticles will be discussed in Section 3.2.

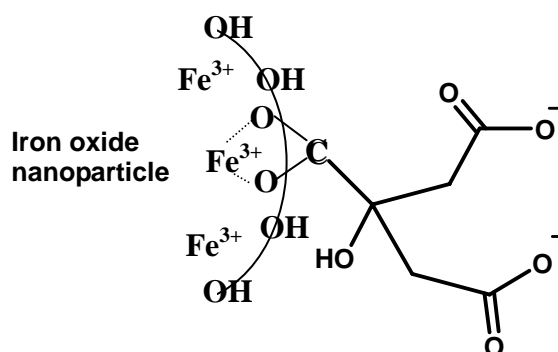


Figure 1.8. Schematic diagram of carboxylic acid chemisorption on the surface of magnetic nanoparticles.

Chapter 2

Applications of Magnetic Iron Oxide Particles

Due to the important features of nano-scale magnetic materials such as high magnetic susceptibility, high surface area to volume ratio and superparamagnetism, there has been an increasing interest in the use of these magnetic nanoparticles for scientific and technological applications, ranging from information storage and electronic devices to medical diagnostic and drug delivery. Among these nanoparticles, magnetic iron oxides (e.g. magnetite and maghemite) have received a great deal of interest because they are non-toxic and biocompatible, and have a good resistance to oxidation.⁸ Hence, applications of these iron oxide nanoparticles are very diverse, including cell separation, immunoassays, drug delivery, magnetic-mediated hyperthermia (MHH), and contrasting enhancers for magnetic resonance imaging (MRI),¹⁷ and electromagnetic interference (EMI) shielding, and ferrofluids. Details of these applications are described as below:

2.1 Magnetic-assisted cell separation and immunoassays

In immunomagnetic separations, antibodies (or other ligands) are attached to the surface of the magnetic particles through condensation reaction between the carboxylic groups of magnetic particles and the amino groups of antibodies (Figure 2.1). Because the antibody can selectively recognize a cell surface antigen, the antibody-attached magnetic particles can selectively bind with the interested cells (e.g. tumors-specific antigens, TSA). Consequently, the resulting conjugates

can be separated from inhomogeneous mixture with the help of a magnet. Molday *et al.* [1984] used immunomagnetic particles conjugated with an antimouse immunoglobulin antibody to separate mouse spleen T and B lymphocytes.¹⁸ The bound cells were then removed by using a magnet. Later, Ugelstad *et al* [1992] used immunomagnetic microspheres coated with anti-sperm antibodies (ASA) for the selective separation of sperms.¹⁹

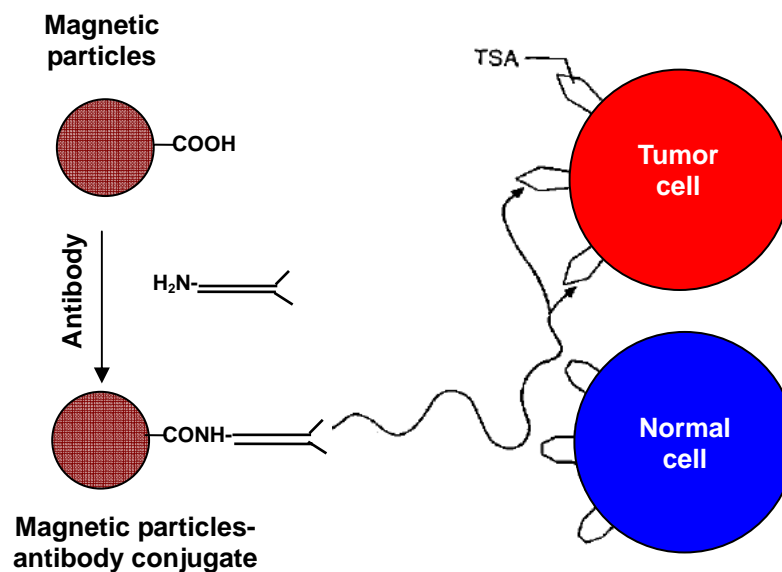


Figure 2.1. Mechanism of immunoselectivity by particle-antibody conjugate.

Magnetic-assisted enzyme immunoassays are an extension of immunomagnetic separation. Figure 2.2 illustrates the principle of magnetic-assisted enzyme immunoassays. The target cells (anti-BSA immunoglobulins) are first bound to BSA-coated magnetic particles, followed by incubation with enzyme-labeled sheep anti-rabbit immunoglobulins (anti-rabbit Ig). After removal of non-target cells and excess anti-rabbit Ig by magnetic separation, the amount of target cells is quantitatively determined.

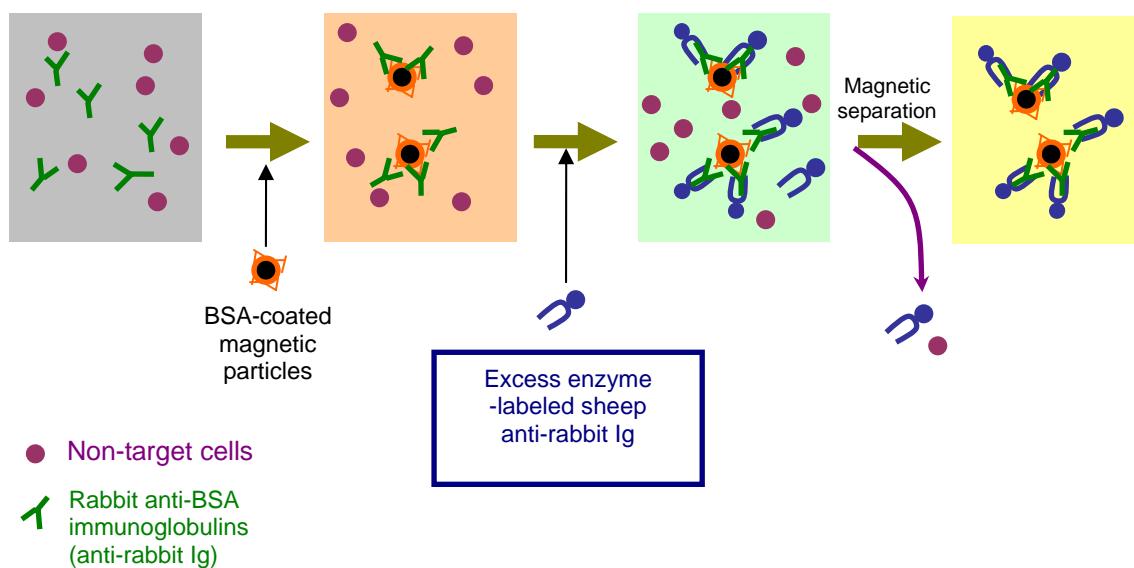


Figure 2.2. Principle of enzyme immunoassays assisted by BSA-coated magnetic particles.

2.2 Drug delivery

In chemotherapy, nonspecific delivery of chemotherapeutic agents always causes toxicity to normal tissue in human body, and easily results in fast reticuloendothelial system (RES) clearance. Therefore, it is of great importance to concentrate and deliver drugs to target organ as precisely as possible and at a controlled delivery rate to reduce the side effects arising from the toxic nature of cancer drugs. Magnetic drug carriers have thus been proposed to achieve this goal. Freeman *et al* [1960] first used fine iron particles for transportation of cancer drugs to the tissues through the vascular system.²⁰ The study showed that the particles carrying drugs were concentrated at a particular point in the body with the aid of a magnetic field (Figure 2.3).

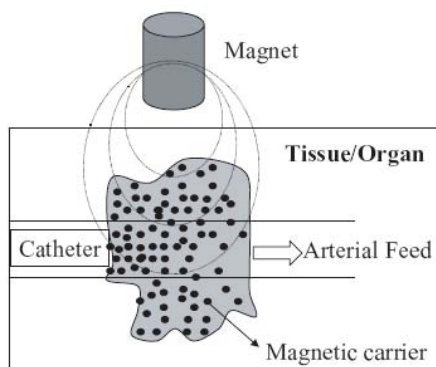


Figure 2.3. Schematic diagram of the magnetic-driven transport of drugs to a specific region. A catheter is inserted into an arterial feed to the tumor and a magnetic stand is positioned over the targeted site.

Magnetic-guidance drug delivery has several advantages: (1) reduce the reticuloendothelial system (RES) clearance of the drugs, hence facilitating extravascular uptake, and (2) lower the drug level in generalized systemic distribution, thereby reducing the side effects to human body.²¹ Due to the high accumulation of the drug in a specific site, small drug dose per administration could be used to further reduce the side effects arising from the drugs. More recently, Gao *et al.* [2004] conducted *in vivo* study in which magnetic microspheres carrying chemotherapeutic drug (aclacinomycin A) were used to treat gastric tumor in a rabbit, resulting a 5 fold dosage higher than non-targeted drugs at the tumor site.²³ The study also showed that there were no toxic effect to other organs such as liver and kidney. Other examples of using magnetic microspheres for drug delivery are summarized in Table 2.1.

Table 2.1. Examples of using magnetic microspheres for drug targeting.

Drug	Target	Magnetic Microcarrier (Size)	Magnetic Content, (wt.%)	Magnetic Field (T*)	Key Results	References
Mitomycin C	VX2 Bladder tumor (Rabbit hind limb)	Ethylcellulose microcapsules	Zinc ferrite (16–50%)	0.35	Complete remission of bladder tumor	Kato <i>et al.</i> (1980) ²⁴
Doxorubicin	Yoshida Sarcoma (Rat tail)	Albumin microcapsules (1 μ m)	Magnetite	0.55	Total remission in 75% of animals	Widder <i>et al.</i> (1981) ²⁵
Inulin	Yoshida sarcoma (Rat foot pad)	Liposomes microcapsules (1 μ m)	Magnetite (20%)	0.2–0.6	Tumor localization	Kiwada <i>et al.</i> (1986) ²⁶
Brilliant blue FCF	Oesophageal cancer (Rabbit)	Bioadhesive granules	Ferrite (50%)	0.19	Granule held in target region at 2 h	Ito <i>et al.</i> (1990) ²⁷
Mitosantrone (MTX)	VX2 Squamous cell carcinoma	Starch coated nanocapsules (~100 nm)	Magnetite (60 %)	1–1.7	Complete remission of tumor	Bergemann, <i>et al.</i> (2000) ²⁸
Doxorubicin (DOX)	Osteosarcoma-bearing hamsters	Liposomes nanospheres (86 nm)	Each liposome contained 1 or 2 magnetite particle(s) (10 nm)	0.4 (60 min)	3-4 fold dosage higher than non-targeted	Nobuto <i>et al.</i> (2004) ²⁹

T* represents tesla (T)

2.3 Magnetic-mediated hyperthermia

Hyperthermia, referred to the treatment of diseases (e.g. cancer, infections) with heat, is one of the promising approaches in cancer therapy. This promising approach is based on the thermal stability difference between tumor and normal cells. Tumors cells no longer exist at temperature higher than 43 °C whereas normal cells do.^{30,31} Therefore, introducing heat elements to tumor sites can give remission of malignant cells.

Various hyperthermia methods for cancer treatment have been well developed and applied in surgical operation during the past two decades. They include: (1) whole body hyperthermia (WBH, with water-filtered infra-red irradiation); (2) radiofrequency capacitance hyperthermia (10-100 MHz) and (3) phased arrays of microwave antennae (requirement of implantation of microwave- or RF-antennas or self-regulating thermoseeds). These methods have already been proven to be effective in providing remission of tumor cells. However, they still have some drawbacks such as unselective or macroscopic heating of the normal tissue around the tumor sites.

Magnetic-mediated hyperthermia (MMH) has thus been developed to solve this problem because this method can allow heating to be restricted within the tumor. The physical principle of this technique is that heat can be induced from magnetic materials when they are placed under an oscillating magnetic field.³² Actually, MMH was first introduced in 1957. Gilchrist *et al.* [1957] conducted *in vitro* study in which ferromagnetic particles were used to embolize

the cancer cell in lymph nodes, followed by applying an external alternating magnetic field to cause heating of the particles.³³ The study showed that ferromagnetic particles were accumulated in regional lymph nodes, and yielded a temperature increase of 14 °C from normal temperature (37 °C) in 3 min. However, heterogeneous and macroscopic heating of surrounding tissues was observed.³³

More recently, because of the rapid growth of nanotechnology, superparamagnetic nanoparticles instead of ferromagnetic particles have been used to treat tumors. Jorden *et al.* [1999] used these nanoparticles for cancer treatment *in vivo*. The study showed that tumor growth was suppressed and controlled within 50 days after subjected to MMH treatment.³⁴ The study also showed that there were no observable macroscopic heating of surrounding tissues.³⁴ This is probably attributed to the high magnetic susceptibility of superparamagnetic nanoparticles at alternating AC magnetic field, producing more uniform heating.^{35,36}

2.4 Contrast Agents for magnetic resonance imaging (MRI)

Magnetic resonance imaging (MRI) is based on the measurement of proton relaxation rate (or time) of water molecules. Different proton relaxation rate is attributed to the water molecules that exist in different physical and chemical environments. MR imaging is a non-invasive technique, and thus it has been an important tool for clinical diagnosis. The development of this technique has prompted the need for a new class of pharmaceuticals, so-called magneto-pharmaceuticals.³⁷ Such pharmaceuticals are called contrast agents and

are used to (1) enhance the contrast between the normal and diseased tissues; and (2) indicate the status of organ functions or blood flow.³⁸ Two types of MRI agents have been suggested (Figure 2.4). Paramagnetic particles have been used as contrast agents such as gadolinium (III) chelates, which is also referred to T1 (longitudinal relaxation time) agents. However, these agents are highly toxic and give low contrast enhancement. On the other hand, superparamagnetic iron oxide (SPIO) nanoparticles such as maghemite and magnetite are considered as T2 (transversal relaxation time) agents that are non-toxic and give high contrast enhancement. Therefore, clinical use of these SPIO agents has been approved.

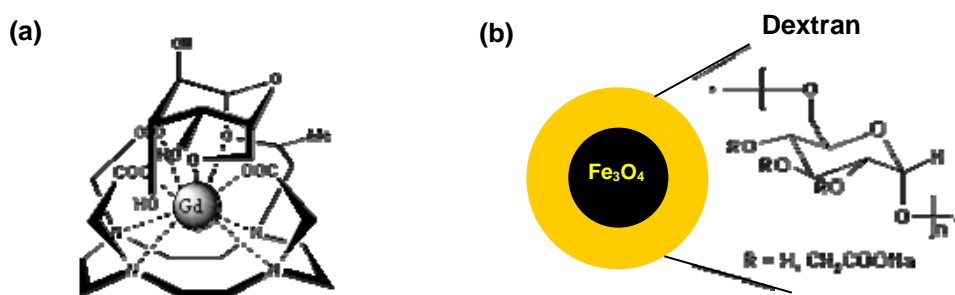


Figure 2.4. (a) T1 agent (e.g. Gd-HPDO3A complex or EGadMe³⁹) and (b) T2 agent (e.g. dextran-coated superparamagnetic nanoparticles).

These SPIO contrasting agents usually consist of *superparamagnetic* iron oxide as a core and biopolymer as a shell. The commonly used biopolymer coatings are dextran, starch, albumin, silicones, and poly(ethylene glycol).⁴⁰ It is notable that dextran-coated iron oxides are biocompatible and are accumulated and excreted via the liver, thus they have been used for liver contrasting.^{41, 42} The SPIO contrasting agents tend to be classified into two main groups according to their size, which significantly influence both their physiochemical and pharmacokinetic properties.⁴³ The first group is SPIO (superparamagnetic iron

oxides) where nanoparticles have a size greater than 50 nm (including the coating); while the second type is USPIO (ultrasmall superparamagnetic iron oxides) where nanoparticles are smaller than 50 nm.

According to the pharmacokinetics, SPIO agents are easily removed from human body by reticuloendothelial system (RES) clearance. Therefore, they are used for imaging of gastrointestinal tract, liver and spleen, lymph nodes.⁴³ Lumirem[®] (silicon-coated magnetic particles with a diameter of 300 nm) and Endorem[®] (magnetite particles with 150 nm) are two example of SPIO agents on the market.⁴⁴ USPIO agents have a longer half-life in the blood stream than SPIO. Therefore, USPIO agents are used for perfusion imaging of brain, central nervous system and myocardial ischemic diseases.^{42,43} Sinerem[®] (magnetite particles with a diameter of 30 nm) is an example of a USPIO agent available in the market, which is currently used for tumor detection.⁴⁴

2.5 Electromagnetic interference (EMI) shielding

Electromagnetic interference (EMI) shielding refers to the reflection and/or absorption of electromagnetic radiation by a material, which thereby acts as a shield against the penetration of the radiation through the shield.⁴⁵ Electromagnetic radiation is composed of electric and magnetic components that oscillate perpendicular to each other, and are in phase with each other (Figure 2.5). Electromagnetic radiation, particularly at high frequencies (e.g. radio waves emanating from cellular phones), tends to interfere with electronics. Furthermore, the radiation may lead to an increase in the risk of coronary artery disease,

Parkinson's and Alzheimer's disease, Leukaemia and brain cancer. Thus, it is of significant importance for development of effective EMI shielding materials.

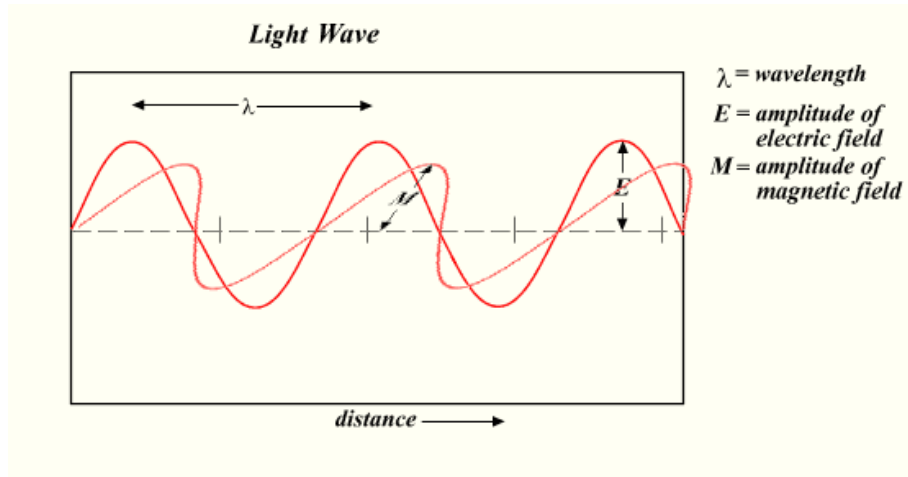


Figure 2.5. Schematic diagram of electromagnetic fields.

An effective EMI shielding material should be the combination of both electrical and magnetic components⁴⁶ because both components can independently interact with electromagnetic field in the radiation, causing reflection and absorption of the radiation. Therefore, composite materials having both conducting and magnetic properties have been widely studied for the EMI application, for example, poly(pyrole-*N*-propylsulfonate)/ γ - Fe_2O_3 ⁴⁷, polypropole/ γ - Fe_2O_3 ,⁴⁸ and polyaniline/ γ - Fe_2O_3 .^{46,49}

2.6 Ferrofluids

Ferrofluids are made up of ferro- or ferri-magnetic single domain particles in dispersing medium with long-range order between the particles. Applications of ferrofluids include sealing, vibration damping, heat transfer, and bearing.⁵⁰

Chapter 3

Magnetic-Responsive Particles: Literature Methods and Our Approach

3.1 Synthesis of surface-modified magnetic iron oxide nanoparticles and their applications

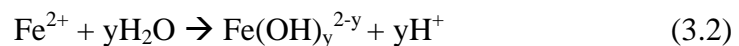
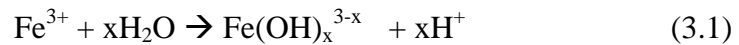
It is of scientific and technological challenge to synthesize magnetic iron oxide nanoparticles with sizes ranging from 5 to 30 nm. Physical methods such as aerosol/vapor deposition, spray pyrolysis and laser pyrolysis can produce ultrafine magnetic nanoparticles with sizes in the range of 5 to 60 nm. However, the nanoparticles obtained tend to aggregate into larger particles, resulting in broad size distribution and loss of their superparamagnetic properties.³⁷ The wet chemical routes to iron oxide nanoparticles are simpler, more tractable and efficient because of their appreciable control over size, composition and even the shape of the nanoparticles.³¹ In this chapter, different strategies based on the wet chemical method will be reviewed, including co-precipitations, microemulsions, and high-temperature decomposition of organic precursors.

3.1.1 Co-precipitations from bulk solutions and their modifications

Magnetic iron oxide nanoparticles (either magnetite or maghemite) can be synthesized via co-precipitations of aqueous salts of Fe^{2+} and Fe^{3+} by addition of a base. Conventionally, magnetite (Fe_3O_4) is synthesized by adding a base to these two iron salts in which the molar ratios of Fe^{2+} and Fe^{3+} are 1 to 2. Formation of

Fe₃O₄ nanoparticles is achieved through the process of deprotonation, oxidation, dehydration and precipitation as illustrated in Figure 3.1. The chemical reaction of Fe₃O₄ formation is given as follows:

Deprotonation:



Oxidation and Dehydration:



Overall reaction:



According to the thermodynamics of this reaction, a complete co-precipitation to form Fe₃O₄ is between pH 9 and 14, if keeping such molar ratio (Fe³⁺:Fe²⁺ = 2:1) under a non-oxidizing oxygen-free environment. By controlling the reaction temperature and the oxygen content during the reaction, Fe₃O₄ are readily transformed to maghemite (γ-Fe₂O₃) through the oxidation reaction (Figure 3.4 and Equation 3.5).



The size, shape and composition of these nanoparticles strongly depend on the type of salt used (e.g. chloride, sulfates, nitrates, perchlorates, etc.), the ratio of Fe²⁺ and Fe³⁺, pH, ionic strength of the medium, and time of annealing.¹⁰ Inappropriate control of such reaction parameters would critically affect the

oxidation rate of iron species (Equation 3.3), the rate of nuclei growth and crystal growth.

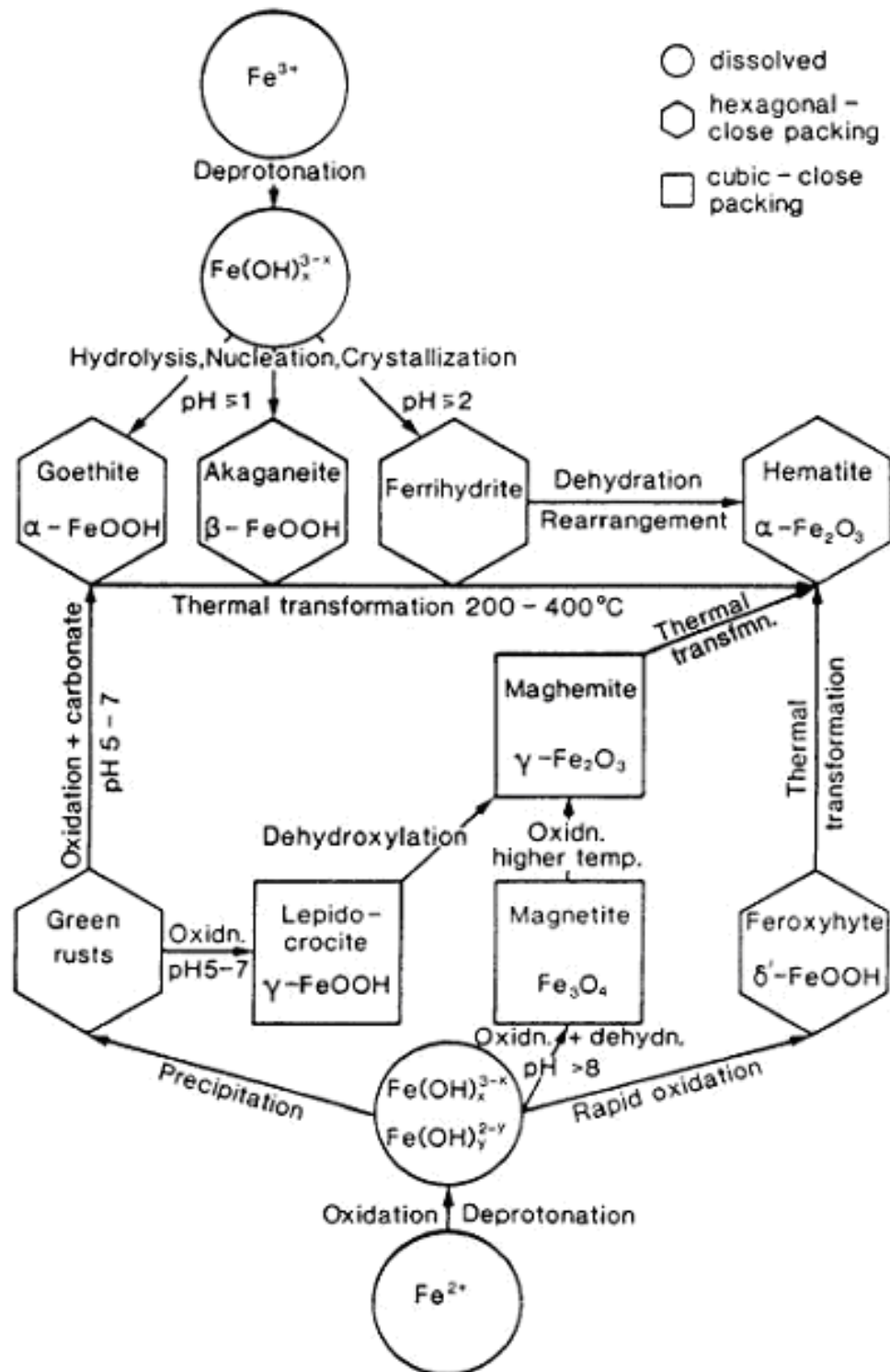


Figure 3.1. Transformation observed in iron oxides [Adapted from ref. 11].

Since the nanoparticles obtained have large *van der Waals* attractive force between each other due to their oxide surface, they tend to aggregate and form large clusters. In addition, these clusters exhibit strong magnetic dipole-dipole attractions between them, resulting in an irreversible agglomeration of the nanoparticle, and subsequent loss of superparamagnetism.⁵¹ Therefore, surface modification of magnetic nanoparticles is often indispensable.³¹

Stabilization of preformed iron oxide nanoparticles can be achieved via either electrostatic or steric stabilization. It is known that carboxylates, phosphates, and sulphates readily adhere to iron oxide surfaces in a specific-substrate manner, as mentioned in Section 1.5.1.2. The nanoparticles with negative surface charges have been prepared by adhering the substances (Figure 3.2): such as trisodium citrate,^{16,52} tetramethylammonium hydroxide (TMAOH), and gluconic acid sodium salt.⁵³

Steric stabilization of iron oxide nanoparticles is achieved by adsorption of amphoretic surfactants on the nanoparticle surface. Assembling a monolayer of these amphoretic surfactant molecules on the nanoparticle surface produces oil-based magnetic fluid (Figure 3.3 a). The aqueous-based magnetic fluid is produced by assemblies of bilayers of surfactant molecules (Figure 3.3 b). The polar head group indicated by the circle at the surface of iron oxide nanoparticles can be either a carboxylate, a phosphate, or a sulfate group. Figure 3.2 shows the example of these surfactants, including sodium laurate, sodium oleate,^{14,54} dodecylphosphonic acid (DPA),⁵⁵ and hexadecylphosphonic acid (HDP).⁵⁵ The aqueous-based magnetic fluid can also be prepared by coating the silica on the

nanoparticle surface via a sol-gel process.

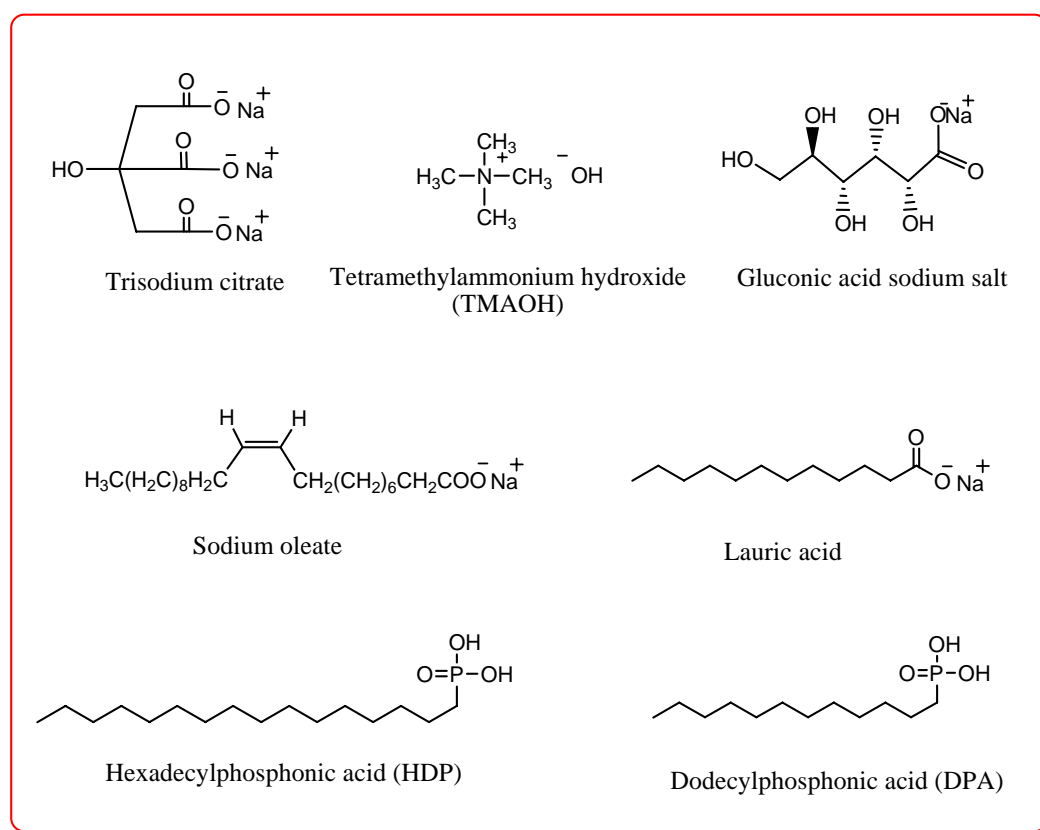


Figure 3.2. Chemical structures of organic salts and surfactants.

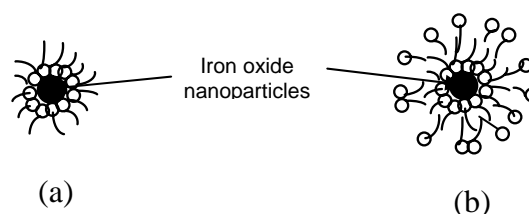


Figure 3.3. Schematic diagram of dispersion states of magnetic fluid: (a) oil-based formed a monolayer of surfactants and (b) aqueous-based formed a bilayer of surfactants.

Coating magnetic nanoparticles with silica is also a promising approach for the preparation of stable magnetic dispersion. Silica coating could effectively protect the nanoparticles from leaching in an acidic environment. Furthermore, the

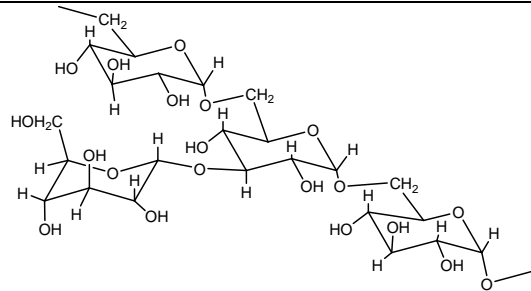
silica coating could be easily activated by introducing silane coupling agents to provide the nanoparticles with various functional groups. Van Ewijk *et al.* [1991] used the sol-gel approach to coat a thin layer of silica on the colloidal magnetic nanoparticles.⁵⁶ The silica-coated magnetic composites showed good magnetic responsiveness, and had sizes ranging from 20 to 40 nm but with broad size distribution. Deng *et al.* [2005] also reported that preparation of well-defined silica-magnetite nanoparticles based on the sol-gel method. The morphology and size of silica-coated magnetic particles could be varied by controlling the ethanol to water volume ratio, NH₃ and tetraethyl orthosilicate (TEOS) concentration.⁵⁷

3.1.2 Co-precipitations in the presence of polymers

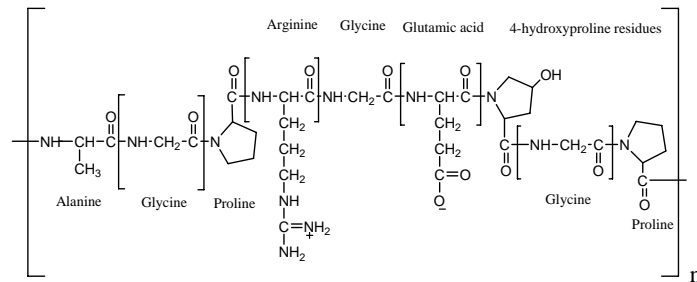
Another approach to prepare surface-modified magnetic nanoparticles is the co-precipitation of the solutions of Fe²⁺ and Fe³⁺ salts with a base in the presence of polymer. The polymer functions as a stabilizer that stabilizes the nucleation and growth of magnetic nanoparticles during co-precipitation process. Thus, the polymer mediated co-precipitation approach can produce iron oxide nanoparticles with smaller sizes (5 to 30 nm), as compared with the particles produced from bulk precipitation (10–50 nm). Such polymer coating on the nanoparticle surface not only provides colloidal stability for the magnetic nanoparticles, but also provides biocompatibility and functionalities for further modifications. Table 3.1 shows a list of polymers that have been used for the synthesis of surface-modified iron oxide nanoparticles. Potential applications of these polymer-coated iron oxide nanoparticles are also illustrated.

Table 3.1. A list of polymers that have been used for the synthesis of surface-modified iron oxide nanoparticles and their potential applications.

Polymers	Properties	Potential applications
Poly(acrylic acid) $\left[\text{CH}_2 - \underset{\text{COOH}}{\text{CH}} \right]_n$ or Poly(methacrylic acid) $\left[\text{CH}_2 - \underset{\text{COOH}}{\overset{\text{CH}_3}{\text{C}}} \right]_n$	<ul style="list-style-type: none"> - Increase biocompatibility of the nanoparticles - Provide functionality for ligand attachment 	Tissue engineering and implant-related application ⁵⁸
Polyethylene glycol (PEG) $\left[\text{CH}_2 - \text{CH}_2 - \text{O} \right]_n$	<ul style="list-style-type: none"> - Increase biocompatibility of magnetic nanoparticles - Improve intracellular uptake and enhance ability to cell targeting 	Magnetic resonance imaging (MRI) ^{59,60}
Polyvinyl alcohol (PVA) $\left[\text{CH}_2 - \underset{\text{OH}}{\text{CH}} \right]_n$	<ul style="list-style-type: none"> - Provide better biocompatibility of the nanoparticles and better affinity to enzymes 	Enzyme immobilization ⁶¹
Chitosan $\left[\text{HOH}_2\text{C} - \text{CH}_2 - \text{NH}_2 \right]_n \left[\text{HOH}_2\text{C} - \text{CH}_2 - \text{NH} - \text{CO} - \text{CH}_3 \right]_m$	<ul style="list-style-type: none"> - Enhance colloidal stability and provide functionalities (-NH₂ and -OH) of the nanoparticles for cell and metal adsorption - Enhance biocompatibility 	Recovery of recombinant <i>Escherichia coli</i> ; ⁶² Recovery of metal ions ⁶³
Dextran	<ul style="list-style-type: none"> - Increase biocompatibility of the nanoparticles - Provide functionalities for cell separation and ligand attachment - Improve cellular uptake 	<i>In vitro</i> study of drug delivery ⁶⁴ <i>In vitro</i> study of drug delivery ^{43,65} Magnetic resonance imaging (MRI) ⁶⁶



Gelatin



- Improve T2 relaxivity

Magnetic resonance imaging (MRI)⁶⁷

Polysaccharide derivatives such as starch, pectine and alginates

- Enhance colloidal stability of the particles
- Provide better biocompatibility
- Enhance cellular uptake

Drug and cell targeting⁶⁴

3.1.3 Water-in-oil (W/O) microemulsions

Water-in-oil (W/O) microemulsion (i.e. reverse micelle solution) is a transparent, isotropic and thermodynamically stable transparent two-phase system consisting: water, amphoteric surfactant molecules and oil. Micro-droplets of water phase are confined within the microcavities (i.e. micelles) formed by assemblies of surfactant molecules, in which the hydrophilic heads of surfactant point towards the aqueous phase while hydrophobic tails extend out into the oil phase. Thus, the aqueous microdroplets can be well dispersed in an oil continuous phase.

Because such microcavities are thermodynamically stable and have sizes in the range of 10 nm, they can be served as a nanoreactor that limits the nucleation, growth and agglomeration of magnetic nanoparticles.⁶⁸ Hence, W/O microemulsions have been shown to be an adequate, versatile and simple method to prepare magnetic nanoparticles. Table 3.2 summarizes various methods for the synthesis of iron oxide nanoparticles using microemulsion technique. López-Quintela and Rivas [1993] prepared magnetite nanoparticles with an average diameter of 4 nm.⁶⁹ Reverse micelle solutions of ferrous and ferric chloride were first prepared by mixing aqueous ferrous and ferric chloride, dioctyl sodium sulfosuccinate (AOT) as a surfactant, and heptane as an oil continuous phase. Subsequent addition of ammonium hydroxide at room temperature yielded the magnetite nanoparticles (Figure 3.4). Feltin *et al.* [1997] also used this system to prepare magnetite nanoparticles with average sizes from 4 to 12 nm and their standard deviation ranging from 0.2 to 0.3.⁷⁰ A ferrous dodecyl sulfate, Fe(DS)₂,

micelle solution was first prepared by mixing sodium dodecyl sulfate and ferrous chloride at 2 °C, followed by addition of methylamine to the micelle solution under continuous stirring at 50 °C to form magnetite nanoparticles. The sizes of the particles were controlled by varying surfactant concentration and reaction temperature. However, the nanoparticles obtained through this route were poorly crystalline, because the synthetic procedure is usually performed at a relatively low temperature. Furthermore, the yield of the nanoparticles is often very low.⁷¹

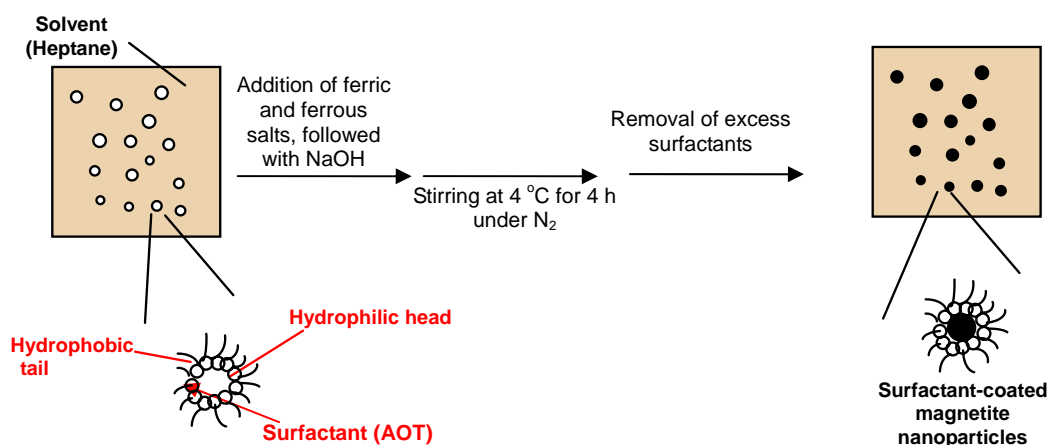


Figure 3.4. Synthesis of AOT-coated magnetite nanoparticles using microemulsion approach.

Recently, significant improvement of the reverse micelle technique has been achieved by Lee *et al.* [2005].⁷¹ Large-quantities of highly crystalline magnetite nanoparticles were synthesized by controlled hydrolysis and high-temperature oxidation. Reverse micelle solution of Fe(DBS)₂ was first prepared by mixing aqueous ferrous and ferric chloride, sodium dodecylbenzene sulfonate (NaDBS), and xylene. Subsequent addition of hydrazine promotes the controlled hydrolysis

of Fe(DBS)₂ solution. Further refluxing the resulting solution at high temperature promotes the formation of highly crystalline magnetite nanoparticles.

Table 3.2. Preparation of surfactant-stabilized magnetic nanoparticles using microemulsion approach.

Authors	Precursors	Surfactants	Size (nm)	Nano-particles	Other related References
López-Quintela and Rivas 1993	FeCl ₂ and FeCl ₃	Diocetyl sodium sulfosuccinate (AOT)	~4	Fe ₃ O ₄	Lee, <i>et al</i> (1992), ⁷² Dresco, <i>et al</i> (1999), ⁷³ O'Connor, <i>et al.</i> (1999) ⁷⁴
Yaacob 1994 ⁷⁵	FeCl ₂	Cetyltrimethylammonium bromide (CTAB)/dedecylbenzenesulphonic acid (DBSA)	2–3	Fe ₃ O ₄	Nil
Feltin, et al 1997	FeCl ₂	Sodium dodecyl sulfate (SDS)	4–12	Fe ₃ O ₄	Nil
Carpenter 2001 ⁷⁶	FeSO ₄	CTAB/butanol	5–30	Fe/Au	Liz, <i>et al.</i> (1993) ⁷⁷
Lee, et al. 2005	FeCl ₂ and FeCl ₃	Sodium dodecylbenzene sulfate (NaDBS)	2–10	Fe ₃ O ₄	Nil

3.1.4 High-temperature decomposition of organic precursors

The decomposition of iron precursors in the presence of hot organic surfactants has recently yielded remarkable improvement of magnetic nanoparticles with controllable size and shape. A good control of size and shape is of significance for applications of magnetic nanoparticles in catalysis, energy storage, magnetic data storage, and sensors.⁷⁸ Alivisatos and co-workers [1999] have demonstrated that injecting the solutions of FeCup_3 (Cup: N-nitrosophenylhydroxylamine) into long-chain amines (octylamine as a surfactant) at 250–300 °C yielded highly crystalline maghemite nanocrystals with average diameters ranging from 4 to 10 nm.⁷⁸ The resulting nanocrystals were readily dispersed in various organic solvents.

Hyeon and co-workers [2001] also used this non-hydrolytic method to prepare maghemite nanocrystallites.⁷⁹ Figure 3.5 illustrates the synthetic reaction conditions. Formation of these nanocrystallites is achieved via decomposition of $\text{Fe}(\text{CO})_5$ in octyl ether in the presence of oleic acid reverse micelle at 100 °C, followed by transformation of the *in situ* generated iron oleate complex to Fe nanoparticles at 300 °C. The nanoparticles were then oxidized to form maghemite using mild oxidant (trimethylamine oxide). The resulting maghemite were highly crystalline. By varying the molar ratio of surfactant and $\text{Fe}(\text{CO})_5$, the nanocrystals with average diameters ranging from 8 to 16 nm were produced.

More recently, Sun and Zeng [2002] reported the size controlled synthesis of magnetite nanoparticles through the combination of the non-hydrolytic and

seed-mediated growth technique.⁸⁰ Magnetite seeds with average size of 4 nm were first prepared by decomposition of iron(III) acetylacetonate ($\text{Fe}(\text{acac})_3$) in phenyl ether in the presence of alcohol, oleic acid, oleylamine at 265 °C. $\text{Fe}(\text{acac})_3$ solution was injected again in order to supersaturate the seed crystals. Further decomposition of $\text{Fe}(\text{acac})_3$ in the presence of magnetite seeds yielded larger nanocrystals with an average size of 20 nm. Park and co-workers [2005] also demonstrated that the seed-mediated growth approach can effectively control the size of maghemite nanocrystallites produced.⁸¹ Despite of the success of these approaches, there are still some limitations such as: (1) the use of expensive and toxic reagents, (2) complicated synthetic steps, and (3) requirement of a precise reaction temperature control. Hence, large-scale and economic production of magnetic nanocrystallites using this non-hydrolytic approach is not viable.

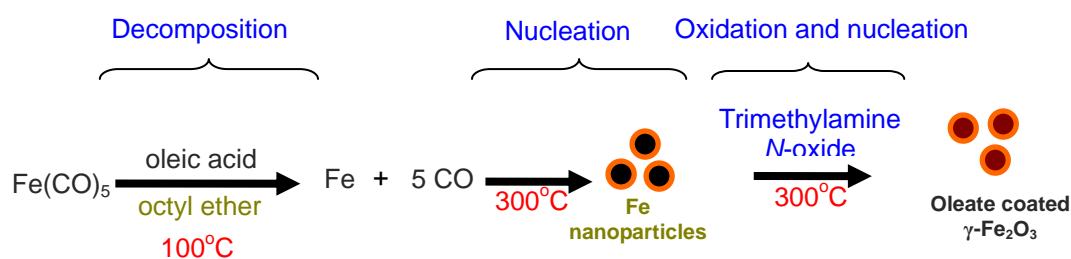


Figure 3.5. Formation of maghemite nanocrystallites using high-temperature decomposition of $\text{Fe}(\text{CO})_5$ in the presence of hot organic surfactants.

3.1.5 Summary

Table 3.3 summarizes the different synthetic methods to prepare magnetic iron oxide nanoparticles.

Table 3.3. Comparison of different synthetic methods to magnetic iron oxide nanoparticles.

Approaches	Size and size distribution	Advantages	Disadvantages	Potential applications
Physical methods (aerosol/vapor deposition; spray and laser pyrolysis)	About 5–60 nm with very broad size distribution	(1) High production rate (2) Large-quantity synthesis	(1) Easy formation of large aggregates	(1) Protective coating (2) Production of magnetic thin film
Precipitation from bulk solution	About 10–50 nm with broad size distribution	(1) Simple synthetic steps (2) Large-quantity synthesis	(1) Poor control over size and shape (2) Poor colloidal stability (3) Dissolution of magnetic nanoparticles under acidic environment	
Precipitation in the presence of natural polymers or surfactants	About 5–30 nm with broad size distribution	(1) Simple synthetic steps (2) Large-quantity synthesis	(1) Poor control over size and shape (2) Leaching of magnetic nanoparticles (3) Dissolution of magnetic nanoparticles under acidic environment	(1) Cell separation (2) Magnetic resonance imaging (MRI) (4) Drug and cell targeting (5) Recovery of metal ions (6) Enzyme immobilization
Microemulsions (hydrolytic approach)	About 4–20 nm with narrow size distribution	(1) Well control over size and particle shape	(1) Requirement of large amounts of surfactants (2) Difficult to remove residue surfactants (3) Particles with poor crystallinity	(1) Catalysis (2) Energy storage (3) Magnetic data storage (4) Sensors
High-temperature decomposition of organic precursors (non-hydrolytic approach)	About 2–20 nm with very narrow size distribution	(1) Well control over size and particle shape (2) Particles with high crystallinity	(1) Use of toxic and air sensitive reagents (2) Use of expensive reagents (3) Only for small-quantity preparation	(1) Catalysis (2) Energy storage (3) Magnetic data storage (4) Sensors

3.2 Synthesis of magnetic core-shell polymeric particles and their applications

Coating of polymers on the surface of magnetic nanoparticles enhances their compatibility with organic ingredients, reduces leaching of the nanoparticles, and protects them from oxidation. Furthermore, magnetic nanoparticles encapsulated into polymer matrixes show better dispersibility, chemical stability and biocompatibility.⁸²

Synthesis of polymer-encapsulated magnetic nanoparticles was pioneered by Ugelstad *et al* [1993].⁸³ The methodology is based on direct precipitation of iron salts inside the pores of porous polystyrene (PS) particles. Iron salts are nucleated and crystallized in the confined pores within the PS particles. As a result, PS particles with magnetic nanoparticles encapsulated inside the pores were produced. The resulting particles showed very good magnetic response. Subsequent attachment of biomolecules on the nanoparticle surface showed selective binding with cells. This innovative work attracted a great deal of interest in the design and fabrication of magnetic polymer particles for cell separation and other biomedical applications. Up to now, various synthetic strategies for the preparation of magnetic polymeric particles have been reported, including (1) suspension cross-linking, (2) layer-by-layer (LBL) self-assembly method, (3) seed precipitation polymerization, (4) emulsion polymerization and (5) miniemulsion polymerization.

3.2.1 Suspension cross-linking approach

Suspension cross-linking approach has been reported as a simple and an efficient method for the encapsulation of magnetic nanoparticles in polymer matrix. Denkbas *et al.* [2002] prepared micro-sized magnetic chitosan particles with magnetic nanoparticles encapsulated inside (Figure 3.6).⁸⁴ Stable magnetic emulsion droplets were first prepared by rigorous stirring the heterogeneous mixture containing aqueous-based magnetic nanoparticles, chitosan, emulsifier and diethyl ether. Subsequently, the chitosan in the emulsion droplets were cross-linked by addition of glutaraldehyde. After removal of the organic solvents and the excess emulsifiers, the magnetic particles obtained were readily dispersed in water. However, the particles produced showed micro-sized with very broad size distribution (100–250 μm). Furthermore, the magnetic nanoparticles were unevenly distributed in chitosan matrix. Besides chitosan, albumin and poly(vinyl alcohol) (PVA) have also been employed for encapsulation of magnetic nanoparticles via suspension cross-linking approach (Table 3.4). However, the resulting particles were usually micron-sized with very broad size distribution.

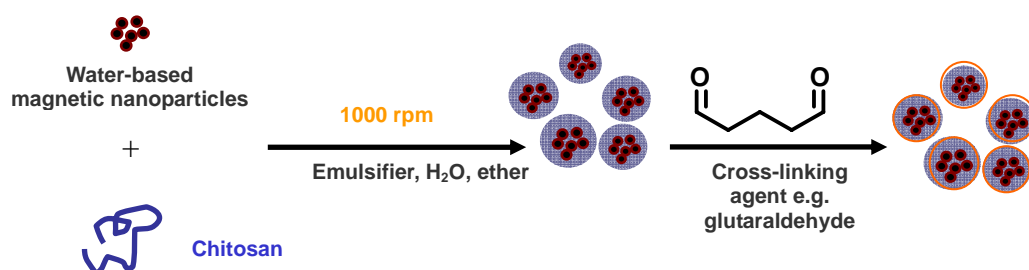


Figure 3.6. Preparation of magnetic chitosan microspheres via suspension crosslinking approach.

Table 3.4. Encapsulation of magnetic nanoparticles via suspension cross-linking.

Polymers	Crosslinker	Size (μm)	Potential Applications	References
Albumin	Glutaraldehyde	~ 1	Drug encapsulation (adriamycin)	Gupta <i>et al.</i> (1988); ⁸⁵ Chatterjee <i>et al.</i> (2003) ⁸⁶
Chitosan	Glutaraldehyde	100–250	Cell separation; removal of metal ions	Hassan <i>et al.</i> (1992); ⁸⁷ Rorrer <i>et al.</i> (1992); ⁸⁸ Honda <i>et al.</i> (1998) ⁸⁹
Polyvinylalcohol (PVA)	Glutaraldehyde	10–30	Detection of haemoglobin	Müller-Schulte (1995) ⁹⁰

3.2.2 Layer-by-layer (LBL) approach

Another strategy to prepare magnetic polymeric particles with improved size distribution is the LBL self-assembly method. This method was first developed for the construction of ultrathin films.^{91,92} Later, Caruso *et al.* [2001] further developed this method for the controlled synthesis of novel magnetic core-shell nanocomposites that consist of alternating layers of magnetic nanoparticles and polyelectrolytes as a shell, polystyrene as a core.⁹³ The synthetic procedure is illustrated in Figure 3.7. Core-shell polymer template was first prepared by deposition of three layers of poly(allylamine hydrochloride) (PAH) onto polystyrene (PS) particle surface. Magnetite nanoparticles with average diameters ranging from 10 to 15 nm were then adsorbed onto the polymer template (640 nm) through electrostatic complexation. Alternating deposition of PAH and magnetite nanoparticles resulted in the formation of multilayer shells on the template surface. The resulting particles had sizes ranging from 600 to 800 nm, depending on the number of layers deposited on the particle surface. In spite of the

success of this approach, this method is time-consuming due to sequential polyelectrolyte and magnetic nanoparticle depositions and purification cycles. In addition, the leaching problem of magnetic nanoparticles from the inner shell layer, and the stability issue of the shell layers to pH and electrolyte changes may still be of concern.

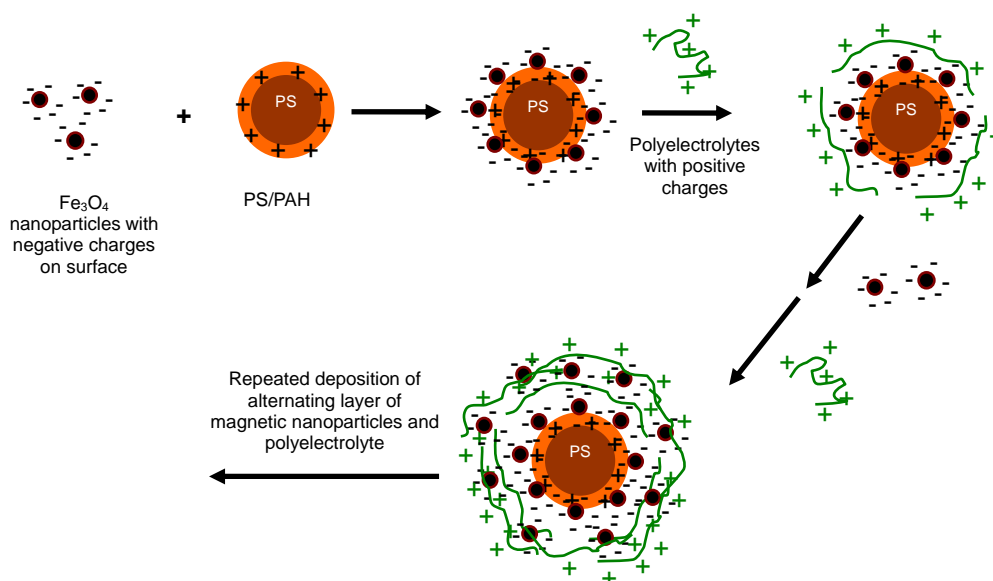


Figure 3.7. Formation of magnetic core-shell nanocomposites using LBL approach.

3.2.3 Seed precipitation polymerization

Micrometer-sized and submicrometer-sized magnetic core-shell polymeric particles have been synthesized based on seed precipitation polymerization. Sauzedde *et al.* [1999] prepared the hydrophilic temperature-sensitive magnetic latexes, as shown in Figure 3.8.^{94,95} Seed magnetic particles were prepared by adsorption of negatively charged iron oxide nanoparticles onto positively charged

colloidal template (i.e. polystyrene/poly(*N*-isopropylacrylamide) core-shell particles) (PS/PNIPAM). The encapsulation was performed via co-polymerization of *N*-isopropylacrylamide (NIPAM), *N,N*-methylene bisacrylamide (MBA), itaconic acid (IA) in the presence of the seed particles. The resulting particles had diameters between 500–800 nm with narrow size distributions. However, this encapsulation process is quite difficult to be controlled.⁹⁶

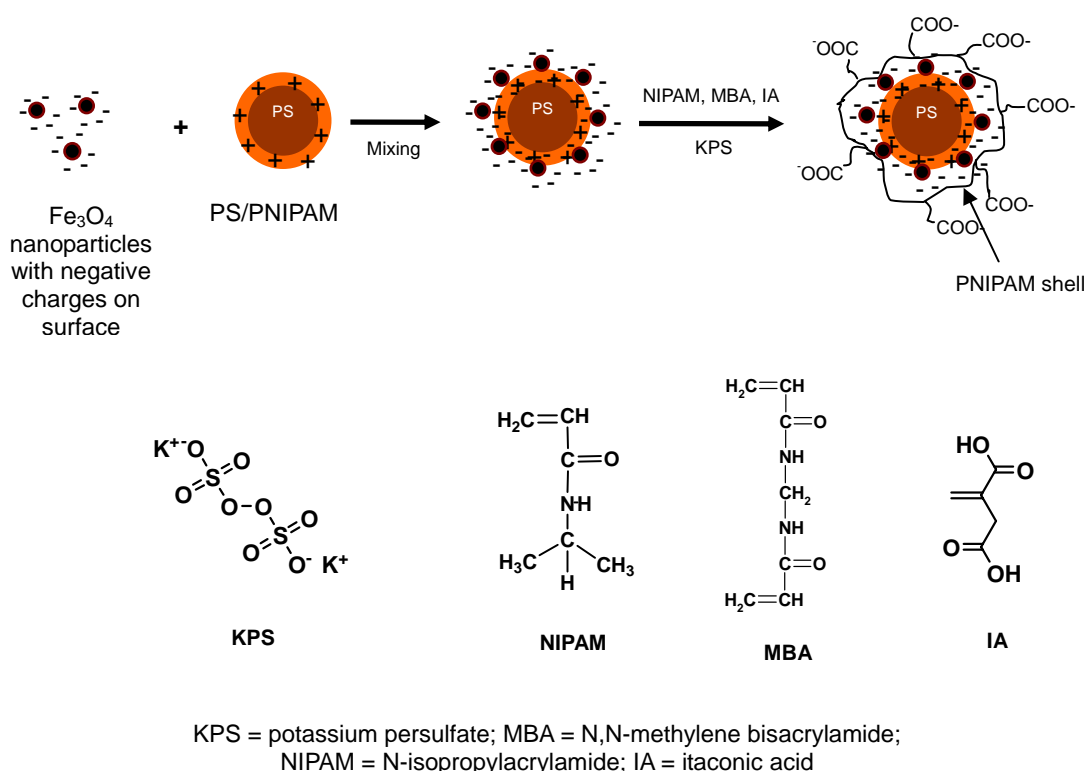
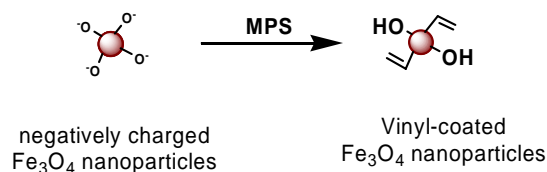


Figure 3.8. Preparation of hydrophilic temperature-sensitive magnetic latexes using seed precipitation polymerization.

Zaitsev *et al.* [1999] also prepared magnetic polymeric particles via seed precipitation polymerization of methacrylic acid and hydroxyethyl methacrylate in the presence of tris(hydroxyl methyl)aminomethane hydroxide-coated magnetite nanoparticles in ethyl acetate medium.⁹⁷ The resulting particles had a diameter around 150 nm but with broad size distribution. Gu *et al.* [2003] first prepared

vinyl-coated magnetic nanoparticles via condensation of a silane coupling agent onto positively charged magnetic nanoparticles (Figure 3.9).⁹⁸ Styrene-swollen polystyrene particles containing silanol groups were then prepared via surfactant-free emulsion polymerization of styrene and the vinyl groups of a silane coupling agent. During this polymerization, the vinyl-coated magnetic nanoparticles were feed into the styrene-swollen polystyrene particles. Subsequent condensation and copolymerization of these vinyl-coated nanoparticles with styrene monomers resulted in the encapsulation of magnetic nanoparticles into the polystyrene matrix. The particles produced had an average diameter of 320 nm with narrow size distribution. Furthermore, the particles had a core-shell nanostructure, where magnetic nanoparticles were embedded inside polystyrene particles.

Step 1: Preparation of vinyl-coated Fe₃O₄ nanoparticles



Step 2: Co-polymerization of styrene and vinyl-coated Fe₃O₄ nanoparticles

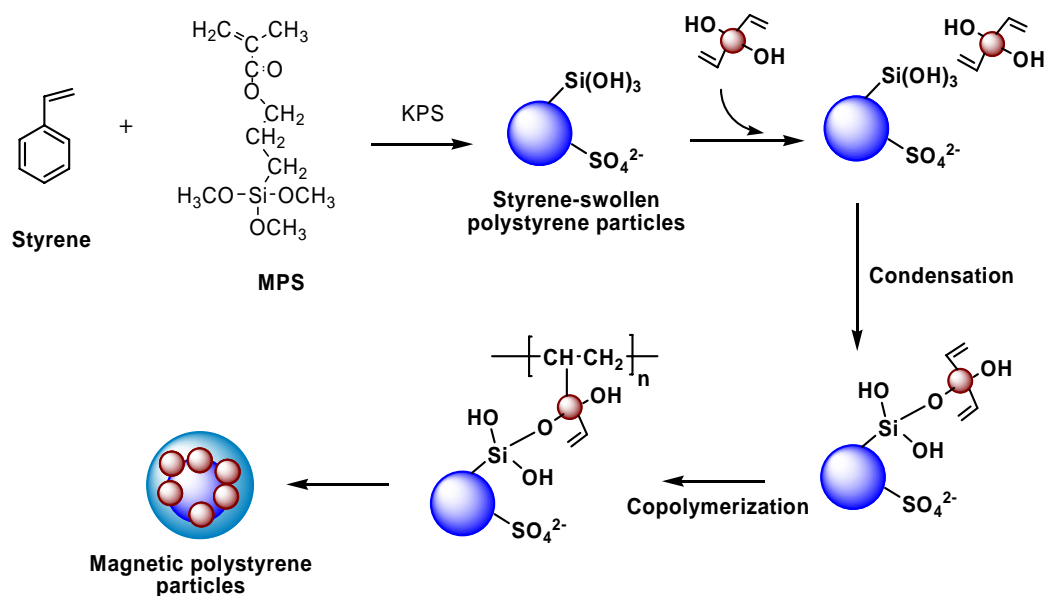


Figure 3.9. Synthesis of magnetic/polystyrene microspheres.

More recently, Deng and co-workers [2003] developed a more convenient and simpler approach to prepare hydrophilic temperature-sensitive magnetic latexes with a well-defined core-shell nanostructure (Figure 3.10).⁹⁶ Vinyl-coated magnetic nanoparticles were first prepared by condensation of silica on the negatively charged nanoparticle surface based on a modified Stöber method, followed by the addition of a silane coupling agent. Subsequently, these vinyl-coated nanoparticles were directly copolymerized with NIPAM and MBA to form stable magnetic temperature-sensitive polymeric particles (Figure 3.10). The particles produced had an average diameter of 350 nm with narrow size distribution. Furthermore, the particles had a well-defined core-shell nanostructure,

where magnetic nanoparticles were encapsulated into the PNIPAM cores. Furthermore, the particles showed good magnetic and temperature responsiveness. However, the particles produced by this method had limited amounts of surface functional groups for further modifications.

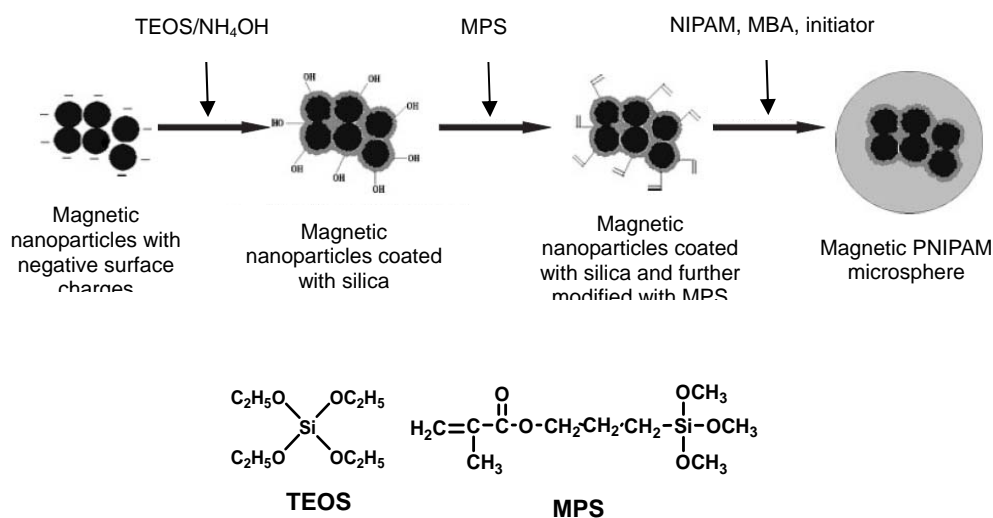


Figure 3.10. Synthesis of magnetic/PNIPAM microspheres.

3.2.4 Emulsion/inverse microemulsion polymerization

One of the promising techniques for the encapsulation of magnetic nanoparticles into polymer matrix is using emulsion polymerization technique. Daniel and co-workers [1982] obtained magnetic polymeric particles by first mixing organic-based magnetic nanoparticles with hydrophobic vinyl monomer and emulsifier.⁹⁹ The mixture was then emulsified in water. Subsequent polymerization of the emulsion droplets resulted in the particles with magnetic nanoparticles as a core and hydrophobic polymer as a shell. However, the resulting particles had very broad size distribution ranging from 30 and 5000 nm.

Charmot and Vidil [1994] used a similar method to prepare magnetic polymeric particles with extra addition of a vinyl cross-linker.¹⁰⁰ Although the size distribution of the particles was improved, the particles produced contained a mixture of magnetizable and non-magnetizable particles.

Dresco and coworkers [1999] reported a one-step synthesis for the encapsulation of magnetite nanoparticles in polymer matrix.⁷³ Inverse microemulsion droplets were first prepared by mixing water-soluble monomers (i.e. methacrylic acid and hydroxyethyl methacrylate), cross-linker, surfactant, aqueous-based magnetite nanoparticles and toluene. Co-polymerization of these emulsion droplets gave stable magnetic polymer composites, where magnetite nanoparticles were coated with hydrophilic polymers. Through changing of monomer concentration and water/surfactant ratio, the size of the particles could be varied in the range of 80-320 nm. However, the resulting particles only contained a magnetic content of 3.3 w/w%. Furthermore, it was difficult to remove the residue surfactants adsorbed on the resulting particle surface.

Wormuth *et al.* [2001] also used this approach for the encapsulation of magnetic nanoparticles in polymer matrix.¹⁰¹ Hydrophilic polymer-coated magnetic nanoparticles were first prepared via precipitation of the solution of iron salt into hydrophilic diblock copolymer [poly(ethylene oxide)-*co*-poly(methacrylic acid)]. The coated nanoparticles were mixed with methacrylic acid and hydroxyethylmethacrylate monomers, and then emulsified in decane with ultrasonication. Polymerization of inverse emulsion droplets generated magnetic composite particles. However, the particles obtained had very broad size distribution.

3.2.5 Miniemulsion/inverse miniemulsion polymerization

Miniemulsions are a thermodynamically stable homogeneous liquid,¹⁰² in which stable oil droplets with sizes between 50 and 500 nm are dispersed in an aqueous continuous phase. The oil droplets are confined by surfactant micelles and a highly water-insoluble compound (i.e. hydrophobe). The function of a hydrophobe is to suppress the diffusional degradation (i.e. Ostwald ripening) of monomer droplets in water and reduce collisions between monomer droplets.¹⁰² Thus, oil droplets (i.e. nanoreactors) have very high dispersion stability in an aqueous continuous phase. Because polymerization takes place within these stable nanoreactors, the particles produced are highly duplicated from the miniemulsion droplets. This means that the polymerization does not change the integrity of miniemulsion droplets. Therefore, miniemulsion polymerization has been widely used for the encapsulation of inorganic particles such as carbon black,¹⁰³ and CaCO_3 .¹⁰⁴

Pamírez and Landfester [2003] used miniemulsion polymerization for the encapsulation of magnetite nanoparticles in a polymer matrix (Figure 3.11).¹⁰⁵ The magnetic polymeric particles were obtained by first dispersing oleate-coated magnetite nanoparticles in an organic phase containing hydrophobe (hexadecane), styrene and sodium dodecylsulfate (SDS). The mixture was then emulsified in water by placing it in a high-power homogenizer to form stable miniemulsion droplets. Initiating the polymerization of the miniemulsion droplets generates magnetic polymer composites with a well-defined core-shell nanostructure, where magnetite nanoparticles are coated with a thick layer of polystyrene. The resulting

particles had narrow size distribution, and the magnetic content with respect to the polymer reached 40 w/w%. Xu *et al.* [2004] also prepared magnetic core-shell particles via the inverse emulsion polymerization of acrylamide and a cross-linker in the presence of poly(methacrylic acid)-coated magnetite nanoparticles.¹⁰⁶ The sizes of the particles ranging from 40 to 170 nm were controlled by varying surfactant concentration. However, this technique requires a large amount of surfactants and hydrophobes. In addition, the magnetic particles produced have limited amount of functional groups on their surface.

Formula:

Oil-soluble monomer (M) + surfactants (S) + hydrophobe (octane) + oleate-coated Fe_3O_4 (o- Fe_3O_4) + continuous phase (H_2O) + water-based Initiator

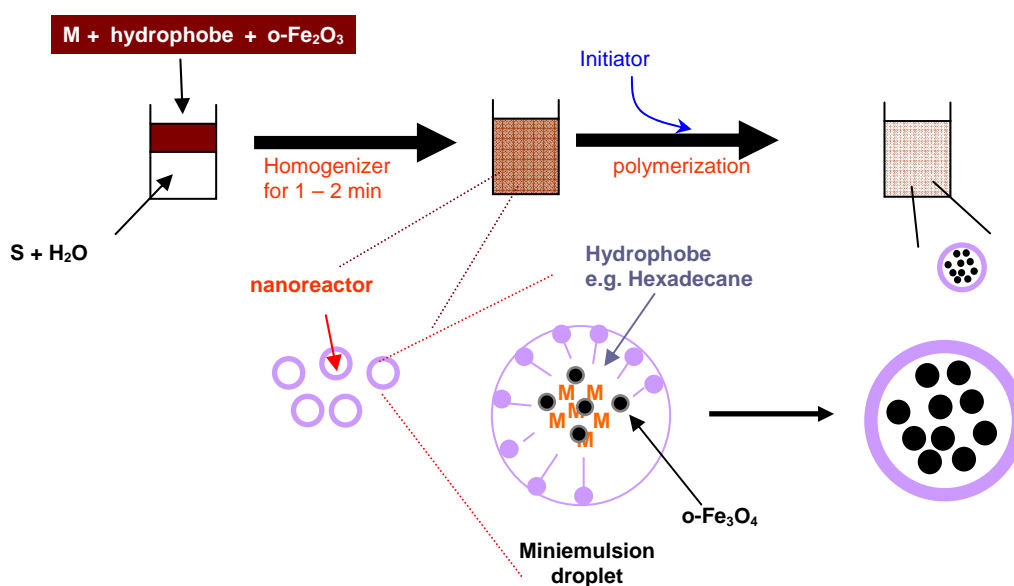


Figure 3.11. Formation of magnetic core-shell particles using miniemulsion approach.

3.2.6 Summary

Table 3.5 compares various approaches for encapsulation of magnetic nanoparticles into polymer matrix.

Table 3.5. Comparison of different encapsulation methods to magnetic polymer composites.

Approaches	Size and size distribution	Advantages	Disadvantages	Potential applications
Suspension cross-linking	About 1–250 μ m with very broad distribution	(1) High production rate (2) Large-quantity synthesis	(1) Use of emulsifier (2) leaching of magnetic nanoparticles	(1) Drug encapsulation (2) Enzyme immobilization (3) Removal of metal ions
Layer-by-layer (LBL) deposition	About 300–600 nm with narrow size distribution	(1) Well control over size and layer compositions (2) Good colloidal stability (3) Good biocompatibility	(1) Tedious synthetic procedures (2) Requirement of sequential deposition and purification cycles (3) Sensitive to electrolytes	(1) Enzyme immobilization (2) Cell separation (3) Drug delivery
Seed precipitation polymerization	About 300–1000 nm with narrow size distribution	(1) Well control over size (2) Good colloidal stability (3) Good biocompatibility	(1) Tedious synthetic procedures (2) Incomplete encapsulation of magnetic nanoparticles (3) Low magnetic content (4) Poor reproducibility	(1) Cell separation (2) Recovery of metal ions (3) Enzyme immobilization (4) Drug encapsulation and drug delivery (5) <i>In vitro</i> diagnostic tools
Emulsion/inverse emulsion polymerization	About 200–1000nm with broad size distribution	(1) Simple synthetic procedures (2) Good colloidal stability	(1) Requirement of surfactants (2) Difficult to remove residue surfactants (3) Incomplete encapsulation of magnetic nanoparticles (4) Low magnetic content (5) broad size distribution	
Miniemulsion/inverse miniemulsion polymerization	About 10–100 nm with very narrow size distribution	(1) Well control over size (2) Complete encapsulation of magnetic nanoparticles (3) Good colloidal stability (4) High magnetic content	(1) Use of hydrophobe (2) Difficult to remove hydrophobe and residue surfactants (3) Requirement of surfactants (4) Limited amounts of surface functional groups	

3.3 Our approach to novel magnetic core-shell (MCS) particles

There has been increasing interest in the design and fabrication of magnetic polymeric particles that consists of magnetic nanoparticle cores coated with polymer shells. Applications of these types of particles are very diverse including electromagnetic interference (EMI) shielding, cell separation, *in vitro* diagnosis, drug delivery, and magnetic resonance imaging (MRI). Such particles have been synthesized via various approaches: (1) co-precipitation of ferrous and ferric salts in the presence of polymer by addition of a base; (2) suspension cross-linking of polymer in the emulsifier-stabilized magnetic nanoparticle dispersion; (3) layer-by-layer (LBL) self-assembly of alternating layers of polyelectrolytes and magnetic nanoparticles onto colloidal template; (4) precipitation polymerization of vinyl monomers onto seed polymer template pre-adsorbed with magnetic nanoparticles; (5) emulsion polymerization of vinyl monomers in surfactant-stabilized micelles containing magnetic nanoparticles; and (6) miniemulsion polymerization of vinyl monomers in surfactant-stabilized nanoreactor containing magnetic nanoparticles.

Despite of the success of these approaches, there are still some drawbacks such as leaching and dissolution problem of magnetic nanoparticles under an acidic environment, broad size distribution, ill-defined core-shell nanostructure, tedious multiple-step syntheses especially in LBL approach, incomplete encapsulation of magnetic nanoparticles, low magnetic content, and the use of large amounts of emulsifiers and surfactants. In addition, magnetic polymeric

particles produced through these approaches have limited amount of functional groups on their particle surface.

3.3.1 Research Aims

The aim of this research was to develop a simple, convenient, and surfactant/emulsifier-free approach to prepare magnetic core-shell (MCS) polymeric particles with a well-defined core-shell nanostructure, where the magnetic nanoparticles were all encapsulated inside the polymer matrix. Besides the well-defined core-shell nanostructure, the particles should have other desirable properties such as 1) narrow size distribution, 2) good colloidal stability in aqueous solution, 3) abundant surface functional groups for subsequent modifications, 4) good magnetic responsiveness, and 5) high antibacterial properties especially when used as coating materials.

3.3.2 Design rationale of MCS particles

To achieve these objectives, we have designed a novel magnetic particle with a well-defined core-shell nanostructure, as shown in Figure 3.12. The core-shell particle consists of poly(methyl methacrylate) (PMMA) and magnetic nanoparticles (γ -Fe₂O₃) as a core, and chitosan as a shell. The PMMA core acts as a solid support and a barrier to prevent γ -Fe₂O₃ nanoparticles from leakage and acid attack. Furthermore, the PMMA core provides a good film-forming ability for MCS particles when used as coating materials. The chitosan shell provides colloidal stability, surface functionalities and anti-bacterial properties. Chitosan

was chosen as a shell material because it is a non-toxic, biocompatible and biodegradable natural polymer. It also possesses antibacterial properties.^{107,108} Furthermore, it contains hydroxyl and amine functional groups which can be used for further chemical modifications. In addition, chitosan has the advantage of low cost because it is produced from deacetylation of chitin, poly- β -(1,4)-*N*-acetyl-*D*-glucosamine (Figure 3.13), where chitin is usually obtained from the shell wastes of crustacean, such as shrimp, lobster, krill, squid and crab. In fact, chitin is the second most abundant biopolymer in nature after cellulose.

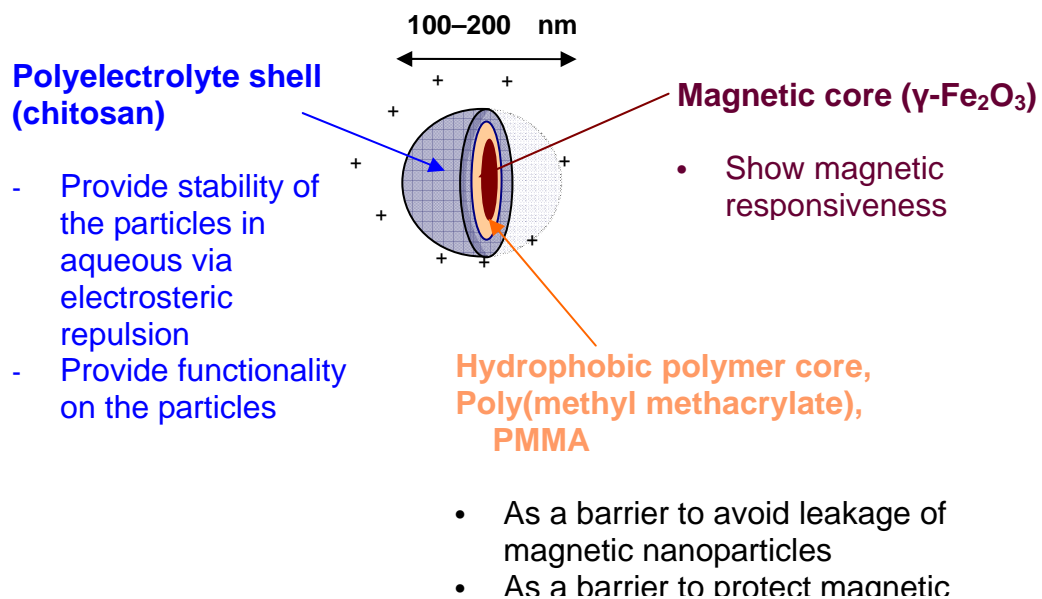


Figure 3.12. Rationale design of MCS particles.

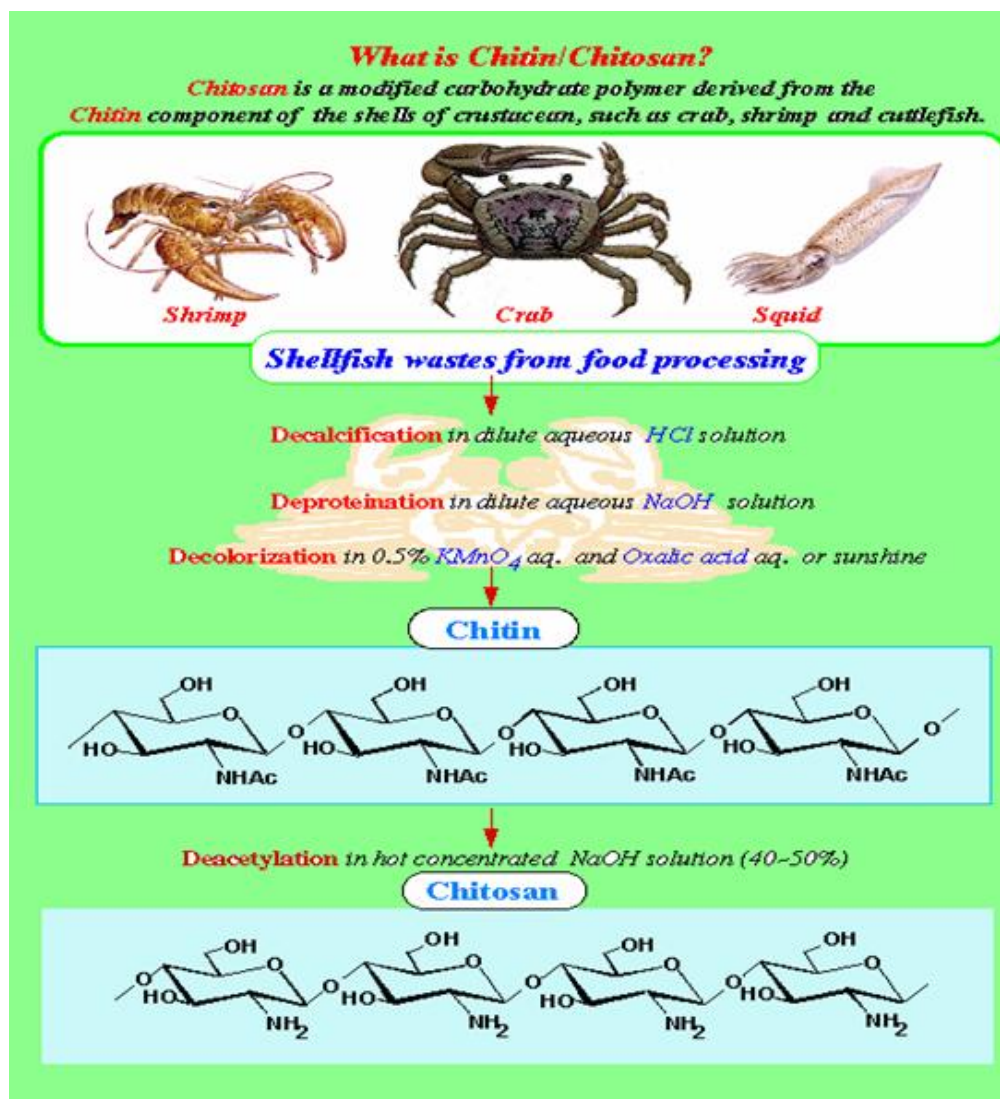


Figure 3.13. Deacetylation of chitin.

3.3.3 Our Strategies to MCS Particles

Formation of MCS particles involved a two-stage process: 1) preparation of surface-modified magnetic nanoparticles; 2) synthesis of MCS particles via hydroperoxide-induced graft copolymerization of methyl methacrylate (MMA) from chitosan in the presence of surface-modified magnetic nanoparticles at 80 °C in aqueous media, which was based on the method for the preparation of amphiphilic core-shell particles.¹⁰⁹ The detailed mechanism of this graft

copolymerization technique to amphiphilic core-shell particles, and their important features will be described in Chapter 5.

In fact, the major challenge of this approach is to encapsulate magnetic nanoparticles inside the *hydrophobic* PMMA core of the core-shell particles. To facilitate the encapsulation of magnetic nanoparticles into the core-shell (PMMA/chitosan) particles, three types of surface-modified magnetic nanoparticles were investigated. They include oleate-coated $\gamma\text{-Fe}_2\text{O}_3$ (o- Fe_2O_3), citrate-coated $\gamma\text{-Fe}_2\text{O}_3$ (c- Fe_2O_3) and vinyl-coated $\gamma\text{-Fe}_2\text{O}_3$ (MPS- Fe_2O_3) nanoparticles. The hydrophobic oleate coating aims to improve the interfacial interaction between $\gamma\text{-Fe}_2\text{O}_3$ nanoparticles and surrounding polymer (PMMA). Thus, the nanoparticles would be encapsulated into the PMMA core of core-shell particles through the hydrophobic interaction. Another strategy to drive the nanoparticles into the PMMA core is that the negatively charged c- Fe_2O_3 nanoparticles were pre-absorbed onto positively charged chitosan through electrostatic interactions. Thus, the adsorbed magnetic nanoparticles become hydrophobic in nature, which may facilitate the encapsulation process. The final approach is to further increase the hydrophobicity of c- Fe_2O_3 nanoparticles by introducing terminal double bonds on the nanoparticle surfaces (MPS- Fe_2O_3). Subsequent copolymerization of the vinyl groups of the MPS- Fe_2O_3 nanoparticles and methyl methacrylate (MMA) could drive the nanoparticles into the cores. Detailed study of MCS particle formation will be discussed in Section 5.3.

3.3.4 Specific Objectives

The major objectives of my research are as follows:

- 1) Preparation and characterization of three types of surface-modified magnetic nanoparticles, including oleate-coated $\gamma\text{-Fe}_2\text{O}_3$, citrate-coated $\gamma\text{-Fe}_2\text{O}_3$, vinyl-coated $\gamma\text{-Fe}_2\text{O}_3$ nanoparticles.
- 2) Preparation of MCS particles consisting of PMMA and $\gamma\text{-Fe}_2\text{O}_3$ nanoparticles as a core, and chitosan as a shell.
- 3) Characterization of these MCS particles with respect to their particle size, size distribution, morphology and nanostructure, surface charge density, and particle stability, and magnetic responsiveness.
- 4) Exploration of the MCS particles ($\gamma\text{-Fe}_2\text{O}_3$ /PMMA/chitosan) as a water-based coating for electromagnetic interference (EMI) shielding application.

Chapter 4

Synthesis and characterization of surface-modified magnetic nanoparticles: oleate-coated γ -Fe₂O₃, citrate-coated γ -Fe₂O₃, vinyl-coated γ -Fe₂O₃ nanoparticles

4.1 Introduction

This chapter focuses on the synthesis and characterization of three types of surface-modified magnetic nanoparticles. They include oleate-coated γ -Fe₂O₃ (o-Fe₂O₃), citrate-coated γ -Fe₂O₃ (c-Fe₂O₃), vinyl-coated γ -Fe₂O₃ (MPS-Fe₂O₃) nanoparticles. These surface-modified magnetic nanoparticles were synthesized via three approaches: (1) Decomposition of Fe(CO)₅ in the presence of oleic acid micelles, followed by nucleation and oxidation to form oleate-coated γ -Fe₂O₃ (o-Fe₂O₃) nanoparticles. (2) Co-precipitation of FeCl₂ and FeCl₃ in an ammonium solution between pH 11 and 12, followed by coating with trisodium citrate to generate citrate-coated γ -Fe₂O₃ (c-Fe₂O₃) nanoparticles with negative surface charges. (3) Condensation of terminal vinyl bonds on the c-Fe₂O₃ nanoparticle surface via a modified Stöber method to form vinyl-coated γ -Fe₂O₃ (MPS-Fe₂O₃) nanoparticles.

Properties of the nanoparticles including particle size, structural information, chemical compositions, surface charge density, and magnetic responsiveness were characterized with transmission electron microscopy (TEM), dynamic light scattering, X-ray diffraction (XRD), Fourier-transform Infrared (FT-IR) spectroscopy, thermogravimetry analysis (TGA), zeta-potential and vibrating sample magnetometer (VSM), respectively.

4.2 Experimental

4.2.1 Materials

Iron pentacarbonyl, $\text{Fe}(\text{CO})_5$, was obtained from Acros. Oleic acid (OA) and octyl ether were obtained from Sigma-Aldrich. Dehydrated trimethylamine *N*-oxide, $(\text{CH}_3)_3\text{NO}$, was purchased from Japanese Reagent Chemical Company. Anhydrous iron (III) chloride (FeCl_3 , Junsei Chemical Co. Ltd), iron (II) chloride tetrahydrate ($\text{FeCl}_2 \cdot 4\text{H}_2\text{O}$, Aldrich), ammonium hydroxide solution (25 w/w%, Acros), and trisodium citrate-2-hydrate (Riedel-de Haen) were all used as received. *n*-Hexane, methanol, ethanol, tetraethyl orthosilicate [$\text{Si}(\text{OC}_2\text{H}_5)_4$, TEOS] and 3-(trimethoxysilyl)propyl methacrylate (MPS, 99 w/w%) were obtained from International Laboratory USA. Freshly deionized and distilled water (D.D. H_2O) or Milli-Q water was used as the dispersion medium.

4.2.2 Synthesis of oleate-coated $\gamma\text{-Fe}_2\text{O}_3$ (o- Fe_2O_3) nanoparticles

The o- Fe_2O_3 nanoparticles were prepared via high-temperature decomposition approach, according to the method reported by Hyeon *et al.*⁷⁹ $\text{Fe}(\text{CO})_5$ (0.2 mL, 1.52 mmol) was injected to the mixture containing oleic acid (1.28 g, 4.56 mmol) and octyl ether (10 mL) at 100 °C under vigorous stirring, giving an orange solution. The resulting solution was then heated under reflux temperature (295–298 °C) for 1 h, and cooled to room temperature. Dehydrated trimethylamine *N*-oxide, $(\text{CH}_3)_3\text{NO}$ (0.34 g, 4.56 mmol) was added into the cooled dispersion under argon (Ar) atmosphere. The resulting mixture was then heated to 130 °C for 2 h, and further increased to the reflux temperature for

another 1 h. The resulting black dispersion was finally cooled to room temperature. The magnetic dispersion was dropwise added into *cold* ethanol to yield black precipitates, which were then separated by a magnet. The supernatant was decanted. The resulting precipitates were dispersed in hexane, and further purified by repeated precipitation, decantation, and re-dispersion cycle for five times.

4.2.3 Synthesis of aqueous-based γ -Fe₂O₃ nanoparticles

4.2.3.1 γ -Fe₂O₃ nanoparticles

γ -Fe₂O₃ nanoparticles were synthesized based on the literature method with minor modifications.^{13,46} FeCl₂•4H₂O (1.99 g) and FeCl₃ (3.25 g) were dissolved in water (20 mL) separately, followed by mixing the two iron salt solutions under vigorous stirring (800 rpm). NH₄OH solution (0.6 M, 200 mL) was then added to the stirring mixture at room temperature, immediately followed by addition of concentrated NH₄OH (25 w/w%, 30 mL) in order to maintain the reaction pH between 11 and 12. The resulting black dispersion was continuously stirred for 1 h, and then heated at reflux temperature for another 1 h to yield a brown dispersion. The brown dispersion was allowed to cool to room temperature. The magnetic nanoparticles were then purified by repeated centrifugation (3000–6000 rpm, 20 min), decantation and re-dispersion cycle for three times, until a stable brown magnetic dispersion (pH 9.4) was obtained.

4.2.3.2 Citrate-coated γ -Fe₂O₃ nanoparticles (c-Fe₂O₃)

The purified γ -Fe₂O₃ nanoparticles (2.42 g) were acidified with HNO₃ solution (2 M, 200 mL), and then centrifuged at 3000 rpm for 20 min to collect the magnetic nanoparticles. Supernatant was then discarded. The concentrated magnetic nanoparticle dispersion was re-dispersed in water (200 mL), at which the pH of the dispersion was 1.10. Subsequently, the acidified dispersion was heated to reflux, followed by addition of trisodium citrate dihydrate (11.7 g). The resulting mixture was heated at refluxing temperature for 1 h to generate citrate-coated iron oxide (c-Fe₂O₃) nanoparticles. The brown dispersion was purified by placing it into a dialysis tube (10,000 Da molecular weight cut-off, Sigma-Aldrich) and dialyzed against water for 8 days with daily changing of water until the conductivity of water was equal to that of D.D.H₂O used (Figure 4.1).

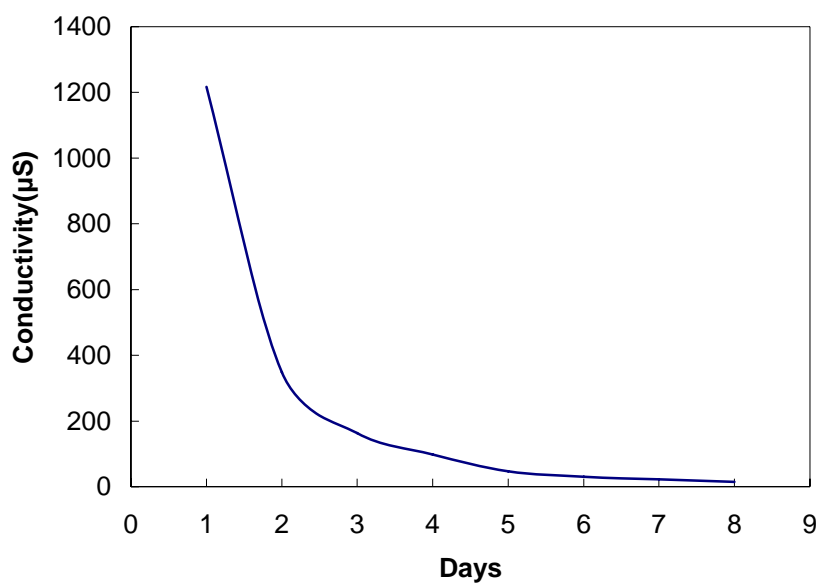


Figure 4.1. Purification process of c-Fe₂O₃ nanoparticles.

4.2.3.3 Preparation of vinyl-coated γ -Fe₂O₃ (MPS-Fe₂O₃) nanoparticles

Coating of a thin layer of silica on the surface of γ -Fe₂O₃ nanoparticles was achieved by pre-mixing a dispersion of the purified citrate-coated nanoparticles (8.5 w/w%, 20 mL) obtained in Section 4.2.3.2 and methanol (80 mL) for 1 h at 40 °C. Concentrated ammonia solution (25 w/w%, 1.8 mL) was then added. The resulting mixture was stirred at 40 °C for 30 min, then tetraethyl orthosilicate (TEOS, 1.0 mL) was charged to the mixture. The resulting dispersion was continuously stirred at 40 °C for 24 h. Finally, an excess amount of 3-(trimethoxysilyl)propyl methacrylate (MPS, 5.3 mL) was added to the mixture, and the reaction took place at 40 °C for another 24 h to give vinyl-coated γ -Fe₂O₃ (MPS-Fe₂O₃) nanoparticles. The MPS-coated nanoparticles were collected by magnetic separation. The supernatant was decanted. The concentrated magnetic dispersion was then re-dispersed in ethanol (20 mL), and subsequently placed it into a dialysis tube (10,000 Da molecular weight cut-off, Sigma-Aldrich). The dispersion was dialyzed against ethanol for a week with daily changing of ethanol in order to remove those un-reacted MPS, TEOS, and NH₃. The purification process was monitored with ultraviolet (UV) measurements of the un-reacted MPS molecules which were dialyzed out (Figure 4.2). A calibration standard of MPS molecules in ethanol at 203.5 nm is shown in Figure A-1, Appendix I, using a Perkin-Elmer UV-VIS spectrophotometer (Lambda 35). Finally, the purified dispersion was concentrated to 10.0 w/w% solid content for subsequent reaction.

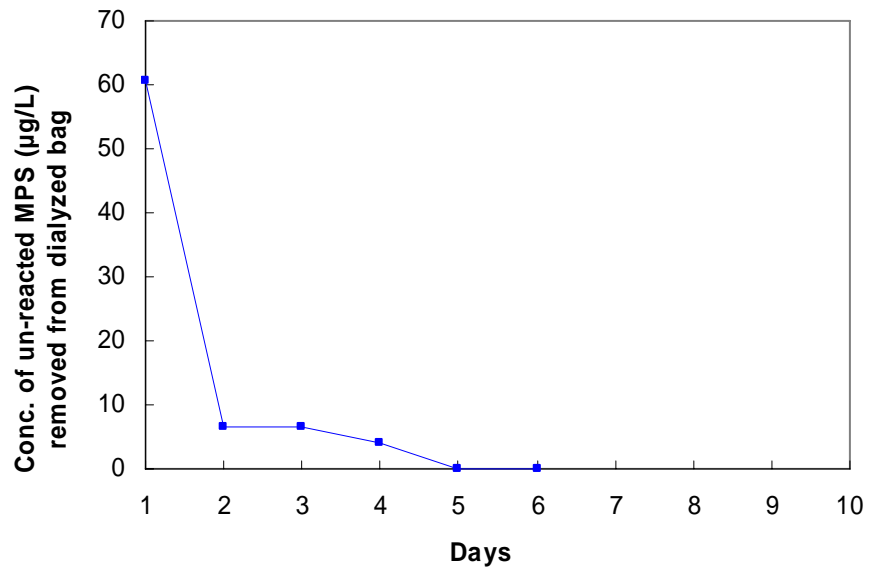


Figure 4.2. Purification process of MPS-Fe₂O₃ nanoparticles.

4.2.4 Measurement and Characterization

Structural crystallography

The crystallographic structure of iron oxide nanoparticles was studied with a rotating anode Bruker D8 advance X-ray diffractometer (Cu K α 1 radiation, $\lambda = 1.544 \text{ \AA}$). The nanoparticle dispersions were dried at $60 \text{ }^\circ\text{C}$ under vacuum overnight. The dried brown powders (about 0.1 g) were grinded and the finely ground powders were placed on the top of the sample holder. XRD measurement was performed using an increment time of 0.02 s. The mean crystal size (D_{hkl}) was estimated from the line broadening of XRD pattern using Scherrer formula (Equation 4.1).

$$D_{\text{hkl}} = \frac{K\lambda}{b \cos \theta} \quad (4.1)$$

where K is a shape factor (0.89 for spheres), λ is the X-ray wavelength, b is the corrected width of the XRD peak at half height and θ is the corrected reference peak width at angle θ .

Particle morphologies and electron diffraction

The transmission electron microscope (TEM) images and electron diffraction (ED) images were obtained using a JEOL 2010 transmission electron microscope at an operating voltage of 200 kV. A small drop of dilute particle dispersion (100–200 mg/L) was placed on a Formvar-coated or carbon-coated grids, and dried at room temperature before analysis.

Chemical compositions

Infrared spectra were recorded on a Nicolet Avatar 360 FT-IR spectrophotometer using potassium bromide (KBr) disks. About 10 mg of finely ground sample and ~0.5 g of spectrophotometric grade anhydrous KBr were mixed and grinded thoroughly using mortar and pestle. To prepare a transparent disk for IR measurement, the powders were pressed at a force of about 7 tonnes for 2 minutes using a level-screw press.

Thermogravimetry analysis (TGA) was studied with a Perkin-Elmer thermogravimetry analyzer TGA7. Exact amount of finely ground powder was weighed and placed in a platinum sample holder. The thermal experiments were performed at temperatures ranging from 30 to 900 °C with a heating rate of 20 °C/min under N₂ atmosphere. The compositions of γ -Fe₂O₃ of the surface-modified magnetic nanoparticles were calculated according to Equation 4.2.

$$\gamma\text{-Fe}_2\text{O}_3 (\%) = \frac{\text{weight remained at } 900\text{ }^\circ\text{C}}{\text{Weight loss due to water at } 100\text{ }^\circ\text{C}} \times 100\% \quad (4.2)$$

Particle size analyses

Hydrodynamic diameter ($\langle D_h \rangle$) of MCS particles was also measured with a Malvern Zetasizer 3000HS (Malvern, UK) with 632.8 nm at 25 °C. Measurements were performed at a fixed angle equal to 90 °. Sample concentration was between 100 and 300 mg/L. For every sample, the

measurements were repeated three times. The intensity correlation function (i.e. correlogram) of the scattered light was illustrated by the relation of $G(\tau) = \int I(t)I(t + \tau)dt$.^{110a} The intensity distribution was obtained using non-negatively constrained least squares (NNLS) analysis of the correlogram.^{110a} D_v and D_n were calculated from a statistical analysis of the intensity distribution.^{110b} For size determination of MPS-Fe₂O₃ nanoparticles, ethanol (refractive index = 1.362; viscosity = 1.19 centipoise, cP) was used as a dispersing solvent. Particle size and size distribution were measured with statistic analysis of 20 particles in TEM micrographs.

Magnetization measurement

The magnetization studies were measured with a vibrating sample magnetometer (VSM) (LDJ MODEL 9500) at room temperature. Temperature-dependent magnetization studies were performed at temperatures ranging from 8 to 300 K. Exact amount of the sample (usually larger than 0.05 g) was weighed, and closely packed into a Teflon holder. The magnetization measurement was studied at room temperature using external magnetic field strengths ranging from 0 to 5 KOe.

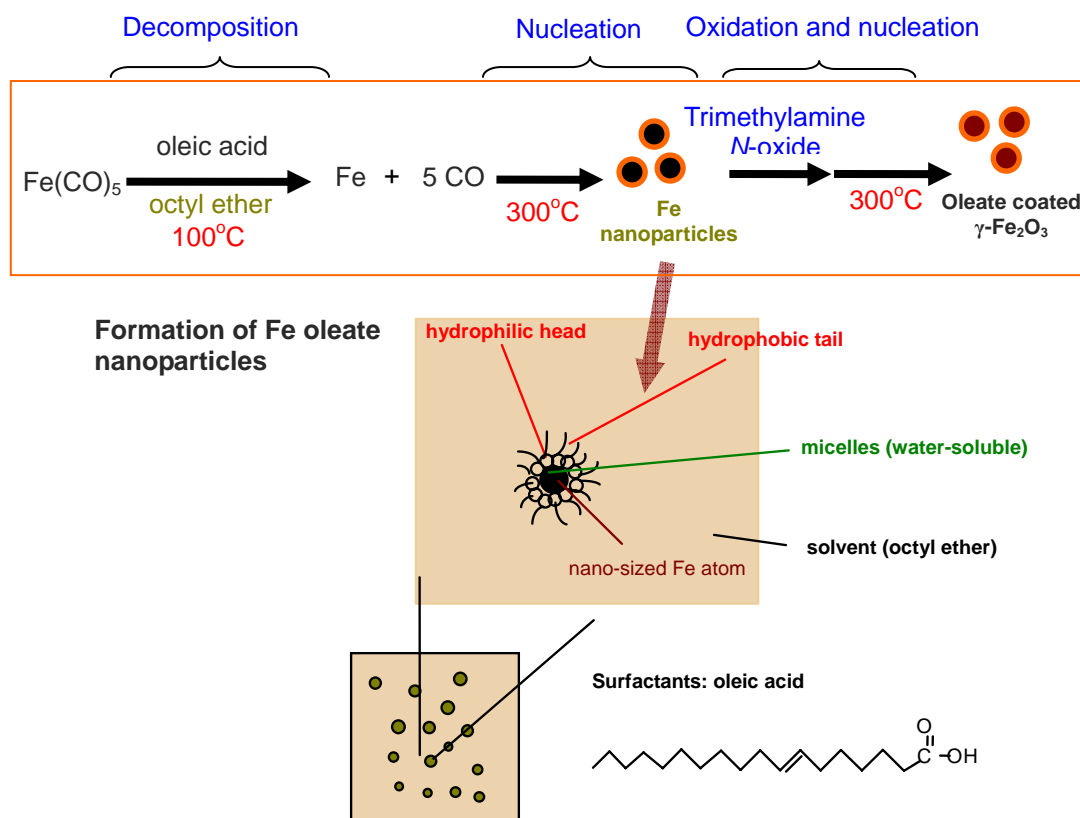
Characterization of particle surface charges

All ζ -potential measurements were determined with a Malvern Zetasizer 3000HS in a 1×10^{-3} M NaCl aqueous solution as a suspension liquid. The sample concentrations were maintained between 100 and 300 mg/L.

4.3 Results and Discussion

4.3.1 Synthesis of oleate-coated γ -Fe₂O₃ (o-Fe₂O₃) nanoparticles

The o-Fe₂O₃ nanoparticles were synthesized via decomposition of Fe(CO)₅ molecules in the presence of organic surfactant under high temperature, based on the method reported by Hyeon *et al.*⁷⁹ Formation of the nanoparticles is a multi-step reaction, including decomposition, nucleation and oxidation as described in Scheme 4.1. Because of the strong interaction between the acid groups of oleic acid and the Fe atoms,¹⁴ the Fe(CO)₅ molecules tend to be inside the oleic acid micelles. As reaction temperature increased, Fe(CO)₅ started to decompose, leaving iron (Fe) atoms in oleic acid micelles. When reaction temperature continued to increase and remained at reflux temperature, Fe atoms then started to nucleate and grow inside the micelles, which were subsequently oxidized using a mild oxidant (trimethylamine *N*-oxide), followed by nucleation of the resulting nanoparticles through thermal annealing process (300 °C) to form γ -Fe₂O₃ nanoparticles. The resulting nanoparticles were readily dispersed in various hydrocarbon solvents such as hexane, chloroform, and toluene. Furthermore, the nanoparticle dispersion was stable up to a year without any observable coagulation.



Scheme 4.1. Formation mechanism of o-Fe₂O₃ nanoparticles.

Chemical composition of o-Fe₂O₃ nanoparticles

The presence of oleate coating on the nanoparticle surface was confirmed by FT-IR spectroscopy. Figure 4.3 (a) shows the IR spectrum of oleic acid, where a strong absorption peak at 1709 cm⁻¹ was the characteristic peak of carbonyl stretching; while the strong bands between 2853 and 2824 cm⁻¹ were corresponding to the methylene and methyl symmetric stretching vibrations, respectively. Compared with the IR spectrum of oleic acid, the IR spectrum of o-Fe₂O₃ nanoparticles in Figure 4.3 (b) shows the strong IR absorption bands between 400 and 630 cm⁻¹, which were the characteristic peaks of Fe-O vibrations related to the γ-Fe₂O₃ nanoparticles.³⁷ Furthermore, a new O=C-O⁻ absorption peak at 1634 cm⁻¹ was observed, indicating that the complexation between the

carboxylate of oleic acids and γ -Fe₂O₃ nanoparticles was formed.¹¹¹ Other characteristic peaks from oleic acid were also observed.

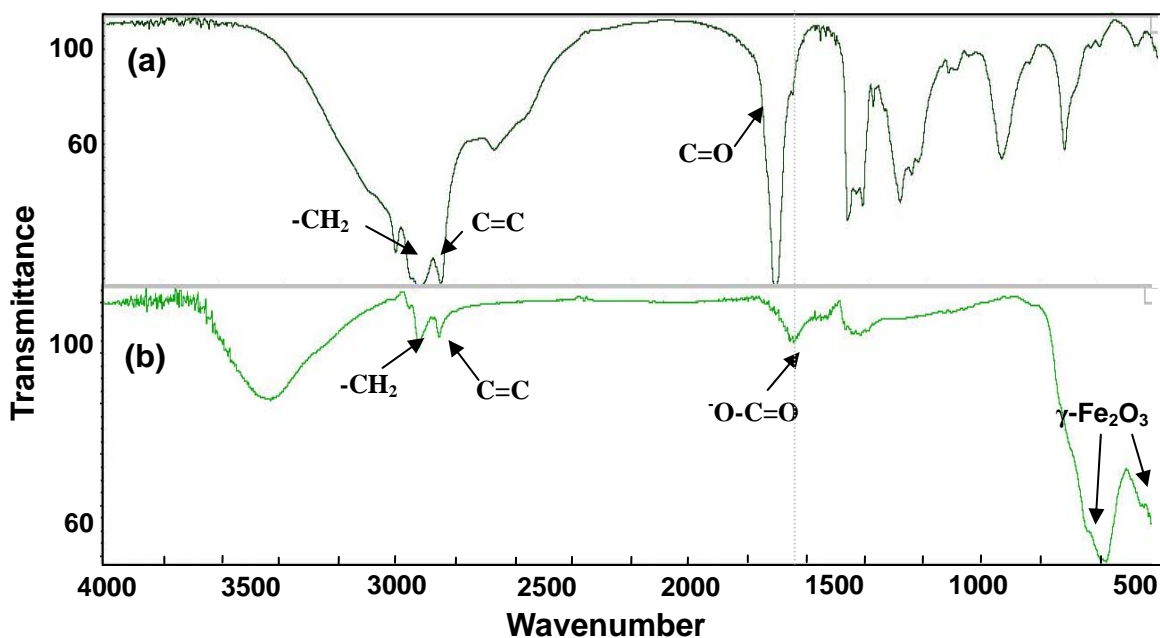


Figure 4.3. FT-IR spectra of: (a) oleic acid and (b) o-Fe₂O₃ nanoparticles.

Particle size and structural information

Figure 4.4 (a) shows the low-resolution TEM image of the o-Fe₂O₃ nanoparticles prepared. They were spherical in morphology, and had very uniform size. To obtain the structural information of the o-Fe₂O₃ nanoparticles, three characterization techniques including, selected area electron diffraction (SAED), high-resolution TEM (HR-TEM) and X-ray diffraction (XRD) were used. The SAED image as shown in Figure 4.4 (b) reveals the continuous ring patterns, indicating that the nanoparticles are polycrystalline. The ring patterns are indistinct, suggesting that some nanoparticles are amorphous. This is possibly attributed to the poor control of annealing temperature and time.¹¹² Figure 4.4 (c)

shows the high-resolution TEM (HR-TEM) image of several α - Fe_2O_3 nanoparticles. The lattice fringes within a nanoparticle (8 nm in diameter) are corresponding to a group of atomic planes, indicating that the nanoparticle is a single crystal.⁹

Figure 4.5 shows the X-ray diffraction analysis (XRD) of the α - Fe_2O_3 nanoparticles. The lattice spacing of the synthesized nanoparticles calculated from the diffraction patterns were in close agreement with bulk γ - Fe_2O_3 standard obtained from International Center for Diffraction Data (ICDD), except that the peak was located at 53.7° . The absence of this peak might be attributed to the presence of amorphous iron oxides, thus resulting in a low signal-to-noise ratio of this peak in XRD measurement. This result suggests that poor crystalline γ - Fe_2O_3 nanoparticles were produced. The mean crystal size of the nanoparticles estimated from the result of XRD data using Scherrer's formula was 10 nm. Such value was close to the average size (8 ± 2 nm) determined by the statistical analysis of the nanoparticles in the TEM image in Figure 4.4 (a).

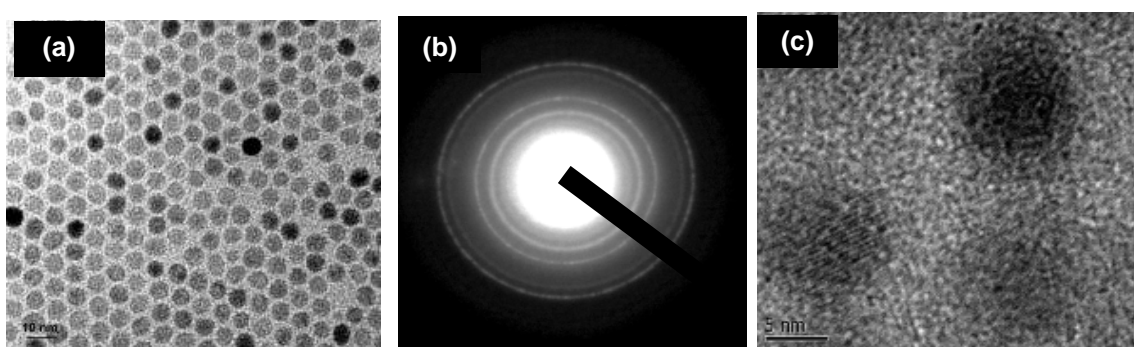


Figure 4.4. TEM images of α - Fe_2O_3 nanoparticles: (a) low-resolution image; (b) SAD image of the low-resolution image and (c) high-resolution image.

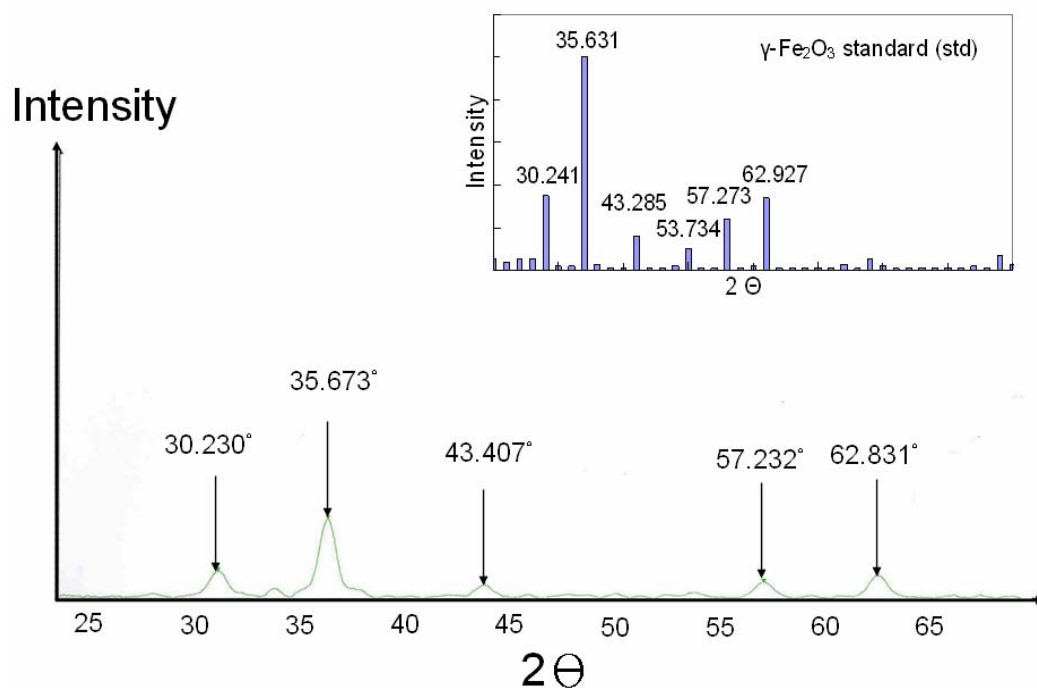


Figure 4.5. XRD pattern of synthesized α -Fe₂O₃ nanoparticles [insertion: γ -Fe₂O₃ standard (file 39-1346 of the database of the International Center for Diffraction Data)].

Magnetization measurement

Magnetization measurement of α -Fe₂O₃ nanoparticles using vibrating sample magnetometer (VSM) showed that the nanoparticles exhibited little hysteresis at room temperature (Figure 4.6). This result indicated that some nanoparticles existed in an aggregated form, thus contributing to hysteresis. The saturation magnetization (M_s) value of α -Fe₂O₃ nanoparticles determined by VSM was 12.5 emu/g. This value is significantly lower than the M_s value of highly crystalline α -Fe₂O₃ nanoparticles (~30 emu/g at 100 Oe) reported by Hyeon *et al.*⁷⁹ Low M_s value is probably due to the fact that the synthesized α -Fe₂O₃ nanoparticles

contained some amorphous iron oxides, which does not contribute to the magnetization.

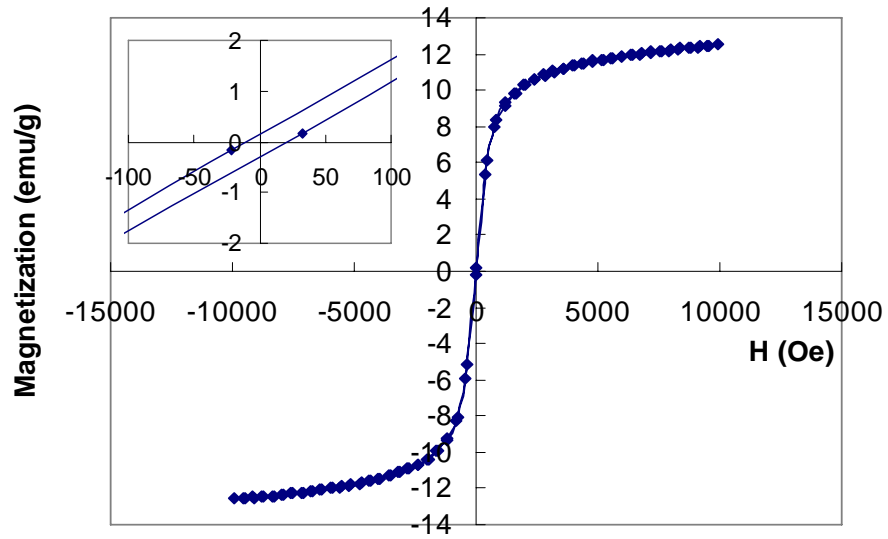
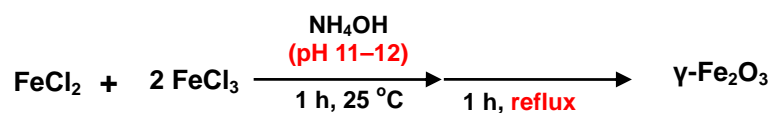


Figure 4.6. Magnetization behavior of o-Fe₂O₃ nanoparticles at room temperature (M_s = 12.5 emu/g).

4.3.2 Synthesis of aqueous-based γ -Fe₂O₃ nanoparticles

4.3.2.1 Synthesis of γ -Fe₂O₃ nanoparticles

The γ -Fe₂O₃ nanoparticles were synthesized via co-precipitation of solutions of Fe(II) and Fe(III) chloride (molar ratio of Fe²⁺ to Fe³⁺ was 1 to 2) in a NH₄OH solution^{13,46} (Scheme 4.2). Formation of γ -Fe₂O₃ was achieved through a multiple-transformation process, including de-protonation, oxidation, dehydration, and precipitation under an oxygen-rich environment.¹⁰ Detailed mechanism of γ -Fe₂O₃ formation has been described in Section 3.1.1. The product yield of the purified γ -Fe₂O₃ nanoparticles determined based on both gravimetric method and thermogravimetry analysis (TGA) was around 90 %.



Scheme 4.2. Synthesis of γ -Fe₂O₃ nanoparticles.

Particle size and structural information

Figure 4.7 (a) shows the low-resolution TEM image of the γ -Fe₂O₃ nanoparticles produced. They were irregular and had broad size distribution. The SAD image of the electron diffraction patterns of the synthesized γ -Fe₂O₃ nanoparticles clearly reveals dense ring patterns, indicating that the nanoparticles are polycrystalline with a high crystallinity (Figure 4.7 b). The HR-TEM image in Figure 4.7 (c) shows an individual γ -Fe₂O₃ nanoparticle. The atomic lattice fringes

corresponding to a group of atomic plane were clearly revealed, suggesting that the nanoparticle is a single crystal.⁹

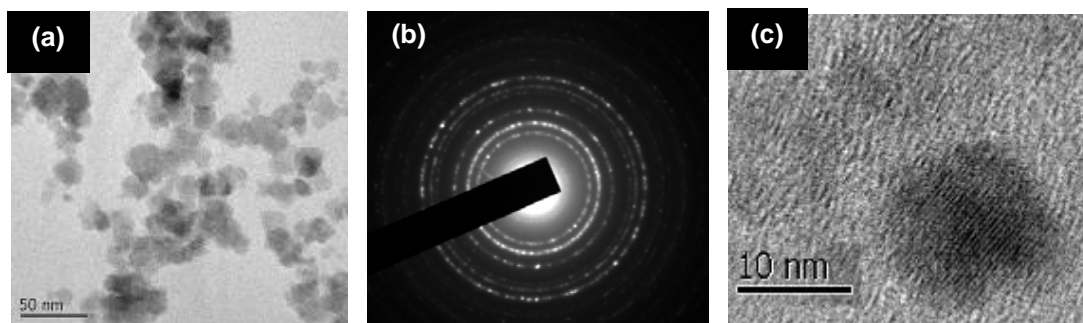


Figure 4.7. TEM images of synthesized $\gamma\text{-Fe}_2\text{O}_3$ nanoparticles: (a) low-resolution image; (b) electron diffraction image of the left image; (c) high-resolution image.

Figure 4.8 shows the XRD pattern of the synthesized nanoparticles. The lattice spacing calculated based on the diffraction patterns had a well match with that of bulk $\gamma\text{-Fe}_2\text{O}_3$ standard obtained from ICDD, indicating that $\gamma\text{-Fe}_2\text{O}_3$ nanoparticles were successfully produced. The mean crystal size of the nanoparticles estimated from the result of XRD data using Scherrer's formula was 11 nm. This value was close to the average size (11 ± 8 nm) determined by the statistical analysis of the nanoparticles in Figure 4.7 (a).

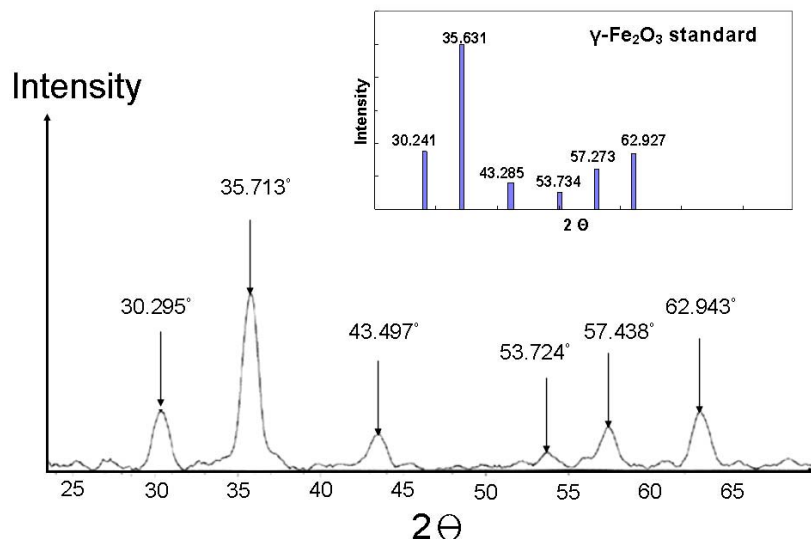


Figure 4.8. XRD pattern of synthesized $\gamma\text{-Fe}_2\text{O}_3$ nanoparticles [insertion: $\gamma\text{-Fe}_2\text{O}_3$ standard (file 39-1346 of the database of the International Center for Diffraction Data)].

Magnetization measurement

Figure 4.9 shows the results of magnetization measurement of the obtained $\gamma\text{-Fe}_2\text{O}_3$ nanoparticles. The nanoparticles exhibited superparamagnetism because of the absence of hysteresis at room temperature. This means that thermal energy (at room temperature) is sufficient to overcome the anisotropy energy barrier of a single particle,⁹ in which magnetic moments are free to rotate during the magnetization/demagnetization process. Therefore, the net magnetization of the particle approached to zero when no external magnetic field was applied. The saturation magnetization (M_s) value of the $\gamma\text{-Fe}_2\text{O}_3$ nanoparticles was 46 emu/g, which was comparable with the values reported by Tang *et al.*⁴⁶ However, this value is lower than the reported value of their bulk counterparts (74 emu/g). It is known that low M_s values in nanoparticles are probably due to the particle

surface³¹ and the internal structural ordering effects.³⁷ These mean that the nanoparticle has much larger surface curvature than bulk particle, which encourages disordered crystal orientation on the surface of the nanoparticle. In addition, the oxide surfaces become more dominant in nanoparticles, compared to bulk particles. Therefore, the nanoparticles have lower M_s values than bulk particles.³¹

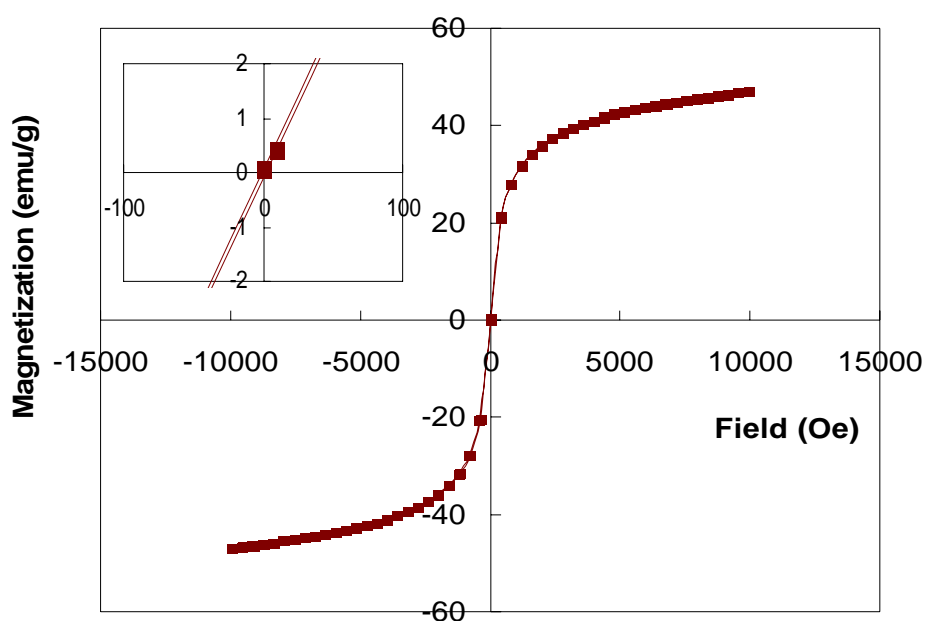


Figure 4.9. Magnetization behavior of γ -Fe₂O₃ nanoparticles at room temperature ($M_s = 46$ emu/g).

One of the important characteristics of superparamagnetism is the temperature-dependent magnetization behavior. Below a critical temperature (i.e. blocking temperature, T_B), the thermal energy is not sufficient to overcome the anisotropy barrier of magnetization orientation in a single particle; therefore, the anisotropy of the particle blocks the free motion of magnetic moments. Hence, a

remnant magnetization (i.e. hysteresis loop) is usually observed during the magnetization/demagnetization process at low temperatures. Figure 4.10 demonstrates the temperature-dependent magnetic behavior of $\gamma\text{-Fe}_2\text{O}_3$ nanoparticles at temperatures varying from 300 K to 5 K. The study clearly revealed that hysteresis loop was only observed below 100 K, but not at room temperature. These results suggest a typical behavior of a superparamagnetic material. In other words, the $\gamma\text{-Fe}_2\text{O}_3$ nanoparticles synthesized are superparamagnetic at room temperature.

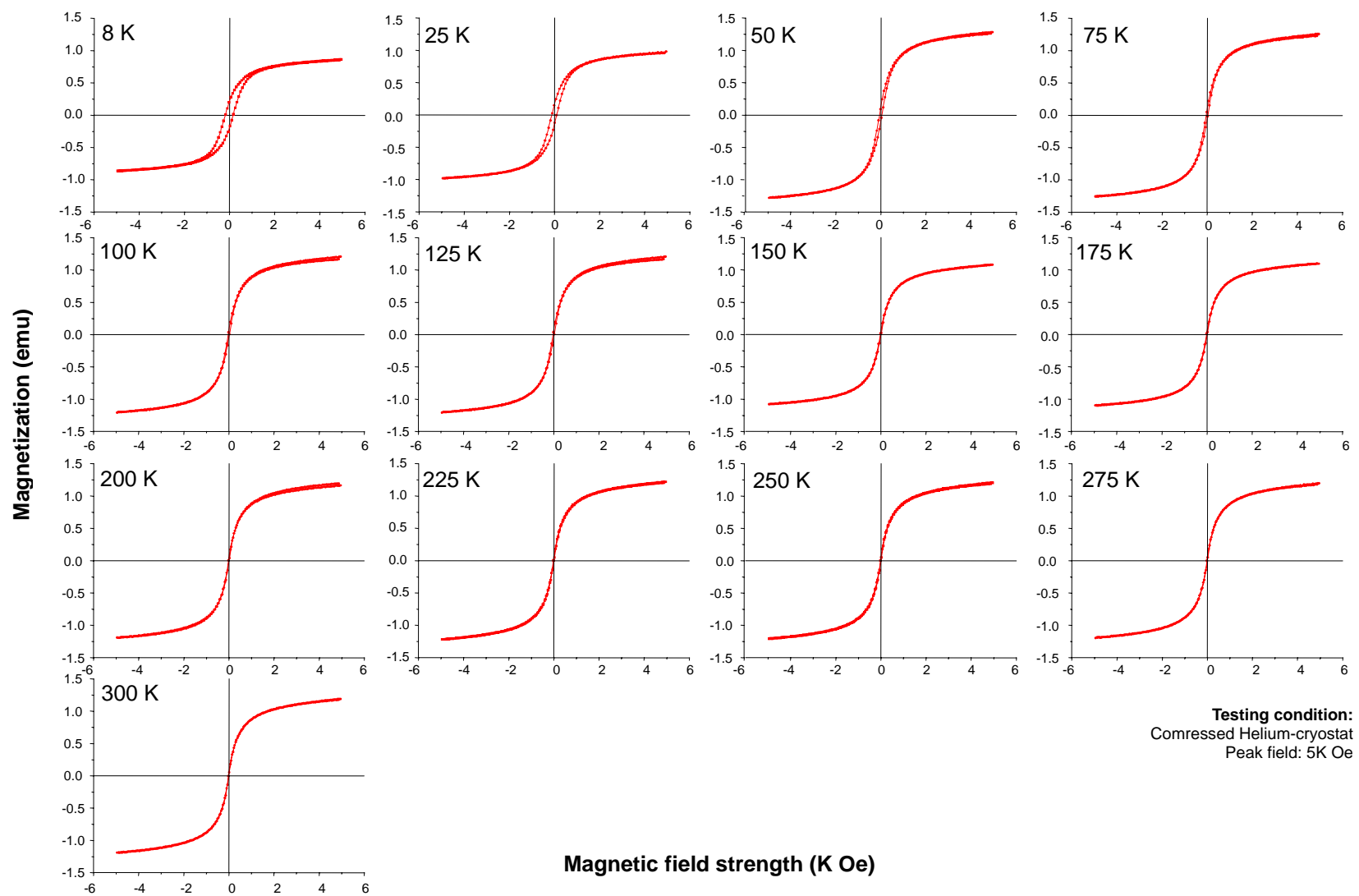
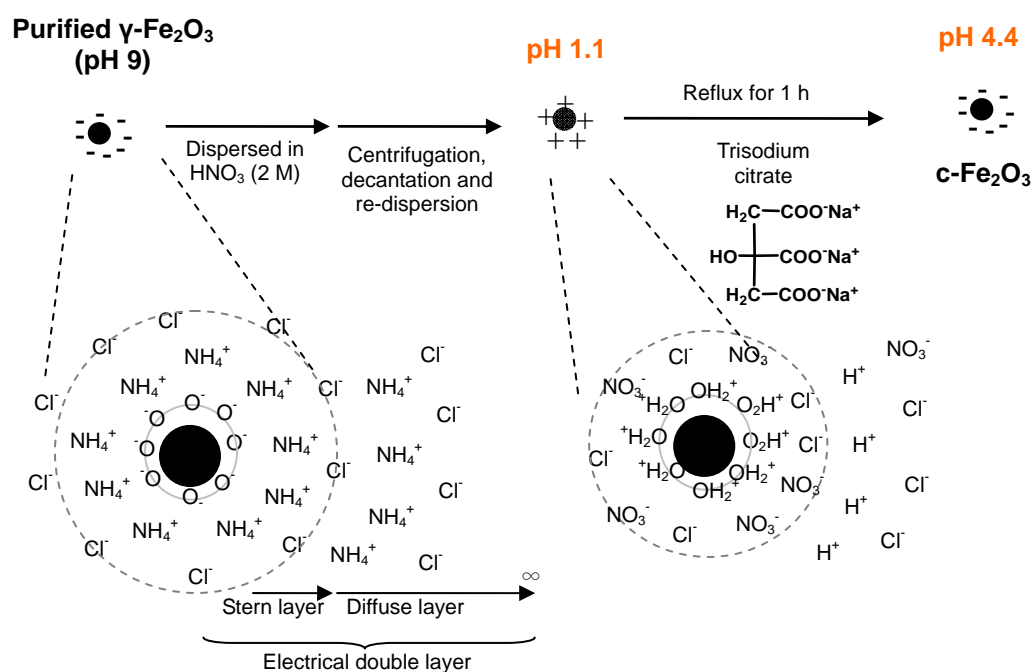


Figure 4.10. Temperature-dependent magnetization of $\gamma\text{-Fe}_2\text{O}_3$ nanoparticles prepared by co-precipitation method.

4.3.2.2 Synthesis of citrate-coated γ -Fe₂O₃ nanoparticles (c-Fe₂O₃)

The c-Fe₂O₃ nanoparticles were prepared by acid pretreatment of the purified γ -Fe₂O₃ nanoparticles obtained in Section 4.3.2.1, followed by adsorption of citrate molecules on the nanoparticle surface via electrostatic complexation, chemisorption and condensation.¹³ Scheme 4.2 illustrates the acid pretreatment process. The purified γ -Fe₂O₃ nanoparticles had a pH around 9, indicating that the nanoparticles carried negative surface charges, thus attracting positive counter ions to form a double layer. Because of these double layers, the counter ions such as ammonium (NH₄⁺) and chloride (Cl⁻) were trapped within these layers. Hence, it was difficult to remove these counter ions from γ -Fe₂O₃ dispersion even after successive purification processes.



Scheme 4.2. Illustration of HNO₃ pretreatment process.

Effect of HNO₃ surface treatment

Removal of counter ions is necessary because these counter ions are highly polarized. They tend to suppress the electrical double layer of the nanoparticles, causing aggregation of the nanoparticles during the coating process. Furthermore, these counter ions hinder the citrate molecules to undergo chemisorption on the nanoparticle surface.⁵² Tourinho *et al.* [1990] proposed a nitric acid (HNO₃) treatment to remove these polarizing ions (NH₄⁺ and Cl⁻) through complexing these polarizing ions to form soluble electrolytes (i.e. NH₄NO₃ and HCl),⁵² as is shown in Scheme 4.2. Thus, these highly polarizing ions could be removed by centrifugation and decantation process. Another purpose of using HNO₃ was to protonate the surface hydroxyls of γ -Fe₂O₃ nanoparticles, thus enhancing their interactions with negatively charged citrate molecules.

To illustrate the importance of HNO₃ treatment, an experiment without HNO₃ surface pretreatment was conducted. The pH of the γ -Fe₂O₃ nanoparticle dispersion was first adjusted to pH 1.10 with a dilute nitric acid (0.5 M), and then allowed to react with trisodium citrate at reflux. The nanoparticles produced were unstable, immediately forming precipitation. ζ -potential measurement as shown in Figure 4.11 suggested that the nanoparticles were actually coated with citrate molecules, as indicated by the shift of isoelectric (ISE) point to negative value. However, the coated nanoparticles had very low surface charge densities (~ -10 mV) in pH 4 to 8. Thus, they were colloidal unstable.

In comparison, when γ -Fe₂O₃ nanoparticles were subjected to the HNO₃ surface treatment prior to citrate coating, the obtained nanoparticle dispersion was stable, and no flocculation was observed up to a year. ζ -potential measurement of

the resulting nanoparticles showed that the nanoparticles had negative surface charges larger than -30 mV in pH 3 to 10 (Figure 4.11). These results indicated that stable citrate coating was formed on the nanoparticle surface. This comparable study concludes that HNO₃ surface treatment is a crucial step in order to obtain stable γ -Fe₂O₃ nanoparticles with citrate coating.

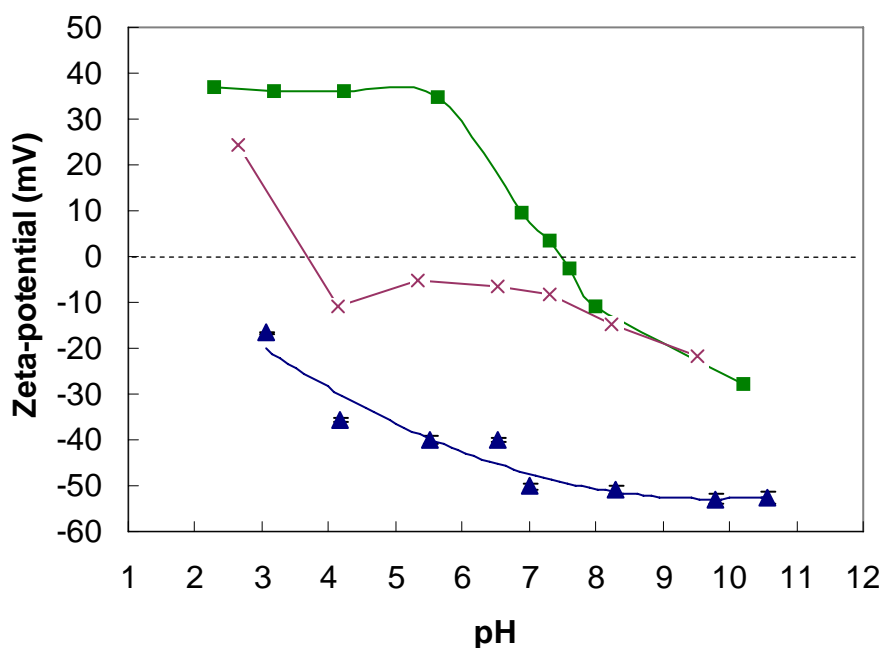


Figure 4.11. pH dependence of the ζ -potential measured in a 1 mM NaCl solution at 25 °C. (■) γ -Fe₂O₃ ; (×) c-Fe₂O₃ (without HNO₃ surface pretreatment); and (▲) c-Fe₂O₃ (with HNO₃ surface pretreatment).

Chemical compositions of α - Fe_2O_3 nanoparticles

The presence of citrate coating on the nanoparticle surface was identified using FT-IR spectroscopy (Figure 4.12 c). The IR spectrum of the α - Fe_2O_3 nanoparticles clearly reveals the strong IR absorption bands between 400 and 630 cm^{-1} , which are the characteristic peaks of Fe-O vibration related to the γ - Fe_2O_3 .³⁷ There are also two peaks at 1625 and 1399 cm^{-1} , which are the characteristic peaks of the symmetrical and asymmetrical valence vibrations of the carboxylate groups ($\text{O}=\text{C}-\text{O}^-$) of citrate molecule, respectively.¹¹³⁻¹¹⁵

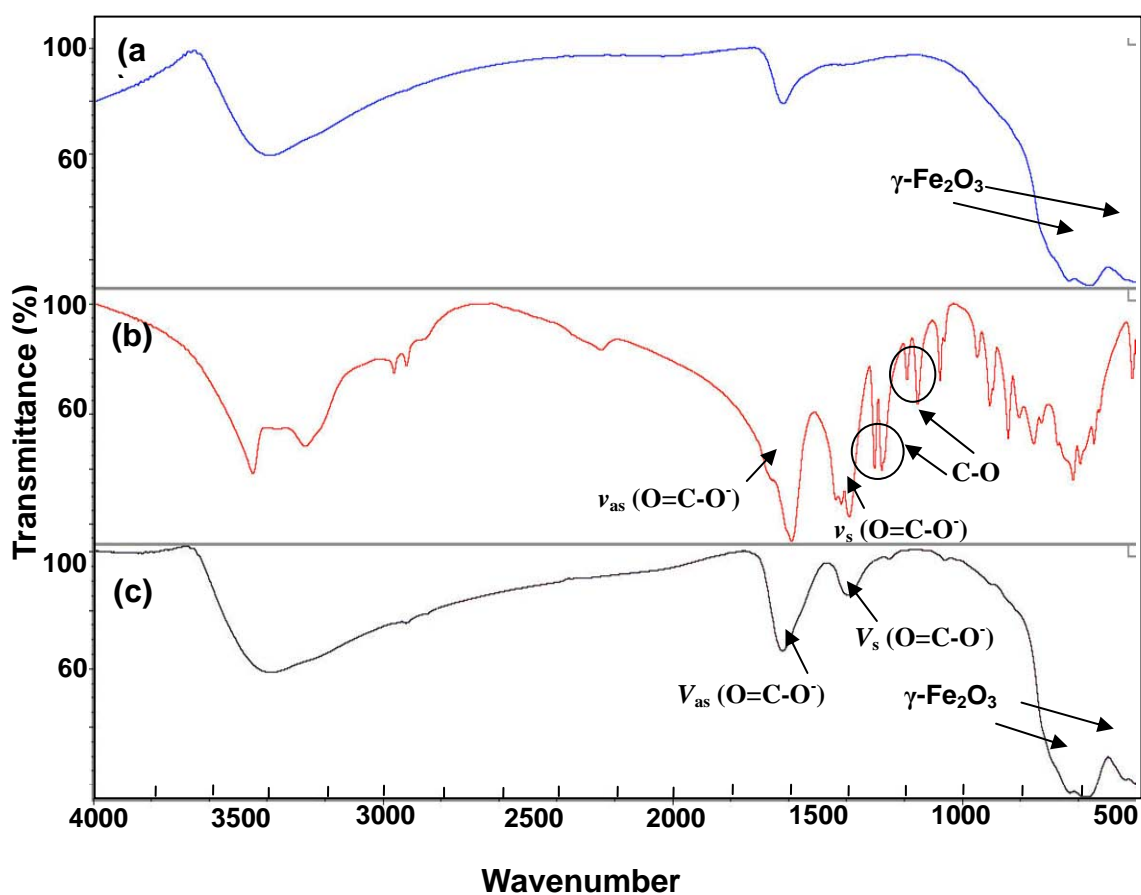


Figure 4.12. FT-IR spectra of: (a) γ - Fe_2O_3 nanoparticles; (b) trisodium citrate; (c) α - Fe_2O_3 nanoparticles.

Thermogravimetry analysis (TGA) was employed to determine the amount of citrate coatings on the nanoparticles. Figure 4.13 (a) shows the TGA thermogram of the uncoated γ -Fe₂O₃ nanoparticles, and their weight loss which can be seen in Figure 4.13 is summarized in Table 4.1. The initial weight loss at 100 °C was due to water evaporation,¹⁵ while the weight loss at higher temperatures (200 to 300 °C) were attributed to the removal of surface hydroxyls and decomposition of amorphous iron hydroxides.¹⁵ Compared with the TGA curve of γ -Fe₂O₃, the TGA curve of c-Fe₂O₃ nanoparticles as shown in Figure 4.13 (b) indicated that they also had initial weight loss similar to γ -Fe₂O₃. However, the citrate-coated nanoparticles resulted in a further weight loss (7.5 %) above 300 °C, which was attributed to the presence of citrate coating. Based on TGA results, composition of c-Fe₂O₃ nanoparticles was determined, which contained 89 w/w% of γ -Fe₂O₃, 8 w/w% of citrate coating and 3 w/w% of surface hydroxyls and amorphous iron hydroxides, respectively.

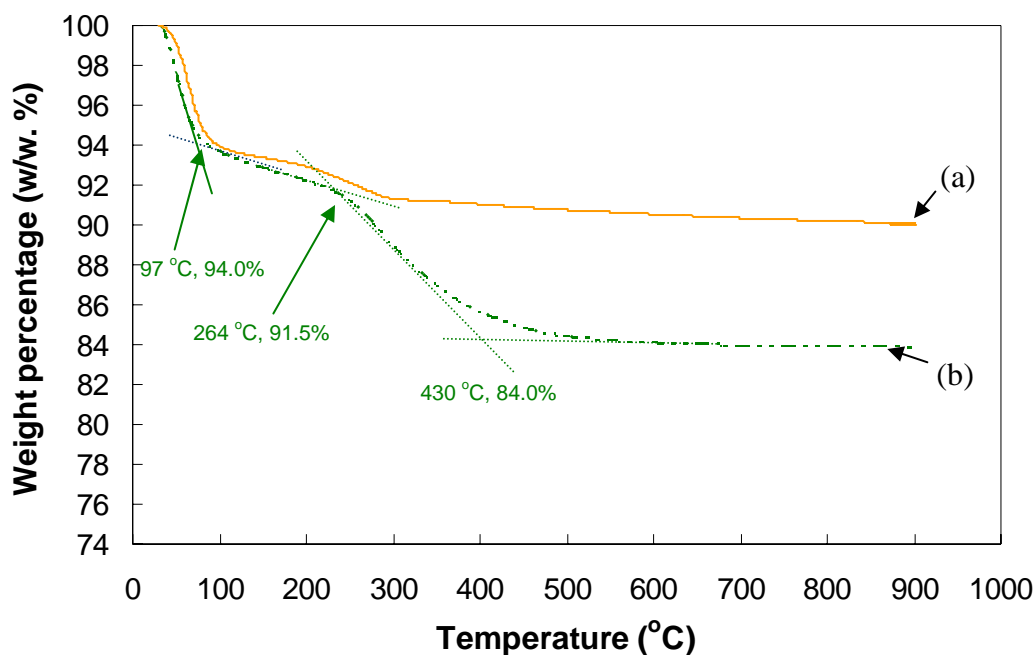


Figure 4.13. TGA thermograms of (a) γ -Fe₂O₃ and (b) c-Fe₂O₃ nanoparticles.

Table 4.1. Compositions of γ -Fe₂O₃ and c-Fe₂O₃ nanoparticles obtained from Figure 4.13.^a

Sample	H ₂ O (%)	Surface hydroxyl (%) and amorphous iron hydroxides	Citrate (%)	γ -Fe ₂ O ₃ (%)
γ -Fe ₂ O ₃	6.0	4.0	0.0	90.0
c-Fe ₂ O ₃	6.0	2.5	7.5	84.0

^aThe thermal experiments were performed at temperatures ranging from 30 to 900 °C using a heating rate of 20 °C/min under N₂ atmosphere.

Particle size measurement and structural information

Figure 4.14 (a) shows the low-resolution TEM image of c-Fe₂O₃ nanoparticles. Statistical analysis of average size of the nanoparticles determined that the nanoparticles had an average diameter of 11 nm, which was similar to the uncoated γ -Fe₂O₃ nanoparticles (Figure 4.7 a). Dynamic light scattering (DLS) measurement of the c-Fe₂O₃ nanoparticles indicated that they had comparable hydrodynamic diameters with γ -Fe₂O₃ nanoparticles (Table 4.2).

SAD image of c-Fe₂O₃ nanoparticles, as shown in Figure 4.14 (b), reveals that the c-Fe₂O₃ nanoparticles have dense ring patterns, which is similar to that of γ -Fe₂O₃ nanoparticles (Figure 4.7 b). The result suggests that the presence of citrate coating shows little influence on the crystallinity of γ -Fe₂O₃ nanoparticles. Figure 4.14 (c) also shows the HR-TEM image of c-Fe₂O₃ nanoparticles. Atomic

lattice fringes were clearly observed, suggesting that the nanoparticle is still a single crystal.

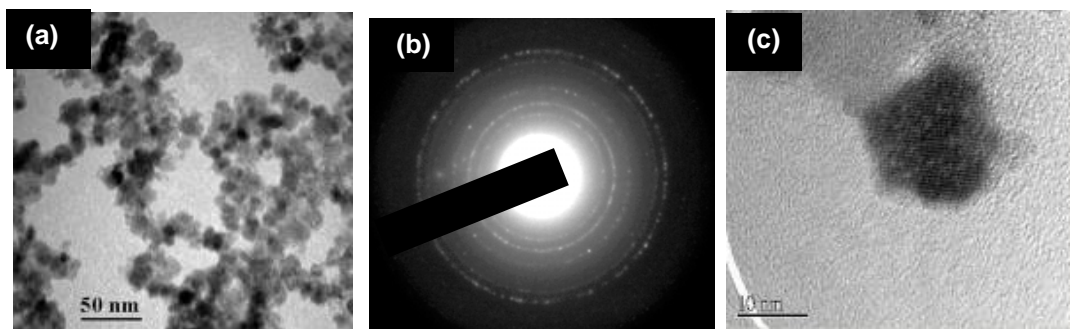


Figure 4.14. TEM images of synthesized $c\text{-Fe}_2\text{O}_3$ nanoparticles: (a) low-resolution image; (b) electron diffraction image of the left image; (c) high-resolution image.

Table 4.2. Hydrodynamic size and its distribution of the $\gamma\text{-Fe}_2\text{O}_3$ and $c\text{-Fe}_2\text{O}_3$ nanoparticles.^a

Types of the synthesized nanoparticles	Hydrodynamic diameter ($\langle D_h \rangle$, nm)
$\gamma\text{-Fe}_2\text{O}_3$ ^b	45 ± 2
$c\text{-Fe}_2\text{O}_3$ ^c	36 ± 4

^aHydrodynamic diameter was determined with a Zetasizer 3000 HS. ^bpH of the $\gamma\text{-Fe}_2\text{O}_3$ dispersion was adjusted to 2 prior to particle size measurement. ^cpH of the $c\text{-Fe}_2\text{O}_3$ dispersion was 6.5.

Magnetization measurement

Magnetization measurement of $c\text{-Fe}_2\text{O}_3$ nanoparticles showed that the nanoparticles displayed superparamagnetism at room temperature, as indicated by the absence of hysteresis loop (Figure 4.15). The saturation magnetization (M_s) of

the nanoparticles was determined as 43 emu/g, which was slightly lower than the value of γ -Fe₂O₃ (46 emu/g). Such slight decrease in magnetization is probably due to the presence of non-magnetic materials such as citrate coating in γ -Fe₂O₃.

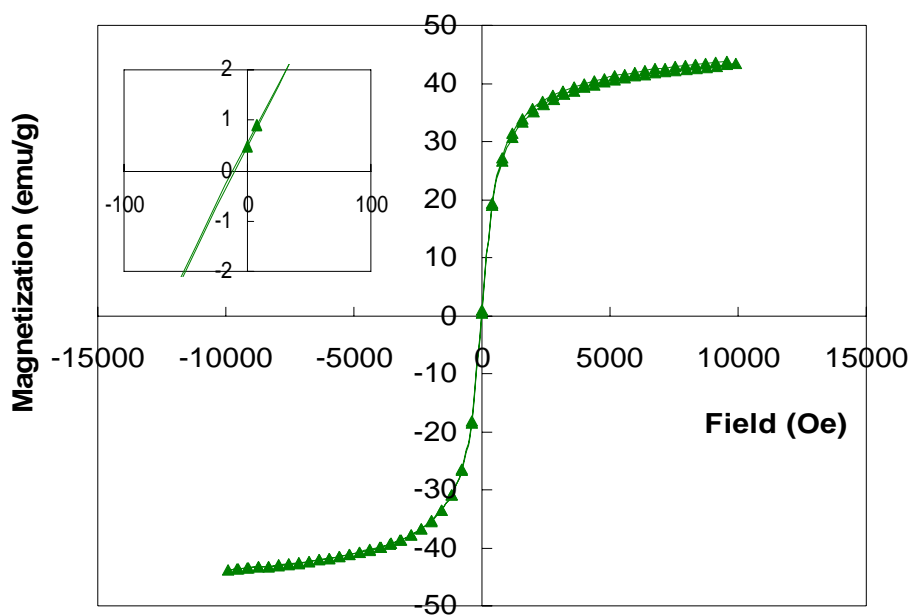
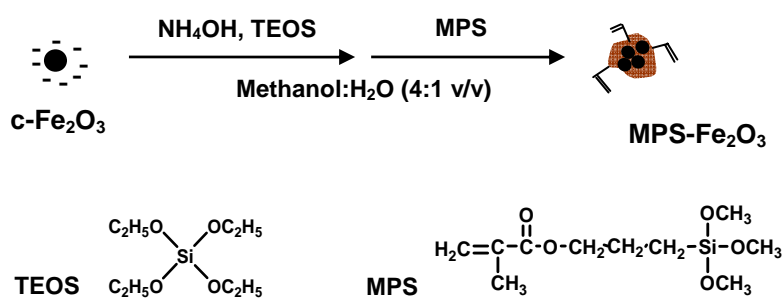


Figure 4.15. Magnetization behavior of c-Fe₂O₃ nanoparticles at room temperature ($M_s = 43$ emu/g).

4.3.2.3 Preparation of vinyl-coated γ -Fe₂O₃ (MPS-Fe₂O₃) nanoparticles

Preparation of MPS-Fe₂O₃ nanoparticles was achieved via a two-step reaction (Scheme 4.4): 1) treating the γ -Fe₂O₃ nanoparticles with ammonium hydroxide and tetraethylorthosilicate (TEOS) in a methanol/water mixture, and forming the silica-coated magnetic particles (Si-Fe₂O₃) as a precursor particle;^{82,96,116} 2) reacting the Si-Fe₂O₃ nanoparticles with a silane coupling agent, 3-(trimethoxysilyl)propyl methacrylate (MPS), to form terminal vinyl-coated magnetic nanoparticles (MPS-Fe₂O₃).^{82,96}



Scheme 4.4. Synthesis of MPS-Fe₂O₃ nanoparticles.

According to the Stöber method, silica spheres with diameters ranging from 20 nm to a few microns were formed through base-catalyzed hydrolysis and condensation of TEOS in a mixture of ethanol, ammonia, and water.^{116,117} Mechanism of the base-catalyzed hydrolysis and condensation reactions of TEOS is illustrated in Figure 4.16. Formation of silica coating on the γ -Fe₂O₃ nanoparticles also involves these base-catalyzed reactions (Figure 4.17). In the first step, the carboxylate groups of the γ -Fe₂O₃ nanoparticles undergo nucleophilic attack to the silica of the TEOS to form silicate-coated magnetic

nanoparticles via the formation of siloxane linkages (i.e. Si-O-C). Ammonium hydroxide then hydrolyzes covalently bonded silicate to silanol groups (-Si-OH). Subsequent condensation of the silanol groups forms a thin layer of silica coating on the nanoparticle surface (Si-Fe₂O₃).

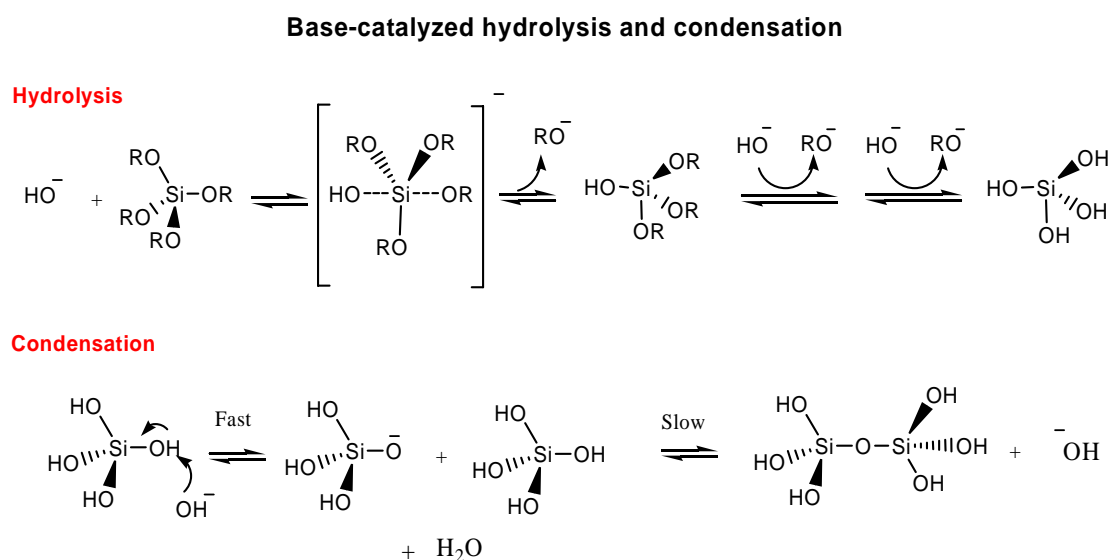


Figure 4.16. Base-catalyzed hydrolysis and condensation reaction of TEOS.

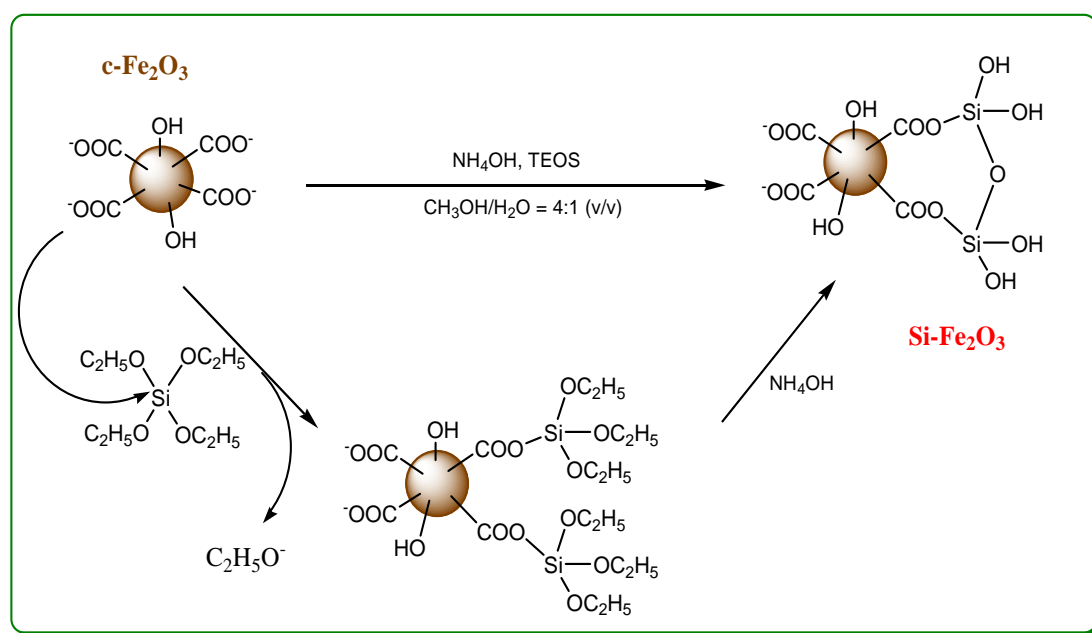


Figure 4.17. Proposed mechanism for the formation of Si-Fe₂O₃ nanoparticles.

Formation of the silica coatings was confirmed with FT-IR analyses (Figure 4.18). Compared with the IR spectrum of γ -Fe₂O₃ nanoparticles, the IR spectrum of Si-Fe₂O₃ nanoparticles showed a new absorption band at 1092 cm⁻¹, characteristic of stretching vibration of the Si-O bonding.¹¹⁸⁻¹²⁰

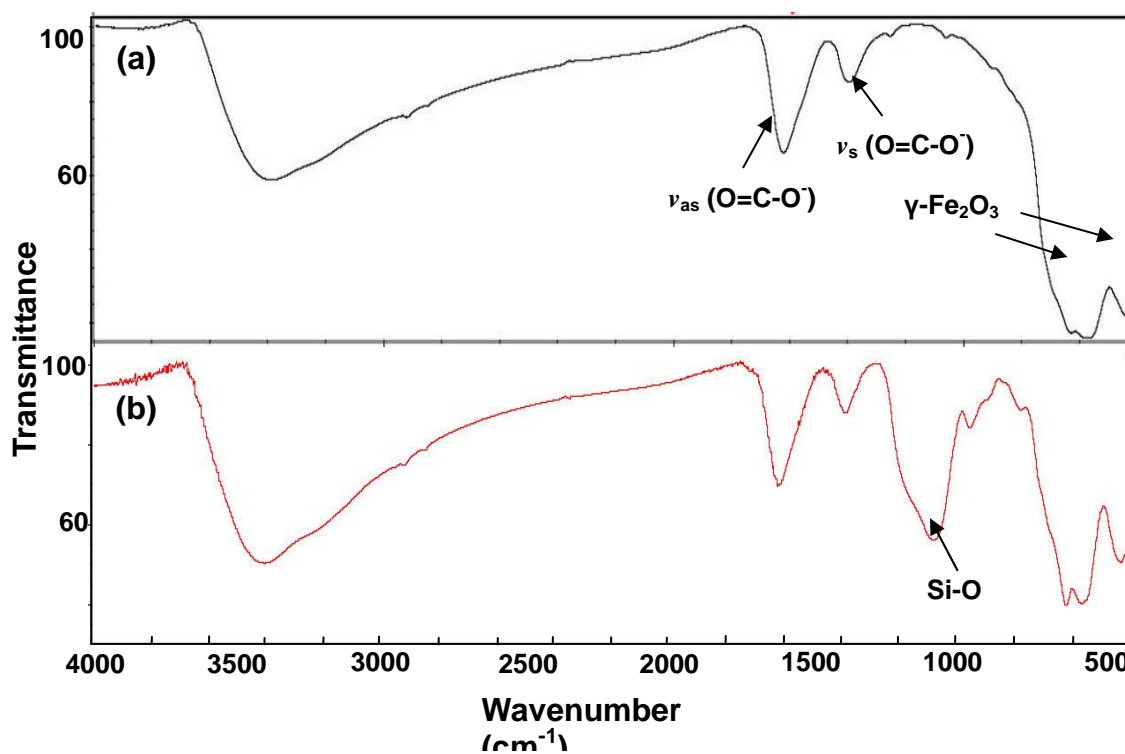


Figure 4.18. FT-IR spectra of: (a) γ -Fe₂O₃ and (b) Si-Fe₂O₃.

To introduce the reactive vinyl end groups on the Si-Fe₂O₃ nanoparticles, a silane coupling agent (MPS) was then added to the nanoparticle dispersion. Grafting of MPS onto the silica layer was achieved via the base-catalyzed reactions described by Bourgeat-Lami and Lang, and the grafting mechanism is shown in Figure 4.19. Because of the hydrophobicity of MPS molecules, the methoxy groups of MPS first undergo a base-catalyzed hydrolysis to form silanol groups (-Si-OH). The silanol groups of MPS molecules then condense and form

MPS oligomers through subsequent base-catalyzed hydrolysis. These oligomers then adsorb on the silica surface of Si-Fe₂O₃ nanoparticles through hydrogen bonding, and finally condense the MPS oligomers on the nanoparticle surface.

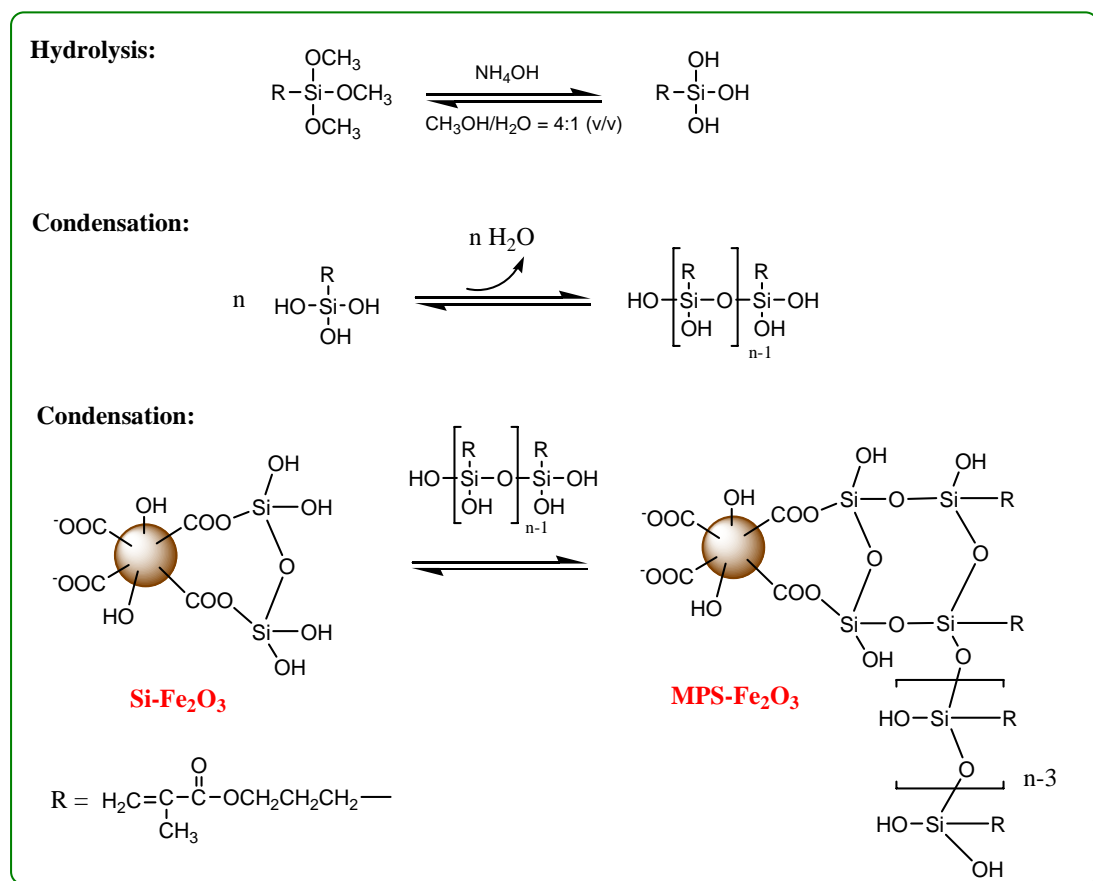


Figure 4.19. Proposed mechanism for the formation of MPS-Fe₂O₃ nanoparticles.

Chemical compositions of MPS-Fe₂O₃ nanoparticles

Grafting of MPS onto Si-Fe₂O₃ nanoparticles was confirmed with FT-IR analyses (Figure 4.20 a). The IR spectrum of MPS-Fe₂O₃ nanoparticles shows a new peak at 1722 cm⁻¹ (C=O) and a new band at 2700–2900 cm⁻¹ (C=C), as compared with the spectrum of Si-Fe₂O₃ nanoparticles (Figure 4.18 b). These two new peaks are contributed from the MPS molecules, as shown in Figure 4.20 (b).

A strong absorption peak at 1720 cm^{-1} is characteristic of the stretching vibration of C=O, and the IR absorption bands at $2700\text{--}2900\text{ cm}^{-1}$ are corresponding to the stretching vibrations of C=C and -CH_2 , respectively. These results suggest that the Si- Fe_2O_3 nanoparticles have been coated with MPS molecules.

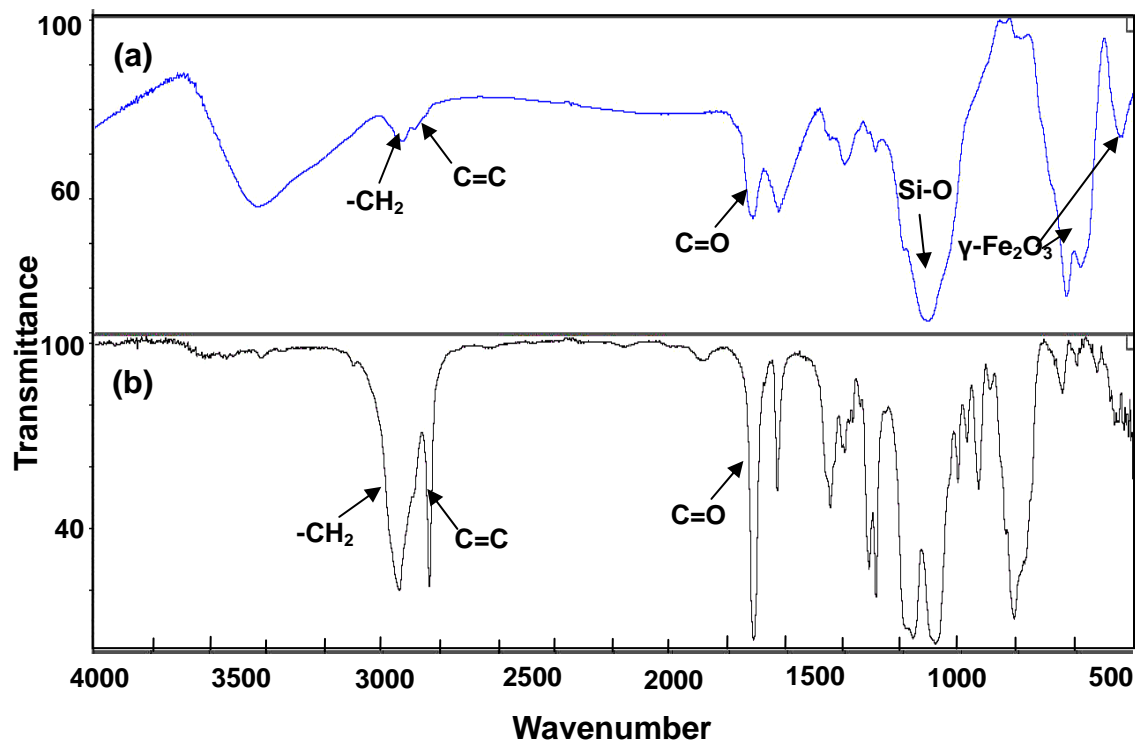


Figure 4.20. FT-IR spectra of: (a) MPS- Fe_2O_3 and (b) MPS.

Analyses of MPS- Fe_2O_3 nanoparticles using TGA also supported that the Si- Fe_2O_3 nanoparticles were coated with MPS molecules. Figure 4.21 shows the TGA thermogram of MPS- Fe_2O_3 nanoparticles, and their weight loss which can be seen in Figure 4.21 is summarized in Table 4.3. There is an initial weight loss (3.2 %) from 100 to 230 $^{\circ}\text{C}$ (removal of water, surface hydroxyl and amorphous iron hydroxides) and the second weight loss (10.3 %) from 230 to 568 $^{\circ}\text{C}$ (removal of citrate coating), respectively. It was found that initial weight loss of

MPS-Fe₂O₃ nanoparticles was smaller than that of Si-Fe₂O₃ nanoparticles. This result suggests that the surface of MPS-Fe₂O₃ nanoparticles is less hygroscopic than that of c-Fe₂O₃ nanoparticles, due to the presence of hydrophobic MPS molecules on the nanoparticle surface. The TGA thermogram of MPS-Fe₂O₃ nanoparticles also showed a two-step additional weight losses (5.8 %) after 510 to 899 °C, which might be attributed to the decomposition of siloxane linkage between citrate and Si coating and the loss of surface functional groups of MPS molecules. It was found that such decomposition temperatures (T_d) were higher than those T_d values (~ 350–400 °C) reported in the literature.^{121,122} Such increase in T_d may be due to the formation of strong Si-O bonding between MPS molecules and a thin layer of silica coating, since Si-O bonding has higher thermal stability than Si-O-C bonding.

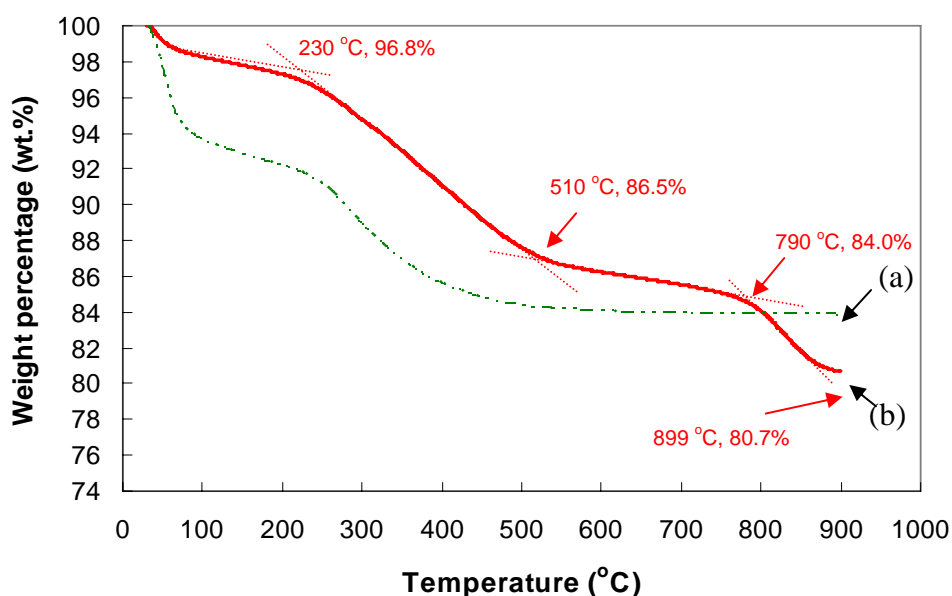


Figure 4.21. TGA thermograms of magnetic nanoparticles: (a) c-Fe₂O₃ and (b) MPS-Fe₂O₃.

Table 4.3. Compositions of Si-Fe₂O₃ and MPS-Fe₂O₃ nanoparticles obtained from Figure 4.21.^a

Sample	H ₂ O (%)	Surface hydroxyl (%) and amorphous iron hydroxides	Citrate (%)	Silica + MPS (%)	γ-Fe ₂ O ₃ (%)
c-Fe ₂ O ₃	6.0	2.5	7.5	0.0	84.0
MPS-Fe ₂ O ₃	1.5	1.7	10.3	5.8	80.7

^aThe thermal experiments were performed at temperatures ranging from 30 to 900 °C using a heating rate of 20 °C/min under N₂ atmosphere.

Effect of TEOS addition

To illustrate the importance of the silica precursor on the formation of MPS-Fe₂O₃ nanoparticles, an experiment was performed, in which c-Fe₂O₃ nanoparticles were directly treated with NH₄OH and MPS molecules without addition of TEOS in a mixture of methanol and water (4:1 v/v) at 40 °C. The obtained nanoparticles had bi-modal size distribution and had hydrodynamic diameter ($\langle D_h \rangle$) of 161 ± 3 nm, which can be seen in Figure 4.22 (a). In contrast, when c-Fe₂O₃ nanoparticles were first treated with NH₄OH and TEOS molecules under the same reaction condition, followed by treatment with MPS molecules, the obtained MPS-coated nanoparticles had mono-modal size distribution with $\langle D_h \rangle$ of 100 ± 1 nm (Figure 4.22 b). These results suggest that the presence of silica precursor layer can overcome the structure incompatibility between the *hydrophilic* citrate coating and the *hydrophobic* MPS coating, thus facilitating the

condensation reaction for MPS oligomers. This comparable study also suggests that formation of the silica precursor layer on the surface of $\alpha\text{-Fe}_2\text{O}_3$ nanoparticles is crucial for obtaining MPS- Fe_2O_3 nanoparticles with narrow size distribution.

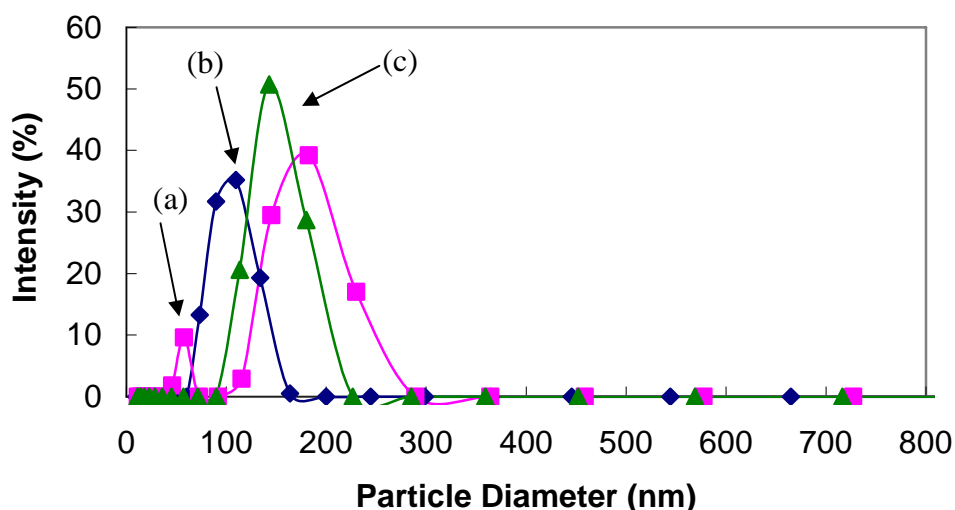


Figure 4.22. Hydrodynamic size and its distribution of MPS-coated magnetic nanoparticles: (a) without TEOS addition at 40 °C ($\langle D_h \rangle = 161 \pm 3$ nm); (b) with TEOS addition at 40 °C ($\langle D_h \rangle = 100 \pm 1$ nm); (c) with TEOS addition at 22 °C ($\langle D_h \rangle = 161 \pm 2$ nm).

Effect of reaction temperature

Variation of reaction temperature also showed significant influence on the formation of MPS-coated nanoparticles. When $\alpha\text{-Fe}_2\text{O}_3$ nanoparticles were treated with the same procedure as the previous experiment with TEOS addition except for lowering the reaction temperature from 40 to 22 °C, the MPS- Fe_2O_3 nanoparticles produced at 22 °C had mono-modal size distribution with a $\langle D_h \rangle$ of 161 ± 2 nm (Figure 4.22 c). Such values were fairly larger than the nanoparticles

($\langle D_h \rangle = 100 \pm 1$ nm, Figure 4.22 a) produced at 40 °C. These results indicate that lower reaction temperature favors formation of larger particle size. This might be attributed to the fact that the degree of hydrolysis and condensation reactions of TEOS and MPS was lower at lower temperature (i.e. 22 °C), thereby forming the silica and MPS hybrid coatings with higher porosity. It is known that the degree of hydrolysis and condensation reactions of TEOS is a key for controlling the porosity (or densification) of silica particles.¹¹⁷ In order to produce MPS-Fe₂O₃ nanoparticles with narrow size distribution, 40 °C was used in all subsequent experiments.

Particle size measurement and structural information

Figure 4.23 (a) shows the low-resolution TEM micrograph of MPS-Fe₂O₃ nanoparticles. The TEM image reveals that the nanoparticles produced were irregular in shape, and existed in small aggregates. Statistical analysis of such small aggregates determined that they had the average diameter of 75 ± 15 nm. Dynamic light scattering (DLS) measurement of the MPS-Fe₂O₃ nanoparticles determined that the volume-average diameter of MPS-Fe₂O₃ nanoparticles was 89 ± 2 nm. These results suggest that the MPS-coated nanoparticles exist in a small aggregated form, as indicated in Figure 4.23 (c). This observation has been reported by Deng *et al.* in their system.⁹⁶ The SAD image inserted in Figure 4.23 (b) shows the electron diffraction patterns of MPS-Fe₂O₃ nanoparticles, which is similar to that of γ -Fe₂O₃ (Figure 4.7 b) and c-Fe₂O₃ nanoparticles (Figure 4.14 b). These results suggest that the presence of silica and MPS coatings has little influence on the crystallinity of γ -Fe₂O₃ nanoparticles.

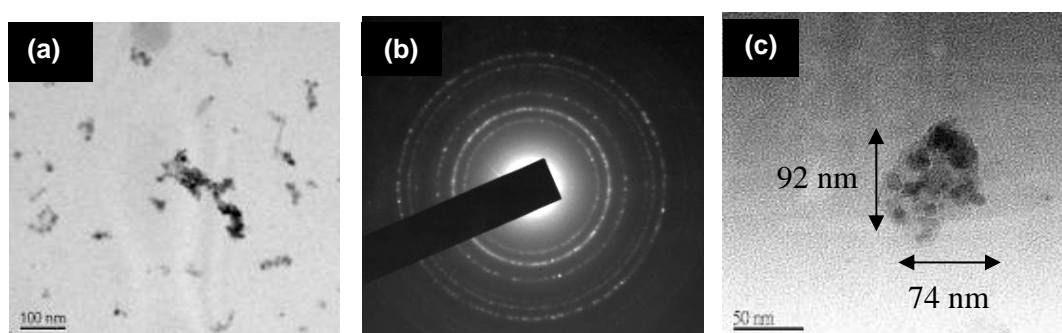


Figure 4.23. TEM images of synthesized MPS-Fe₂O₃ nanoparticles: (a) low-resolution image; (b) electron diffraction image of the left image; (c) high-resolution image.

Characterization of particle surface charges

ζ -Potential measurement of the MPS-Fe₂O₃ nanoparticles showed that the nanoparticles had lower negative charge densities than the c-Fe₂O₃ nanoparticles (Figure 4.24), indicating that some carboxylic acid groups of trisodium citrate on the particle surface had been converted to neutral vinyl groups.

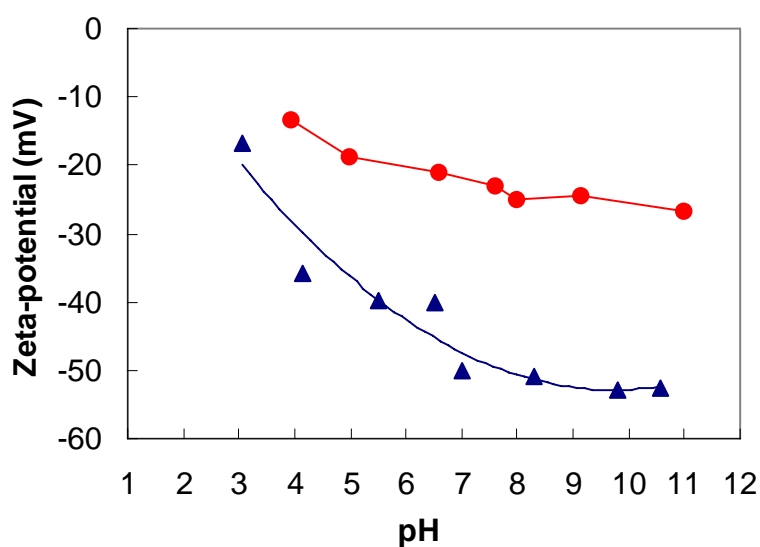


Figure 4.24. pH dependence of the ζ -potential measured in a 1 mM NaCl solution at 25 °C: (▲) c-Fe₂O₃ and (●) MPS-Fe₂O₃ nanoparticles.

Magnetization measurement

Magnetization measurement showed that the MPS-Fe₂O₃ nanoparticles still had high magnetic responsiveness (36 emu/g), and exhibited little hysteresis at room temperature, which might be attributed to the slight aggregation of γ -Fe₂O₃ nanoparticles (Figure 4.25).

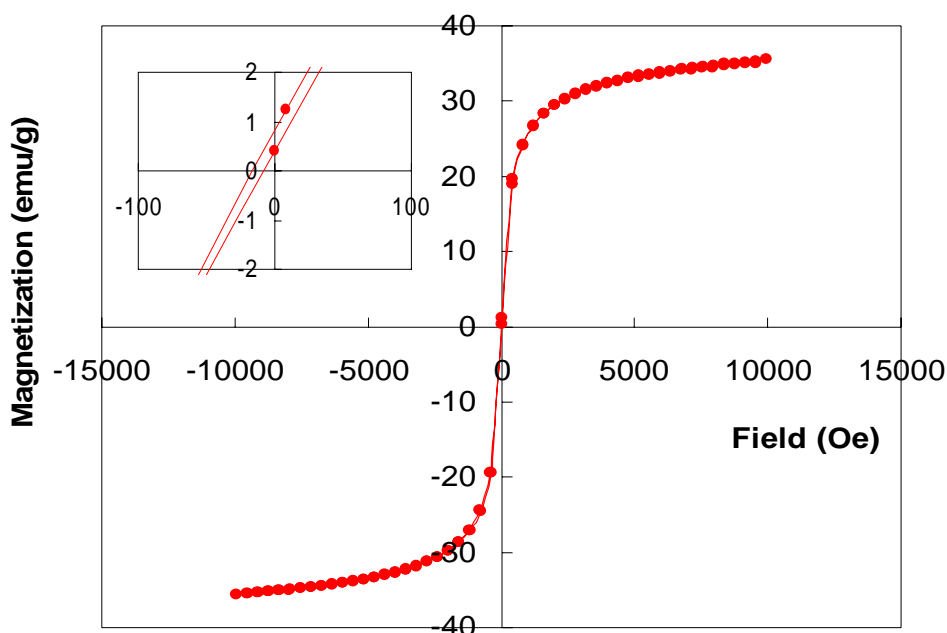


Figure 4.25. Magnetization behavior of MPS-Fe₂O₃ nanoparticles at room temperature ($M_s = 36$ emu/g).

4.4 Conclusions

Magnetic γ -Fe₂O₃ nanoparticles with three types of surface modifications were successfully synthesized. They include (1) oleate-coated γ -Fe₂O₃ (o-Fe₂O₃) nanoparticles; (2) citrate-coated γ -Fe₂O₃ (c-Fe₂O₃) nanoparticles; (3) vinyl-coated γ -Fe₂O₃ (MPS-Fe₂O₃) nanoparticles. Fourier-transform infrared (FT-IR) spectra confirmed that the γ -Fe₂O₃ nanoparticles were successfully modified with oleate, citrate, and silica coatings, respectively. Transmission electron microscopy (TEM) images showed that the organic-based o-Fe₂O₃ nanoparticles produced from decomposition of organic precursor approach had sizes of 8 ± 2 nm, and had

narrow size distribution. The aqueous-based γ -Fe₂O₃ nanoparticles produced through a chemical co-precipitation approach had an average size around 11 nm with broad size distribution. Subsequent surface modifications of the γ -Fe₂O₃ nanoparticles gave c-Fe₂O₃ nanoparticles with an average size around 11 nm, and MPS-Fe₂O₃ nanoparticles with an average size of 75 nm, respectively.

Selected area diffraction (SAD) and high-resolution TEM (HR-TEM) images showed that the o-Fe₂O₃ nanoparticles were polycrystalline with low crystallinity; while the aqueous-based γ -Fe₂O₃ nanoparticles were polycrystalline with high crystallinities. Furthermore, the presence of surface coating showed little influence on the crystallinity of γ -Fe₂O₃ nanoparticles. X-ray diffraction (XRD) of three surface-modified nanoparticles proved that maghemite (γ -Fe₂O₃) nanoparticles were successfully produced. Magnetization measurement of the synthesized nanoparticles showed that uncoated γ -Fe₂O₃ and c-Fe₂O₃ exhibited superparamagnetic at room temperature; while o-Fe₂O₃ and MPS-Fe₂O₃ nanoparticles exhibited little hysteresis at room temperature. The saturation magnetization (M_s) of o-Fe₂O₃ nanoparticles was 12.5 emu/g; while the M_s values of uncoated γ -Fe₂O₃, c-Fe₂O₃, and MPS-Fe₂O₃ nanoparticles were 46, 43, 36 emu/g, respectively.

Chapter 5

Synthesis and characterization of magnetic core-shell (MCS) particles

Following the detailed study of the synthesis and characterization of three types of surface-modified $\gamma\text{-Fe}_2\text{O}_3$ nanoparticles (oleate-coated $\gamma\text{-Fe}_2\text{O}_3$, citrate-coated $\gamma\text{-Fe}_2\text{O}_3$, and vinyl-coated $\gamma\text{-Fe}_2\text{O}_3$), this chapter will describe the synthesis of magnetic core-shell (MCS) particles using these modified $\gamma\text{-Fe}_2\text{O}_3$ nanoparticles. The MCS particles were synthesized in a one-step reaction which involved hydroperoxide-induced graft copolymerization of methyl methacrylate (MMA) from chitosan in the presence of the surface-modified magnetic nanoparticles. Investigations of reaction variables on monomer conversion, particle size and size distribution, grafting percentage of chitosan on MCS particles, encapsulation percentage of $\gamma\text{-Fe}_2\text{O}_3$, as well as particle morphology are discussed. Colloidal stability and magnetic-responsiveness of MCS particles are also examined.

5.1 *Tert*-hydroperoxide-induced graft copolymerization of vinyl monomer from water-soluble polymer containing amino groups

This section introduces the detailed mechanism of *tert*-hydroperoxide-induced graft copolymerization of vinyl monomers from water-soluble polymer containing amino groups, and the important features of this process.

5.1.1. Mechanism of the Graft Copolymerization

Recently, our research group has developed a novel method to prepare amphiphilic core-shell particles via a direct graft copolymerization of vinyl monomers from water-soluble polymers containing amino groups.¹⁰⁹ Our previous work have demonstrated that hydrophilic biopolymers and synthetic polymers containing primary amino groups can interact with a small amount of *tert*-butyl peroxide (TBHP) in water at 80 °C, generating free radicals on the amine nitrogens. The mechanism of this process is described in Figure 5.1. The TBHP (*t*-BuOOH) initially interacts with amino groups on the polymer backbone, forming redox pairs. One electron is then transferred from amine nitrogen to *t*-BuOOH, resulting in the formation of a nitrogen cation radical and a *tert*-butoxy (*t*-BuO•) radical. Subsequently, the amino radicals can initiate polymerization of vinyl monomers dissolved in water (route 1). The *t*-BuO• radical can either initiate the homopolymerization of monomers (route 2) to form a homopolymer or abstract hydrogen atom from the backbone of the polymer (route 3) to form a homopolymer. The amphiphilic macroradicals generated *in situ* are able to

self-assemble to form polymeric micelle-like microdomains that facilitate the emulsion polymerization of the monomer. Thus, well-defined, amphiphilic core-shell particles are produced in the absence of surfactant.

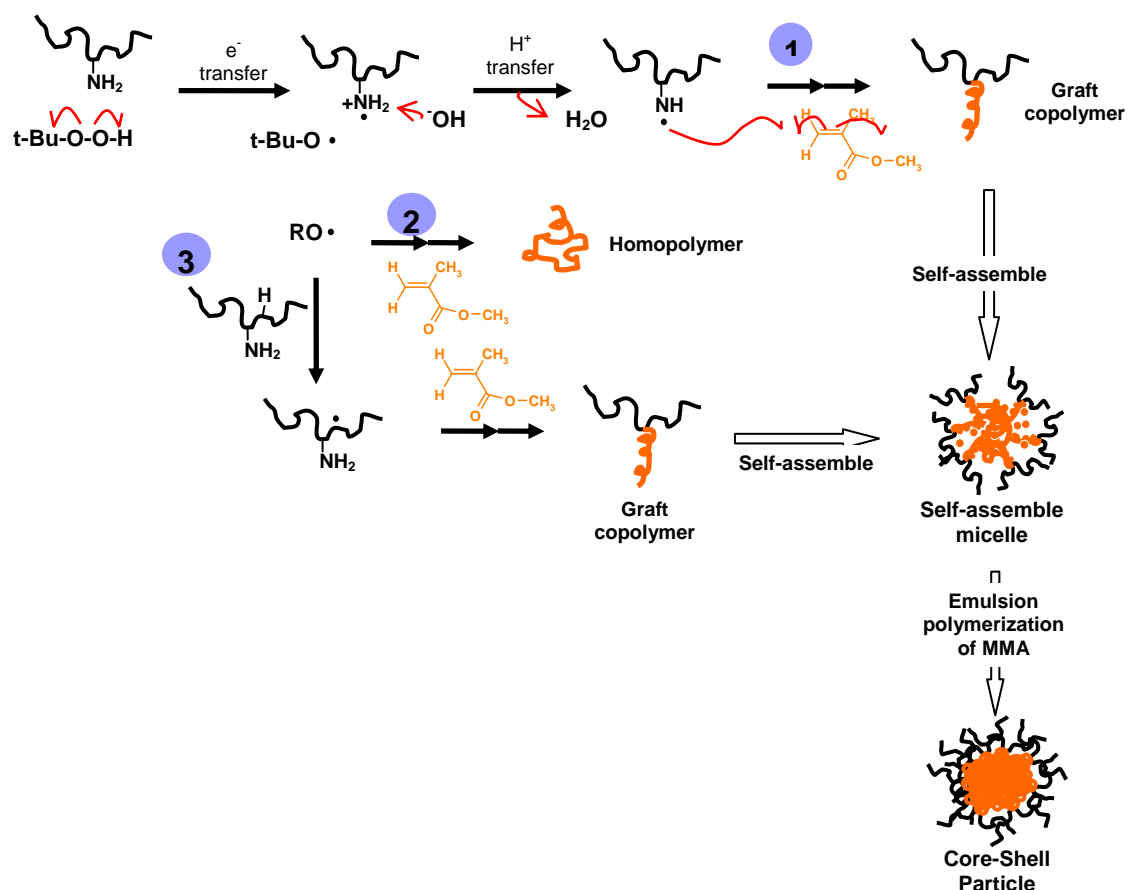


Figure 5.1. Mechanism of graft copolymerization of MMA from a water-soluble polymer containing amino groups.¹⁰⁹

5.1.2 Important features

Since the core-shell particles can be produced at a high solid content (up to 30 w/w%), this process appears to be amenable to the commercial production of a wide variety of novel amphiphilic core-shell nanomaterials with different sizes, compositions, structures, and functions. This process also include the following

features: (1) the particles are easy to synthesize; (2) the core-shell particle range from 60 to 500 nm with narrow size distributions; (3) the core and the shell are covalently linked; (4) No surfactants are required; (5) the process uses aqueous-based chemistry, which is environmentally benign; (6) the core properties of the particles can be varied using different types of monomers (e.g. hard, soft, temperature-sensitive and hollow; (7) the shell component can use a wide range of amine containing water-soluble polymers including biopolymers and (8) surface functionalities and properties can be easily altered. Thus, new materials produced by this process have been applicable in a wide range of applications such as gene delivery,¹²³ drug delivery,¹²⁴ anti-bacterial coating for textile clothing,¹²⁵ enzyme immobilization, and waste-water treatment. Because of these desirable properties, this method was employed to encapsulate magnetic nanoparticles into the core-shell particles. Detailed synthesis of magnetic core-shell (MCS) particles using the graft copolymerization technique will be described in the following section.

5.2 Experimental

5.2.1 Materials

Oleate-coated γ -Fe₂O₃ (o-Fe₂O₃), citrate-coated γ -Fe₂O₃ (c-Fe₂O₃) and MPS-Fe₂O₃ nanoparticles were synthesized, which have been described in Section 4.2. Chitosan (medium, Aldrich) was purified by dissolving it in a dilute acetic acid solution (1 v/v%) at 60 °C, followed by precipitating in a sodium hydroxide solution (10 w/w%) under stirring at room temperature. The chitosan was then filtered off and washed with distilled water to neutral, and finally dried in a vacuum oven at 60 °C. Molecular-weight measurement using dilute-solution viscosity suggested that the M_v of chitosan was approximately 80,000 (Appendix, Figure A-1). The degree of deacetylation of chitosan, as estimated by ¹H-NMR spectroscopy, using the method reported by Hirai *et al.*,¹²⁶ was 74 % (Appendix, Figure A-2). PEI (M_w 60,000 g mol⁻¹, 50 w/w%) and cellulase (from *Aspergillus* species) solutions were purchased from Aldrich Chemical Co, and used as received. Poly(vinyl amine) (PVAm) was synthesized by Mr. Li Wei Ying. Casein (5 %, Acros) was purified by mixing it with a 1 w/w% of ethylenediaminetetraacetic acid, disodium salt dehydrate (EDTA) solution at 50 °C for 48 h in order to remove metal ions in the casein. The purified casein was dried at 50 °C under vacuum for 48 h.

The phenolic inhibitors in methyl methacrylate (MMA, 0.936 g/cm³, Aldrich), and *n*-butyl acrylate (BA, 0.894 g/cm³, Aldrich) were removed by washing three times with a 10 w/w% of sodium hydroxide solution and then with deionized water until the pH of the water layer dropped to 7. The monomer was

further purified by vacuum distillation. *N*-isopropylacrylamide (NIPAM, Aldrich) was purified by repeated recrystallization in a mixture of toluene and hexane (1:5 v/v), giving spindle-like crystals. The purified NIPAM was dried at room temperature under vacuum for 48 h. *tert*-butyl hydroperoxide (TBHP) (70 w/w% solution in water), hydrogen peroxide (H₂O₂) (35 w/w% solution in water) and *N,N*-methylenebisacrylamide (MBA) were obtained from Aldrich Chemical Co., and used without further purification. Freshly deionized and distilled water was used as the dispersion medium.

5.2.2 Graft copolymerization of MMA from chitosan in the presence of surface-modified magnetic nanoparticles

5.2.2.1 α -Fe₂O₃ nanoparticles

For a total solution of 25 mL, the purified chitosan powder (0.25 g) was completely dissolved in an acetic acid solution (0.6 v/v%, 22.50 mL). The solution was transferred into a water-jacketed flask equipped with a thermometer, a condenser, a magnetic stirrer, and a nitrogen inlet. The resulting solution was then stirred at 300 rpm with a mixture of MMA (1.0 g), octane (2 mL) and α -Fe₂O₃ nanoparticles (0.04 g) at room temperature for 20 min under N₂ atmosphere, followed by heating at 80 °C for 1 h. TBHP solution (0.25 mL, 0.1 mM) was then added, and the resulting mixture was allowed to react at 80 °C for 2 h under nitrogen. After the reaction, the obtained particle dispersion was filtered to separate any precipitates generated (if any) during the polymerization. The ppt.

filtered were dried and weighed, and the percentage of ppt. (ppt.%) obtained was calculated using the following equation:

$$\text{ppt. (\%)} = \frac{\text{weight of ppt. obtained after the polymerization}}{\text{total weight of substances initially added}} \times 100 \quad \% \quad (5.1)$$

Monomer conversion (Conv.%) was determined gravimetrically, according to following procedure: 2 mL of filtered dispersion was withdrawn from the reaction mixture and dried overnight at 80 °C. It was further dried in a vacuum oven (25 inch Hg) at 80 °C for 24 hours. Assuming that the un-reacted MMA monomer and other small molecules such as *t*-BuOOH were removed during the vacuum dry process, the dried solids only contained the un-reacted chitosan, PMMA/chitosan core-shell particles, un-reacted MPS-Fe₂O₃ nanoparticles, magnetic PMMA/chitosan core-shell particles. Thus, the total weight of solids (W_t) was determined according to following formula:

$$W_t = \left(\left(\frac{W_{disp}}{2} \right) (V_{disp}) + W_{ppt} \right) \quad (5.2)$$

where W_{disp} is the weight of the 2 mL filtered dispersion obtained, V_{disp} is the total volume of filtered dispersion obtained, W_{ppt} is the weight of precipitate obtained from Equation 5.1. Based on the W_t , monomer conversion was able to be determined using the following Equation:

$$\text{Conv. \%} = \left(\frac{W_t - W_{WSP} - W_{MNP}}{W_{MMA}} \right) \times 100\% \quad (5.3)$$

where W_{WSP} is the weight of water-soluble polymers (e.g. chitosan) initially added, W_{MNP} is the weight of magnetic nanoparticles initially added and W_{MMA} is the weight of MMA initially added. The obtained particles were then purified by repeated centrifugation (13000 rpm, 1 h), decantation and re-dispersion until the conductivity of the supernatant was close to that of distilled water.

5.2.2.2 c-Fe₂O₃ nanoparticles

For a total solution of 25 mL, the purified chitosan powder (0.25 g) was completely dissolved in an acetic acid solution (0.8 v/v%, 18.75 mL). The c-Fe₂O₃ dispersion (2 w/w%, 5 mL) was added dropwise into the chitosan solution under stirring, giving a stable brown homogeneous dispersion, which was then transferred into a water-jacketed flask equipped with a thermometer, a condenser, a magnetic stirrer, and a nitrogen inlet. The dispersion was stirred at 300 rpm and purged with nitrogen for 20 min at 80 °C prior to addition of purified MMA (1.0 g), and TBHP (10 mM, 0.25 mL). The resulting mixture was continuously stirred at 80 °C for 2 h under nitrogen. After the reaction, the obtained particle dispersion were filtered to separate any precipitates (if any) generated during the polymerization. The amount of precipitates was determined using the Equation 5.1. Monomer conversion (Conv.%) was determined gravimetrically, according to the Equation 5.3. The particles were then purified by repeated centrifugation (13,000 rpm, 1 h), decantation and re-dispersion until the conductivity of the supernatant was close to that of distilled water.

5.2.3 Graft copolymerization of MMA from chitosan in the presence of MPS-Fe₂O₃ nanoparticles initiated with *tert*-butyl hydroperoxide (TBHP) or hydrogen peroxide (H₂O₂)

For a total solution of 25 mL, 0.05 to 0.2 g of MPS-Fe₂O₃ nanoparticles (10 w/w% in ethanol) and ethanol were mixed using a homogenizer (Sonics VC130PB, output watt = 6 W) with a chitosan solution (0.25 g, 22.5 mL) containing a 0.6 v/v% of acetic acid, giving the final volume ratio of H₂O to ethanol of 12.5 to 1. The viscous dispersion was homogenized for 10 min, and then transferred into a water-jacketed flask equipped with a thermometer, a condenser, a magnetic stirrer, and a nitrogen inlet. The dispersion was purged with nitrogen for 20 min, and stirred at 80 °C prior to the addition of appropriate amount of MMA (0.2–0.79 g). Appropriate amounts of either TBHP (0.05–0.4 mM) or H₂O₂ (0.05–1.2 mM) were then added to the mixture. The resulting mixture was continuously stirred at 80 °C for 2 h under nitrogen. After the reaction, the obtained particle dispersion were filtered to separate any precipitates (if any) generated during the polymerization. The amount of precipitates was determined using the Equation 5.1. Monomer conversion (Conv.%) was determined gravimetrically, according to the Equation 5.3. The particles were then purified by repeated centrifugation (13,000 rpm, 1 h), decantation and re-dispersion until the conductivity of the supernatant was close to that of distilled water.

The percentage of chitsoan (CTS) actually reacted to form particles was calculated as follows:

$$\text{Weight of reacted CTS} = W_{\text{CTS1}} - W_{\text{CTS2}}$$

$$\text{CTS\% reacted} = \frac{\text{Weight of reacted CTS}}{W_{\text{CTS1}}} \times 100\% \quad (5.3)$$

Where W_{CTS1} is the total weight of CTS added, and W_{CTS2} is the weight of un-reacted CTS which was determined by first drying the crude product to fine powder, and then extracted with a 1 v/v% of acetic acid for 48 h using a Soxhlet extractor (Figure 5.2).

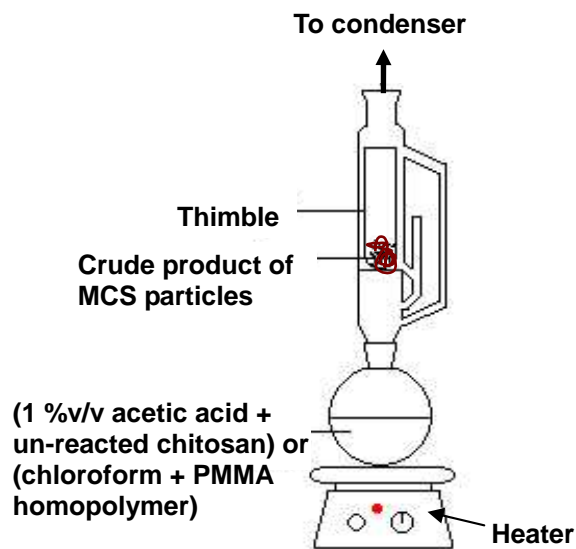


Figure 5.2. A diagram of Soxhlet extractor.

The percentage of PMMA homopolymer and PMMA grafts on chitosan (PMMA grafting efficiency %) backbone were calculated as follows:

$$\text{Weight of PMMA branches} = (W_{\text{MMA}} \times \text{conversion \%}) - W_{h\text{-PMMA}}$$

$$\text{PMMA grafting efficiency (\%)} = \frac{\text{Weight of PMMA branches}}{W_{\text{MMA}} \times \text{Conversion\%}} \times 100 \% \quad (5.4)$$

where W_{MMA} is the weight of MMA initially added, and $W_{h\text{-PMMA}}$ is the weight of PMMA homopolymer which was determined by first drying the crude mixture to fine powders; followed by extraction with chloroform for 48 h using a Soxhlet extractor (Figure 5.2).

5.2.4 Measurement and characterization

Particle morphologies

The transmission electron microscope (TEM) images were obtained using a JEOL 2010 transmission electron microscope at an operating voltage of 200 kV. A small drop of dilute particle dispersion (100–200 mg/L) was placed on a formvar-coated or carbon-coated grids, and dried at room temperature before analysis. The morphologies of MCS particles were also examined with a field emission scanning electron microscopy (FE-SEM, JEOL JSM 6335F) after coating the dried sample with a thin layer of gold to a depth of approximately 5 Å under vacuum.

Chemical compositions

Infrared spectra were recorded on a Nicolet Avatar 360 FT-IR spectrophotometer using potassium bromide (KBr) disks. About 10 mg of finely grounded sample and about 0.5 g of spectrophotometric grade anhydrous KBr were grinded thoroughly using a mortar and a pestle. To yield a transparent disk

for IR measurement, the mixture was pressed at a force of about 7 tonnes for 2 minutes using a level-screw press.

Differential scanning calorimetry (DSC) thermograms were recorded on a Mettler Toledo DSC 822^o. Accurate weight of finely grounded sample was placed into an aluminum cup and sealed. An empty cup was used as reference. The thermal analysis was performed by heating the sample from 30 to 550 °C at a heating rate of 10 °C/min under a continuous flow of dry nitrogen gas (10 mL/min).

Thermogravimetry analysis (TGA) was conducted using a Perkin-Elmer thermogravimetry analyzer TGA7 (TGA). Exact amount of finely grounded powder was weighed and placed in a platinum sample holder. The thermal experiments were performed at temperatures varying from 30 to 900 °C at a heating rate of 20 °C/min under N₂ atmosphere. The percentage of γ -Fe₂O₃ content in MCS particles was calculated as follows:

$$\gamma\text{-Fe}_2\text{O}_3 (\%) = \frac{\text{weight remained at } 900\text{ }^\circ\text{C}}{\text{weight loss due to H}_2\text{O evaporation at } 100\text{ }^\circ\text{C}} \times 100\% \quad (5.5)$$

Particle size analyses

Volume-average (D_v) and number-average (D_n) diameters of MCS particles were measured with a Coulter LS 230 Particle Size Analyzer using a polarization intensity differential scattering (PIDS) module. Hydrodynamic

diameter ($\langle D_h \rangle$) of MCS particles was also measured with a Malvern Zetasizer 3000HS (Malvern, UK) with 632.8 nm at 25 °C. Measurements were performed at a fixed angle equal to 90 °. Sample concentration was between 100 and 300 mg/L. For every sample, the measurements were repeated three times.

Characterization of particle surface charge density

All zeta-potential measurements were determined with a Malvern Zetasizer 3000HS in a 1×10^{-3} M NaCl aqueous solution as a suspension liquid. Sample concentrations were maintained between 100 and 300 mg/L.

Colloidal stability and critical coagulation concentrations (CCC) of MCS particles

Colloidal stability of MCS particles was studied with two methods: (1) measuring changes in hydrodynamic diameter of MCS particles at various pHs and sodium chloride (NaCl) concentrations (0 to 2.0 M) using a dynamic light scattering (i.e. Malvern Zetasizer 3000 HS); (2) measuring intensity change of absorbance peak of MCS particle dispersion (at pH 6.0) at various NaCl concentrations (0 to 2.0 M) using a UV-VIS spectroscopy.¹²⁷

A typical experiment for the UV-VIS measurement is described as follows: For a total volume of 5 mL, the dispersion of MCS particles was first diluted to 100 mg/L, followed by the addition of various NaCl solutions with known concentration. These suspensions were gently shaken for 10 min, then standing for

60 min at room temperature. The suspensions were centrifuged at 2000 rpm for 15 min, in which the supernatants were collected. The absorbance of the collected supernatant was measured with a Perkin-Elmer UV-VIS spectrophotometer (Lambda 35) with an incident wavelength of 450 nm. Turbidities (A/A_0) were plotted against c , where c was the electrolyte concentration, A_0 and A were the absorbance of the MCS particle dispersion before and after addition of electrolyte, respectively. The critical coagulation concentration (CCC) was determined by extrapolating the sharply decreasing part of the turbidity curve.

Magnetization measurement

The saturation magnetizations (M_s) were determined with a vibrating sample magnetometer (VSM) (LDJ MODEL 9500) at room temperature. Exact amount of a sample (usually larger than 0.05 g) was weighed, and closely packed into a Teflon holder. The magnetization measurement was studied at room temperature using external magnetic fields ranging from 0 to 5 KOe.

5.3 Results and Discussion

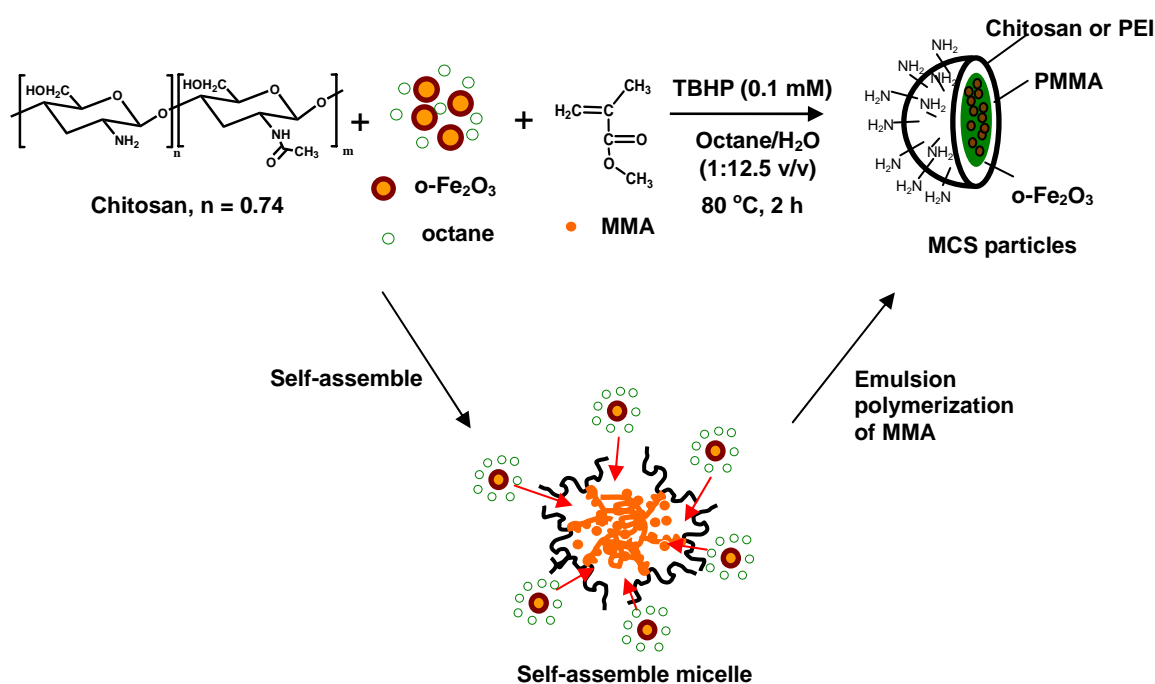
5.3.1 Graft copolymerization of MMA from chitosan in the presence of surface-modified magnetic nanoparticles

5.3.1.1 Oleate-coated γ -Fe₂O₃ (o-Fe₂O₃) nanoparticles

The o-Fe₂O₃ nanoparticles were synthesized via thermal decomposition of iron pentacarbonyl, Fe(CO)₅, in the presence of oleic acid micelles. Detailed synthesis of the nanoparticles has been described in Section 4.2.2. The rationale of preparing *hydrophobic* o-Fe₂O₃ nanoparticles was that the hydrophobic nature of the nanoparticles allowed their efficient encapsulation into the hydrophobic PMMA cores during the polymerization. However, the o-Fe₂O₃ nanoparticles dispersed poorly in water and chitosan solution due to their long alkyl chains. Thus, they had to be dispersed in a small amount of hydrophobic solvent (2 mL). Octane was used because of its high boiling point (~125 °C), thus it could be retained during the graft copolymerization at 80 °C for 2 h.

The o-Fe₂O₃/octane dispersion was first mixed with a chitosan solution containing a 0.6 v/v% of acetic acid to form a two-phase mixture. Subsequent stirring of this heterogeneous mixture at 80 °C gave a metastable brown emulsion. Graft copolymerization of MMA from chitosan in this heterogeneous mixture was induced with a small amount of TBHP and the polymerization took place at 80 °C for 2 h (Scheme 5.1). A milky brown dispersion was finally obtained at the end of the reaction (2 h). Although high MMA conversion (91 %) was achieved, 67 % of

the total charged substances were converted to form precipitates (Table 5.1, code 010107-2). These precipitates were then analyzed with a FT-IR spectroscopy (Figure 5.3). The IR spectrum of these precipitates showed the characteristic peaks including N-H stretching of chitosan at 3400 cm^{-1} , carbonyl (C=O) stretching of PMMA at 1731 cm^{-1} and Fe-O vibration of iron oxide between 400 and 600 cm^{-1} , suggesting that the precipitates consisted of chitosan, PMMA and oleate-coated iron oxide nanoparticles. As compared with their peak intensities in Figure 5.3, it was noted that the iron oxide content in the precipitates was quite high, when compared with both chitosan and PMMA. This result may indicate that octane was unable to stabilize the oleate-coated nanoparticles, resulting in serious precipitation during the polymerization.



Scheme 5.1. Proposed schematic representation of the graft copolymerization of MMA from chitosan in the presence of $\alpha\text{-Fe}_2\text{O}_3$ nanoparticles.

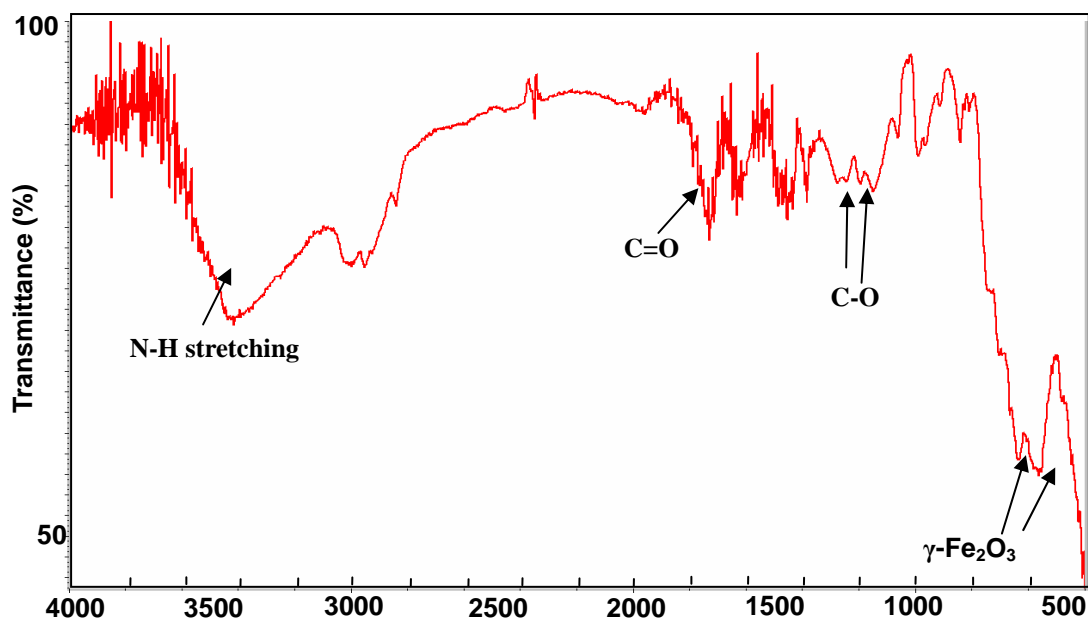


Figure 5.3. IR spectrum of brown precipitates obtained after the polymerization.

Figure 5.4 shows the TEM images of the particles produced which were mainly PMMA/chitosan core-shell particles without iron oxide nanoparticles inside the PMMA cores. The magnetic nanoparticles were preferably located outside the core-shell particles. This result indicated that encapsulation of α -Fe₂O₃ nanoparticles into the PMMA cores failed under these experimental conditions. Unsuccessful encapsulation might be due to the fact that α -Fe₂O₃ nanoparticles have a very limited dispersing ability in water. As a result, they preferably dispersed inside oil droplets of octane rather than diffusing to the self-assembled micelle cores during the graft copolymerization. Thus diffusing hydrophobic nanoparticles with octane droplet into the PMMA cores was not feasible which may be due to two reasons: 1) low mass transfer of α -Fe₂O₃ nanoparticles in water and 2) their poor miscibility with water. Therefore, magnetic nanoparticles were

unable to be encapsulated into the core-shell particles.

Table 5.1. TBHP-induced graft copolymerization of MMA from chitosan in the presence of surface-modified magnetic nanoparticles.^a

Expt. code	Surface-modified magnetic nanoparticles	Solid content%	Conv.% (ppt.%)	Encapsulation ^t
010107-2	o-Fe ₂ O ₃ ^d	5.4	91 (67)	No
240505	c-Fe ₂ O ₃ ^e	3.8	79	No

^aRefer to the procedure described in the Section 5.2.2. TBHP (0.1 mM) was used in all cases. All reactions were carried out at 80 °C for 2 h Chitosan was dissolved in a 0.6 v/v% of acetic acid, where the pH of the chitosan solution was pH 4.12. ^bEncapsulation of magnetic nanoparticles into the core of core-shell particles was determined by TEM images. ^cThe weight ratio of chitosan to MMA to o-Fe₂O₃ nanoparticles was 2.5 : 10 : 1; ^dThe weight ratio of chitosan to MMA to c-Fe₂O₃ nanoparticles was 2.5 : 6 : 1.

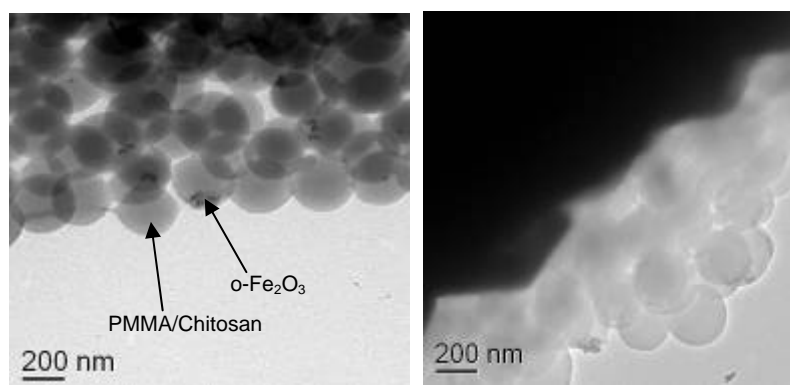
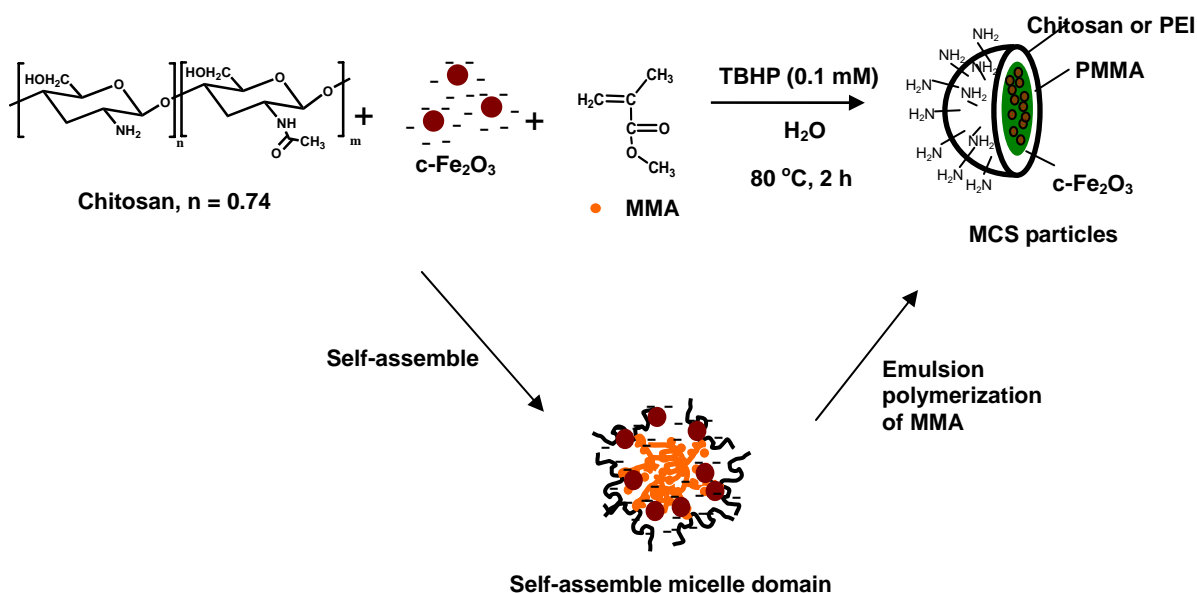


Figure 5.4. TEM images of PMMA/chitosan particles produced in the presence of o-Fe₂O₃ nanoparticles.

5.3.1.2 Citrate-coated γ -Fe₂O₃ (c-Fe₂O₃) nanoparticles

As mentioned in the previous section, encapsulation of hydrophobic iron oxide nanoparticles dispersing in oil droplets into the hydrophobic PMMA cores

of the core-shell particles was very difficult because of the incompatibility between oil and water phase and low mass transfer of magnetic nanoparticle. To address this problem, synthesis of water-based magnetic nanoparticles was attempted. To facilitate the encapsulation of water-based nanoparticles into the hydrophobic cores, it was assumed that negatively charged nanoparticles could first complex with positively charged chitosan, followed by the TBHP-induced graft copolymerization (Scheme 5.2). Thus, negatively charged $c\text{-Fe}_2\text{O}_3$ nanoparticles were synthesized, which has been described in Section 4.2.3.2. The $c\text{-Fe}_2\text{O}_3$ nanoparticles were able to complex with the chitosan via electrostatic interactions, thus the adsorbed magnetic nanoparticles became more hydrophobic due to the neutralization of their surface charges. As a result, subsequent copolymerization enabled the nanoparticles to be encapsulated into the PMMA cores.



Scheme 5.2. Schematic representation of the graft copolymerization of MMA from chitosan in the presence of $c\text{-Fe}_2\text{O}_3$ nanoparticles

The graft copolymerization of MMA from chitosan in the presence of $c\text{-Fe}_2\text{O}_3$ nanoparticles was induced with a small amount of TBHP at 80 °C for 2 h (Table 5.1, code 240505). The particles produced gave a reasonable conversion (79 %). No precipitates were formed after the reaction. However, TEM images of the particles produced showed that magnetic nanoparticles were mainly located outside the PMMA/chitosan particles (Figure 5.5). This result indicated that encapsulation of $c\text{-Fe}_2\text{O}_3$ nanoparticles into the PMMA cores was unsuccessful which might be due to two possible reasons: 1) Structural incompatibility between the *hydrophilic* surface of $c\text{-Fe}_2\text{O}_3$ nanoparticles and the *hydrophobic* PMMA cores. 2) Complexation between the iron oxide nanoparticles and chitosan confined the nanoparticles to the shell.

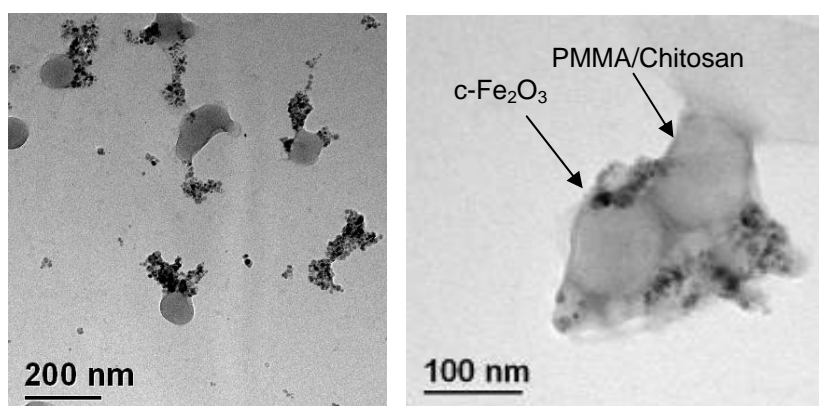


Figure 5.5. TEM images of PMMA/chitosan particles produced in the presence of $c\text{-Fe}_2\text{O}_3$ nanoparticles.

5.3.2 Graft Copolymerization of MMA from Chitosan in the Presence of MPS-Fe₂O₃ Nanoparticles

To overcome this incompatibility problem, the α -Fe₂O₃ nanoparticles were further modified by introducing terminal double bonds onto the nanoparticle surface. This emerged idea was based on two reasons: 1) Modification of hydrophilic α -Fe₂O₃ nanoparticles with hydrophobic molecules containing terminal double bonds could favor encapsulation of the nanoparticles into the PMMA cores because of their improved compatibility and 2) The double bonds on the nanoparticle surface could be copolymerized with MMA, thus driving the nanoparticles into the PMMA cores. The modification procedure of α -Fe₂O₃ to vinyl-coated γ -Fe₂O₃ (MPS-Fe₂O₃) nanoparticles has been described in Section 4.2.3.3. However, MPS-coated nanoparticles could not be dispersed well in water or chitosan solution due to their hydrophobic vinyl end groups. Thus, they were mixed with chitosan solution with a small amount of ethanol and homogenized for 10 min to form a stable brown viscous dispersion. The formation of this stable dispersion was probably attributed to the adsorption of cationic chitosan molecules onto the surface of negatively charged MPS-Fe₂O₃ nanoparticles, and hydrogen-bonding between hydroxyl groups of chitosan and MPS-Fe₂O₃ nanoparticles (Figure 5.6).

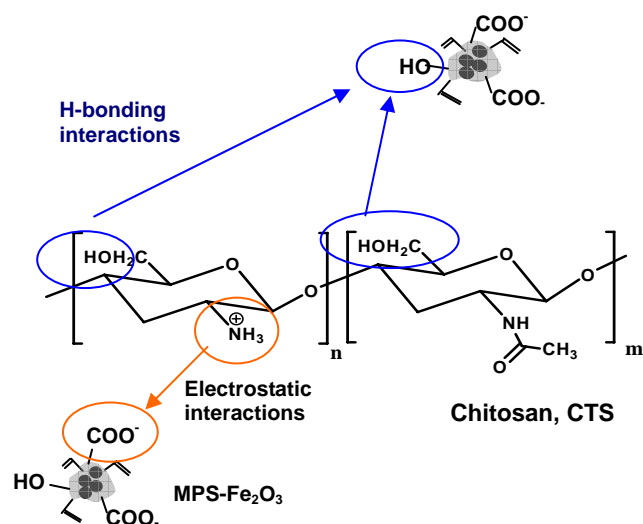
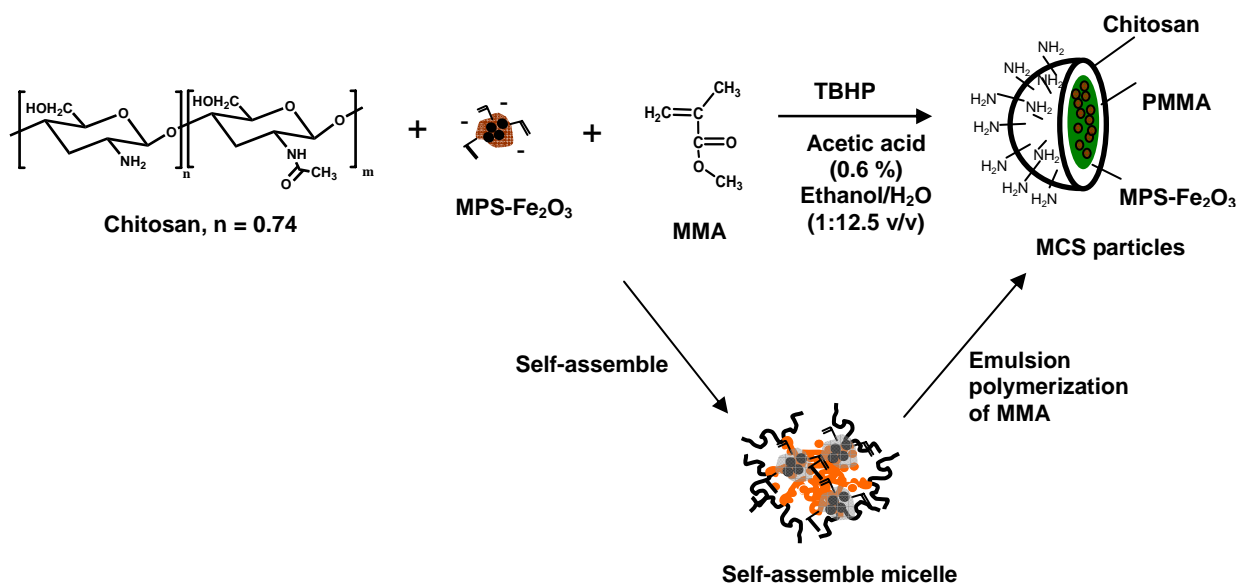


Figure 5.6. Possible interactions between chitosan and MPS-Fe₂O₃ nanoparticles.

Graft copolymerization of MMA from chitosan in the presence of MPS-Fe₂O₃ nanoparticles was initiated with a small amount of TBHP at 80 °C for 2 h (Scheme 5.3). When a weight ratio of CTS to MMA to MPS-Fe₂O₃ of 2.5 : 9 : 1 was used, a milky brown dispersion was produced after 2 h. Although the MMA conversion was only 55 % with a small amount of precipitates (0.19 g), TEM images of the particles revealed that the MPS-Fe₂O₃ nanoparticles were mainly located inside the PMMA core of the particles (Figure 5.7 a). This result indicated that encapsulation of MPS-Fe₂O₃ nanoparticles into the PMMA cores was finally achieved. Therefore, modification of γ -Fe₂O₃ nanoparticles to contain terminal vinyl groups on the surface is a crucial step for successful encapsulation of magnetic nanoparticles into the PMMA cores.



Scheme 5.3. Schematic representation of the graft copolymerization of MMA from chitosan in the presence of MPS-Fe₂O₃ nanoparticles.

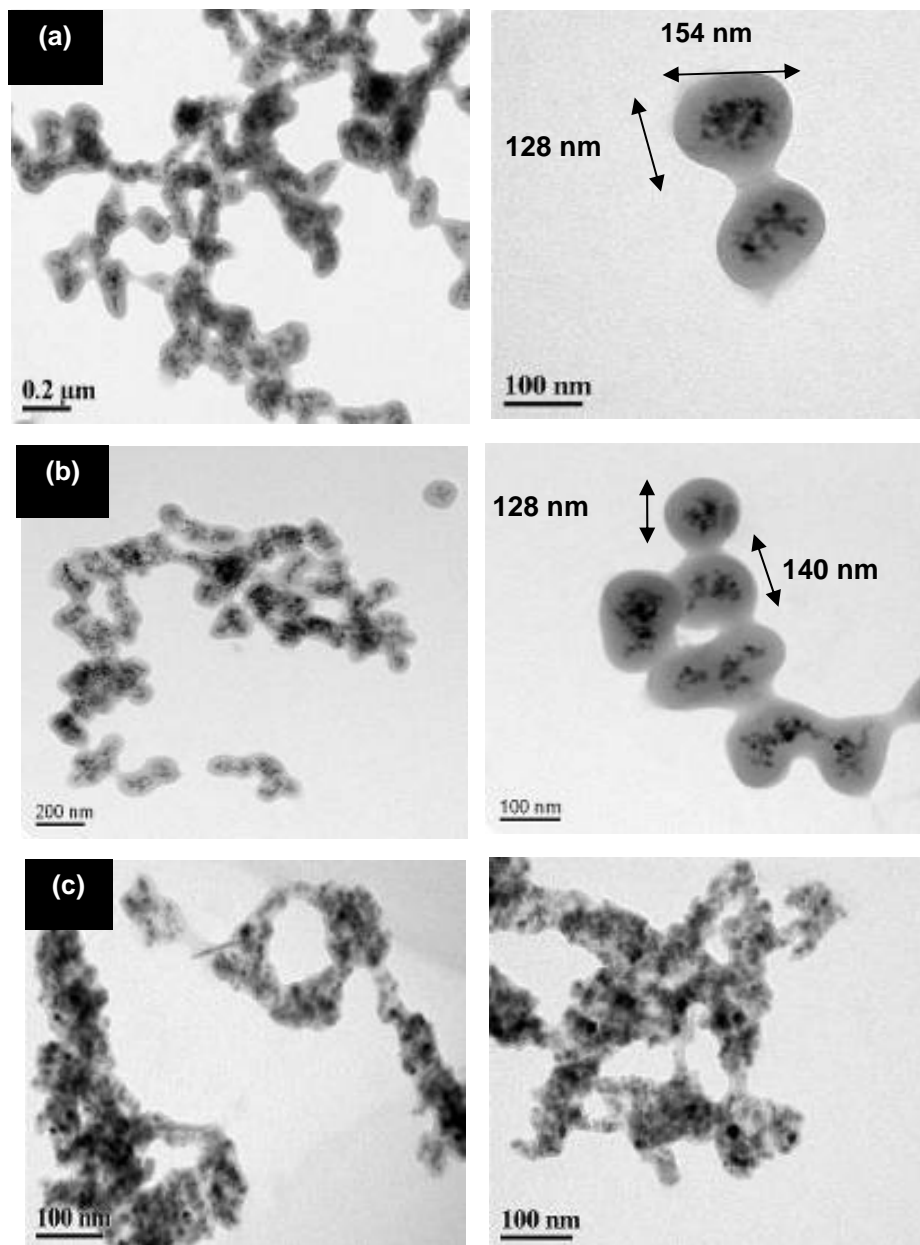


Figure 5.7. TEM micrographs of MCS particles produced from different weight ratios of CTS to MMA to MPS-Fe₂O₃: (a) 2.5 : 9 : 1; (b) 2.5 : 6 : 1; (c) 2.5 : 4 : 1.

5.3.2.1 Preparation of MCS particles using *tert*-butyl hydroperoxide as an initiator

Effect of chitosan, MMA and MPS-Fe₂O₃ weight ratio

Although successful encapsulation was achieved, low MMA conversion (55 %) and very broad particle size distribution ($D_v/D_n = 1.70$) were still unsatisfactory. Thus, different weight ratios of CTS to MMA and MPS-Fe₂O₃ nanoparticles (2.5 : 9 : 1, 2.5 : 6 : 1, 2.5 : 4 : 1 w/w/w) were investigated. Table 5.2 shows that varying these weight ratios still could not improve the MMA conversion. In addition, small amounts of brown precipitates (0.12–0.19 g) were often obtained after the graft copolymerization, indicating that the particles produced were not very stable.

Table 5.2. Effect of chitosan, MMA and MPS-Fe₂O₃ ratio on the graft copolymerization of MMA from chitosan (CTS) in the presence of MPS-Fe₂O₃ nanoparticles.^a

Expt. Code	CTS : MMA : MPS-Fe ₂ O ₃ (w/w/w)	MMA	SC.% ^b	Conv.% (ppt, g)	D_v^c (nm)	D_v/D_n^d
040105-1	2.5 : 9 : 1	0.45	2.5	55 (0.19)	239±22	1.70
310105	2.5 : 6 : 1	0.30	1.9	30 (0.13)	171±1	1.11
030205	2.5 : 4 : 1	0.20	1.5	36 (0.12)	144±2	1.15

^aRefer to the procedures described in the Section 5.2.3. TBHP concentration was 0.1 mM in all cases.. 0.6 v/v% of acetic acid was used to dissolve chitosan in all cases. All reactions were carried out at 80 °C for 2 h ^bSolid content of the reaction mixture. ^c D_v and D_n are the volume and number average particle diameters, respectively. ^d D_v/D_n is the polydispersity index of the particle size distribution.

The precipitates were identified using a Fourier transform-infrared (FT-IR) spectroscopy. Figure 5.8 (a) shows a strong absorption peak at 1731 cm^{-1} (C=O stretching vibration of PMMA), two peaks at 1148 and 1271 cm^{-1} (stretching vibrations of -C-O-) and Fe-O vibration peaks at 400 to 600 cm^{-1} ($\gamma\text{-Fe}_2\text{O}_3$). These characteristic peaks clearly indicated that the precipitates mainly consisted of PMMA and MPS- Fe_2O_3 nanoparticles.

Extraction of the precipitates with chloroform using a Soxhlet extractor was able to isolate the insoluble PMMA-grafted MPS- Fe_2O_3 composite from the soluble PMMA homopolymer. Analysis of the grafted composite using FT-IR spectroscopy as shown in Figure 5.8 (b) revealed the characteristic peaks of C=O, C-O, Si-O and Fe-O. These results suggested that some PMMA chains were covalently grafted onto the surface of MPS- Fe_2O_3 nanoparticles. Similar radical copolymerizations between styrene or MMA with vinyl-coated silica particles has been reported in the literature.^{82,129,130}

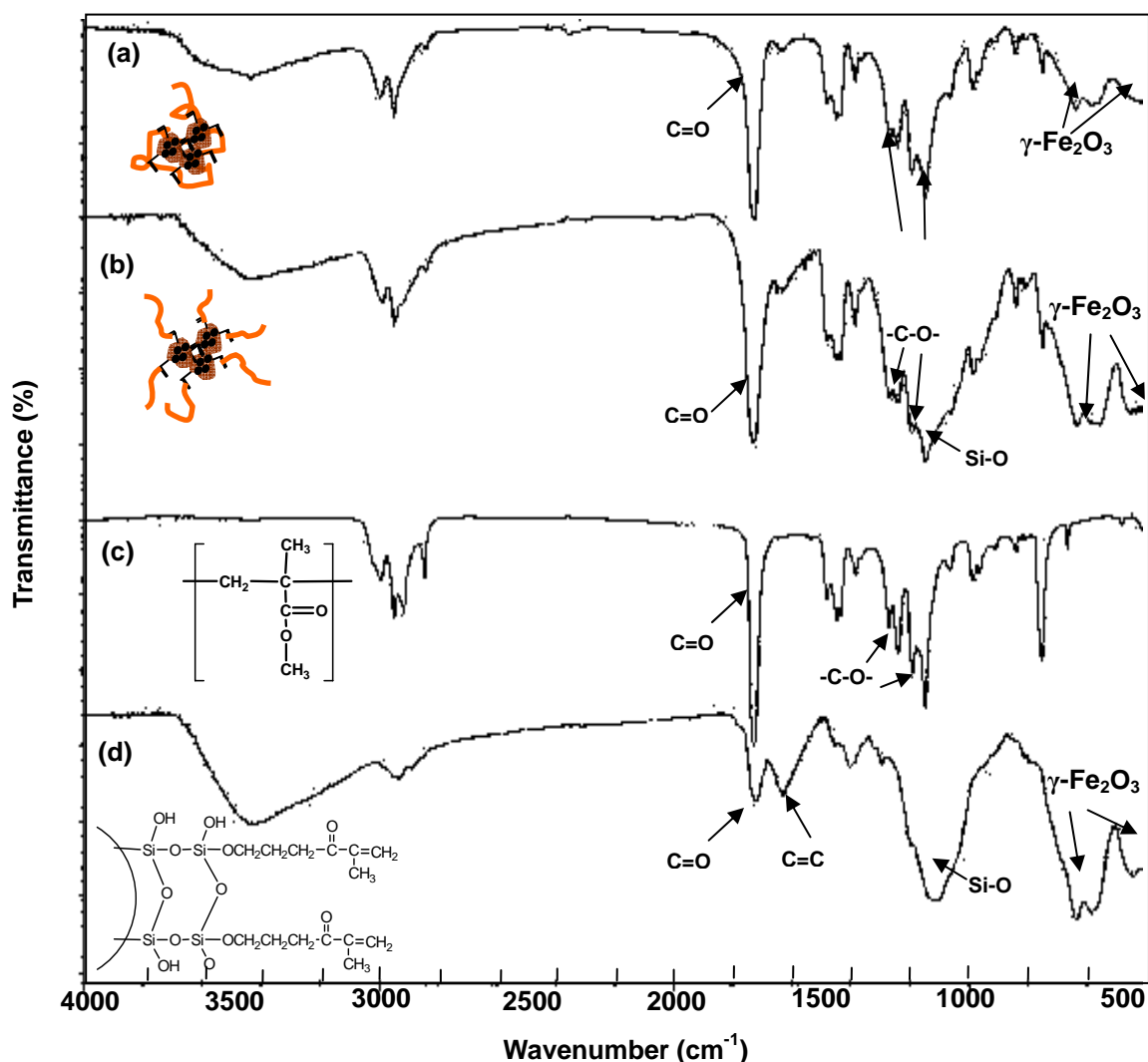


Figure 5.8. FT-IR spectra of (a) precipitates obtained after the copolymerization; (b) isolated PMMA-g-MPS- Fe_2O_3 ; (c) extracted *homo*-PMMA; (d) MPS- Fe_2O_3 nanoparticles.

Grafting of PMMA onto the MPS- Fe_2O_3 nanoparticles was further confirmed with differential scanning calorimetry (DSC) analyses. Figure 5.9 (a) shows the DSC thermogram of the brown precipitates. A strong exothermic peak at 390 °C, characteristic of the decomposition temperature (T_d) of PMMA¹³¹ was detected, but there was not endothermic peak at 309 °C, characteristic of the T_d of chitosan.¹³² This result suggested that the precipitates mainly contained PMMA. Although some chitosan might be grafted onto the surface of the PMMA-coated MPS- Fe_2O_3 particles during the copolymerization, it seemed that the grafting

amounts were insufficient to stabilize the PMMA-coated MPS-Fe₂O₃ nanoparticles in solution. Hence, the nanoparticles tended to form aggregates, and finally precipitated out. Figure 5.9 (b) shows the DSC thermogram of the isolated PMMA-grafted MPS-Fe₂O₃ composite after chloroform extraction. The exothermic peak of PMMA was still detected, suggesting the presence of PMMA grafts.

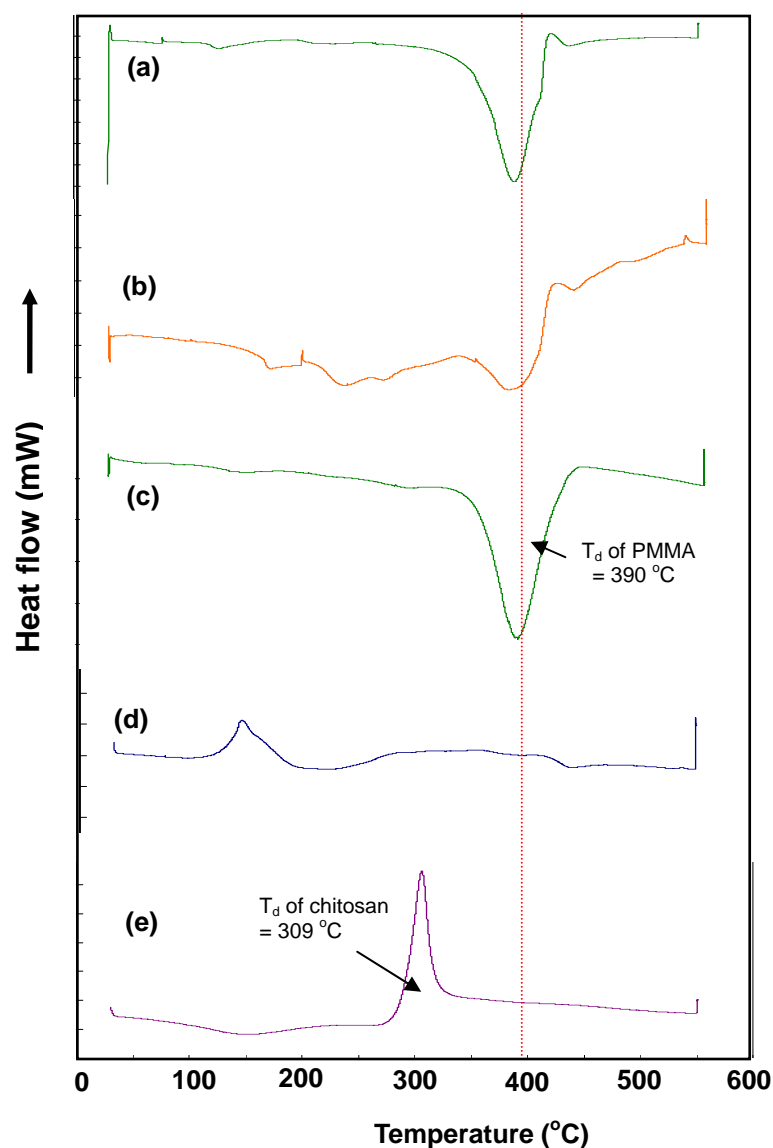


Figure 5.9. DSC thermograms of (a) precipitates obtained after the copolymerization; (b) precipitates after chloroform extraction; (c) extracted *homo*-PMMA polymer; (d) MPS-Fe₂O₃ nanoparticles; (e) chitosan powder.

The formation of PMMA-grafted MPS-Fe₂O₃ composites might be caused by the presence of *t*-BuO• radicals, which could undergo copolymerization between MMA and methacrylate groups on the surface of MPS-Fe₂O₃ nanoparticles. The resulting particles contained *hydrophobic* PMMA coated on the surface of the MPS-Fe₂O₃ nanoparticles (Figure 5.10). Because the PMMA coating was hydrophobic and incompatible with water, the composite nanoparticles had poor dispersing ability in water and tended to form aggregates, and finally precipitated out in aqueous solution.

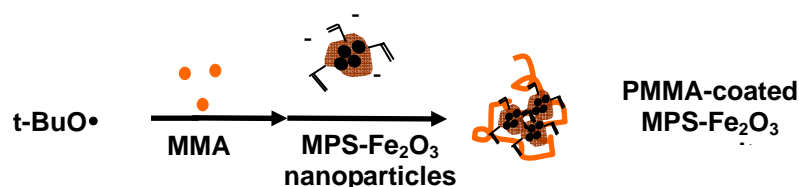


Figure 5.10. Formation of *hydrophobic* PMMA-coated MPS-Fe₂O₃ composites.

TEM micrographs of magnetic core-shell (MCS) particles produced from different weight ratios are shown in Figure 5.7 (a–c). These images clearly reveal that the MPS-Fe₂O₃ nanoparticles have been successfully encapsulated into the core of the core-shell particles. Varying MMA content had significant influence on the morphology of MCS particles produced. With low MMA content, the morphology of the MCS particles changed from spherical to irregular (Figure 5.7 c). Thus, the optimal weight ratio of CTS to MMA with respect to MPS-Fe₂O₃ had to be higher than 2.5 to 6 in order to form spherical particles. TEM micrographs also show that the MCS particles easily form aggregates, which may be due to the strong magnetic dipole-dipole attractions exerted between the particles during drying. Such aggregations are commonly observed in TEM characterization of magnetic materials.⁵⁷

Effect of solid content

The effect of solid content on MMA conversion, particle size and size distribution was examined (Table 5.3) Doubling the solid content of the optimum weight ratio (CTS:MMA:MPS-Fe₂O₃ = 2.5 : 6 : 1) produced MCS particles with a higher conversion (78 %). A further increase of the solid content up to 5 % could give a conversion as high as 99 %. This might be due to the fact that increasing the solid content may *increase initiator efficiency*. Thus, *the rate of radical entry into a particle* is faster than *that of aqueous-phase termination*, according to the Maxwell-Morrison mechanism.¹³³ However, higher solid content also resulted in more precipitate formation (0.31–1.09 g), which was probably caused by a poor mixing of highly viscous chitosan solution during the copolymerization. These results suggested that the optimal solid content was around 4 w/w% in order to achieve reasonable conversion. Furthermore, the chitosan concentration had to be lower than 1 w/w% to ensure a good mixing.

Table 5.3. Effect of solid content on the graft copolymerization of MMA from chitosan (CTS) in the presence of MPS-Fe₂O₃ nanoparticles.^a

Expt. Code	CTS : MMA : MPS-Fe ₂ O ₃ (w/w/w)	MMA	SC.% ^b	Conv.% (ppt, g)	D _v ^c (nm)	D _v /D _n ^d
310105	2.5 : 6 : 1	0.30	1.9	30 (0.13)	171± 1	1.11
060505	2.5 : 6 : 1	0.60	3.8	78 (0.31)	202±6	1.09
130306-2	2.5 : 6 : 1	0.79	5.0	99 (1.09)	N/A ^e	N/A ^e

^aRefer to the procedures described in the Section 5.2.3. TBHP concentration was 0.1 mM in all cases. 0.6 v/v% of acetic acid was used to dissolve chitosan in all cases. All reactions were carried out at 80 °C for 2 h ^bSolid content of the reaction mixture. ^cD_v and D_n are the volume and number average particle diameters, respectively. ^dD_v/D_n is the polydispersity index of the particle size distribution. ^eN/A means that particle size and its distribution were not determined.

Effect of TBHP

In order to obtain a higher MMA conversion and overcome the precipitation problem, the effect of TBHP concentration on MMA conversion was examined, and results are shown in Figure 5.11. In the absence of TBHP, less than 5 % of MMA was converted after 2 h at 80 °C. When 0.1 mM of TBHP concentration was used, high MMA conversion (78 %) was achieved. A further increase of the TBHP concentration from 0.1 to 0.4 mM had little influence on the conversion and particle size as well as size distribution ($D_v/D_n = 1.09\text{--}1.17$). These results suggested that 0.1 mM was the optimal TBHP concentration on the formation of MCS particles. On the other hand, around 35 w/w% solid precipitates were still obtained. Thus, higher TBHP concentrations were still unable to resolve the precipitation problem.

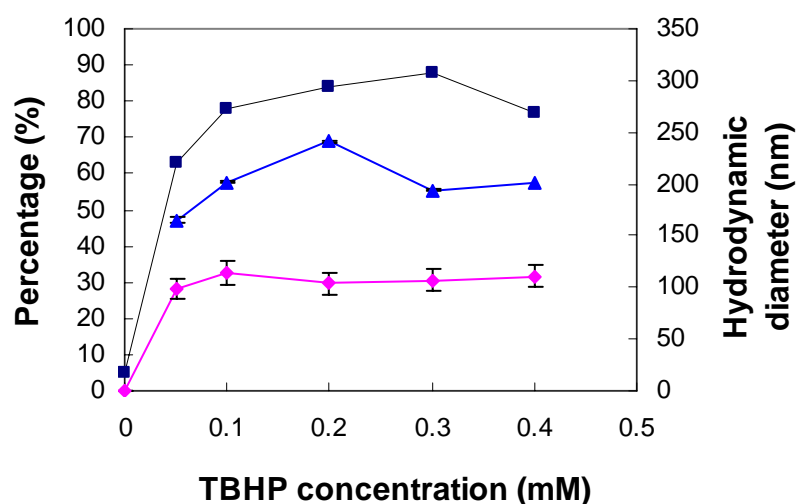


Figure 5.11. Effect of TBHP concentration on the graft copolymerization of MMA from chitosan (CTS) in the presence of MPS-Fe₂O₃ nanoparticles (CTS : MMA : MPS-Fe₂O₃ = 2.5 : 6 : 1). (■) conversion; (◆) precipitates obtained after the copolymerization; (▲) volume-average particle diameter (D_v).

It was found that the increase of TBHP concentration affected the amount of chitosan being grafted onto the MCS particles. Figure 5.12 shows that the percentage of chitosan being grafted onto MCS particles (i.e. CTS% graft) was only 38 % at the 0.1 mM of TBHP concentration. This means that only 38 % of chitosan charged into the reaction mixture was grafted onto the particle surface. Low CTS% graft is probably attributed to the presence of a small amount of acetic acid that is required to dissolve the chitosan in water. It is known that acid induces free-radical decomposition of TBHP to *tert*-butoxy and hydroxyl radicals based on the mechanism as shown in Figure 5.13.¹³⁴ The HO• and *t*-BuO• radicals generated could initiate the homopolymerization of MMA without interacting with the chitosan. When TBHP concentration increased from 0.1 to 0.4 mM, the CTS% graft was further reduced as shown in Figure 5.12. This effect may be due to the fact that higher TBHP concentrations result in higher *tert*-butoxy (*t*-BuO•) and HO• concentrations through thermal decomposition. These reactive radicals subsequently initiate the homopolymerization of MMA, generating more PMMA homopolymers.¹⁰⁹ This means that higher TBHP concentrations favor the homopolymerization of MMA rather than the graft copolymerization of MMA from chitosan, thus leading to a decrease in CTS% reacted.

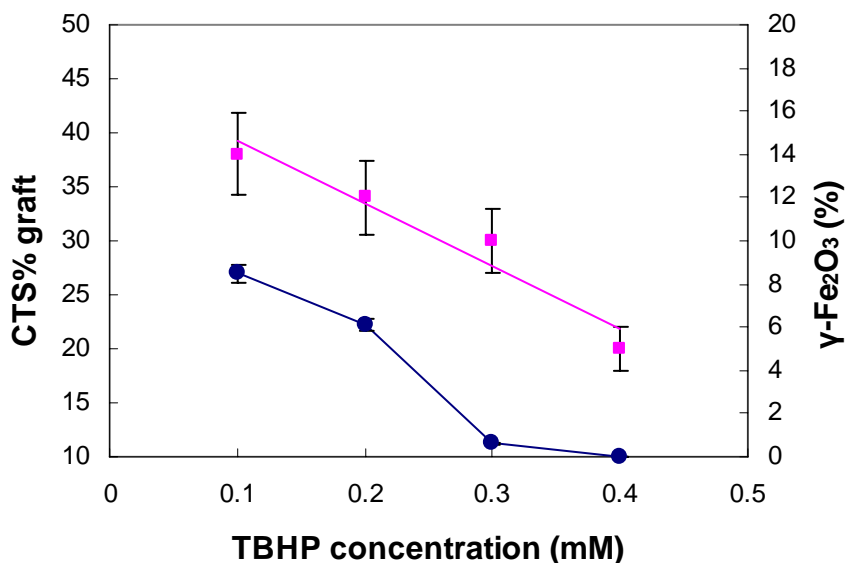


Figure 5.12. Effect of TBHP concentration on the graft copolymerization of MMA from chitosan (CTS) in the presence of MPS-Fe₂O₃ nanoparticles (CTS : MMA : MPS-Fe₂O₃ = 2.5 : 6 : 1): (■) CTS% reacted and (●) γ-Fe₂O₃ % content in MCS particles.

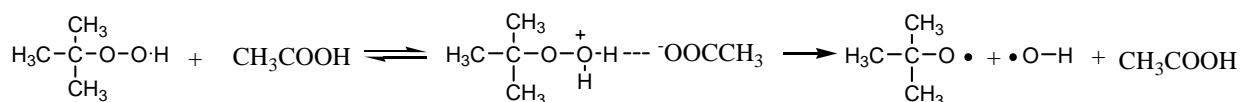


Figure 5.13. Acetic acid-induced decomposition of TBHP.

Figure 5.12 also shows that an increasing TBHP concentration leads to lower γ-Fe₂O₃ content encapsulated in MCS particles. This result indicates that higher TBHP concentrations may boost the copolymerization between MMA monomer and the vinyl-coated nanoparticles to form composite particles. As a result, the amount of iron oxide nanoparticles in the PMMA/γ-Fe₂O₃ composite increases. The PMMA coated- γ-Fe₂O₃ nanoparticles are unstable, and eventually precipitate out in water. This hypothesis was confirmed by TGA analysis of these

brown precipitates produced at different TBHP concentrations. Figure 5.14 indicates that the precipitates produced at higher TBHP concentrations gave higher γ -Fe₂O₃ content. This finding helps explain why the iron oxide content decreases in the MSC particles with the increase of TBHP concentration. This is due to the fact that more MPS-Fe₂O₃ nanoparticles are consumed through the formation of the precipitates at higher TBHP concentrations, the less MPS-Fe₂O₃ nanoparticles could be encapsulated through the graft copolymerization, leading to lower γ -Fe₂O₃ content in MCS particles.

Above results suggest that CTS% reacted seems to be one of the factors in controlling the γ -Fe₂O₃ content in MCS particles. If less chitosan is grafted onto the particles, lower the γ -Fe₂O₃ content in MCS particles is obtained. Therefore, TBHP concentration should be lower than 0.1 mM in order to obtain reasonable percentages of CTS grafts and γ -Fe₂O content.

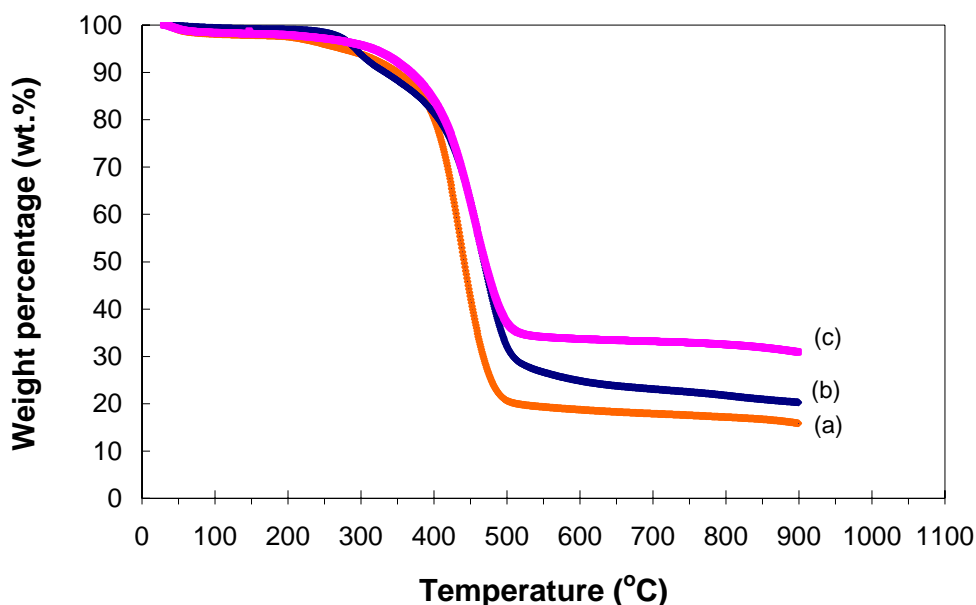


Figure 5.14. TGA analysis of the precipitates obtained from different TBHP concentrations: (a) 0.1 mM (γ -Fe₂O₃% = 16.2 %); (b) 0.3 mM (γ -Fe₂O₃% = 20.4 %) and (c) 0.4 mM (γ -Fe₂O₃% = 31.4 %).

Effect of MPS-Fe₂O₃ content

Variation of MPS-Fe₂O₃ content while keeping the CTS to MMA weight ratio constant was examined in an attempt to increase the amount of γ -Fe₂O₃ being encapsulated in MCS particles. Table 5.4 shows that an increase of MPS-Fe₂O₃ content from 0.2, 0.4, 0.48 to 0.6 % gave comparable MMA conversions ranging from 75 to 87%, but there were more brown precipitates formed while increasing the amount of MPS-Fe₂O₃ nanoparticles in the reaction mixture. This may be due to the increase of collisions among MPS-Fe₂O₃ nanoparticles, MMA and *t*-BuO• radicals, resulting in the formation of more aggregates. Since more MPS-Fe₂O₃ nanoparticles were consumed by the formation of these aggregates, less MPS-Fe₂O₃ nanoparticles could be encapsulated through the graft copolymerization, resulting in lower γ -Fe₂O₃ contents (Table 5.4).

Table 5.4. Effect of MPS-Fe₂O₃ content on the graft copolymerization of MMA from chitosan (CTS).^a

Expt. code	CTS : MMA : MPS-Fe ₂ O ₃ (w:w:w)	MPS-Fe ₂ O ₃ (g)/(w/w%)	Conv.% (ppt.%)	<i>D_v</i> (nm) ^b	<i>D_v</i> / <i>D_n</i> ^c	CTS% reacted	γ -Fe ₂ O ₃ %
200906-1	2.5 : 6 : 0.5	0.05 (0.2)	75 (13)	206±1	1.14	38	2
220305	2.5 : 6 : 1.0	0.10 (0.4)	78 (33)	202±6	1.09	38	8
111006-1	2.5 : 6 : 1.2	0.12 (0.48)	87 (43)	220±2	1.28	21	2
111006-2	2.5 : 6 : 1.5	0.15 (0.6)	79 (50)	290±13	2.12	17	2

^aRefer to the procedures described in the Section 5.2.3. TBHP concentration used was 0.1 mM in all cases. All reactions were carried out at 80 °C for 2 h. ^b*D_v* and *D_n* are the volume and number average particle diameters, respectively. ^c*D_v*/*D_n* is the polydispersity index of the particle size distribution.

Table 5.4 also shows that an increasing MPS-Fe₂O₃ content leads to a reduction of the CTS% graft. These results are in agreement with previous findings that the decrease of CTS% graft is a result of the formation of a large amount of precipitates. Larger particle size and broader size distribution of MCS particles were also produced at lower CTS% reacted because of lack of particle stability provided by chitosan molecules (Table 5.4).

TEM micrographs of the MCS particles produced from two weight ratios are shown in Figure 5.15 (a and b), which reveal that MPS-Fe₂O₃ nanoparticles have been encapsulated successfully inside the polymer cores. The TEM images also illustrate that fewer MPS-Fe₂O₃ nanoparticles are encapsulated inside the polymer cores (black dots) when using a higher MPS-Fe₂O₃ content (CTS : MMA : MPS-Fe₂O₃ = 2.5 : 6 : 1.2). This result is consistent with the γ -Fe₂O₃ content determined with TGA (Table 5.4). In conclusion, the optimal substrate weight ratio is CTS : MMA : MPS-Fe₂O₃ = 2.5 : 6 : 1.0 that was used for subsequent experiments.

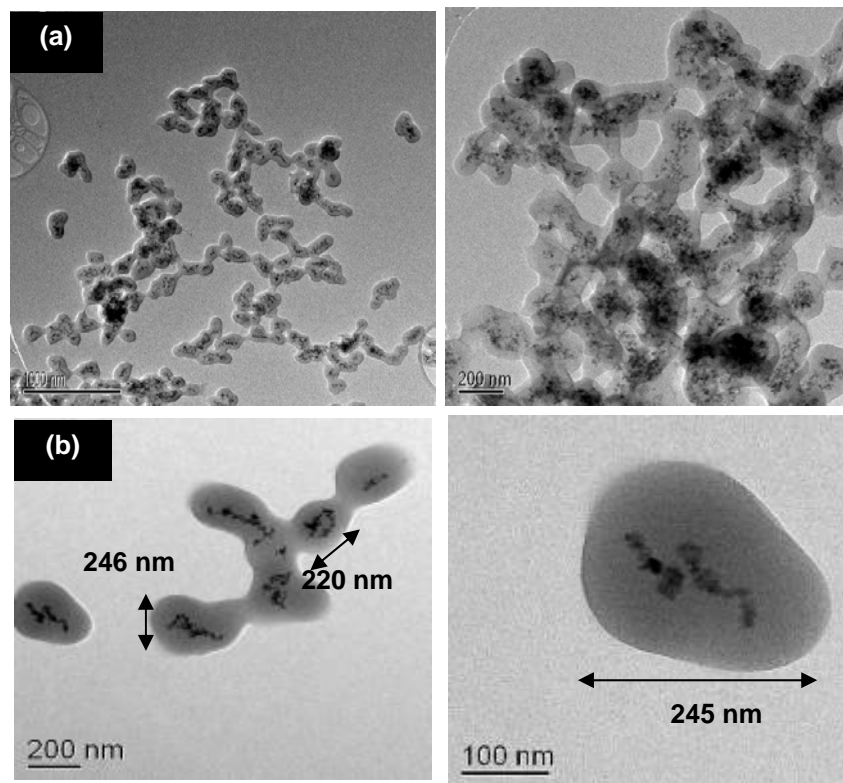


Figure 5.15. TEM images of MCS particles with different weight ratios of CTS to MMA to MPS-Fe₂O₃: (a) 2.5 : 6 : 1.0; (b) 2.5 : 6 : 1.2.

Effect of other amino containing water-soluble polymers (WSP)

To explore the scope of other shell materials, various amino-containing water-soluble polymers (WSP) such as polyethylenimine (PEI), poly(vinyl amine) (PVAm), casein and cellulase have been investigated. Similar to the use of chitosan, they were first mixed with MPS-Fe₂O₃ nanoparticle dispersion, then subjected to the copolymerization conditions at 80 °C for 2 hours. Results are summarized in Table 5.5, and are compared with the use of chitosan. PEI is a branched polymer, which contains 25 % primary, 50 % secondary, and 25 % tertiary amino groups (Figure 5.16).

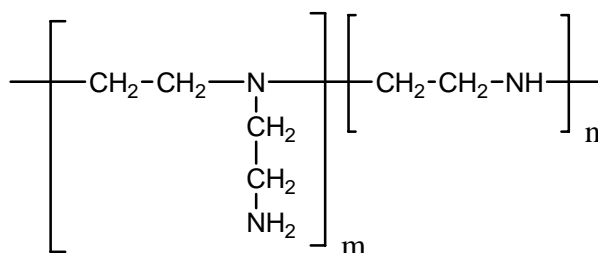


Figure 5.16. A repeating unit of branched PEI.

When PEI solution (pH around 11) was mixed with MPS-Fe₂O₃ nanoparticles in the absence of monomer, an immediate precipitation was observed (Table 5.5, code 230604-1). The more MPS-Fe₂O₃ nanoparticles were added to the PEI solution, the more precipitates were then found (Table 5.5, code 230604-2, 230604-3). The formation of precipitates was probably attributed to the charge neutralization between the negative surface charges of the MPS-Fe₂O₃ nanoparticles and amine groups of the PEI. Because of low positive charges of

PEI molecules at pH greater than 9 and possible bridging of iron oxide nanoparticles with PEI,¹³⁵ the complexed nanoparticles were unstable, resulting in aggregation (Figure 5.17). A similar phenomenon has been reported in which PEI could effectively destabilize the negatively charged silica particles at basic pH via electrostatic interaction and polymer bridging.¹³⁵

Table 5.5. TBHP-induced graft copolymerization of MMA from WSP containing amino groups in the presence of MPS-Fe₂O₃ nanoparticles.^a

Entry	Water-soluble polymer (WSP)	pH	WSP : MMA : MPS-Fe ₂ O ₃ (w:w:w)	ppt. generated after mixing (g)	Conv.(%)	ppt. (%) ^b	Encap. ^c
220305	Chitosan	4.5	2.5 : 6 : 1.0	0.00	78	35	Yes
230604-1	PEI	11	2.5 : 0 : 0.064	0.12	N/A	N/A	N/A
230604-2	PEI	11	2.5 : 0 : 0.5	0.21	N/A	N/A	N/A
230604-3	PEI	11	2.5 : 0 : 1.0	0.24	N/A	N/A	N/A
011104	PEI ethanol/H ₂ O (1:1 v/v)	11	2.5 : 6 : 0.5	0.00	67	N/A	No
250604-1	PEI	7	2.5 : 6 : 0.064	0.00	83	0	Partial
230604-4	PEI	7	2.5 : 0 : 0.5	0.18	N/A	N/A	N/A
230604-5	PEI	7	2.5 : 0 : 1.0	0.22	N/A	N/A	N/A
230604-6	PVAm (0.25 g) ^d	7	2.5 : 0 : 0.5	0.20	N/A	N/A	N/A

^aRefer to the procedure described in the Section 5.2.3. The volume ratio of ethanol to water was kept at 1 : 12.5 v/v, except for the code 011104. TBHP concentration (0.1 mM) was used in all cases. All reactions were carried out at 80 °C for 2 h. ^bPrecipitates obtained after reaction. ^cEncapsulation of the MPS-Fe₂O₃ nanoparticles into the cores of the core-shell particles was observed by TEM images. ^dPoly(vinyl amine), (PVAm) was dissolved in distilled water, followed by adjusting the solution to pH 11.

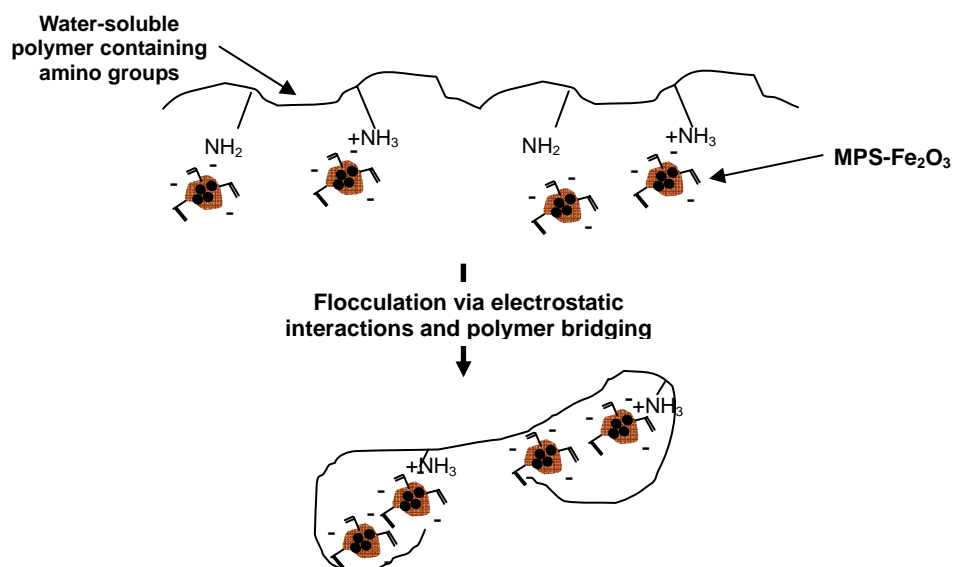


Figure 5.17. Schematic representation of electrostatic interaction and polymer bridging between cationic polymers and MPS-Fe₂O₃ nanoparticles.

To alleviate the precipitation problem, higher amounts of ethanol (i.e. ethanol : H₂O = 1 : 1 v/v) were used to disperse the MPS-Fe₂O₃ nanoparticles in the PEI solution (Table 5.5, code 011104). When MPS-Fe₂O₃ nanoparticle dispersion containing 12.5 mL of ethanol was added to the PEI solution (2 w/w%, 12.5 mL), no precipitation was observed. Copolymerization of this homogeneous mixture with MMA formed a stable dispersion with 67 % of MMA conversion. However, TEM images of the particles produced indicated that magnetic nanoparticles were mainly located on the shell of the core-shell particles rather than in the core (Figure 5.18). Thus encapsulation of iron oxide nanoparticles failed in this PEI-based system. Unsuccessful encapsulation may be attributed to the fact that MPS-Fe₂O₃ nanoparticles likely dispersed in an ethanol/H₂O phase (1 : 1 v/v) rather than located in the PMMA core since the ethanol is a good dispersing solvent for MPS-Fe₂O₃ nanoparticles. Thus, a low volume ratio of ethanol to water (1 : 12.5 v/v) was kept in the subsequent experiments.

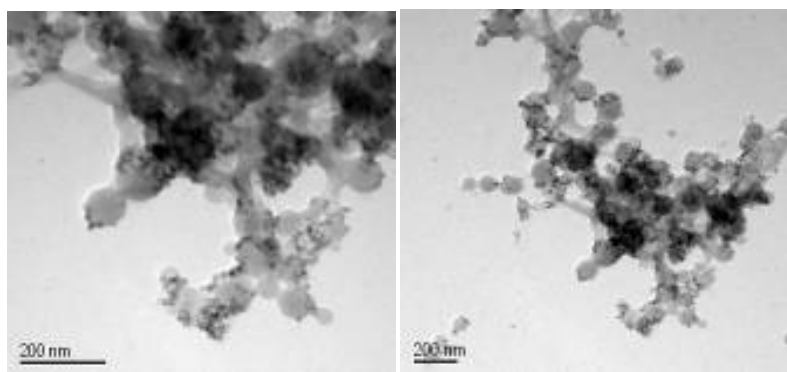


Figure 5.18. TEM images of PMMA/PEI (pH 11, ethanol : H₂O = 1 : 1 v/v) produced in the presence of MPS-Fe₂O₃ nanoparticles.

To further address the precipitation problem, the pH of PEI solution was adjusted from 11 to 7 prior to mixing with MPS-Fe₂O₃ nanoparticle dispersion. Since PEI molecules are highly positive at pH 7, this may provide a better electrostatic stabilization after complexing with negatively charged MPS-Fe₂O₃ nanoparticles. As expected, no precipitation was observed when PEI (0.25 g) was mixed with MPS-Fe₂O₃ nanoparticles (6.4 mg) at pH 7 (Table 5.6, code 250604-1). Subsequent graft copolymerization of MMA from PEI in the presence of MPS-Fe₂O₃ nanoparticles gave a high MMA conversion up to 83%. No precipitates were found after the polymerization. TEM images of the particles showed that some core-shell particles contained MPS-Fe₂O₃ nanoparticles in the core, while some particles did not (Figure 5.19). In an attempt to encapsulate the magnetic nanoparticles into all core-shell particles, more MPS-Fe₂O₃ nanoparticles were added. However, this resulted in the formation of more precipitates. Thus the weight ratio of PEI to MPS-Fe₂O₃ nanoparticles had to be higher than 2.5 : 6 : 0.064 in order to obtain a stable PEI/MPS-Fe₂O₃ dispersion for subsequent copolymerization.

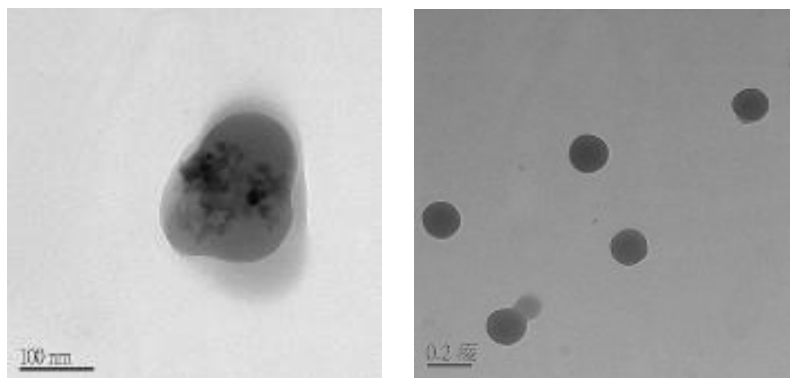


Figure 5.19. TEM images of PMMA/PEI (pH 7; ethanol : H₂O = 1 : 12.5 v/v) produced in the presence of MPS-Fe₂O₃ nanoparticles.

In order to provide more electrostatic stabilization for MPS-Fe₂O₃ nanoparticles, PVAm containing only primary amino groups on its backbone was examined (Figure 5.20). It was expected that the PVAm might stabilize more MPS-Fe₂O₃ nanoparticles because of its higher positive charge density at pH 7 as compared with PEI molecules. However, when PVAm was mixed with MPS-Fe₂O₃ nanoparticle dispersion, a large amount of precipitates was formed (Table 5.5 code 230604-6). This result suggested that electrostatic complexation alone was not sufficient to stabilize MPS-Fe₂O₃ nanoparticles.

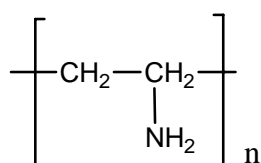


Figure 5.20. A repeating unit of Poly(vinyl amine) (PVAm).

Up to now, chitosan still seemed to be a better water-soluble polymer for stabilization of MPS-Fe₂O₃ nanoparticles. For example, 0.25 g of chitosan could

stabilize up to 0.2 g of MPS-Fe₂O₃ nanoparticles without any observable aggregation. This might be due to the fact that hydroxyl groups on chitosan backbone also provided an extra dispersing stability for MPS-Fe₂O₃ nanoparticles through hydrogen bonding. In summary, successful encapsulation of MPS-Fe₂O₃ nanoparticles in the core of the core-shell particles strongly depends on the structure of WSP. Polymers containing both hydroxyl and amino groups such as chitosan are more effective than those containing only amino groups.

Preparation of PMMA/iron oxide cores with biopolymer shells such as cellulase and casein was also investigated using this approach. Cellulase is an enzyme that catalyzes the hydrolysis of cellulose. It has a jelly-roll fold structure, where the active site located at the open cleft is used for cellulose hydrolysis. Its surface is mainly composed of peptide chains with a small amount of amino residues such as lysine, histidine and arginine on its surface (Figure 5.21). Therefore, the surface of cellulase is slightly positive at pH 4.5.^{136a&b}

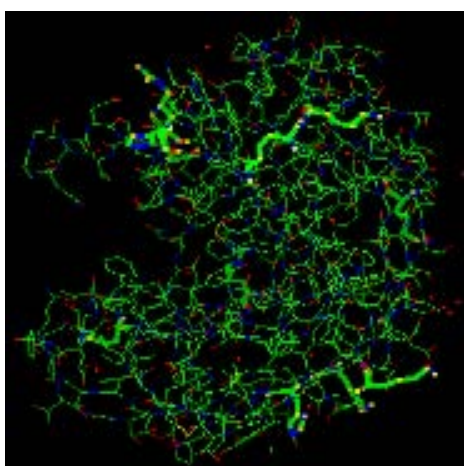


Figure 5.21. Structures of cellulase (The highlighted areas represent the position of amino groups).^{136c}

Surprisingly, when cellulase solution was mixed with MPS-Fe₂O₃ nanoparticle dispersion, no precipitation was observed (Table 5.6 code 260305). This might be attributed to the fact that electrostatic attraction between cellulase and MPS-Fe₂O₃ nanoparticles was weak. Subsequent copolymerization of this stable dispersion gave a high MMA conversion (> 99 %) and only a small amount of precipitates (5 %) (Table 5.6, code 260305). However, TEM images of the particles showed that no MPS-Fe₂O₃ nanoparticles were encapsulated into the PMMA core of the particles (Figure 5.22). Furthermore, it seemed that there was no direct interaction between PMMA/cellulase core-shell particles and MPS-Fe₂O₃ nanoparticles, Thus unsuccessful encapsulation was probably due to the poor interactions between cellulase and MPS-Fe₂O₃ nanoparticles.

Table 5.6 TBHP-induced graft copolymerization of MMA from WSP containing amino groups in the presence of MPS-Fe₂O₃ nanoparticles.^a

Entry	Water-soluble polymer (WSP)	pH	WSP : MMA : MPS-Fe ₂ O ₃ (w:w:w)	ppt. generated after mixing (g)	Conv.(%)	ppt. (%) ^b	Encap. ^c
260305	Cellulase (0.1 g) ^d	4.5	0.10 : 6 : 0.5	0	100	5	No
181006-1	Casein (0.25 g) ^e	10	2.5 : 10 : 1.0	0	88	0	Yes* (form composites)

^aRefer to the procedure described in the Section 5.2.3. The volume ratio of ethanol to water was kept at 1 : 12.5 v/v. TBHP concentration (0.1 mM) was used in all cases. All reactions were carried out at 80 °C for 2 h. ^bPrecipitates obtained after reaction. ^cEncapsulation of the MPS-Fe₂O₃ nanoparticles into the cores of the core-shell particles was observed by TEM images. ^dCellulase (19.8 mg/mL) was dissolved in water, followed by adjusting the solution to pH 4.5. N/A means that polymerization did not take place. ^eCasein (0.25 g) was dissolved in a 0.4 w/w% sodium carbonate aqueous solution.

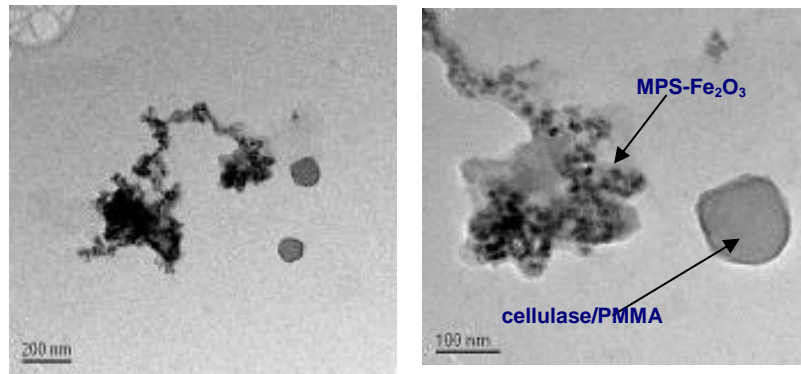


Figure 5.22. TEM images of PMMA/cellulase produced in the presence of MPS-Fe₂O₃ nanoparticles.

Caseins, a family of phosphorylated proteins, consist of α_{S1} -, α_{S2} -, β -, and κ -casein in the ratio of 4 : 1 : 4 : 1. Caseins are linear proteins without secondary structure, which are similar to random coil polymers. Individual caseins exhibit a strong tendency to self-associate and form casein micelles. A casein micelle is a roughly spherical, fairly swollen particle of about 100 nm in diameter (Figure 5.23). It has a hydrophobic interior, surrounded with a hydrophilic and negatively charged diffuse surface layer that stabilizes the micelle through steric and electrostatic effects.^{137a}

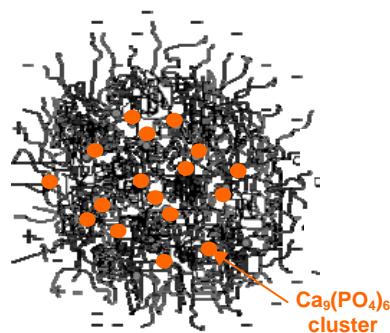


Figure 5.23. Structures of casein micelle.^{137b}

When casein solution was mixed with a MPS-Fe₂O₃ nanoparticle dispersion, there was no precipitation (Table 5.6 code 171006-1). Subsequent graft copolymerization of this stable brown dispersion gave a high conversion (88 %) and no precipitates. It was also noted that the dispersion was much more transparent as compared to the previous systems. In addition, they were very stable in water, and no flocculation was observed even after a month. Figure 5.24 shows the TEM images of the particles produced. Core-shell particles with a size around 100 nm, in fact, were not observed. Instead, nanoparticles less than 20 nm in diameter were revealed. These nanoparticles tended to aggregate together, suggesting that they had very strong attraction between them.

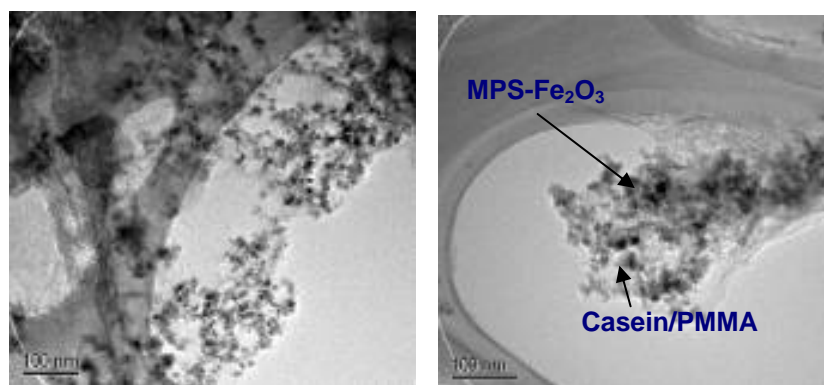


Figure 5.24. TEM images of PMMA/casein particles produced in the presence of MPS-Fe₂O₃ nanoparticles.

Because this result was very different from our previous systems, more experiments were performed. Particle size measurement using laser diffraction (Coulter LS 230) indicated that the obtained nanoparticles had a multi-modal distribution with sizes ranging from 40 nm to a few hundred microns. This result suggested that magnetic composites, instead of well-defined magnetic core-shell particles with narrow size distribution, were formed. FT-IR analyses of the

purified composites (Figure 5.25) showed a broad N-H stretching peak of casein at 3300 cm^{-1} , a strong carbonyl peak (C=O) of PMMA at 1732 cm^{-1} , and the strong bands of Fe-O bonding between 400 and 600 cm^{-1} . This result indicated that the composites consisted of casein, PMMA and iron oxides. The PMMA grafting efficiency of the obtained composites was also determined by extraction of their crude product by chloroform for 48 h using a Soxhlet extractor. The result suggested that the composites contained 60 % grafted PMMA and 40 % PMMA homopolymer, respectively. This means that 60 % of PMMA may be either grafted onto the casein backbone or the MPS- Fe_2O_3 nanoparticle surface. Those 40 % of PMMA homopolymers may be formed inside the hydrophobic interior of casein micelles during the polymerization. This explains why high MMA conversion (88 %) was achieved, but no magnetic well-defined core-shell particles were observed in the TEM images (Figure 5.24).

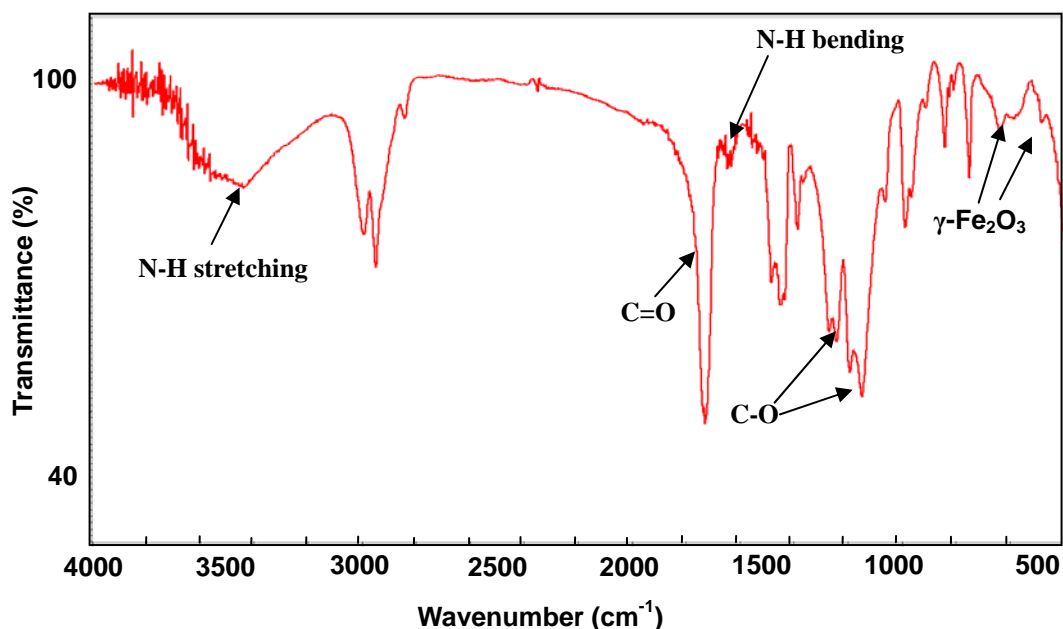


Figure 5.25. FT-IR spectrum of purified $\gamma\text{-Fe}_2\text{O}_3$ /PMMA/casein composites.

Thus, two important criteria for the water-soluble polymer (WSP) must be satisfied in order to obtain successful encapsulation of MPS-Fe₂O₃ nanoparticles in the core of the core-shell particles: (1) WSP should have some interactions with the nanoparticles such as electrostatic interaction or hydrogen bonding or hydrophobic interaction. (2) The resulting mixture of WSP and MPS-Fe₂O₃ nanoparticles should be colloidal stable in an aqueous solution. In other words, if polymers could provide any interactions and an extra dispersing stability for MPS-Fe₂O₃ nanoparticles, the encapsulation of magnetic nanoparticles in the core-shell particles would be achieved.

Composition of the MCS particles and magnetic-graft copolymers

To determine the chemical composition of MCS particles, the crude particles were purified by repeated centrifugation, decantation and re-dispersion cycles in order to remove any un-grafted chitosan in the dispersion. The purified MCS particles were then dried, and identified with FT-IR spectroscopy (Figure 5.26). IR spectrum of the purified MCS particles showed a broad N-H peak of chitosan at 3400 cm⁻¹, a strong carbonyl peak (C=O) of PMMA at 1735 cm⁻¹, N-H bending peaks of the chitosan between 1550 and 1600 cm⁻¹, ester peaks (-C-O-) of PMMA between 1247 and 1272 cm⁻¹, and γ -Fe₂O₃ absorption peaks between 400 and 600 cm⁻¹. The IR spectrum clearly verified that the purified MCS particles were composed of chitosan, PMMA and γ -Fe₂O₃.

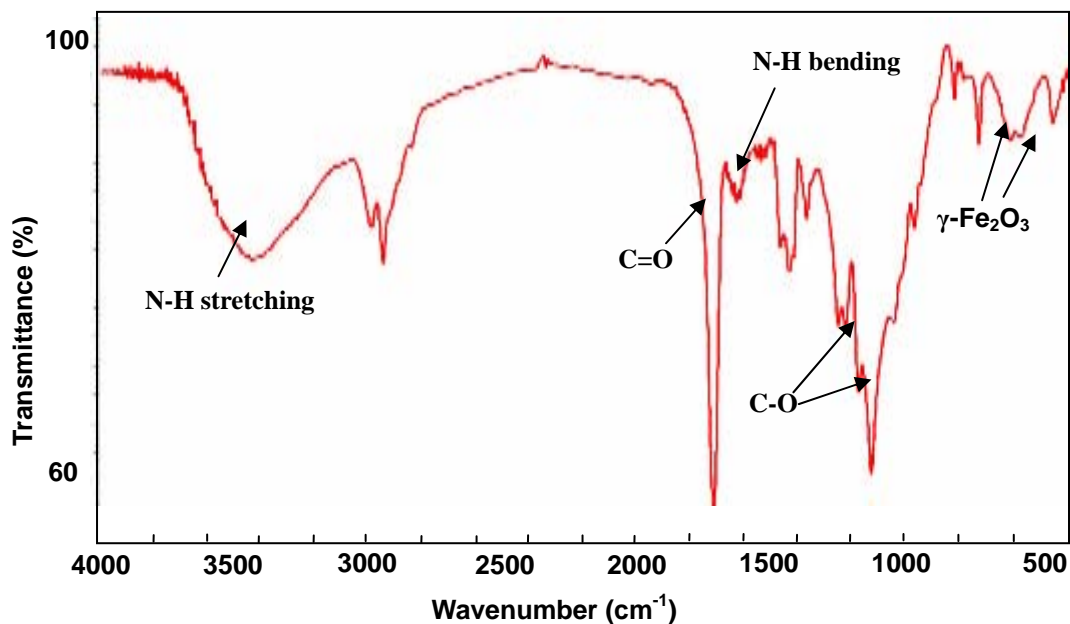


Figure 5.26. FT-IR spectra of purified MCS particles (CTS : MMA : MPS-Fe₂O₃ = 2.5 : 6 : 1; TBHP = 0.1 mM).

To confirm the formation of both magnetic *graft*-PMMA and *homo*-PMMA and to determine their compositions, the crude product of MCS particle dispersion was first freeze-dried. The resulting brown solids were then subjected to the chloroform extraction for 48 h. PMMA homopolymer dissolved in chloroform was separated from the insoluble magnetic graft copolymer that remained inside the thimble. The amounts of both PMMA dissolved in chloroform and insoluble polymer composites were determined gravimetrically. The composition of PMMA formed was then calculated. This result suggested that the PMMA homopolymer and the grafted PMMA were 12 % and 88 %, respectively. The high percentage of the grafted PMMA was unusual when compared with our previous work, in which the grafted PMMA percentage had only 15%.¹⁰⁹ Such a dramatic increase in grafting efficiency may be attributed to the presence of reactive methacrylate groups of the MPS-Fe₂O₃ nanoparticles. Since these reactive groups are close to

chitosan due to the interaction between MPS-Fe₂O₃ nanoparticles and chitosan, their copolymerization with MMA enhances the chance of grafting from/onto the chitosan chains. The isolated chitosan/graft-PMMA/γ-Fe₂O₃ composites were further identified with FT-IR analyses (Figure 5.27). The spectrum clearly illustrated the characteristic peaks of PMMA such as the carbonyl peak at 1735 cm⁻¹ and the ester peaks between 1247 and 1272 cm⁻¹.

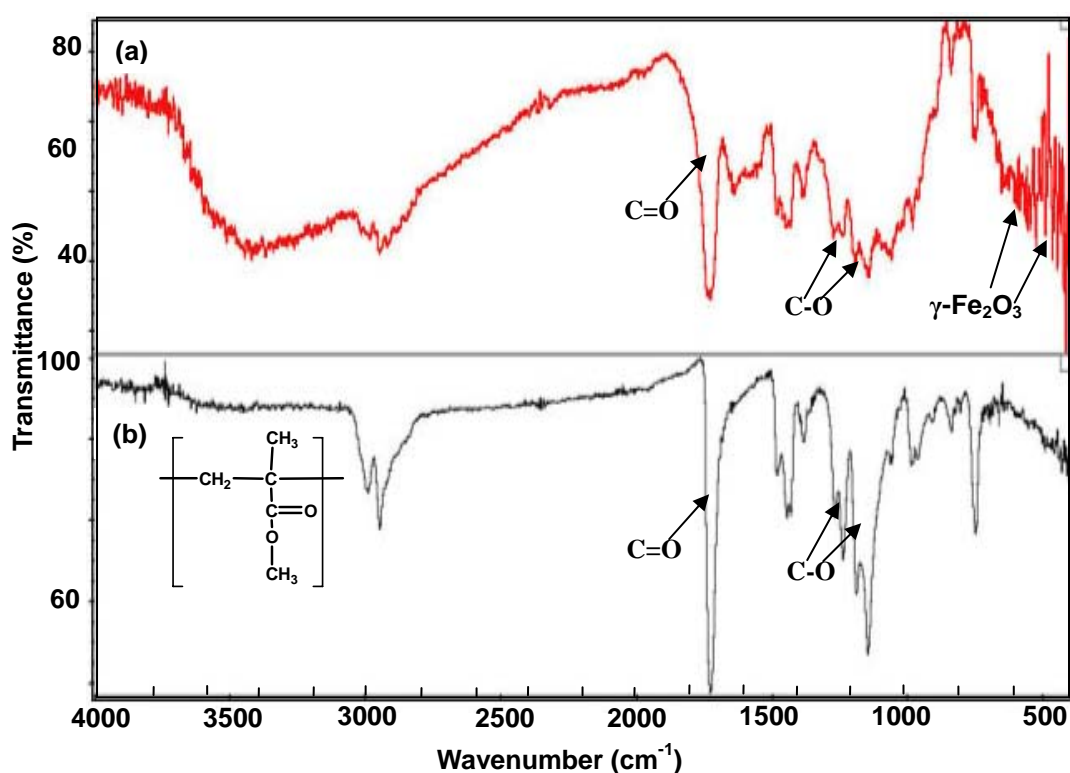


Figure 5.27. FT-IR spectra of (a) isolated chitosan/graft-PMMA/γ-Fe₂O₃ copolymer composites and (b) isolated PMMA in the chloroform.

To separate the chitosan-*grafted* copolymers and *un-grafted* chitosan in the copolymer composites and determine their compositions, the freeze-dried MCS particles were extracted with a 1 v/v% of acetic acid solution for 48 h. *Un-grafted* chitosan dissolved in an acetic acid solution, was separated from the insoluble magnetic graft copolymer composites which remained in the thimble. The actual

amounts of chitosan dissolved in an acetic acid solution and those that were insoluble were determined gravimetrically. The *un-grafted* chitosan and chitosan-*grafted* were 62 % and 38 %, respectively. In other words, there was 62% of the charged chitosan, which did not take part in the grafting reaction. It was either dissolved in solution or was adsorbed on the resulting particles. The isolated magnetic chitosan-*grafted* copolymer composites were further characterized with FT-IR analyses. Figure 5.28 shows the characteristic peaks of chitosan, which are the amine peak of chitosan at 3400 cm^{-1} and the N-H bending of chitosan between 1550 and 1600 cm^{-1} . This result indicates that chitosan was grafted onto the graft copolymer composites.

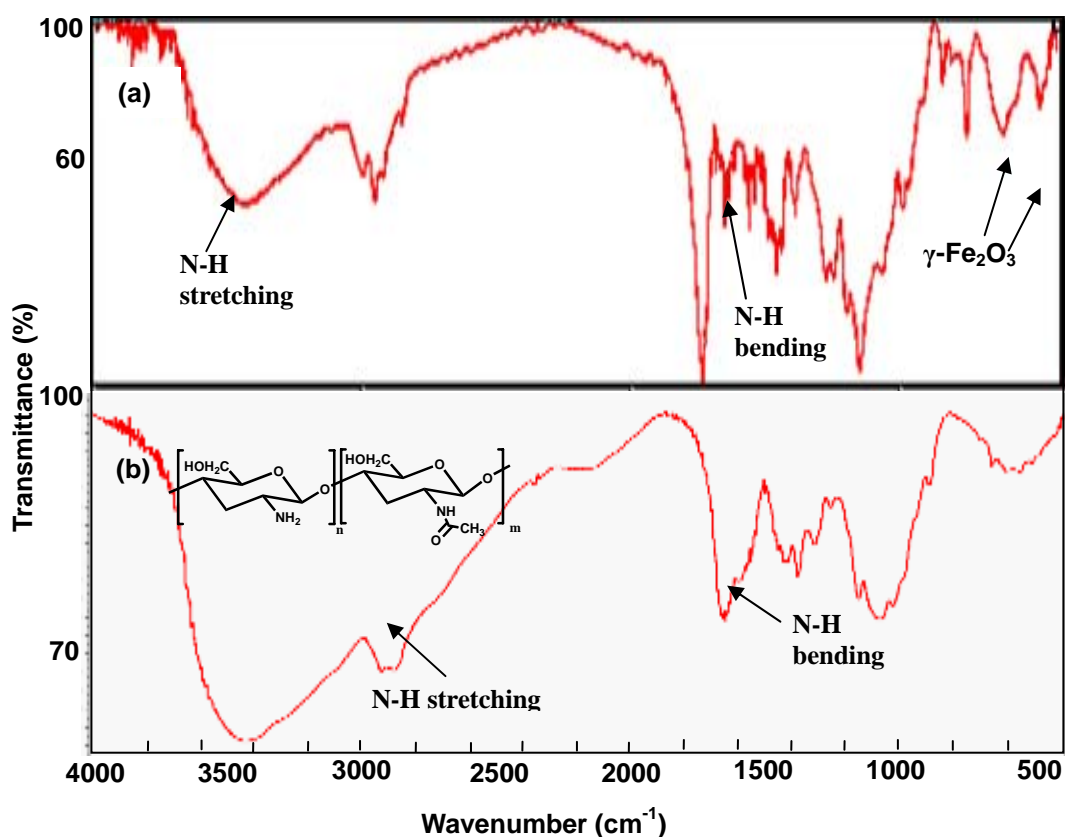


Figure 5.28. FT-IR spectra of (a) isolated chitosan-*grafted* copolymer composites using a 1 v/v% of acetic acid solution extraction and (b) isolated chitosan in a 1 v/v% acetic acid.

The composition of $\gamma\text{-Fe}_2\text{O}_3$ nanoparticles in MCS particles was determined with thermogravimetry analyses (TGA). Figure 5.29 shows the TGA thermogram of PMMA/chitosan core-shell particles, showing a complete weight loss at above 500 °C. For MCS particles, the thermogram shows that there is 85% weight loss from 380 to 500 °C, which is due to the loss of polymers. However, there is 8.4% weight remained at 900 °C, which is probably attributed to the presence of $\gamma\text{-Fe}_2\text{O}_3$ nanoparticles, since the nanoparticles have a high thermal stability below 1000 °C, as indicated in Figure 4.13.

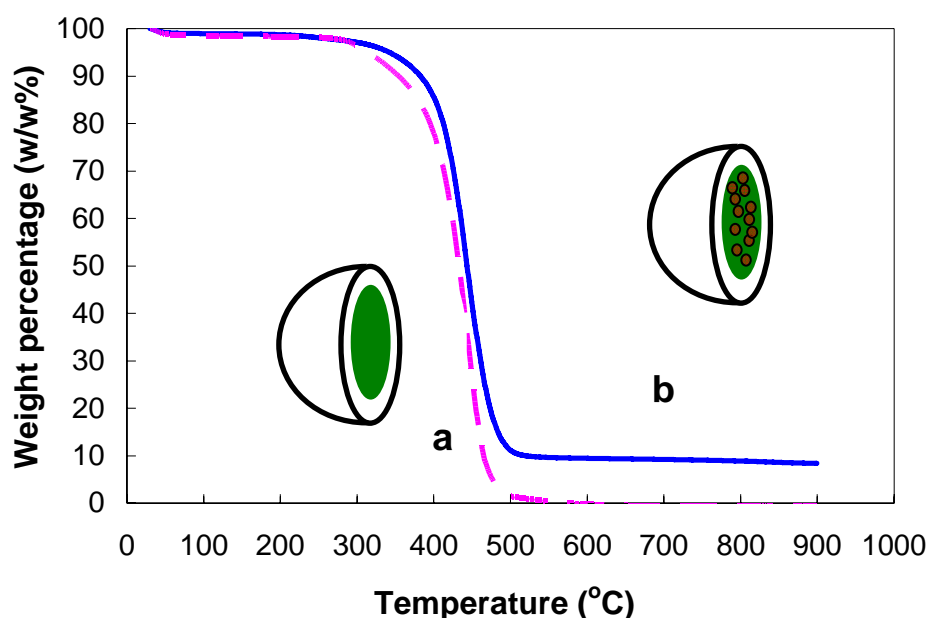


Figure 5.29. TGA thermograms of a) PMMA/chitosan core-shell particles without magnetic nanoparticles, and b) MCS particles (containing 8.4 w/w% of $\gamma\text{-Fe}_2\text{O}_3$).

Based on the monomer conversion, the Soxhlet extraction of ungrafted chitosan and the thermogravimetry analysis (TGA) of encapsulated $\gamma\text{-Fe}_2\text{O}_3$, the compositions of the MCS particles were determined, and the detailed calculation are illustrated in Appendix, B-1. The magnetic core-shell particles contained 65

w/w% of PMMA cores, 27 w/w% of chitosan, and 8 w/w% of $\gamma\text{-Fe}_2\text{O}_3$, respectively (Figure 5.30).

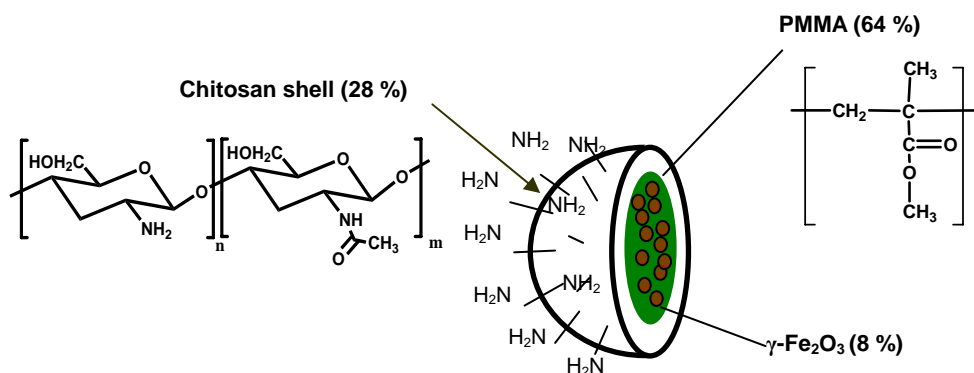


Figure 5.30. Schematic diagram of the composition of MCS particles.

Particle size and size distribution of MCS particles

Particle size and size distribution of MCS particles were determined with the Coulter LS 230 Particle Size Analyzer. Figure 5.31 illustrates that MCS particles produced (CTS : MMA : MPS- Fe_2O_3 = 2.5:6:1; TBHP = 0.1 mM) under standard conditions at pH 4.12 had a volume-average diameter (D_v) of 202 nm, and a number-average diameter (D_n) of 185 nm. The polydispersity index (D_v/D_n) was 1.09, indicating a very narrow size distribution of the MCS particles.

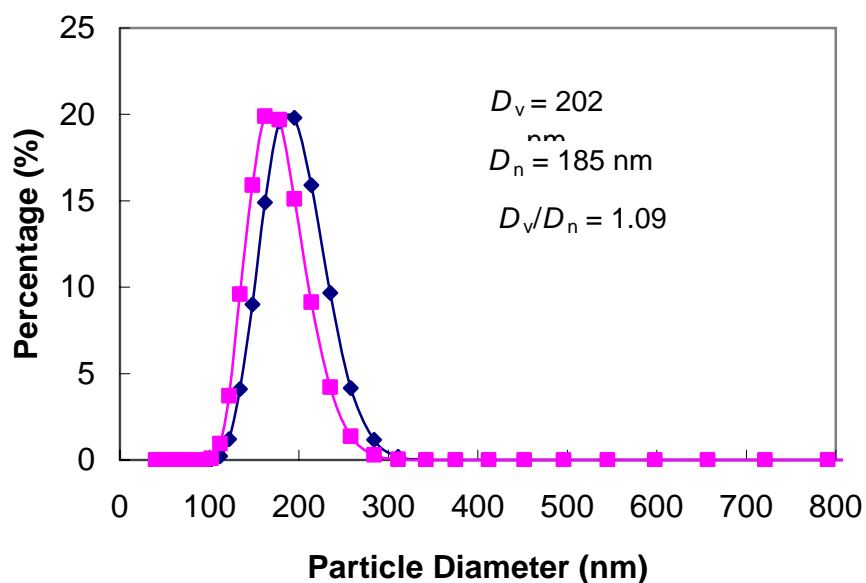


Figure 5.31. Particle size and size distribution of MCS particles measured by Coulter LS 230 Particle Size Analyzer. (◆) D_v and (■) D_n .

Morphologies of MCS particles

Morphologies of the MCS particles were examined with both Field emission scanning electron microscopy (FE-SEM) and TEM. The FE-SEM images clearly reveal that the MCS particles have quite uniform size distribution (Figure 5.32); however, some of them are not spherical. Furthermore, the particles tend to form aggregates, which may be attributed to the strong magnetic dipole-dipole interactions exerted between the particles during drying. Figure 5.33 shows the TEM images of the MCS particles, in which the chitosan shells were purposely stained with phosphotungstic acid (PTA, $\text{WO}_3 \cdot \text{H}_3\text{PO}_4 \cdot x\text{H}_2\text{O}$) solution for 2 min. The images clearly reveal the core-shell nanostructures, where the PMMA core containing magnetic nanoparticles are coated with chitosan shell (Figure 5.33).

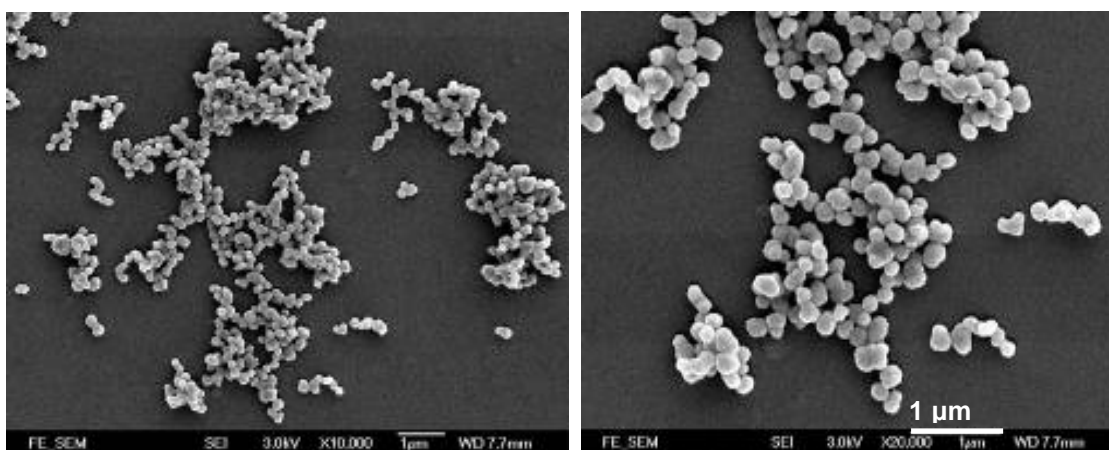


Figure 5.32. SEM images of MCS particles produced (CTS : MMA : MPS-Fe₂O₃ = 2.5 : 6 : 1; TBHP = 0.1 mM).

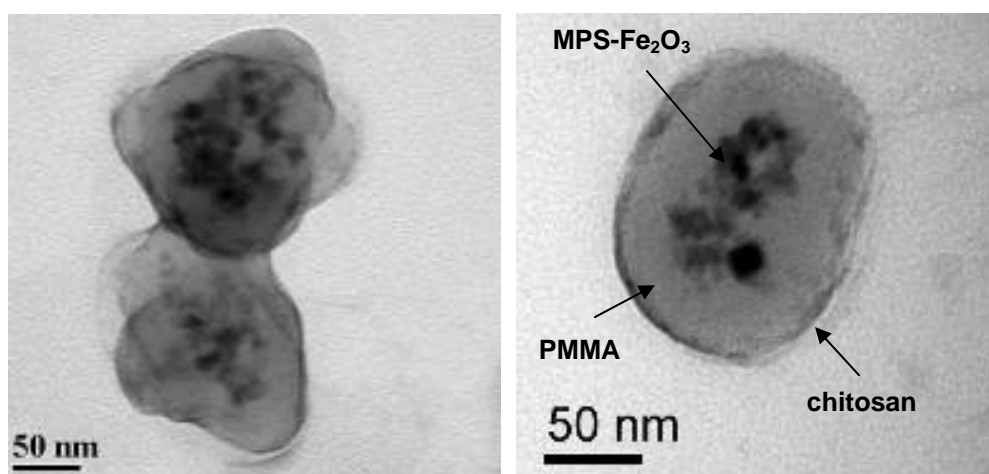


Figure 5.33. TEM images of MCS particles (CTS : MMA : MPS-Fe₂O₃ = 2.5 : 6 : 1; TBHP = 0.1 mM) stained with a 0.5 w/w% of phosphotungstic acid for 2 min on either formvar or carbon-coated grids.

Characterization of MCS particle surface charges

The presence of chitosan shells was verified by ζ -potential measurements as a function of pH in a 1 mM NaCl solution at 25 °C. Figure 5.34 shows that the positive ζ -potential of MCS particles decreases from + 50 to 0 mV as the pH increases from pH 3.0 to 8.0. This effect is probably due to the de-protonation of quaternary ammonium ions of chitosan. When compared with PMMA/chitosan core-shell particles without magnetic nanoparticles, the ζ -potential values of the MCS particles at various pHs are lower, which may be attributed to the complexation and encapsulation of the negatively charged MPS-Fe₂O₃ nanoparticles.

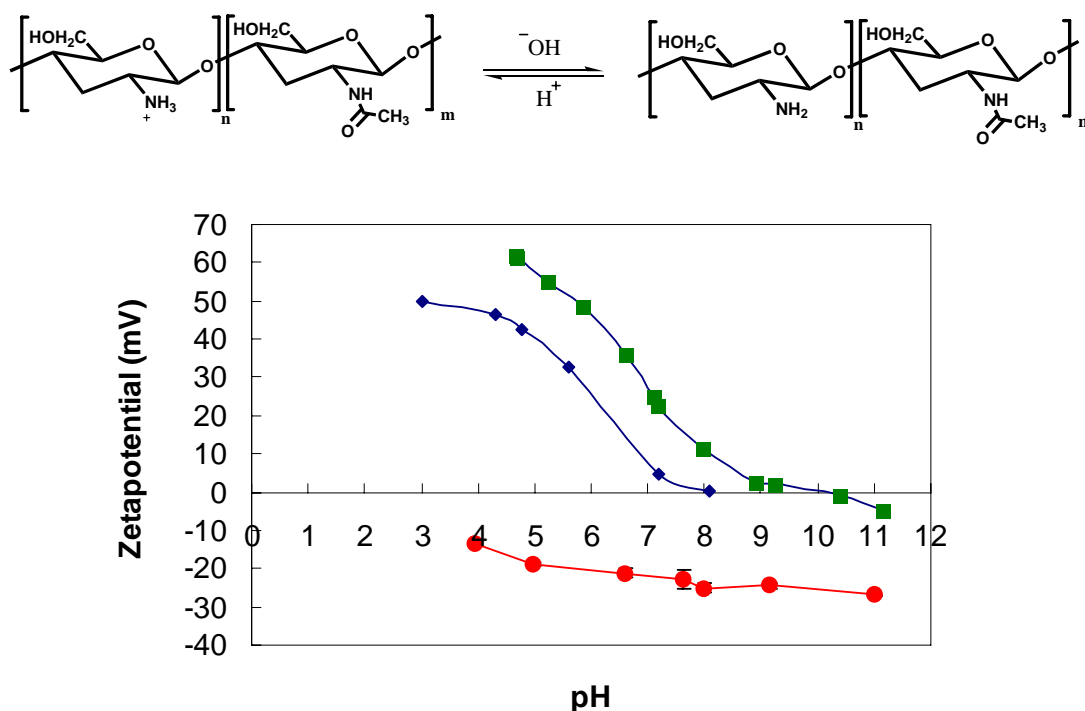


Figure 5.34. pH dependence of the ζ -potential measured in a 1 mM NaCl solution at 25 °C. (■) PMMA/chitosan particles; (◆) MCS particles (CTS : MMA : MPS-Fe₂O₃ = 2.5 : 6 : 1; TBHP = 0.1 mM); and (●) MPS-Fe₂O₃ nanoparticles.

Colloidal stability and critical coagulation concentration (CCC) of MCS particles

The stability of MCS particles at different pHs was studied with a dynamic light scattering (Malvern Zetasizer 3000 HS). Figure 5.35 shows the hydrodynamic diameter ($\langle D_h \rangle$) of MCS particles as a function of pH in tris(hydroxymethyl)aminomethane hydrochloride (Tris-HCl) as a buffer solution. Increasing the pH of the MCS particle dispersion from 4.3 to 7.0 had little influence on the hydrodynamic diameter ($\langle D_h \rangle$) of the particles (393–413 nm). However, a further increase of the pH from 7.0 to 7.9 significantly increased their sizes from 413 to 3304 nm in diameter. This effect was probably attributed to the coagulation of MCS particles because they had low surface charge densities (+ 7 to 0 mV) between pH 7.0 and 8.0 (Figure 5.34). This result suggests that the MCS particles are colloidal stable below pH 6.5.

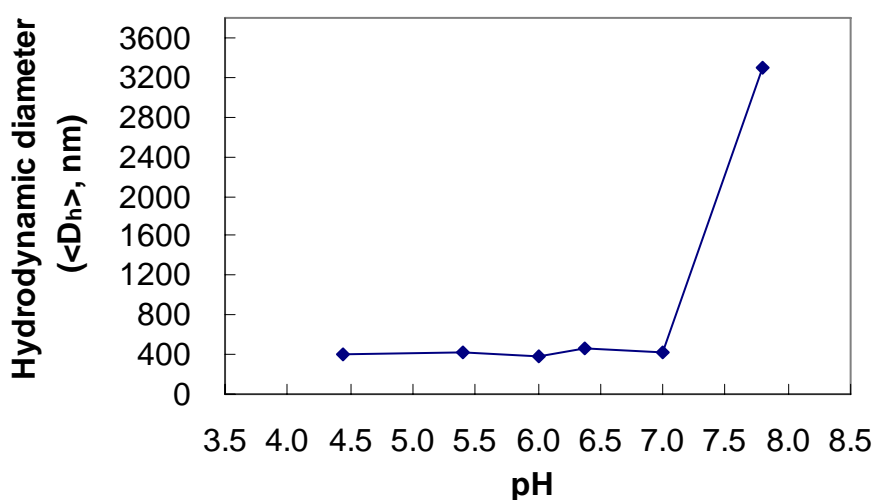


Figure 5.35. Effect of pH on the (\blacklozenge) hydrodynamic diameter ($\langle D_h \rangle$) of MCS particles (CTS : MMA : MPS-Fe₂O₃ = 2.5 : 6 : 1; TBHP = 0.1 mM) at 25 °C using a 1 mM of Tris-HCl as a buffer solution.

The stability of MCS particles in electrolyte solution was studied, based on the changes of hydrodynamic diameters as a function of NaCl concentration. Figure 5.36 shows that increasing NaCl concentration from 0 to 1.0 M had little influence on the hydrodynamic size ($\langle D_h \rangle$) of the particles (390–493 nm). However, a further increase of the concentration from 1.1 to 1.5 M resulted in significant increases in their sizes from 493 to 992 nm in diameter. Formation of larger particles is probably caused by the suppression of electrical charges of the chitosan with the increase of NaCl concentration.

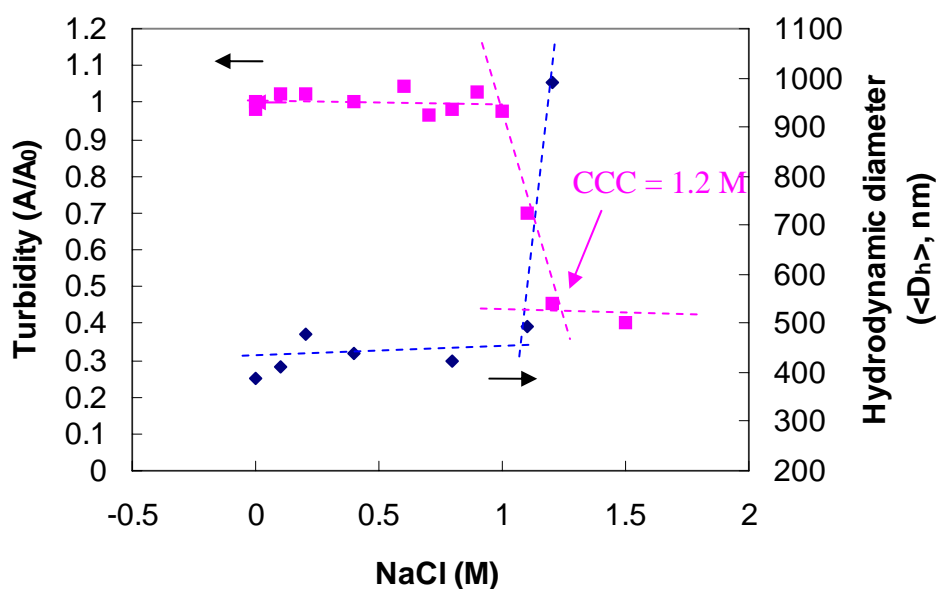


Figure 5.36. Effect of NaCl on the (■) turbidity and (◆) hydrodynamic diameter ($\langle D_h \rangle$) of MCS particles (CTS : MMA : MPS-Fe₂O₃ = 2.5 : 6 : 1; TBHP = 0.1 mM) dispersed in pH 6.0 solution.

The colloidal stability of MCS particles against various electrolyte concentrations was further examined by determining the critical coagulation concentration (CCC) value of MCS particles. This value was determined based on the measurement of turbidity (A/A_0) changes as a function of various NaCl concentrations, by extrapolating the sharply decreasing part of the turbidity curve,

as shown in Figure 5.36. The determined CCC value of MCS particle dispersion at pH 6.0 was 1.2 M. This value shows a good agreement with the result obtained from dynamic light scattering measurement. Such CCC value is significantly higher than the PMMA particles (CCC = 50–60 mM NaCl at pH 7) produced by emulsifier-free emulsion polymerization of MMA initiated with 2,2'-azobis(2-amidinopropane) dihydrochloride (V-50) as reported in the literature.¹³⁸ In other words, the MCS particles can withstand high electrolyte concentration up to 1.0 M without serious coagulation. Compared with the CCC value of chitosan-modified PMMA particles (172–177 mM NaCl at pH 3.0) having only 0.08 to 1.7 w/w of chitosan on the shell reported by Chern *et al*, our particles with 27 w/w% chitosan on the shell shows higher stability in NaCl solution. Thus, the thicker shell of MCS particles contributes to a higher stability in electrolyte solution. This superior stability of MCS particles is an advantage for their applications in various biological systems.

Magnetization measurement of MCS particles

Magnetization measurement of the MCS particles containing a 8.4 w/w% of $\gamma\text{-Fe}_2\text{O}_3$ was conducted by applying external magnetic fields from 0 to 5 KOe. Results shown in Figure 5.37 indicate that the MCS particles exhibited superparamagnetic properties at room temperature, because the data from both scans were overlapped, indicating the absence of hysteresis loop. The saturation magnetization (M_s) was 2.7 emu/g, which is comparable to magnetic particles produced by other encapsulation methods such as seeded precipitation and microemulsion polymerizations (1–3 emu/g latexes) reported by other groups.^{73,139-141}

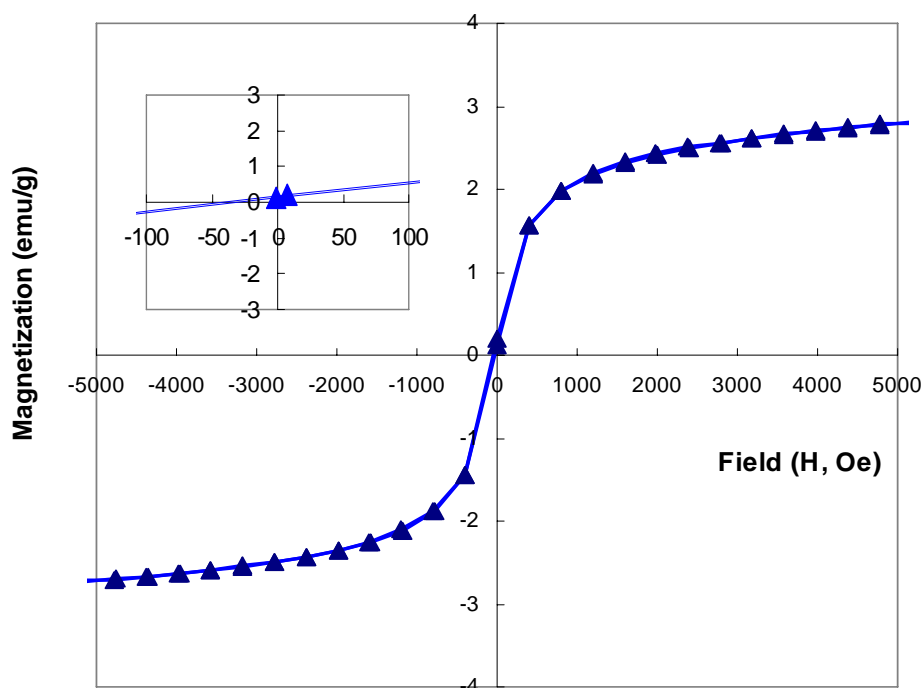
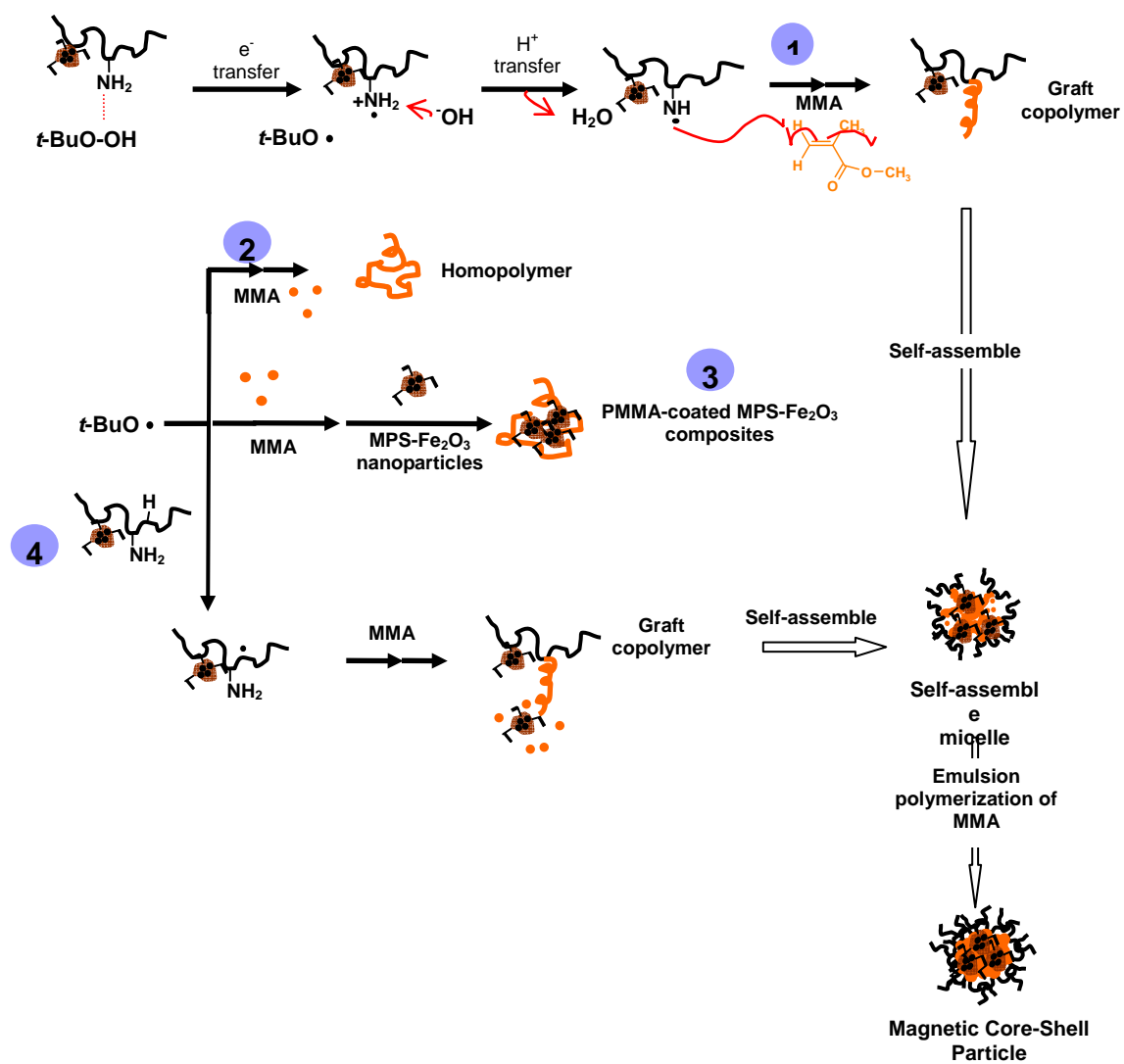


Figure 5.37. Room temperature magnetization measurement of MCS particles (CTS : MMA : MPS- Fe_2O_3 = 2.5 : 6 : 1; TBHP = 0.1 mM) with a 8 w/w% of $\gamma\text{-Fe}_2\text{O}_3$ content.

Proposed reaction mechanisms for MCS particle formation

Plausible grafting and particle formation of MCS particles are proposed in Scheme 5.4. The TBHP (t -BuO-OH) initially interacts with the amino groups on chitosan backbone, forming amino and *tert*-butoxy (t -BuO•) radicals. Subsequently, the amino radicals on chitosan backbone initiate the graft copolymerization of MMA, forming amphiphilic graft copolymers (chitosan-*g*-PMMA•) (route 1). The t -BuO• radicals could either initiate the homopolymerization of MMA (route 2) or the copolymerization between MMA and the methacrylate groups of MPS-Fe₂O₃ nanoparticles to form *hydrophobic* PMMA-coated composites (route 3). The t -BuO• radicals could also abstract hydrogen atoms from the chitosan backbone, generating macro-radicals, which could then initiate polymerization of MMA to form amphiphilic graft copolymers (route 4). The amphiphilic copolymers generated *in situ* (from route 1 and 4) could self-assemble to polymeric micelle-like micro-domains that facilitate the emulsion polymerization of MMA and the methacrylate groups of MPS-Fe₂O₃ nanoparticles. Thus, well-defined, core-shell particles containing magnetic nanoparticles in the cores can be produced in the absence of surfactant.



Scheme 5.4. Proposed mechanism for the graft copolymerization of MMA from chitosan in the presence of MPS-Fe₂O₃ nanoparticles.

Summary

Magnetic core-shell (MCS) particles with narrow size distribution have been successfully synthesized. Key findings of this synthetic system using TBHP as an initiator are summarized as follows, and the mechanistic rationalization of MCS particle synthesis is also discussed.

- 1) MPS-coated iron oxide nanoparticles can be encapsulated into the hydrophobic core of core-shell particles; however, encapsulations of oleate- and citrate-coated iron oxide nanoparticles in polymer cores fail.
- 2) The optimal weight ratio of chitosan to MMA to MPS-Fe₂O₃ nanoparticles is 2.5 : 6 : 1, and the solid content should be around 4 %. The compositions of MCS particle are 27 w/w% of chitosan, 65 w/w% of PMMA, and 8 w/w% of iron oxides.
- 3) An increase of the TBHP concentration decreases the amount of iron oxide encapsulated. Suitable TBHP concentration is approximately 0.1 mM.
- 4) An increase of the MPS-Fe₂O₃ content up to 0.4 w/w% can increase the amount of iron oxide encapsulated. Further increasing the content to 0.6 w/w% results in serious precipitation.
- 5) Various water-soluble polymers containing amino groups such as chitosan, PEI, PVAm, cellulase and casein have been investigated under the optimal reaction conditions. Among them, only chitosan can produce stable core-shell particles containing iron oxide nanoparticles in the cores with a narrow size distribution.
- 6) The MCS particles (iron oxide/PMMA/chitosan) have been carefully characterized, including the particle size, surface charge densities, morphologies, colloidal stability and magnetic responsiveness.

- 7) The MCS particles had average diameters ranging from 140 to 200 nm with PMMA cores containing iron oxide nanoparticles coated with chitosan shell. The surface charge density was around +25 mV at pH 6.0. The CCC value at pH 6.0 was 1.0 M.
- 8) The MCS particles exhibit superparamagnetism at room temperature, and their saturation magnetization was 2.7 emu/g.

From the mechanistic point of view, there are a number of reactions that occur concurrently during MCS particle synthesis. They are:

- (i) Graft copolymerization of MMA from the amino radical of chitosan backbone (desirable).
- (ii) Graft copolymerization of MMA and methacrylate groups of MPS-Fe₂O₃ nanoparticles from the amino radical of chitosan (desirable).
- (iii) Hydrogen abstraction of chitosan backbone by *t*-BuO • radical, followed by initiating the (i) and (ii) (desirable).
- (iv) Homopolymerization of MMA from *t*-BuO • radical. The rate of this reaction *is enhanced with increasing TBHP concentration.*
- (v) Homopolymerization of the methacrylate groups of MPS-Fe₂O₃ nanoparticles initiated with *t*-BuO • radical. The rate is enhanced by *increasing TBHP and MPS-Fe₂O₃ concentration.*
- (vi) Copolymerization of MMA and methacrylate groups of MPS-Fe₂O₃ nanoparticles from *t*-BuO • radical. The rate is enhanced by *increasing TBHP and MPS-Fe₂O₃ concentration.*

In spite of the success of making PMMA/chitosan cores-shell particles containing iron oxide nanoparticles using the TBHP initiation system, precipitation of reaction mixture (around 30 %) due to the formation of *hydrophobic* PMMA-coated iron oxide composites is still a major drawback in this system. Thus, other initiation system has been developed and is described in the next Section.

5.3.2.2 Preparation of MCS particles using *hydrogen peroxide* as an initiator

The presence of *hydrophobic* $t\text{-BuO}\cdot$ radicals may be the one responsible for forming PMMA-coated iron oxide composites as discussed earlier. It was proposed that the use of *hydrophilic* $\text{HO}\cdot$ radicals would overcome this problem. Hydrogen peroxide (H_2O_2) is a water-soluble oxidant, and has a similar chemical reactivity to TBHP. Thus, it was chosen for the subsequent studies.

H_2O_2 is seldom used alone to initiate a polymerization reaction because H_2O_2 has a low polymerization efficiency.¹⁴¹ Low efficiency is probably due to the fact that H_2O_2 readily decomposes to form water and oxygen,^{141,142} in which the decomposition rate of H_2O_2 increases about 2.3 times when reaction temperature is raised by 10 °C.^{142b} Then, the produced oxygen acts as a radical scavenger, leading to decreasing the polymerization efficiency. On the other hand, H_2O_2 can be activated by other reagents. For example, it has been extensively used with metal ions to form redox pairs, which can initiate polymerization at low temperatures.^{142,143} It can also be decomposed by ammonium hydroxide to give $\text{HO}\cdot$ radicals that can initiate polymerization under relatively mild conditions

(70–90 °C). Recently, the decomposition of H₂O₂ to HO• radicals has also been reported using Fe containing horseradish peroxidase through formation of redox pairs.¹⁴² These radicals can then initiate polymerization at low temperatures. Although there has been extensive studies of the reactions between H₂O₂ and metal ions, organic reagents and biomolecules, the decomposition of H₂O₂ induced by the amino groups of water-soluble polymers for graft copolymerization has never been reported. Because HO• radical is more hydrophilic than *t*-BuO• radical, the formation of *hydrophobic* PMMA-coated iron oxide composites is expected to be much less than the case using TBHP.

and the encapsulated $\gamma\text{-Fe}_2\text{O}_3$ % was studied, and results are shown in Table 5.7. An increase of reaction temperature from 60 to 80 °C increased the MMA conversions from 62 to 92 %. Higher temperature (> 70 °C) also generated more uniform MCS particles ($D_v/D_n < 1.2$). In addition, higher temperature produced less precipitates (19 to 26 % of the total charged substances), and higher percentage of encapsulated $\gamma\text{-Fe}_2\text{O}_3$ (1.0 to 7.0 %). However, since the decomposition temperature of H_2O_2 is around 90 °C,¹⁴¹ a further increase of reaction temperature from 80 to 90 °C would likely produce more undesirable PMMA homopolymers. The above results suggested that the optimal reaction temperature in this system was 80 °C, which was used for subsequent studies.

Table 5.7. Effect of reaction temperature on the H_2O_2 -induced graft copolymerization of MMA from chitosan (CTS) in the presence of MPS- Fe_2O_3 nanoparticles.^a

Expt code	Temp (°C)	Conv.% (ppt.%)	D_v^b (nm)	D_v/D_n^c	$\gamma\text{-Fe}_2\text{O}_3$ (%)
160306-2	80	92 (19)	194±1	1.18	7.0
120406-3	70	77 (26)	171±1	1.19	2.7
140406-1	65	64 (25)	274±77	1.76	1.0
130406-1	60	62 (30)	217±63	1.53	0.0

^aRefer to the procedure described in the Section 5.2.3. H_2O_2 concentration used was 0.1 mM in all cases. Polymerization was carried out at 80 °C for 2 h. Weight ratio of chitosan to MMA to MPS- Fe_2O_3 was 2.5 : 6 : 1 in all cases. Solid content = 3.8 %. ^b D_v and D_n are the volume and number average particle diameters, respectively. ^c D_v/D_n is the polydispersity index of the particle size distribution.

Effect of H₂O₂ concentration

Figure 5.39 shows the effect of H₂O₂ concentration on the monomer conversion, the precipitate percentage, the CTS% graft, the PMMA grafting efficiency, and the encapsulated percentage of γ -Fe₂O₃ nanoparticles. In the absence of H₂O₂, less than 5 % of MMA was converted to polymer after 2 h at 80 °C. When H₂O₂ solutions with concentrations from 0.1 to 0.2 mM were added, over 80 % of MMA conversions were achieved; however, a further increase of the concentrations from 0.2 to 1.2 mM slightly decreased MMA conversions from 88 to 75 %. This effect is probably attributed to the formation of a higher concentration of radicals, which increases the chance of radical termination. In all of the aforementioned concentrations, comparable amounts of precipitates (~ 20 % of total charged substances) were obtained.

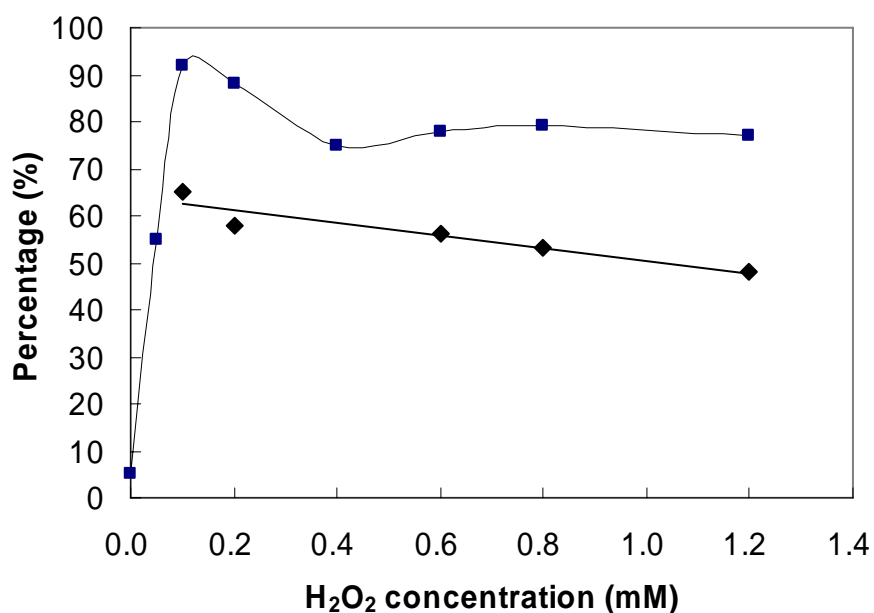


Figure 5.39. Effect of H₂O₂ concentration on the graft copolymerization of MMA in the presence of MPS-Fe₂O₃ nanoparticles. (■) MMA conversion and (◆) PMMA grafting efficiency.

The grafting efficiency of PMMA was determined by extraction of the crude product of MCS particles with CHCl_3 using a Soxhlet extractor. Figure 5.36 shows that the grafting efficiency of PMMA in MCS particles slightly decreased from 65 to 48 % as the H_2O_2 concentration increased from 0.05 to 1.2 mM. This means that more PMMA homopolymers were formed at higher H_2O_2 concentrations.

MCS particles produced using H_2O_2 concentrations between 0.4 to 1.2 mM were subjected to Soxhlet extraction using a 1 v/v% of acetic acid in order to determine the amount of un-reacted chitosan. It was found that the acetic acid phase was milky in all cases. After removal of acetic acid solution, the resulting white solids were analyzed with a FT-IR spectroscopy. Figure 5.40 (a–d) shows the FT-IR spectra of the solids obtained, in which strong carbonyl peaks of PMMA at 1721 cm^{-1} were observed. These results suggested that the solid may contain some low-molecular weight of PMMA (Figure 5.41) or graft copolymers (chitosan-g-PMMA) with short PMMA chains. This phenomenon was not observed in the TBHP initiation system. The presence of a high concentration of $\text{HO}\bullet$ radicals may result in the formation of undesirable low-molecular weight PMMA and graft copolymers with short PMMA chains. Thus, H_2O_2 concentration should be kept to around 0.1 mM.

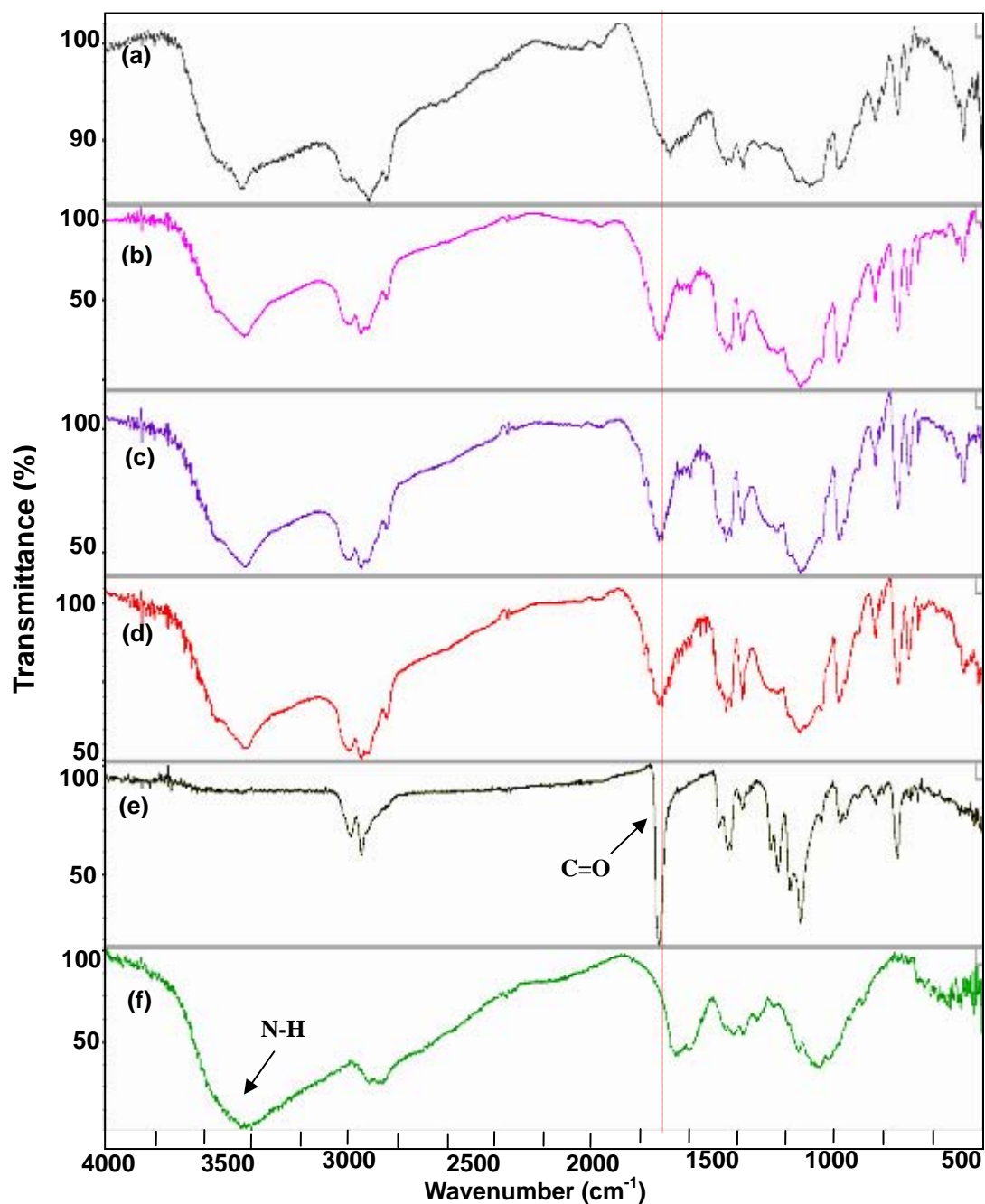
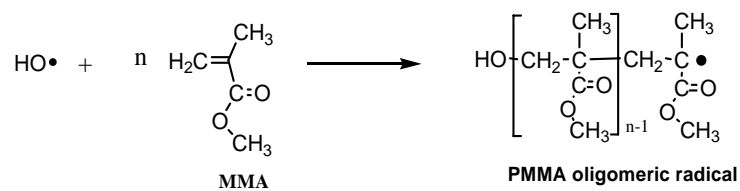


Figure 5.40. FT-IR spectra of the solids isolated from acetic acid extraction of the crude product produced with different H_2O_2 concentrations: (a) 0.4 mM; (b) 0.6 mM; (c) 0.8 mM; (d) 1.2 mM; (e) *homo*-PMMA and (f) extracted chitosan.

Initiation:



Termination:

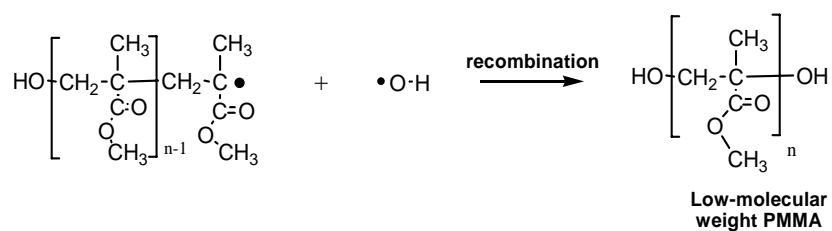
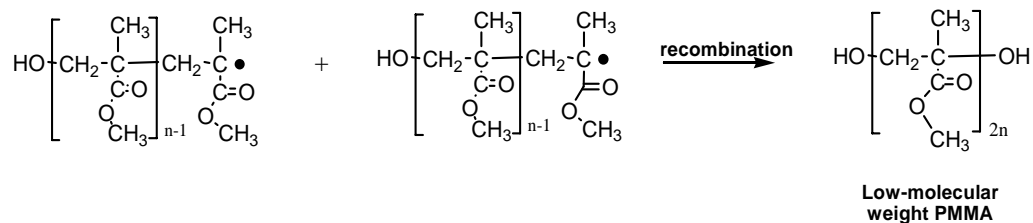


Figure 5.41. Formation of low-molecular weight PMMA in water phase through HO• radical-induced polymerization.

The effect of H_2O_2 concentration on the particle size of MCS particles was examined (Figure 5.42). In general, an increase in H_2O_2 concentration slightly reduced the particle size except for 0.1 mM of H_2O_2 . A larger particle size (~ 200 nm) at this concentration may be attributed to higher MMA conversion (92 %). The slight decrease in particle size probably arose from (1) lower MMA conversions, and (2) higher amounts of *water-soluble* hydroxyl-terminated low-molecular weight of PMMA. The particle size distributions were similar in all H_2O_2 concentrations examined ($D_v/D_n = 1.13\text{--}1.21$). Thus, 0.1 mM of H_2O_2 concentration was the optimal concentration for the formation of MCS particles.

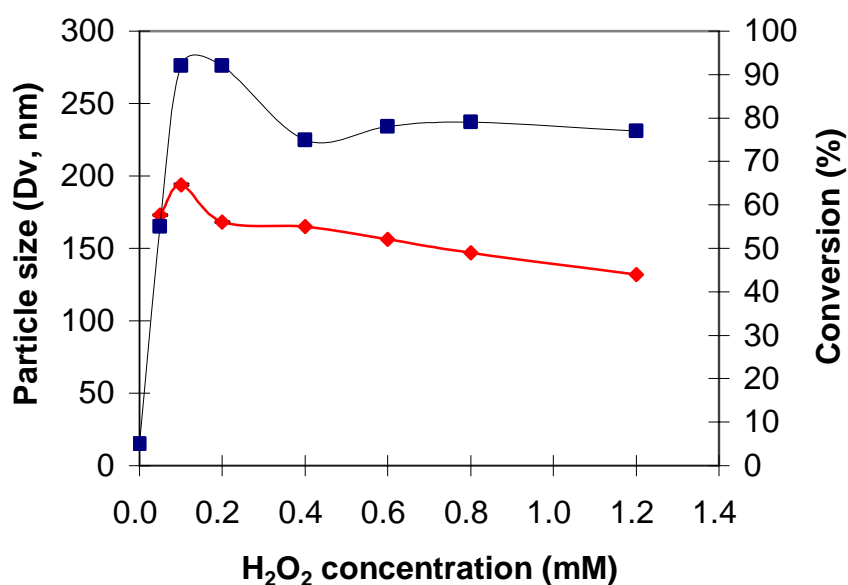


Figure 5.42. Effect of H_2O_2 concentration on the particle size and size distribution of MCS particles. (\blacklozenge) volume-average particle diameter (D_v) and (\blacksquare) MMA conversion.

Figure 5.43 shows the TEM micrographs of MCS particles produced at different H_2O_2 concentrations (0.05–1.2 mM). Encapsulation of the magnetic nanoparticles (black dots) into the cores was observed in all cases. At lower H_2O_2 concentrations (0.05–0.2 mM), all particles produced contained iron oxide nanoparticles in the cores. However, the use of higher H_2O_2 concentrations (0.4–1.2 mM) resulted in a mixture of blank core-shell particles and MCS particles (Figure 5.43 d–f). This effect may be explained by the fact that higher H_2O_2 concentrations (> 0.4 mM) give higher amounts of $\text{HO}\bullet$ radicals, thus increasing the rate of homopolymerization of MMA rather than the graft copolymerization. Therefore, H_2O_2 concentration should be less than 0.2 mM to ensure the formation of homogeneous MCS particles. The compositions of iron oxide encapsulated in MCS particles in the suitable concentrations (0.1–0.2 mM) were around 7 %, which is comparable to the TBHP system (8 %).

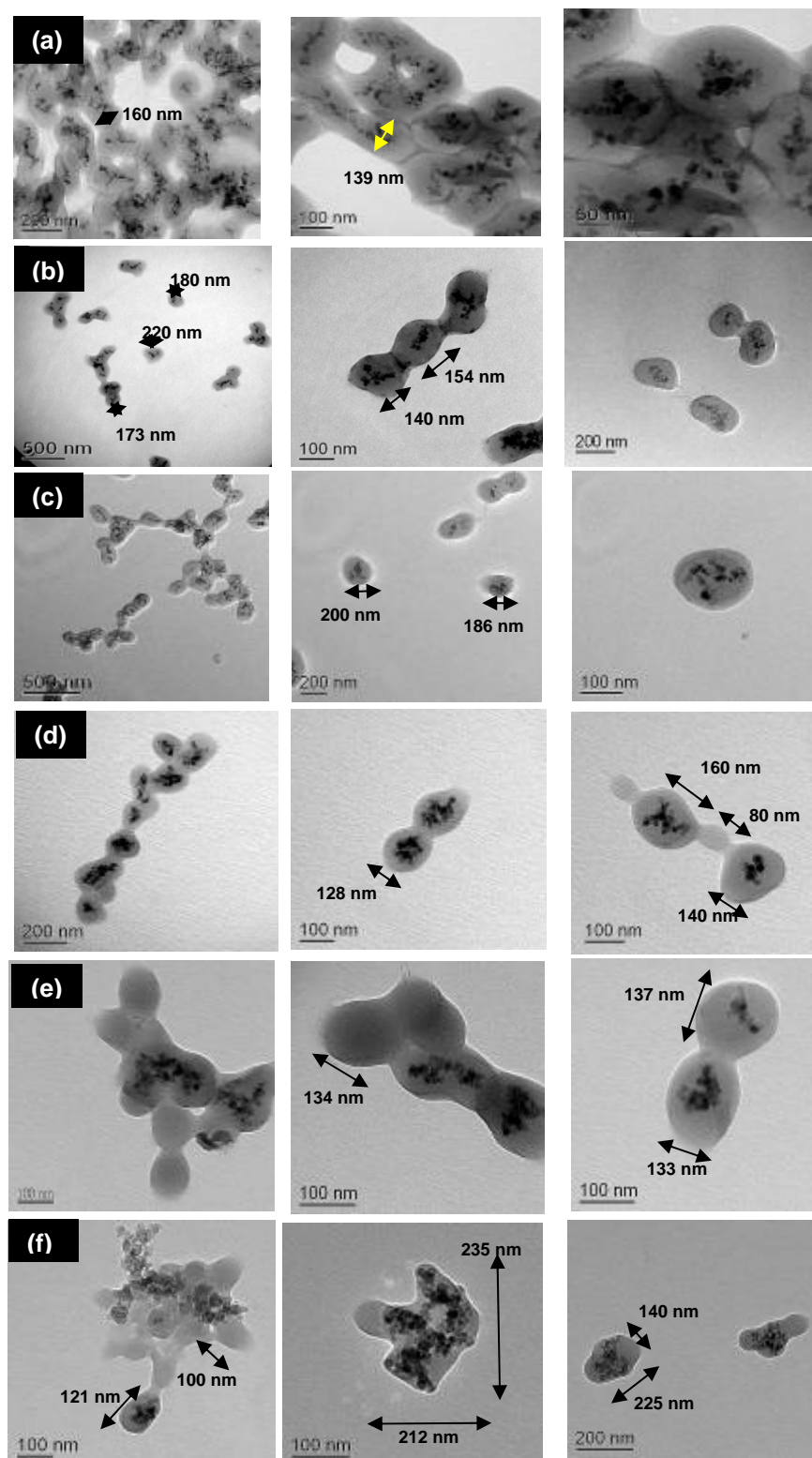


Figure 5.43. TEM images of MCS particles produced at different H_2O_2 concentrations. (a) 0.05 mM; (b) 0.1 mM; (c) 0.2 mM; (d) 0.4 mM; (e) 0.6 mM; (f) 1.2 mM.

Effect of MPS-Fe₂O₃ content

When no MPS-Fe₂O₃ nanoparticles were added to the copolymerization recipe, a low MMA conversion (46 %) was obtained. However, high conversion up to 92 % was reached in the presence of 0.1 g of MPS-Fe₂O₃ nanoparticles. Such high MMA conversion is not caused by metal-induced decomposition of H₂O₂ based on our control experiment. This effect may be attributed to the complexation between chitosan and MPS-Fe₂O₃ nanoparticles, which assists the graft copolymerization of MMA forming amphiphilic copolymers (chitosan-g-PMMA). The copolymers could subsequently self-assemble to form micelle-like micro-domains, and facilitate the emulsion polymerization of MMA.

In an attempt to increase the percentage γ -Fe₂O₃ in MCS particles, higher MPS-Fe₂O₃ content was examined (Table 5.8). An increase of MPS-Fe₂O₃ content from 0.4 to 0.8 w/w% resulted in a significant decrease in the conversion from 92 to 53 %. Furthermore, more precipitates were generated. This effect might be attributed to the fact that higher MPS-Fe₂O₃ contents could enhance the copolymerization with MMA, forming unstable PMMA-coated MPS-Fe₂O₃ composites. Such precipitation subsequently caused poor formation of micelle-like microdomain, resulting in lower MMA conversion. Determination of percentage of chitosan reacted (CTS% reacted, Table 5.8) indicated that higher MPS-Fe₂O₃ content lowered the amount of chitosan grafted on MCS particles. This effect may be explained by the reduction of radical concentration due to the precipitation. Table 5.8 shows that particle sizes and their size distribution had

small variations. The increase in MPS-Fe₂O₃ content did not, in fact, increase the amount of iron oxide encapsulated.

Table 5.8. Effect of MPS-Fe₂O₃ content on the graft copolymerization of MMA from chitosan (CTS).^a

Expt. code	CTS : MMA: MPS-Fe ₂ O ₃ (w:w:w)	MPS-Fe ₂ O ₃ (g)/(w/w%)	Conv. % (ppt.%)	<i>D_v</i> (nm) ^b	<i>D_v</i> / <i>D_n</i> ^c	CTS% reacted	γ-Fe ₂ O ₃ (%)
111006-3	2.5 : 6 : 0	0.00	46 (0)	137± 1	1.14	N/A	N/A
160306-2	2.5 : 6 : 1.0	0.10 (0.40)	92 (19)	194± 1	1.13	33	7.0
250706-2	2.5 : 6 : 1.2	0.12 (0.48)	77 (21)	177 ±1	1.18	37	6.4
200306-2	2.5 : 6 : 1.5	0.15 (0.60)	60 (37)	169 ±2	1.23	23	4.9
180306-1	2.5 : 6 : 2.0	0.20 (0.80)	53 (48)	156 ±1	1.20	26	5.3

^aRefer to the procedures described in the Section 5.2.3. H₂O₂ concentration was 0.1 mM in all cases. All reactions were carried out at 80 °C for 2 h. ^b*D_v* and *D_n* are the volume and number average particle diameters, respectively. ^c*D_v*/*D_n* is the polydispersity index of the particle size distribution.

Figure 5.44 (a–c) shows the TEM images of MCS particles produced at different MPS-Fe₂O₃ contents. All magnetic nanoparticles were encapsulated inside the cores. There were no blank core-shell particles. The MCS particles produced using 0.4 and 0.6 w/w% of MPS-Fe₂O₃ nanoparticles gave quite uniform MCS particles, as shown in Figure 5.44 (a and b). Higher MPS-Fe₂O₃ content (0.8 w/w%) started to form large aggregates (Figure 5.44 c). Based on above findings, the most suitable MPS-Fe₂O₃ content was 0.4 w/w%.

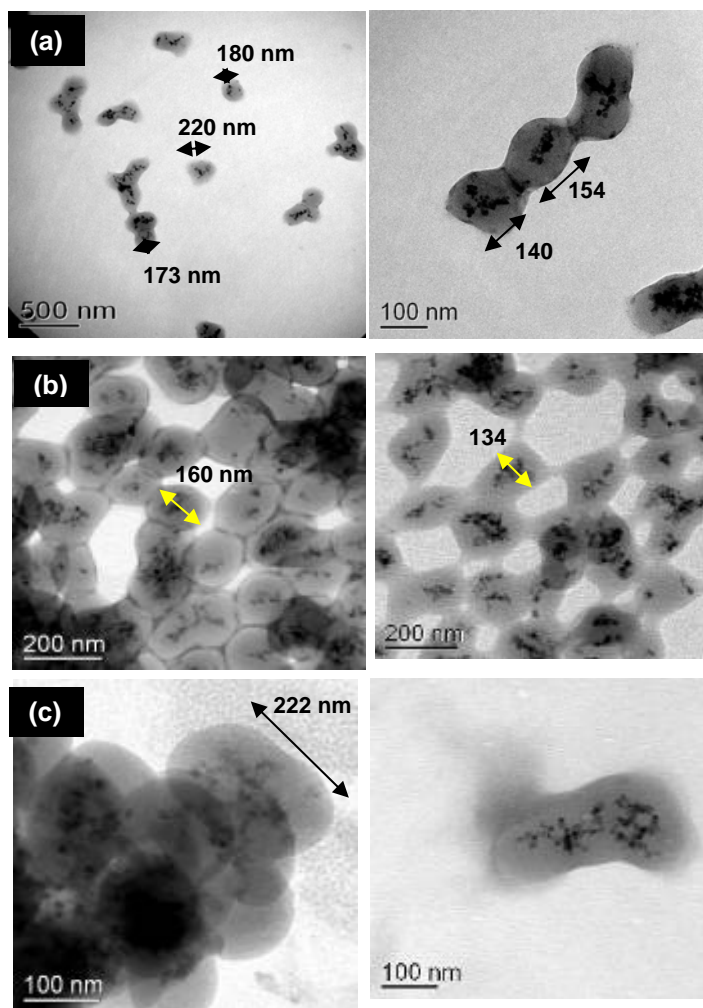


Figure 5.44. TEM images of MCS particles with different weight ratios of CTS to MMA to MPS-Fe₂O₃: (a) 2.5 : 6 : 1(0.4 %); (b) 2.5 : 6 : 1.5(0.6 %); (c) 2.5 : 6 : 2.0(0.8 %).

Effect of MMA content

Variation of MMA content on MCS particle formation has been investigated, aiming to increase the amount of iron oxide encapsulated in the particles. Table 5.9 shows that decreasing the MMA content from 2.4 to 1.2 w/w% resulted in the decrease of conversions from 92 to 66 %, but it had little influence on the amount of precipitates generated (ppt.%) and the chitosan reacted (CTS% reacted). Table 5.9 also shows that a decrease in MMA content from 2.4 to 1.6 w/w% resulted in increasing encapsulated γ -Fe₂O₃ content from 7 to 16 % with particle sizes less than 200 nm. But, a further decrease of MMA content from 1.6 to 1.2 w/w% resulted in lower encapsulation percentage (γ -Fe₂O₃ %). This study concluded that the optimum weight ratio of chitosan to MMA to MPS-Fe₂O₃ should be 2.5:4:1 for maximum encapsulation of iron oxide nanoparticles up to 16 w/w%.

Table 5.9. Effect of MMA content on the graft copolymerization of MMA from chitosan in the presence of MPS-Fe₂O₃ nanoparticles.^a

Expt. code	CTS : MMA : MPS-Fe ₂ O ₃ (w:w:w)	MMA (g)/(w/w%)	Conv.% (ppt.%)	D_v (nm) ^b	D_v/D_n ^c	CTS% reacted	γ -Fe ₂ O ₃ (%)
160306-2	2.5 : 6 : 1	0.6 (2.4)	92 (19)	194±1	1.13	33	7.0
210406-4	2.5 : 5 : 1	0.5 (2.0)	86 (13)	145±1	1.19	33	8.4
120906-1	2.5 : 4 : 1	0.4 (1.6)	80 (17)	148±1	1.12	40	16
240406-1	2.5 : 3 : 1	0.3 (1.2)	66 (24)	137±2	1.16	38	12

^aRefer to the procedures described in the Section 5.2.3. H₂O₂ concentration used was 0.1 mM in all cases. All reactions were carried out at 80 °C for 2 h. ^b D_v and D_n are the volume and number average particle diameters, respectively. ^c D_v/D_n is the polydispersity index of the particle size distribution.

Figure 5.45 shows the TEM micrographs of the MCS particles produced at the optimal weight ratio (CTS : MMA : MPS-Fe₂O₃ = 2.5 : 4 : 1). All the iron oxide nanoparticles were encapsulated inside the polymer cores. There were no blank particles. Although the TEM images showed that some of these particles formed aggregates in the dried-state, particle size measurement indicated that they were actually well dispersed in water, and had an average size of around 150 nm in diameter with a size distribution index of 1.12.

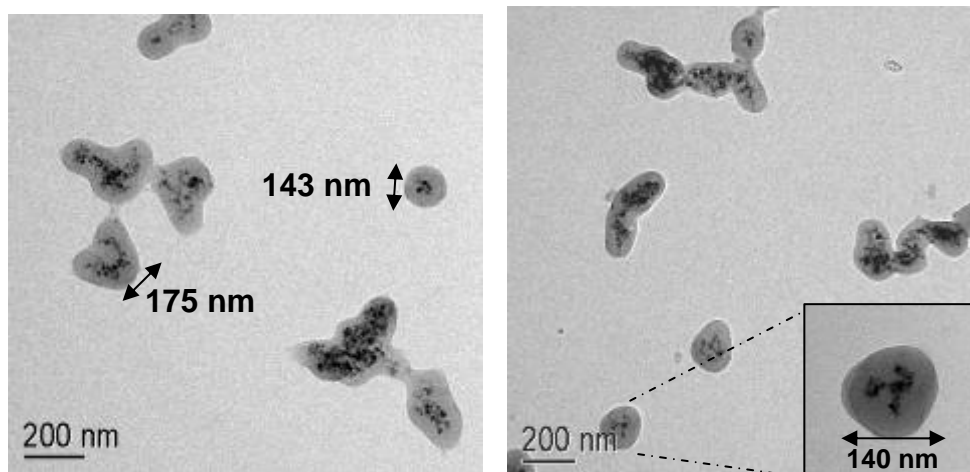


Figure 5.45. TEM images of MCS particles produced at the optimal weight ratio (CTS : MMA : MPS-Fe₂O₃ = 2.5 : 4 : 1; H₂O₂ = 0.1 mM).

Scope of other vinyl monomers

Multi-functional particles that are able to alter their physical and chemical properties in response to environmental stimuli, such as pH, temperature, and magnetic field, are attractive candidates for many potential applications, including drug delivery, biosensor, affinity separation, enzyme immobilization, and soft actuators.¹⁴⁶⁻¹⁴⁸ To demonstrate the versatility of the H₂O₂-induced graft copolymerization technique for the preparation of multi-functional core-shell particles, two types of vinyl monomers such as *n*-butyl acrylate (BA) and *N*-isopropyl acrylamide (NIPAM) were examined (Figure 5.46).

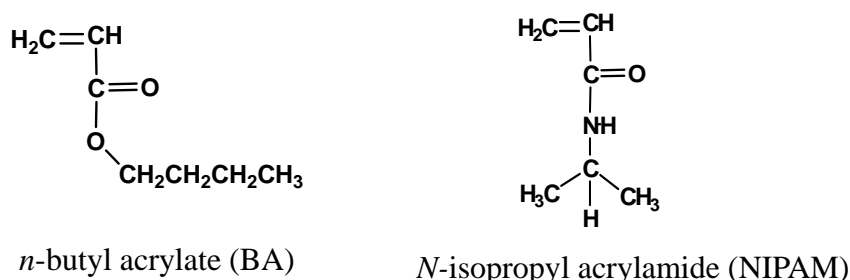
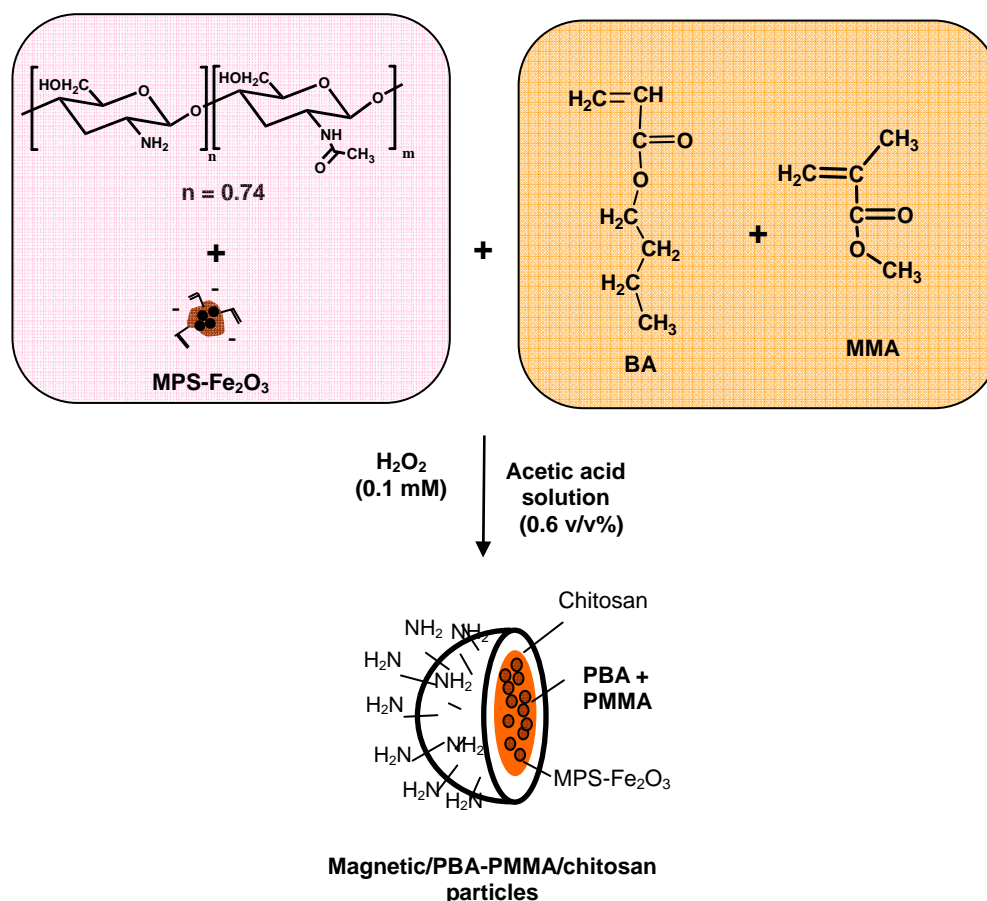


Figure 5.46. Chemical structure of *n*-butyl acrylate (BA) and *N*-isopropyl acrylamide (NIPAM).

Preparation of magnetic/PBA-PMMA/chitosan core-shell particles

In this study, BA was chosen because poly(*n*-butyl acrylate) (PBA) has a good film-forming property at room temperature due to its low glass transition temperature ($T_g = -54$ °C).¹⁴⁹ This property may improve the film formation if the cores contain a mixture of PMMA and PBA. Scheme 5.4 illustrates the synthesis of MCS particles using a mixture of BA and MMA under the optimal conditions determined in the previous studies.



Scheme 5.4. Synthesis of magnetic/PBA-PMMA/chitosan core-shell particles.

Table 5.10 shows the results of H₂O₂-induced graft copolymerization of MMA and BA from chitosan in the presence of MPS-Fe₂O₃ nanoparticles. Variation of MMA to BA weight ratios (90:10, 80:20, 70:30, 60:40, 50:50) all gave high monomer conversions (> 85 %) and comparable particle sizes ($D_v = 161\text{--}177$ nm) with narrow size distribution ($D_v/D_n = 1.14\text{--}1.22$). However, higher BA content resulted in more precipitates, which may be due to the formation of more *hydrophobic* PBA-PMMA/iron oxide composites.

Table 5.10. H₂O₂-induced graft copolymerization of vinyl monomers from chitosan in the presence of MPS-Fe₂O₃ nanoparticles.^a

Expt. code	[M] ^b	Conv.%	ppt.%	D _v (nm) ^c	D _v /D _n ^d
160306-2	MMA	92	19	194±1	1.13
131206-1	MMA:BA (90:10)	87	20	177±1	1.22
141106-1	MMA:BA (80:20)	99	29	188±2	1.17
110107-1	MMA:BA (60:40)	100	36	163±1	1.14
120107-1	MMA:BA (50:50)	100	60	161±1	1.14

^aRefer to the procedure described in the Section 5.2.3. H₂O₂ concentration (0.1 mM) was used in all cases. All reactions were carried out at 80 °C for 2 h. ^bWeight ratio of chitosan to monomers (MMA and BA) to MPS-Fe₂O₃ nanoparticles was 2.5 : 6 : 1. ^cD_v and D_n are the volume and number average particle diameters, respectively. ^dD_v/D_n is the polydispersity index of the particle size distribution.

Figure 5.47 shows the TEM images of MCS particles produced using a weight ratio of MMA:BA = 80:20 w/w). The magnetic nanoparticles were successfully encapsulated into the polymer cores, and distributed all over the particles. This is different from the case of PMMA as a core in which the magnetic nanoparticles were all localized in the center of the particles. This effect may have arisen from the hydrophobic nature of PBA, resulting in fast phase separation during the particle growth.

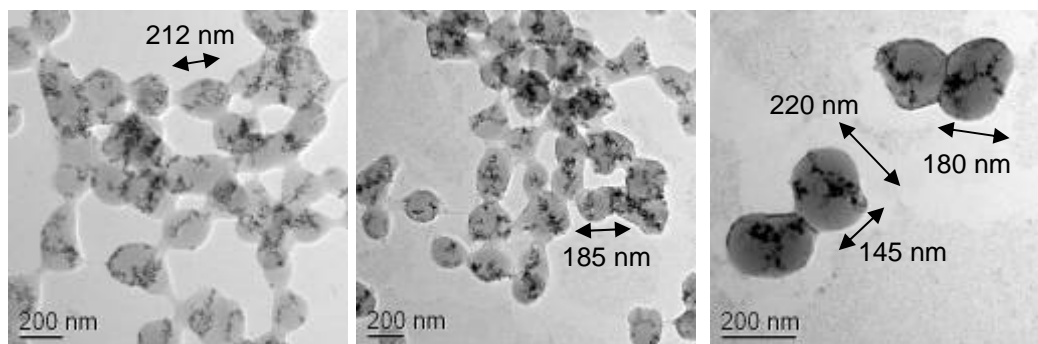
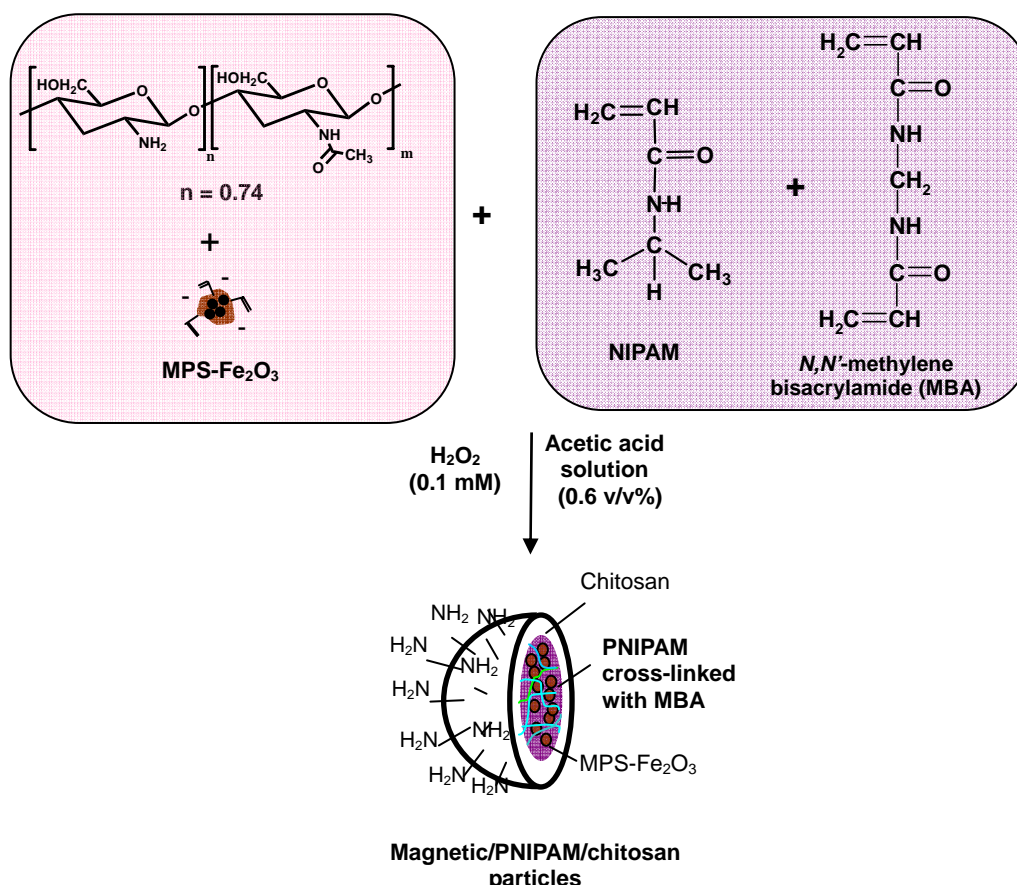


Figure 5.47. TEM images of the magnetic/PBA-PMMA/chitosan core-shell particles (MMA:BA = 80:20 w/w)

Preparation of magnetic/PNIPAM/chitosan core-shell microgels

Poly(*N*-isopropylacrylamide) (PNIPAM) is a well-known thermo-responsive linear polymer, which exhibits a coil-globule transition in an aqueous solution at a lower critical solution temperature (LCST) of about 32 °C. The cross-linked PNIPAM forms spherical microgel, which exhibits a dramatic and reversible volume transition in water at about 33 °C. It was of interest to explore the use of NIPAM as the vinyl monomer in our system for the preparation of MCS particles having multiple responsiveness of pH, temperature and magnetic field. This type of smart material has great potential in diverse applications. Scheme 5.5 illustrates the synthesis of MCS particles using the NIPAM as the vinyl monomer and MBA as a cross-linker under the optimal conditions.



Scheme 5.5. Synthesis of magnetic/PNIPAM/chitosan core-shell particles.

The effect of cross-linker (*N,N*-methylenebisacrylamide, MBA) content for H_2O_2 -induced graft copolymerization of NIPAM from chitosan in the presence of $\text{MPS-Fe}_2\text{O}_3$ nanoparticles was examined (Table 5.11). It was found that increasing the cross-linking percentage from 1 to 10 % resulted in the increase of the conversion from 61 to 84 %, and an improvement in the particle size distribution. However, a further increase in the cross-linking percentage from 10 to 15 % lowered the conversion from 84 to 58 %. Thus, the MBA charged contents of 8 and 10 % were most suitable for producing microgel particles having diameters of 200 and 240 nm with narrow size distributions ($D_v/D_n = 1.15\text{--}1.23$), respectively.

The TEM images showed in Figure 5.48 clearly reveal that the magnetic nanoparticles were all located inside the polymer cores, indicating the successful encapsulation of the nanoparticles. They also showed that these microgels tended to form aggregates in the dried-state. In fact, they were very stable in water, as indicated by the particle size measurement ($D_v = 200$ nm; $D_v/D_n = 1.15$). In summary, magnetic/PBA-PMMA/chitosan core-shell particles and magnetic/PNIPAM/chitosan microgels have been successfully synthesized. Thus, this is a versatile method which can be applied for a broad range of other vinyl monomers.

Table 5.11. H₂O₂-induced graft copolymerization of NIPAM from chitosan (CTS) in the presence of MBA as the cross-linker and MPS-Fe₂O₃ nanoparticles.^a

Expt. code	[M] ^b	Conv.%	ppt.%	D_v (nm) ^d	D_v/D_n ^e
201206-1	NIPAM (with a 1% of MBA) ^c	61	7	160±3 1739±13	1.93 1.12
281206-1	NIPAM (with a 5% of MBA) ^c	73	21	280±6	1.43
291206-1	NIPAM (with a 8% of MBA) ^c	70	16	200±2	1.15
010107-1	NIPAM (with a 10% of MBA) ^c	84	18	245±3	1.23
271206-2	NIPAM (with a 15% of MBA) ^c	58	17	263±6	1.24

^aRefer to the procedure described in the Section 5.2.3. H₂O₂ concentration (0.1 mM) was used in all cases. All reactions were carried out at 80 °C for 2 h. ^bWeight ratio of chitosan to monomers [M] to MPS-Fe₂O₃ nanoparticles was 2.5 : 6 : 1. ^c*N,N*-methylenebisacrylamide (MBA) is a cross-linker of NIPAM. ^d D_v and D_n are the volume and number average particle diameters, respectively. ^e D_v/D_n is the polydispersity index of the particle size distribution.

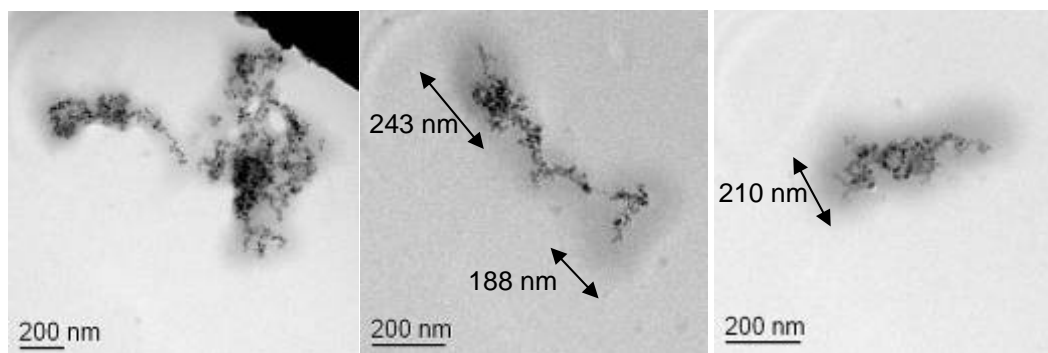


Figure 5.48. TEM images of the γ -Fe₂O₃/PNIPAM/chitosan (8 w/w% of MBA) core-shell microgels.

Composition of the MCS particles and magnetic-graft copolymers.

To determine the chemical composition of MCS particles, their crude product were purified by repeated centrifugation, decantation and re-dispersion process in order to remove any un-grafted chitosan in the dispersion. The purified MCS particles were then dried. The composition of the purified MCS particles was examined with FT-IR spectroscopy (Figure 5.49), and its spectrum was compared with PMMA homopolymer and chitosan. IR spectrum of the purified MCS particles clearly shows the broad N-H peak of chitosan at 3400 cm^{-1} , the carbonyl peak (C=O) of PMMA at 1735 cm^{-1} , the N-H bending of chitosan between 1550 and 1600 cm^{-1} , the ester peaks (-C-O-) of PMMA between 1247 and 1272 cm^{-1} , and the $\gamma\text{-Fe}_2\text{O}_3$ absorption bands between 400 and 600 cm^{-1} . This result indicates that the purified MCS particles were composed of chitosan, PMMA and $\gamma\text{-Fe}_2\text{O}_3$.

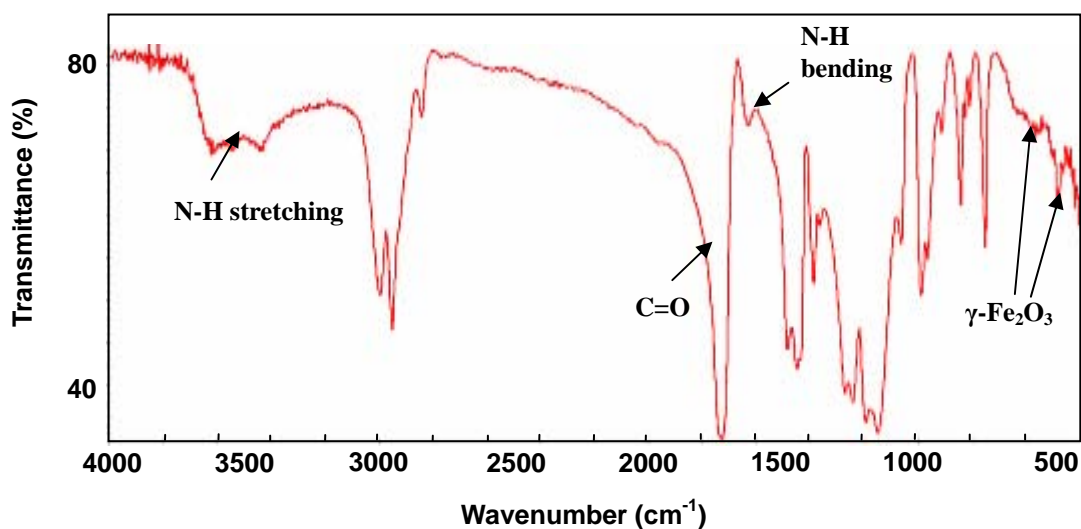


Figure 5.49. FT-IR spectra of purified MCS particles (CTS : MMA : MPS- Fe_2O_3 = 2.5 : 6 : 1; H_2O_2 = 0.1 mM).

To confirm the formation of both magnetic *graft*-PMMA and *homo*-PMMA in the copolymer composites and their compositions, the crude product of MCS particle dispersion was first freeze-dried. The resulting brown solids were then subjected to the chloroform extraction for 48 h. PMMA homopolymer, which was dissolved in chloroform, was separated from the insoluble magnetic graft copolymer composites that remained inside the thimble. The amounts of both PMMA dissolved in chloroform and insoluble polymer composites were determined gravimetrically. The PMMA homopolymer and grafted PMMA were 35 % and 65 %, respectively. The high percentage of the grafted PMMA was unusual when compared with our previous work, in which the grafting percentage was only 15 %.¹⁰⁹

Such a dramatic increase in grafting efficiency may be attributed to the presence of reactive methacrylate groups of the MPS-Fe₂O₃ nanoparticles. Since these reactive groups are close to chitosan due to the interaction between MPS-Fe₂O₃ nanoparticles and chitosan, their copolymerization with MMA enhances the chance of grafting from/onto the chitosan chains. The isolated chitosan/graft-PMMA/ γ -Fe₂O₃ composites were further identified with FT-IR analyses (Figure 5.50). The spectrum clearly illustrated the characteristic peaks of PMMA such as the carbonyl peak at 1735 cm⁻¹ and the ester peaks between 1247 and 1272 cm⁻¹.

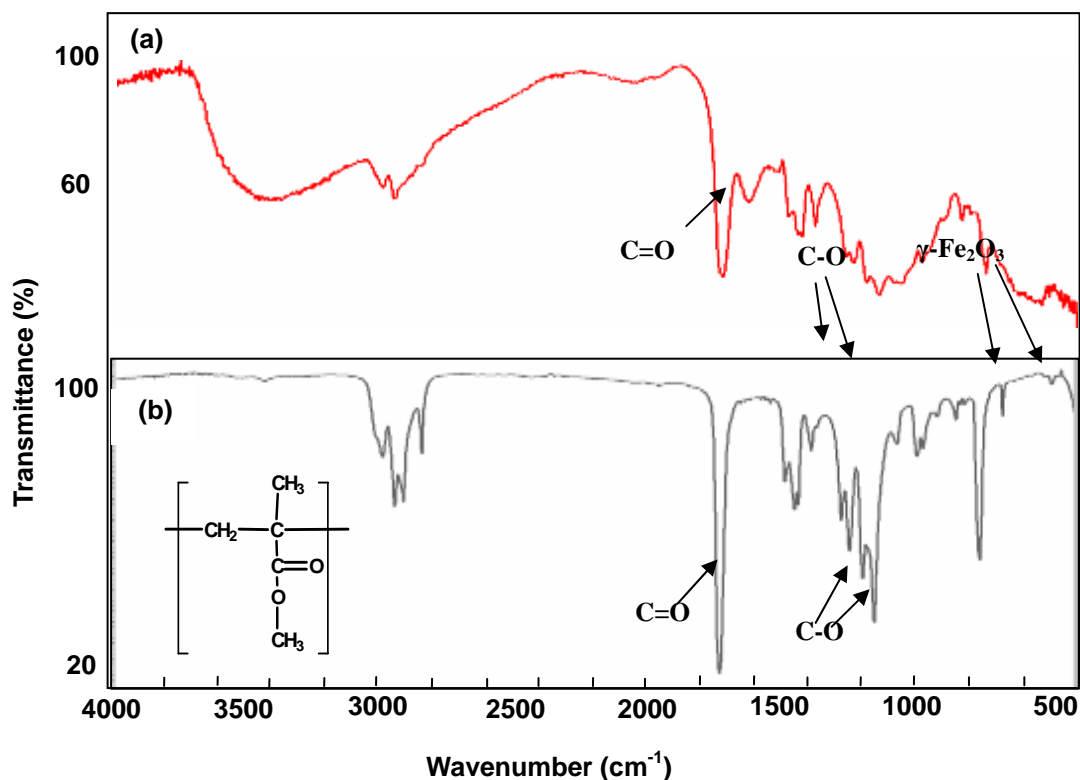


Figure 5.50. FT-IR spectra of (a) isolated chitosan/*graft*-PMMA/ γ -Fe₂O₃ copolymer composites using a chloroform extraction and (b) isolated PMMA in the chloroform.

To separate the chitosan-*grafted* copolymers and *un-grafted* chitosan in the copolymer composites and determine their compositions, the freeze-dried MCS particles were extracted with a 1 v/v% of acetic acid solution for 48 h. *Un-grafted* chitosan, which was dissolved in an acetic acid solution, was separated from the insoluble magnetic graft copolymer composites which remained in the thimble. The actual amounts of chitosan dissolved in the acetic acid solution and those insoluble composites were determined gravimetrically. The *un-grafted* chitosan and chitosan-*grafted* were 67 % and 33 %, respectively. In other words, 67 % of the chitosan charged did not take part in the grafting reaction. It was either dissolved in the solution or was adsorbed on the resulting particles. The isolated

magnetic chitosan-*grafted* copolymer composites were further characterized with FT-IR analyses. Figure 5.51 (c) shows the characteristic peaks of chitosan, which are the amine peak of chitosan at 3400 cm^{-1} and the N-H bending of chitosan between 1550 and 1600 cm^{-1} . This result indicates that chitosan was grafted onto the graft copolymer composites.

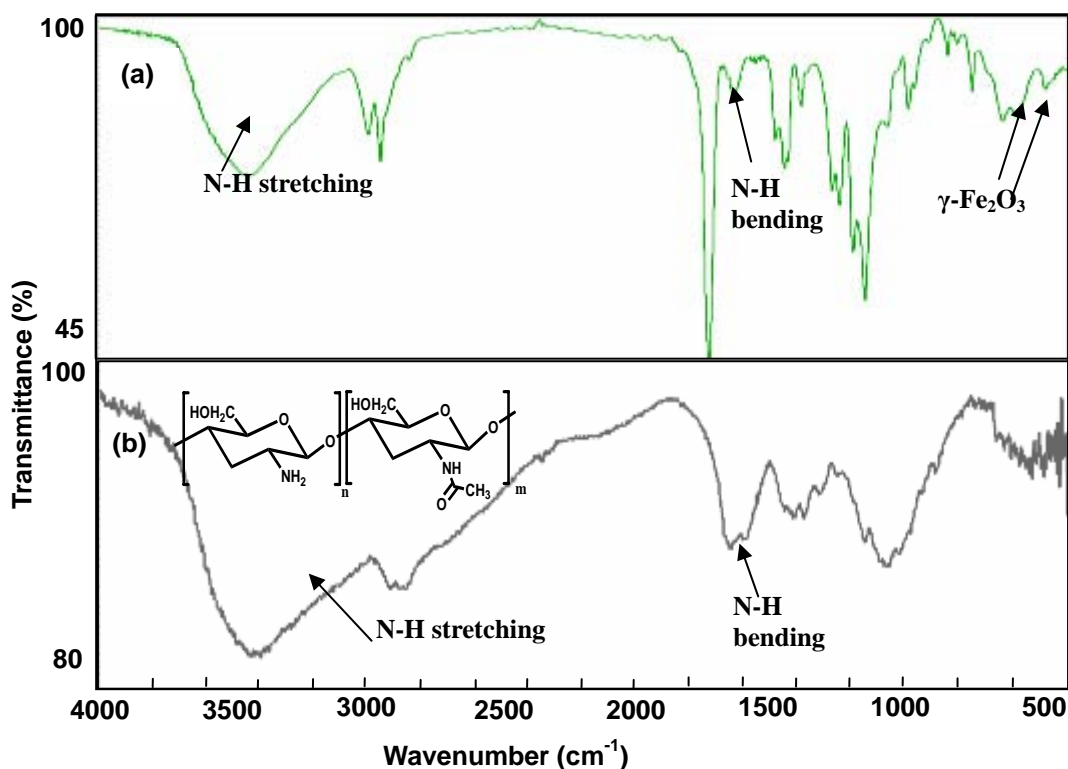


Figure 5.51. FT-IR spectra of (a) isolated chitosan-*grafted* copolymer composites using a 1 v/v% of acetic acid solution extraction and (b) isolated chitosan in a 1 v/v% acetic acid.

The composition of $\gamma\text{-Fe}_2\text{O}_3$ nanoparticles in MCS particles was determined with thermogravimetry analyses (TGA). Figure 5.52 shows the TGA thermogram of PMMA/chitosan core-shell particles, which has a complete weight loss at above $500\text{ }^\circ\text{C}$. For MCS particles, the thermogram shows that there is 81 % weight loss from 380 to $500\text{ }^\circ\text{C}$, which is due to the loss of polymers. However,

there is 7 % weight remained at 900 °C, which is probably attributed to the presence of γ -Fe₂O₃ nanoparticles, since the nanoparticles have a high thermal stability below 1000 °C.

Based on the monomer conversion, the Soxhlet extraction of un-grafted chitosan and the thermogravimetry analysis (TGA) of encapsulated γ -Fe₂O₃, the compositions of the MCS particles were determined, and the detailed calculation was illustrated in Appendix, B-2. The MCS particles contained 78 w/w% of PMMA cores, 15 w/w% of chitosan, and 7 w/w% of γ -Fe₂O₃, respectively.

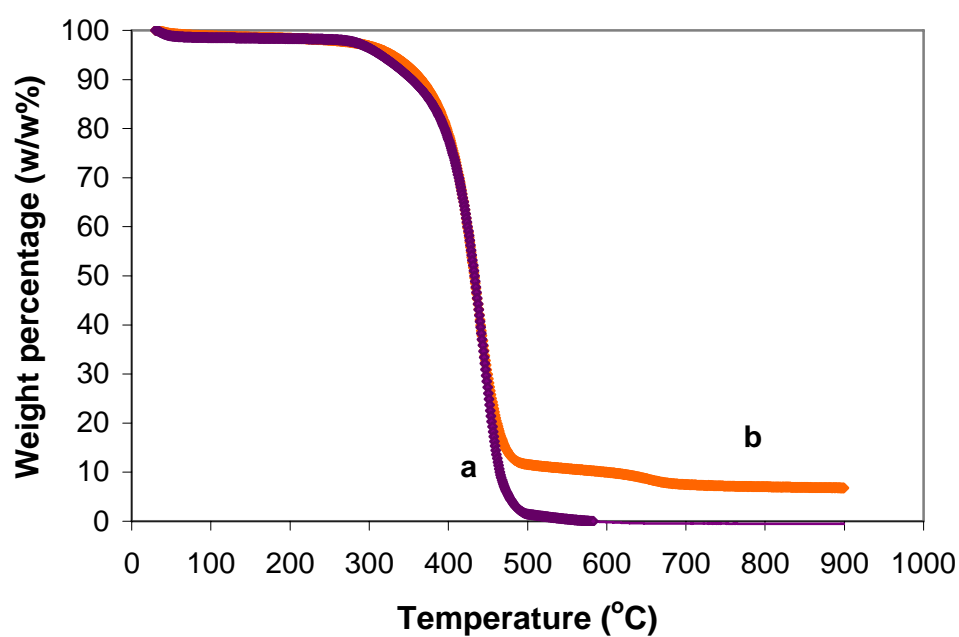


Figure 5.52. TGA thermograms of a) PMMA/chitosan core-shell particles without magnetic nanoparticles, and b) MCS particles (containing 7 w/w% of γ -Fe₂O₃).

Particle size and size distribution of MCS particles

Particle size and size distribution of MCS particles were determined with the Coulter LS 230 Particle Size Analyzer. Figure 5.53 illustrates that MCS particles produced (CTS : MMA : MPS-Fe₂O₃ = 2.5 : 6 : 1; H₂O₂ = 0.1 mM) under standard conditions at pH 4.12 had an average volume diameter (D_v) of 194 nm, and an average number diameter (D_n) of 172 nm. The polydispersity index (D_v/D_n) was 1.13, indicating a narrow size distribution of the MCS particles.

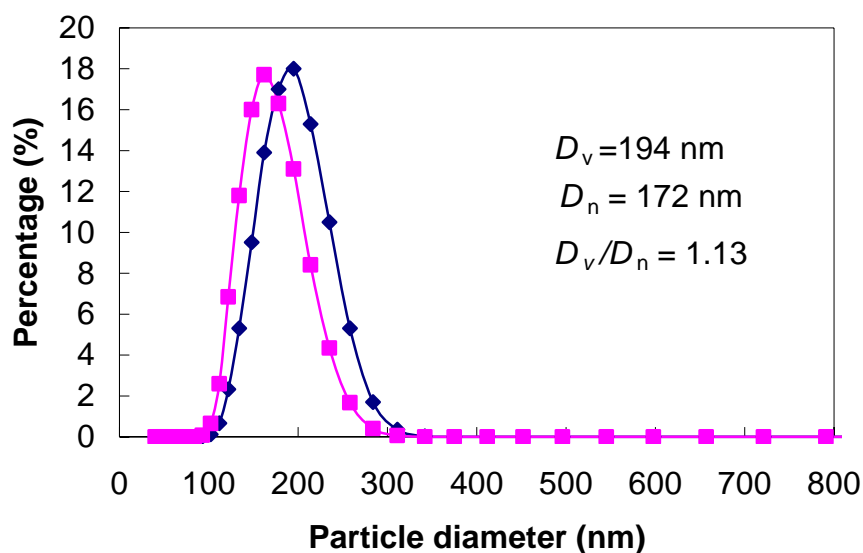


Figure 5.53. Particle size and size distribution of MCS particles measured by Coulter LS 230 Particle Size Analyzer. (◆) D_v and (■) D_n .

Morphologies of MCS particles

Morphologies of the MCS particles were examined with both Field emission scanning electron microscopy (FE-SEM) and TEM. Figure 5.54 shows the FE-SEM images of the MCS particles produced. The FE-SEM images clearly reveal that the MCS particles have a quite uniform size. However, some of them are not spherical. Furthermore, the particles tended to form aggregates, which might be attributed to the strong magnetic dipole-dipole interactions exerted between the particles during drying. Figure 5.45 shows the TEM images of the MCS particles, in which the chitosan shells were purposely stained with phosphotungstic acid (PTA, $\text{WO}_3 \cdot \text{H}_3\text{PO}_4 \cdot x\text{H}_2\text{O}$) solution for 2 min. The TEM images clearly reveal the core-shell nanostructures, where the PMMA core containing magnetic nanoparticles are coated with chitosan shell (Figure 5.55).

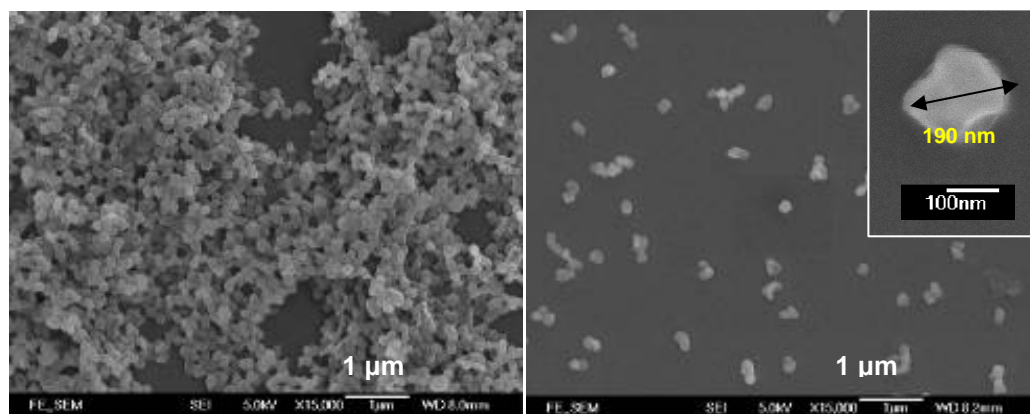


Figure 5.54. SEM images of MCS particles (CTS : MMA : MPS- Fe_2O_3 = 2.5 : 6 : 1; H_2O_2 = 0.1 mM).

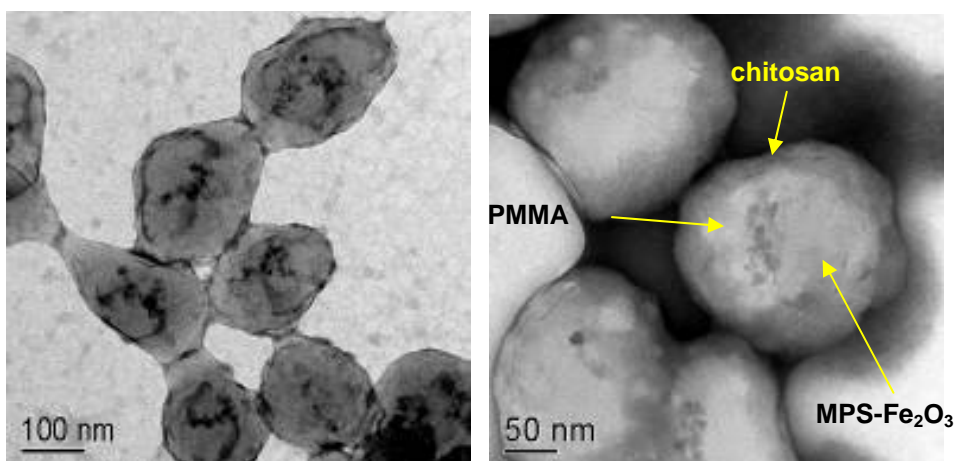


Figure 5.55 TEM images of MCS particles (CTS : MMA : MPS-Fe₂O₃ = 2.5 : 6 : 1; H₂O₂ = 0.1 mM) stained with a 0.5 w/w% of phosphotungstic acid for 2 min on either Formvar or carbon-coated grids.

Characterization of MCS particle surface

The presence of chitosan shells was verified by ζ -potential analyses. Figure 5.56 shows that the positive ζ -potential of MCS particles decreases from + 50 to 0 mV as the pH increases from pH 3.0 to 8.0. This effect is probably due to the de-protonation of quaternary ammonium ions of chitosan. When compared with PMMA/chitosan core-shell particles without magnetic nanoparticles, the ζ -potential values of the MCS particles at various pHs are lower, which may be attributed to the complexation and encapsulation of the negatively charged MPS-Fe₂O₃ nanoparticles.

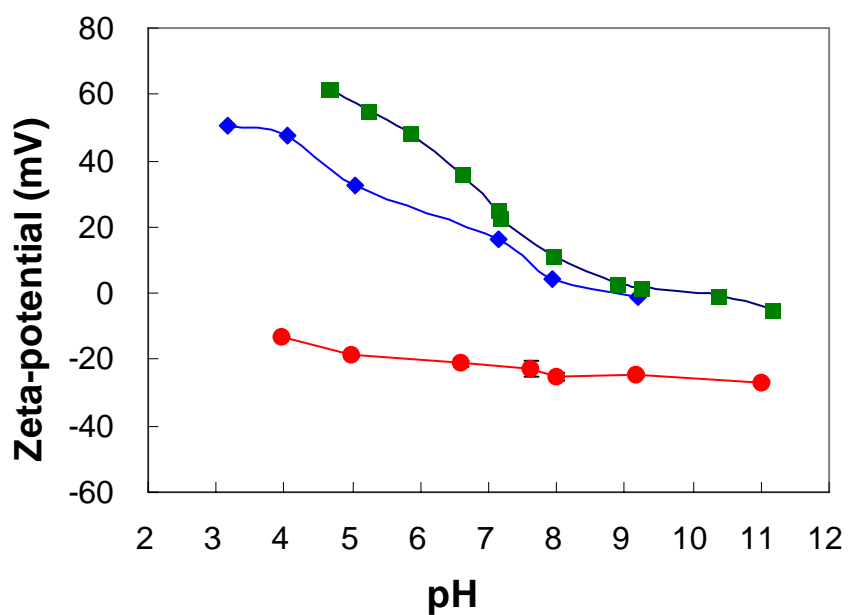
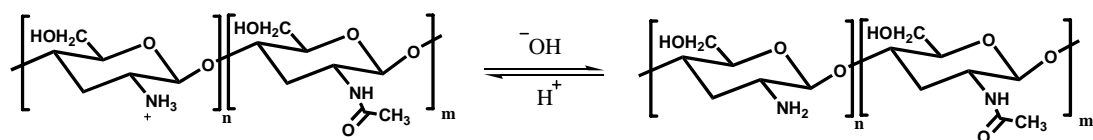


Figure 5.56. pH dependence of the ζ -potential measured in a 1 mM NaCl solution at 25 °C. (■) PMMA/chitosan particles; (◆) MCS particles produced using H₂O₂ as an initiator; (●) MPS-Fe₂O₃ nanoparticles.

Colloidal stability and critical coagulation concentration (CCC) of MCS particles

The stability of MCS particles at different pHs was studied with a dynamic light scattering (Malvern Zetasizer 3000 HS). Figure 5.57 shows the hydrodynamic diameter ($\langle D_h \rangle$) of MCS particles as a function of pH in tris(hydroxymethyl)aminomethane hydrochloride (Tris-HCl) as a buffer solution. Increasing the pH of the MCS particle dispersion from 4.0 to 6.5 had little influence on the hydrodynamic diameter ($\langle D_h \rangle$) of the particles (430–500 nm). However, a further increase of the pH from 6.5 to 7.5 significantly increased their sizes from 500 to 1952 nm in diameter. This effect was probably attributed to the coagulation of MCS particles because they had low surface charge densities (+ 20 to + 5 mV) between pH 6.5 and 7.5 (Figure 5.56). This result suggests that the MCS particles are colloidal stable below pH 6.5.

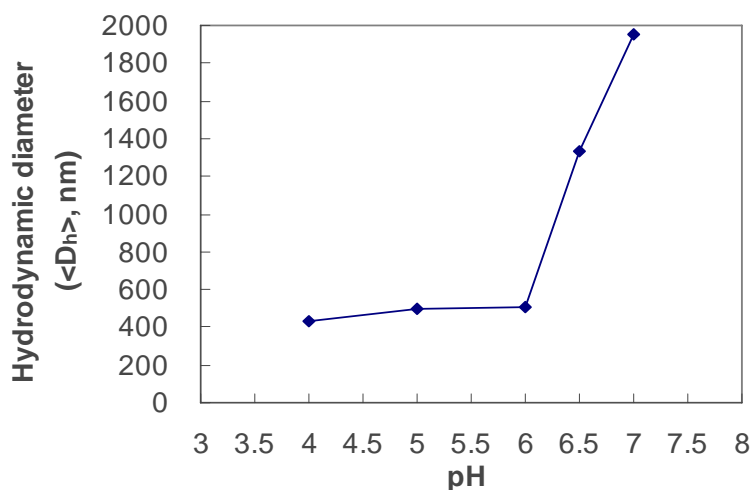


Figure 5.57. Effect of pH on the (\blacklozenge) $\langle D_h \rangle$ of MCS particles (CTS : MMA : MPS-Fe₂O₃ = 2.5 : 6 : 1; H₂O₂ = 0.1 mM) at 25 °C using a 1 mM of tris(hydroxymethyl)aminomethane hydrochloride (Tris-HCl) as a buffer solution.

The stability of MCS particles in electrolyte solution was studied based on the changes of hydrodynamic diameters as a function of NaCl concentration. Figure 5.58 shows that increasing NaCl concentration from 0 to 0.7 M had little influence on the hydrodynamic diameter ($\langle D_h \rangle$) of the particles (433–462 nm). However, a further increase of the concentration from 0.7 to 1.0 M resulted in significant increases in their sizes from 462 to 3354 nm in diameter. Formation of larger particles is probably caused by the suppression of electrical charges of the chitosan, when NaCl concentration increases. Suppression of the electrical charges was confirmed by ζ -potential analyses (Figure 5.59). These analyses clearly revealed that the surface charges of MCS particles significantly decreased with increasing the NaCl concentration.

The colloidal stability of MCS particles against various electrolyte concentrations was further examined by determining the critical coagulation concentration (CCC) value of MCS particles. This value was determined based on the measurement of turbidity (A/A_0) changes as a function of various NaCl concentrations by extrapolating the sharply decreasing part of the turbidity curve, as shown in Figure 5.58. The determined CCC value of MCS particle dispersion at pH 6.0 was 0.8 M. This value shows a good agreement with the result obtained from dynamic light scattering measurement. Such CCC value is significantly higher than the PMMA particles (CCC = 50–60 mM NaCl at pH 7) produced by emulsifier-free emulsion polymerization of MMA initiated with 2,2'-azobis(2-amidinopropane) dihydrochloride (V-50) as reported in the literature.¹³⁸ In other words, the MCS particles can withstand high electrolyte concentration up to 0.8 M without serious coagulation. Compared with the CCC value of chitosan-modified PMMA particles (172–177 mM at pH 3.0) having only

0.08 to 1.7 w/w of chitosan on the shell reported by Chern *et al.*,¹³⁸ our particles with 15 w/w% chitosan on the shell show higher stability in NaCl solution. Thus, the thicker shell of MCS particles contributes to a higher stability in electrolyte solution. This superior stability of MCS particles is an advantage for their applications in various biological systems.

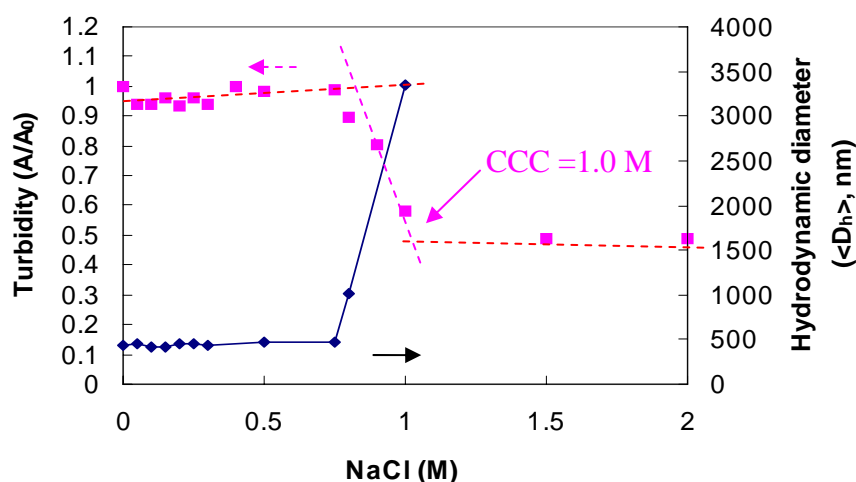


Figure 5.58. Effect of NaCl on the (■) turbidity and (◆) hydrodynamic diameter (<D_h>) of MCS particles (CTS : MMA : MPS-Fe₂O₃ = 2.5 : 6 : 1; H₂O₂ = 0.1 mM) dispersed in pH 6.0 solution.

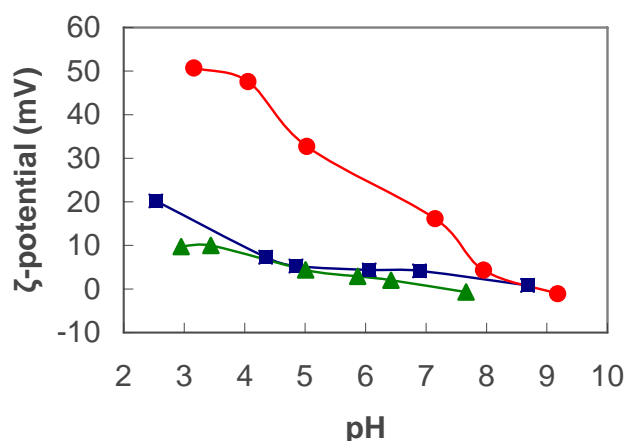


Figure 5.59. pH dependence of the ζ -potential of MCS particles (CTS : MMA : MPS-Fe₂O₃ = 2.5 : 6 : 1; H₂O₂ = 0.1 mM) measured at different NaCl solutions: (●) 1 mM; (■) 0.5 M; (▲) 1.0 M.

Magnetization measurement of MCS particles

Magnetization measurement of the MCS particles containing 5, 7 and 16 w/w% of $\gamma\text{-Fe}_2\text{O}_3$ encapsulation content was conducted by applying external magnetic fields from 0 to 5 KOe. Results shown in Figure 5.60 indicate that all three MCS particles exhibited superparamagnetic properties at room temperature, indicating the absence of hysteresis loop in all cases. Figure 5.60 also shows that the saturation magnetizations of MCS particles strongly depends on the amounts of $\gamma\text{-Fe}_2\text{O}_3$ encapsulated in MCS particles. In general, the higher the $\gamma\text{-Fe}_2\text{O}_3$ content encapsulated in the MCS particles, the higher saturation magnetization reached.

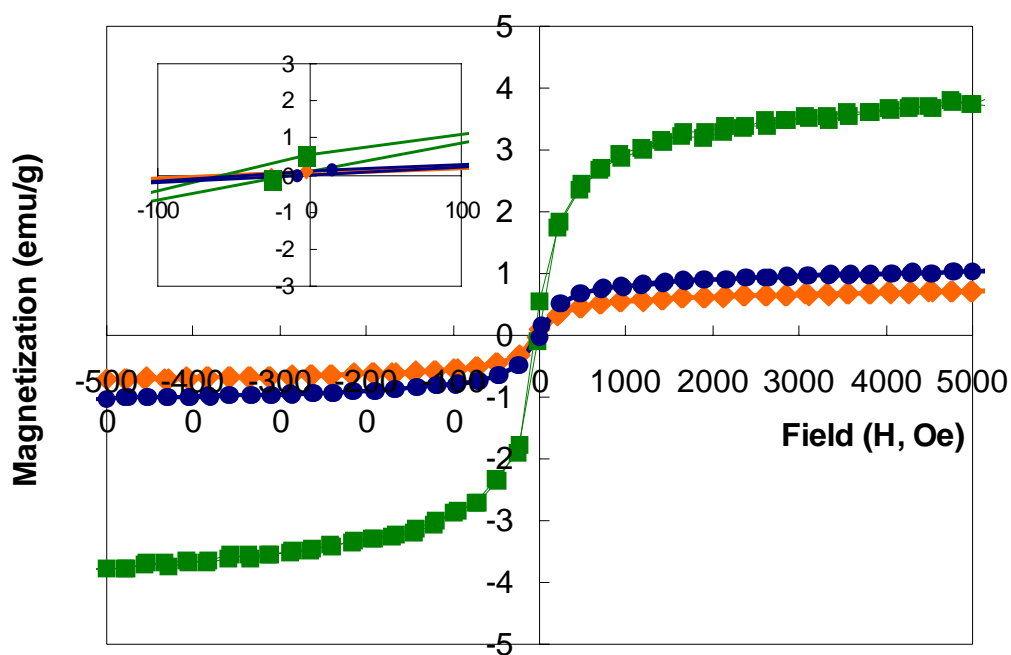


Figure 5.60. Room temperature magnetization measurement of MCS particles containing different weight percentage of $\gamma\text{-Fe}_2\text{O}_3$: (\blacklozenge) 5 w/w% (0.7 emu/g); (\bullet) 7 w/w% (1.1 emu/g); (\blacksquare) 16 w/w% (3.9 emu/g).

5.4 Conclusions

Magnetic core-shell (MCS) particles with narrow size distribution have been successfully synthesized using a H_2O_2 initiation system. Key findings of this synthetic system using TBHP as an initiator are summarized as follows:

- 1) Encapsulation of iron oxide nanoparticles into the hydrophobic polymer cores has been achieved using MPS-coated iron oxide nanoparticles.
- 2) The optimal reaction temperature was $80\text{ }^\circ\text{C}$ for high conversion and good particle formation
- 3) The optimal weight ratio of chitosan to MMA to MPS- Fe_2O_3 nanoparticles was 2.5 : 4 : 1, and the solid contents were around 3 %. The highest encapsulating percentage of $\gamma\text{-Fe}_2\text{O}_3$ in MCS particles was 16 w/w%.
- 4) H_2O_2 concentration should be less than 0.2 mM to completely encapsulate magnetic nanoparticles in the polymer cores.
- 5) The most suitable MPS- Fe_2O_3 content was 0.4 w/w%.
- 6) Magnetic/PBA-PMMA/chitosan core-shell particles and magnetic/PNIPAM/chitosan microgels have been successfully synthesized.
- 7) The MCS particles had average diameters ranging from 140 to 200 nm with PMMA core containing iron oxide nanoparticles coated with chitosan shell. The surface charge density was around + 25 mV at pH 6.0. The CCC value at pH 6.0 was 0.8 M.
- 8) The highest saturation magnetization of MCS particles was 3.9 emu/g.
- 9) H_2O_2 is able to form redox pair with the amino groups of chitosan, as the TBHP/amine (chitosan) initiation system.

10) H_2O_2 -initiated graft copolymerization has very similar reactivity to TBHP-initiated system, as the mechanistic rationalizations of MCS particle synthesis described in Scheme 5.4.

Chapter 6

Multi-functional core-shell nanocomposites as a water-based coating for electromagnetic interference (EMI) shielding applications

This chapter illustrates how magnetic core-shell (MCS) particles can be used to form nanocomposites with single-walled carbon nanotubes (SWNTs) for electromagnetic interference (EMI) shielding application. Formation of this nanocomposite was achieved via the simple mixing of the MCS particles prepared previously, with carboxylic acid functionalized single-walled carbon nanotubes (SWNTs) to form MCS particles-SWNTs nanocomposites.

Optimal loading ratio of the SWNTs and MCS particles to form stable complexes in aqueous has been determined. Properties of the nanocomposites including their structural morphology, surface topology, cross-sectional morphology and magnetic-responsiveness were investigated with transmission electron microscopy (TEM), atomic force microscopy (AFM), field-emission scanning electron microscopy (FE-SEM), and vibrating sample magnetometer (VSM), respectively.

6.1 Introduction

Electromagnetic interference (EMI) is a well-known problem in electronic circuits. Electromagnetic radiation, particularly at high frequencies, not only interferes with electronics, but may also pose potential hazards to human beings.⁴⁵ Thus, there is a growing demand for the development of versatile and effective EMI shielding materials. The following sub-sections will introduce some of the currently used EMI shielding materials, especially those carbon nanotubes containing polymer nanocomposites. Their fabrication and drawbacks in EMI shielding applications will also be discussed.

6.1.1 Mechanisms of EMI shielding

This Section introduces the fundamental concepts of EMI shielding mechanisms. These concepts will help us in understanding of property requirements of EMI shielding materials. Shielding of electromagnetic radiation can be achieved via three mechanisms, including reflection, absorption and multiple reflections as shown in Figure 6.1. When materials have *mobile electrons*, they shield the radiation by reflection. Therefore, metals shield electromagnetic fields mainly by reflection,

due to their abundant mobile electrons. EMI shielding due to reflection loss (R) is expressed by the following equation:

$$R = \sigma_r / \mu_r \quad (6.1)$$

where σ_r is the electrical conductivity relative to copper, μ_r is the relative magnetic permeability and the unit for the loss is in dB.

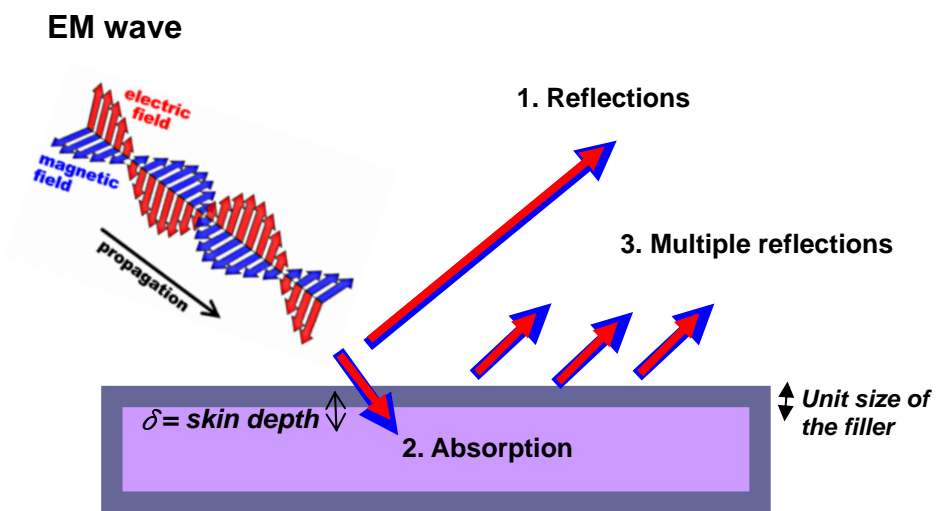


Figure 6.1. Illustration of the mechanisms of EMI shielding.

The second mechanism for EMI shielding is based on the absorption of electromagnetic fields. When materials have both *electric and/or magnetic dipoles*, they shield electromagnetic fields by absorption. The electric dipoles may be provided by BaTiO₃ or other materials having a high value of dielectric constant (e.g. silver, gold and copper), while the magnetic dipoles may be provided by Fe₃O₄ or other

materials having a high value of magnetic permeability (e.g. superpermalloy and mumetal, Ni-Fe-Cu-Mo alloy). EMI shielding due to absorption loss (A) is expressed by the following equation:

$$A = \sigma_r \mu_r \quad (6.2)$$

The absorption loss increases with increasing electric conductivity and magnetic permeability. Furthermore, the loss is dependent on the thickness of the shielding materials.

Besides reflection and absorption, multiple reflections is the third mechanism for EMI shielding. This mechanism requires a shielding material with a large surface area or interface area in the shielding materials,⁴⁵ which means that the loss due to multiple reflections can be achieved when the unit size of a filler is comparable or less than the skin depth (Figure 6.1). The skin depth is defined as the distance (δ) through which the amplitude of a traveling plane wave decreases by a factor of $1/e$,⁴⁵ which is given by:

$$\delta = \frac{1}{\sqrt{\pi f \mu \sigma}} \quad (6.3)$$

where f is the frequency of electromagnetic radiation; μ is magnetic permeability

$(\mu_0\mu_r)$; μ_0 is the $4\pi \times 10^{-7}$ H/m; μ_r is the relative magnetic permeability, and σ is electrical conductivity ($\Omega^{-1}\text{m}^{-1}$). Hence, the skin depth decreases with increasing frequency, with increasing magnetic permeability and with the conductivity. For copper, $\mu_r = 1$ and $\sigma = 5.8 \times 10^7 \Omega^{-1}\text{m}^{-1}$, so δ is $2.09 \mu\text{m}$ at 1 GHz. For nickel, $\mu_r = 100$ and $\sigma = 1.15 \times 10^7 \Omega^{-1}\text{m}^{-1}$, so δ is $0.47 \mu\text{m}$ at 1 GHz. Therefore, if a filler has a unit size equal or less than $0.3 \mu\text{m}$, the loss due to multiple reflections would be achieved.

The losses, whether due to reflection, absorption, or multiple reflections, are commonly expressed in dB. The sum of all the losses is the shielding effectiveness (dB). The EMI shielding effectiveness (SE) of a material is defined as $\text{SE (dB)} = -10 \log(P_t/P_0)$, where P_t and P_0 are the transmitted and incident electromagnetic power, respectively. For example, an attenuation of the incident beam by a factor of 100 (1% transmission) is equivalent to 20 decibels (dB) of attenuation. In summary, the EMI shielding efficiency of a composite material depends on several factors, including (1) the intrinsic conductivity of the filler; (2) dielectric constant; (3) magnetic permeability; (4) filler size; (5) aspect ratio; and (6) skin depth.

6.1.2 Types of EMI shielding materials

An effective EMI shielding material generally consists of both electric and magnetic components that can interfere with electric and magnetic parts from electromagnetic radiations. Metals are one of the most effective EMI shielding materials because of their high conductivity and magnetic permeability. Thus, metal coatings made by electroplating or vacuum deposition are commonly used for the shielding applications.⁴⁵ However, such coatings have poor scratch and corrosion resistances (Appendix, Table A-2). To reduce this problem, metal particles mixed with a cement matrix are used. Since cement is a semi-conducting material, it provides a better conducting network for metal particles. Therefore, the cement-metal composites usually give a high EMI shielding effectiveness even with low metal contents. However, these composites are usually bulky and heavy. In addition to this, metal corrosion in the composites is still a serious concern.

Recently, the inclusion of conductive fillers such as metal, conducting polymers and carbon nanostructured materials in insulating polymer matrices has attracted great interest, because these composite materials possess desirable properties such as light weight, flexible, and good processing applicability.¹⁵⁰ Examples of these materials are

illustrated in Appendix, Table A-2. Their applications are very diverse, including antenna systems, lightning-protected aircraft composite panels, avionics line replaceable unit (LRU) enclosures, connector gaskets, electrostatic and space charge dissipation materials, and different types of electronic pressure sensitive switches or sensors.¹⁵⁰⁻¹⁵³ Such types of conductive polymer composites have been prepared via physical blending of conductive fillers with insulating polymers. Generally, a higher filler loading in a polymer matrix gives a higher electrical conductivity, resulting in a higher EMI shielding effectiveness. However, too much filler is not desirable because of its high cost. It may also affect the physical properties of the resulting composites, such as their mechanical strength, moldability, and optical transparency.¹⁵⁴ Thus, a continuous development of advanced materials which can attain a high shielding effectiveness at a low filler loading is highly desirable.

6.1.3 Carbon nanotube/polymer composites for EMI shielding applications

Carbon nanotubes, including single-walled and multi-walled carbon nanotubes (SWNTs and MWNTs) have emerged as attractive materials for EMI shielding applications because of their low mass density, high aspect ratio (i.e. length-to-diameter ratio, typically 300–1000), high electrical conductivity and

mechanical strength.^{155,156} A high aspect ratio is one of the important features of carbon nanotubes. According to the electromagnetic wave percolation theory, if the conductive filler in the polymer matrix possesses a high aspect ratio, as illustrated in Figure 6.2, it can easily form a conductive network (i.e. percolation network) as compared to the spherical fillers. Thus, the critical concentration (i.e. percolation threshold) of the conductive filler needed to achieve the EMI shielding effect is low.¹⁵⁰ It is known that carbon nanotubes can achieve a significant EMI shielding effect at a very low nanotube concentration in a polymer matrix. The low nanotube concentration has several advantages such as smaller perturbations of bulk physical properties (e.g. optical transparency and moldability) and low cost.¹⁵⁴

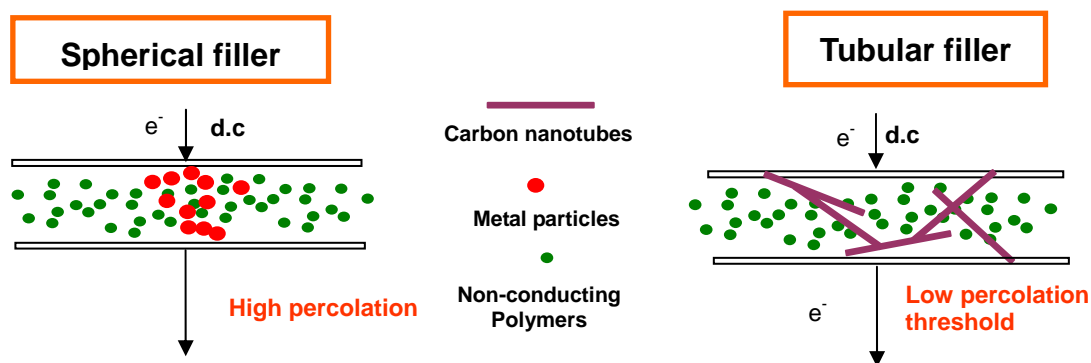


Figure 6.2. Illustration of influence of filler shape on percolation threshold.

Carbon nanotube/polymer composites have been prepared via different approaches such as melt blending, *in situ* polymerization and solution-casting.¹⁵⁵

Some examples are illustrated in Table 6.1. Among these methods, solution-casting is the simplest and most widely adopted approach because it only involves dispersing functionalized carbon nanotubes in an appropriate solvent, followed by mixing with polymer solutions, and subsequent casting of the resulting composites into a continuous film. Various composites such as MWNTs/polyhydroxyaminoether (PHAE),¹⁶⁰ carbon nanotubes/poly(vinyl alcohol) (PVA),¹⁶¹ MWNTs/polystyrene (PS),¹⁶² SWNTs/epoxy,¹⁵⁶ and MWNTs/poly(*m*-phenylenevinylene-*co*-2,5-dioctyloxy-*p*-phenylenevinylene)(PmPV)¹⁶³ have been prepared using this approach.

6.1.4 Limitations of current technologies

The solution-casting method has two major drawbacks: (1) It usually requires the use of a large amount of toxic solvent such as chloroform (CHCl₃), tetrahydrofuran (THF) and *N,N*-dimethyl formamide (DMF) in order to solubilize the polymer for incorporation of carbon nanotubes. (2) Carbon nanotubes tend to saturate at 1 to 2 w/w% nanotube contents in a polymer matrix, and then form large aggregates in the composites due to their hydrophobic sidewalls.¹⁵⁴ As a result, the EMI effectiveness of the carbon nanotubes-containing composite film is usually limited to below 30 dB,

even at a high MWNTs percentage (40 w/w%), as reported by Kim *et al.*¹⁵⁷ (Table 6.1).

Although various stabilization methods have been used to reduce the aggregation of the nanotubes in order to enhance the EMI effectiveness, there are still some major problems. For example, electrostatic stabilization of carbon nanotubes via covalent functionalization introduces defective sites to carbon nanotubes, thus deteriorating their intrinsic electrical conductivity. On the other hand, steric stabilization using polymer wrapping or surfactant molecules hinders the nanotubes from forming a conductive network, thus affecting the properties of the resulting nanocomposites.^{154,155} Besides the poor dispersing ability of carbon nanotubes in a polymer solution, the EMI shielding performance of carbon nanotube/polymer composites is also frequency-dependent, because the skin depth of multiple reflections in conducting polymer composites decreases with increasing frequency.⁴⁵ This means that carbon nanotube-based polymer composites have a limited EMI shielding effectiveness at high frequency. One approach to overcome this problem is to incorporate magnetic components such as iron (Fe) into carbon nanotube/polymer composites, as attempted by Kim *et al.*¹⁵⁷

Table 6.1. Current approaches to prepare carbon nanotube/polymer composites for EMI shielding applications.

CNTs (%)	Polymer matrix	Preparation methods	Frequency range	Shielding effectiveness (dB) ^a	References
SWNT (23 w/w%)	Poly(ethyl methacrylate)	<i>Melt blending method^b</i>	500 MHz–5.50 GHz	N/A	Grimes <i>et al.</i> (2000) ¹⁶⁴
SWNT (8.5 w/w%)	Polystyrene (PS)	<i>In situ polymerization^c</i> (e.g. <i>Miniemulsion approach</i>)	1x10 ⁻¹ –1x10 ⁶ Hz	N/A	Resasco <i>et al.</i> (2002) ¹⁶⁵
MWNTs (40 w/w%)	Poly(methyl methacrylate), PMMA	<i>Solution-casting method^d</i>	50 MHz–13.5 GHz	27	Kim <i>et al.</i> (2004) ¹⁶⁶
MWNTs (7 w/w%)	Polystyrene (PS) foam	<i>Solution casting method^d</i>	8.2–12.4 GHz (X-band)	20	Yang <i>et al.</i> (2005) ¹⁵⁰
SWNT (15 w/w%)	Epoxy	<i>Solution-casting method^d</i>	10 MHz 500 MHz–1.5 GHz	49 20	Li <i>et al.</i> (2006) ¹⁵⁶

^aThe EMI shielding effectiveness (SE) of a material is defined as $SE \text{ (dB)} = -10 \log(P_t/P_0)$, where P_t and P_0 are the transmitted and incident electromagnetic power. N/A means that no EMI data was reported.

SWNTs (single-walled carbon nanotubes); MWNTs (multi-walled carbon nanotubes).

^bMelt blending uses high temperature and high shear forces to disperse carbon nanotubes in a polymer matrix.¹⁵⁵

^c*In situ* polymerization involves the dispersion of functionalized-carbon nanotubes (*f*-CNTs) in monomer droplets stabilized by surfactants, followed by polymerizing the monomers.

^dSolution-casting method involves dispersing *f*-CNTs in an appropriate solvent, followed by mixing with a polymer solution, and subsequent casting the resulting composites into a continuous film.

6.1.5 Design rationale of novel EMI shielding coating materials

To address these limitations, we have designed a novel multi-functional core-shell nanocomposite as a water-based coating for EMI shielding applications (Figure 6.3). The multi-functional core-shell nanocomposite consists of a well-defined core-shell nanostructure with three different components: 1) the γ -Fe₂O₃ nanoparticles are able to provide a magnetic dipole to *absorb* electromagnetic fields at *high frequencies*. 2) The PMMA core acts as a barrier to prevent γ -Fe₂O₃ nanoparticles from leakage. It may also be able to protect those air-sensitive magnetic nanoparticles such as Cobalt (Co) nanoparticles from oxidation. Furthermore, the core is able to provide a good film-forming ability. 3) The chitosan shell provides amine-functional group to complex with carboxylated SWNTs, reducing the formation of large SWNTs bundles. The adsorbed SWNTs on the chitosan shell could provide an electric dipole to *reflect* electromagnetic fields at *low frequencies*. The chitosan shell is also able to offer an anti-bacterial property for the coating.

In this chapter, we present the synthesis of the nanocomposites, which have been prepared through a two-step synthesis: (1) preparation of MCS particles via graft copolymerization of either methyl methacrylate (MMA) or a mixture of MMA and

n-butyl acrylate (*n*-BA) in the presence of vinyl-coated magnetic nanoparticles from chitosan, based on the method described in Chapter 5; and (2) mixing of the MCS particles with acid-treated single-walled carbon nanotubes (SWNTs) to form stable nanocomposite dispersion in water. Details of the synthesis and properties of these nanocomposites are discussed as follows.

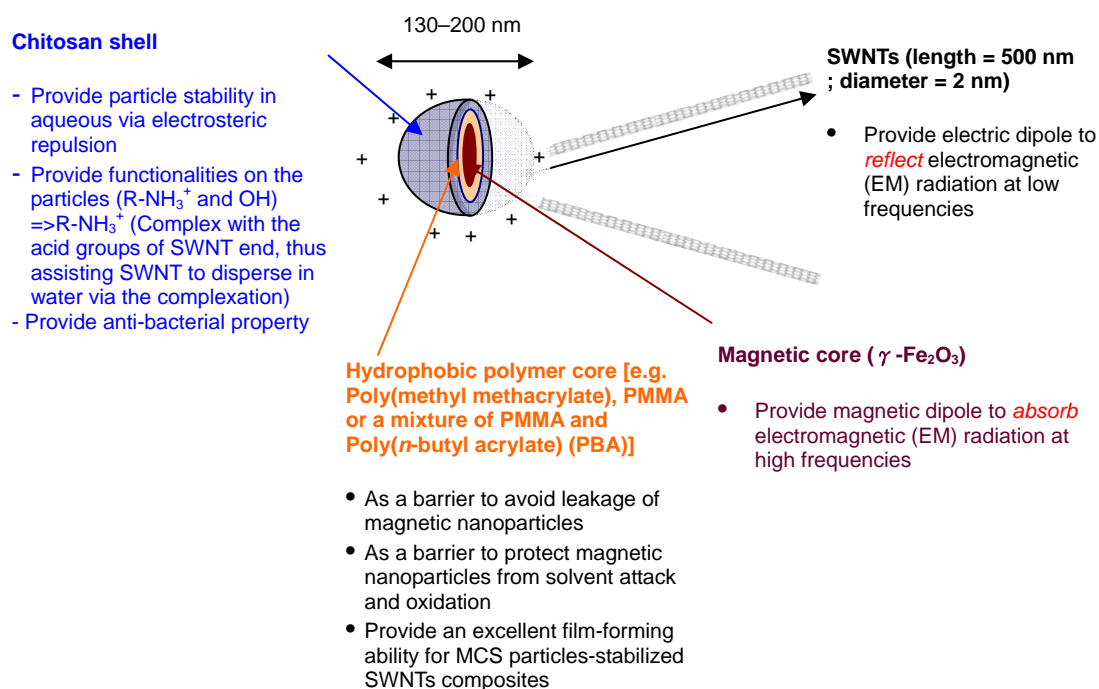


Figure 6.3. Design rationale of MCS particles-SWNTs nanocomposites.

6.1.6 Desirable properties of MCS particles-SWNTs nanocomposites

Desirable properties of the MCS particles-SWNTs nanocomposites include:

1. High colloidal stability
2. Good film-forming ability

3. Well-defined nanostructure
4. High magnetic permeability
5. Broad spectrum of electromagnetic interference shielding effectiveness

6.2 Experimental

6.2.1 Materials

MPS-Fe₂O₃ nanoparticles were synthesized as described in Section 4.3. Chitosan (medium, Aldrich) was purified by dissolving it in a dilute acetic acid solution at 60 °C, followed by precipitating in a 10 v/v% of sodium hydroxide solution under stirring at room temperature. The chitosan was then filtered off and washed with distilled water to neutral, and finally dried in a vacuum oven at 60 °C for 24 h. Molecular-weight measurement using solution viscosity indicated that the M_v of chitosan was approximately 80,000 (Appendix, A-1). The degree of deacetylation of chitosan, as estimated by ¹H-NMR spectroscopy using the method reported by Hirai *et al.*,¹²⁶ was 74 % (Appendix, A-2). The phenolic inhibitor in methyl methacrylate (MMA, $\rho = 0.936 \text{ gcm}^{-3}$, Aldrich) was removed by washing three times with a 10 % of sodium hydroxide solution and then with deionized water until the pH of the water layer dropped to 7. The monomer was further purified by a vacuum distillation. Hydrogen peroxide (H₂O₂) (35 % solution in water) was obtained from Aldrich Chemical Co., and used without further purification. Freshly deionized and distilled water was used as the dispersion medium. As-prepared single-walled carbon

nanotubes (*AP*-SWNTs) were obtained from the Center for Nanoscale Science and Technology in Nankai University (China).

6.2.2 Experimental procedures

6.2.2.1 Synthesis of magnetic core-shell (MCS) particles

The MCS particles were synthesized based on the method described in Chapter 5. A typical procedure is as follows: For a total solution of 25 mL, MPS-Fe₂O₃ nanoparticles (0.1 g, 10 w/w% in ethanol) and ethanol were mixed using a homogenizer (Sonics VC130PB, output watt = 6 W) with a chitosan solution (0.25 g, 22.5 mL) containing a 0.6 v/v% of acetic acid, giving the final volume ratio of H₂O to ethanol of 12.5 to 1. The viscous dispersion was homogenized for 10 min, and then transferred into a water-jacketed flask equipped with a thermometer, a condenser, a magnetic stirrer, and a nitrogen inlet. The dispersion was purged with nitrogen for 20 min, and stirred at 80 °C prior to the addition of MMA. H₂O₂ (0.25 mL, 10 mM) was then added to the mixture. The resulting mixture was continuously stirred at 80 °C for 2 h under nitrogen.

After the reaction, the obtained particle dispersion was filtered to separate any precipitates (ppt.) generated (if any) during the polymerization. The ppt. filtered were

dried and weighed, and the percentage of ppt. (ppt.%) obtained was calculated using the following equation:

$$\text{ppt. (\%)} = \frac{\text{weight of ppt. obtained after the polymerization}}{\text{total weight of reactants initially added}} \times 100 \% \quad (5.1)$$

Monomer conversion (Conv.%) was determined gravimetrically, according to following procedure: 2 mL of filtered dispersion was withdrawn from the reaction mixture and dried overnight at 80 °C. It was further dried in a vacuum oven (25 inch Hg) at 80 °C for 24 hours. Assuming that the un-reacted MMA monomer and other small molecules such as *t*-BuOH were removed during the vacuum dry process, the dried solids only contained the un-reacted chitosan, PMMA/chitosan core-shell particles, un-reacted MPS-Fe₂O₃ nanoparticles, magnetic PMMA/chitosan core-shell particles. Thus, the total weight of solids (W_t) was determined according to following formula:

$$W_t = \left(\left(\frac{W_{disp}}{2} \right) (V_{disp}) + W_{ppt} \right) \quad (5.2)$$

where W_{disp} is the weight of the 2 mL filtered dispersion obtained, V_{disp} is the total volume of filtered dispersion obtained, W_{ppt} is the weight of precipitate obtained from Equation 5.1. Based on the W_t , monomer conversion was determined according to

following formula:

$$\text{Conv. \%} = \left(\frac{W_t - W_{WSP} - W_{MNP}}{W_{MMA}} \right) \times 100\% \quad (5.3)$$

where W_{WSP} is the weight of chitosan initially added, W_{MNP} is the weight of magnetic nanoparticles initially added and W_{MMA} is the weight of MMA initially added. The obtained particles were then purified by repeated centrifugation (13000 rpm, 1 h), decantation and re-dispersion until the conductivity of the supernatant was close to that of distilled water.

6.2.2.2 Purification of single-walled carbon nanotubes (SWNTs)

As-prepared single-walled carbon nanotubes (*AP*-SWNTs, 0.5 g) were mixed with a 3 M of nitric acid solution (HNO_3 , 250 mL). The resulting black mixture was heated to reflux temperature and maintained at that temperature for 16 h. The resulting black dispersion was then cooled to room temperature. The acid-treated SWNTs were purified by repeated centrifugation (10,000 to 18,000 rpm, 1 h), re-dispersion and decantation until the pH of the supernatant was around 4.0.

6.2.2.3 Preparation of MCS particles-SWNTs nanocomposites

Table 6.2 summaries the recipes and conditions used for the preparation of

various weight ratios of MCS particles-SWNTs nanocomposites. An example of the MCS particles(90)-SWNTs(10) nanocomposite at pH 4 is shown as follows. The pH of MCS particles and acid-treated SWNTs dispersion were first adjusted to around 4, respectively. A different amount of acid-treated SWNTs dispersion (1.20 w/w%) was slowly added into a different amount of MCS particle dispersion (2.5 w/w%) under homogenization (Sonics VC130PB, output watt = 2 W). The resulting MCS particles-SWNTs dispersions were then agitated under sonication for 10 min.

Table 6.2. Recipes and conditions used for the preparation of various weight ratios of MCS particles-SWNTs nanocomposites^a

MCS particles:SWNTs (w/w)	MCS particles (g)	SWNT (g)	MCS particles (mL) ^b	SWNTs (mL) ^c	H ₂ O (mL)
99:1	0.1188	0.0012	4.75	0.10	1.15
95:5	0.114	0.006	4.56	0.50	0.94
90:10	0.108	0.012	4.32	1.00	0.68
85:15	0.102	0.018	4.08	1.50	0.42
80:20	0.096	0.024	3.84	2.00	0.16

^aTotal volume of MCS particles-SWNTs nanocomposites was 6 mL. Solid content of MCS particles-SWNTs nanocomposites was 2 w/w%. The pH of MCS particle and acid-treated SWNTs dispersions were first adjusted to appropriate pHs (pH 3 to 5) respectively, prior to complexation at room temperature. ^bWeight percentage of MCS particles was 2.5 w/w%. ^cWeight percentage of acid-treated SWNTs was 1.2 %.

6.2.3 Measurement and characterization

Particle morphologies

The transmission electron microscope (TEM) images were obtained using a JEOL 2010 transmission electron microscope at an operating voltage of 200 kV. A small drop of dilute particle dispersion (100–200 mg/L) was placed on either a formvar-coated or carbon-coated grid, and dried at room temperature before analysis.

Chemical compositions

Infrared spectra were recorded on a Nicolet Avatar 360 FT-IR spectrophotometer using potassium bromide (KBr) disks. About 10 mg of finely grounded sample and about 0.5 g of spectrophotometric grade anhydrous KBr were grinded thoroughly using mortar and pestle. To prepare a transparent disk for IR measurement, the mixture was pressed at a force of about 7 tonnes for 2 minutes using a level-screw press.

Thermogravimetry analysis (TGA) was carried out using a Perkin-Elmer thermogravimetry analyzer TGA7 (TGA). Exact amount of finely grounded powder was weighed and placed in a platinum sample holder. The thermal experiments for

MCS particles were performed at temperatures varying from 30 to 900 °C at a heating rate of 20 °C/min under N₂ atmosphere. The percentage of γ -Fe₂O₃ content, γ -Fe₂O₃ (%), in MCS particles was calculated as follows:

$$\gamma\text{-Fe}_2\text{O}_3 (\%) = \frac{\text{weight remained at } 900\text{ }^\circ\text{C}}{\text{weight loss due to H}_2\text{O evaporation at } 100\text{ }^\circ\text{C}} \times 100\% \quad (6.7)$$

The thermal experiments for carbon nanotubes were performed at temperatures from 30 to 900 °C using a heating rate of 2 °C/min under N₂ (80 %) and O₂ (20 %) atmosphere.

Particle size analyses

Particle size and size distribution of MCS particles were measured with a Coulter LS 230 Particle Size Analyzer using a polarization intensity differential scattering (PIDS) module.

Characterization of surface charge density

All zeta-potential measurements were determined with a Malvern Zetasizer 3000HS in a 1×10^{-3} M NaCl aqueous solution as a suspension liquid. Sample concentrations for MCS particles were maintained between 100 and 300 mg/L; while sample concentrations for SWNTs were maintained below 50 mg/L in order to prevent SWNTs aggregation.

Film morphology studies

Atomic force microscopy (AFM) and magnetic force microscopy (MFM) measurements were performed on a Digital Instruments NanoScope IV in a tapping mode, using MESP-etched Silicon tips (i.e. magnetic force tip). Sample dispersion (2 mL, 2 w/w%) was placed onto a glass substrate, and dried at different temperatures (130 and 155 °C) for 2 h. All measurements were performed under ambient conditions.

The cross-sectional image of the nanocomposites was investigated with a field emission scanning electron microscopy (FE-SEM, JEOL JSM 6335 F). Sample

dispersion (2 mL, 2 w/w%) was placed onto a Teflon holder, and dried at 155 °C. The dried film was cut and placed onto a custom-made aluminum holder (Figure 6.4). Finally, the dried sample was coated with a thin layer of gold to a depth of approximately 5 Å under vacuum, prior to FE-SEM characterization.

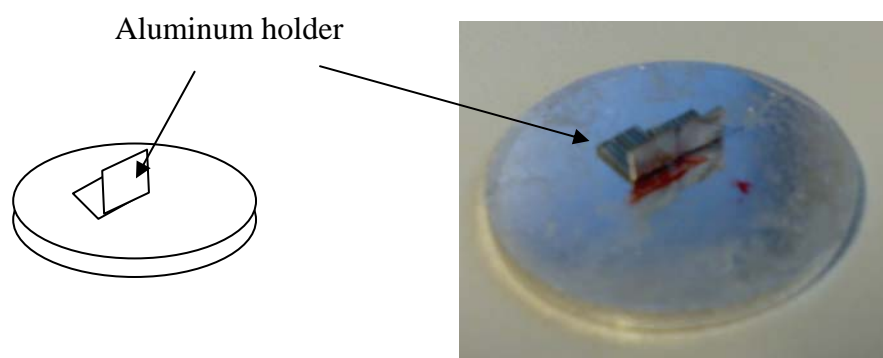


Figure 6.4. A custom-made aluminum holder for cross-sectional FE-SEM.

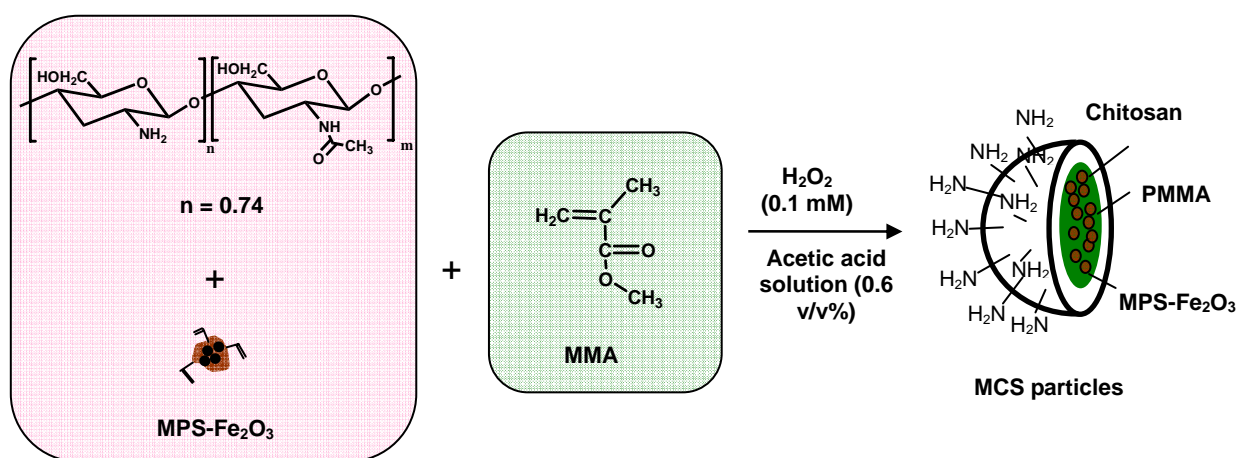
Magnetization measurement

The saturation magnetizations (M_s) of magnetic nanoparticles were determined with a vibrating sample magnetometer (VSM) (LDJ MODEL 9500) at room temperature. Exact amount of a sample (usually larger than 0.05 g) was weighed, and closely packed into a Teflon holder. The magnetization measurement was studied at room temperature using external magnetic fields ranging from 0 to 5 KOe.

6.3 Results and discussion

6.3.1 Synthesis of magnetic core-shell (MCS) particles

The MCS particles were synthesized via H_2O_2 -induced graft copolymerization of MMA from chitosan in the presence of MPS- Fe_2O_3 nanoparticles (Scheme 6.1), based on the method as we described in Chapter 5. High monomer conversion (80%) was achieved at 80 °C for 2 h. The product yield of MCS particles was 53 %. Compositions of the particles were determined based on the monomer conversion, the Soxhlet extraction of un-grafted chitosan and the thermogravimetry analysis (TGA) of encapsulated $\gamma\text{-Fe}_2\text{O}_3$. Thus, MCS particles were comprised of 59 w/w% of PMMA, 25 w/w% of chitosan, and 16 w/w% of $\gamma\text{-Fe}_2\text{O}_3$, respectively. Detailed calculations are illustrated in Appendix, B-3.



Recipe: Chitosan:MMA:MPS- Fe_2O_3 = 2.5:4:1 (w/w/w)

Scheme 6.1. Preparation of MCS particles.

Particle size measurement indicated that the volume-average hydrodynamic diameter of MCS particles was 148 nm, and the particle size distribution (D_v/D_n) was 1.12 (Figure 6.5). The presence of the chitosan shell on the particle surface was confirmed with ζ -potential analyses. Figure 6.6 shows that the positive ζ -potential of MCS particles decreases considerably with the increase in pH, which is probably attributed to the deprotonation of quaternary ammonium ions of chitosan on the particle surface.

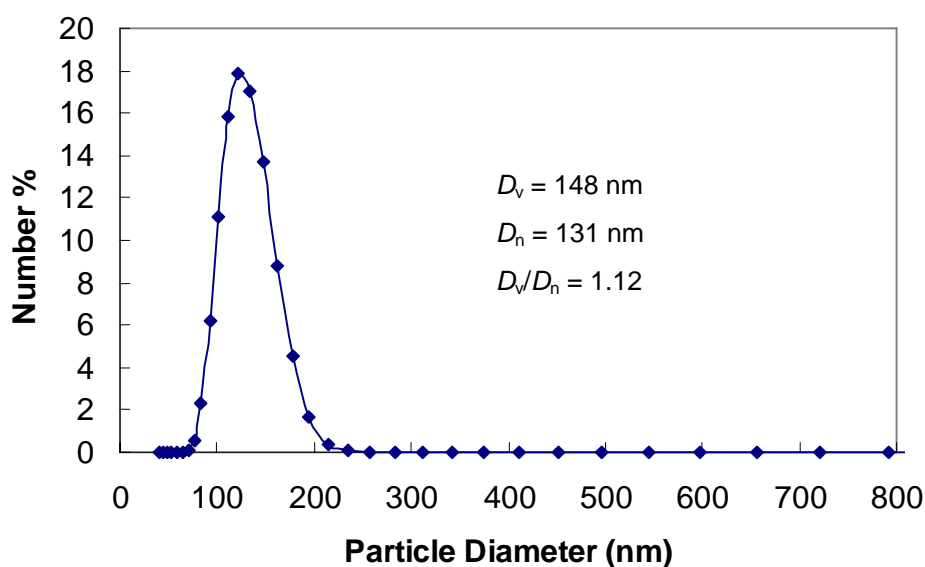


Figure 6.5. Particle size and size distribution of MCS particles (chitosan:MMA:MPS-Fe₂O₃ = 2.5:4:1; H₂O₂ = 0.1 mM).

Morphologies of the MCS particles were examined with a transmission electron microscopy (TEM) (Figure 6.7). The magnetic nanoparticles (black spots) were all located inside the PMMA cores, indicating the successful encapsulation of

MPS-Fe₂O₃ nanoparticles into the PMMA cores. However, some of the particles were not spherical, and they tended to form aggregates, which might be due to the strong magnetic dipole-dipole attractions exerted between the particles during drying.

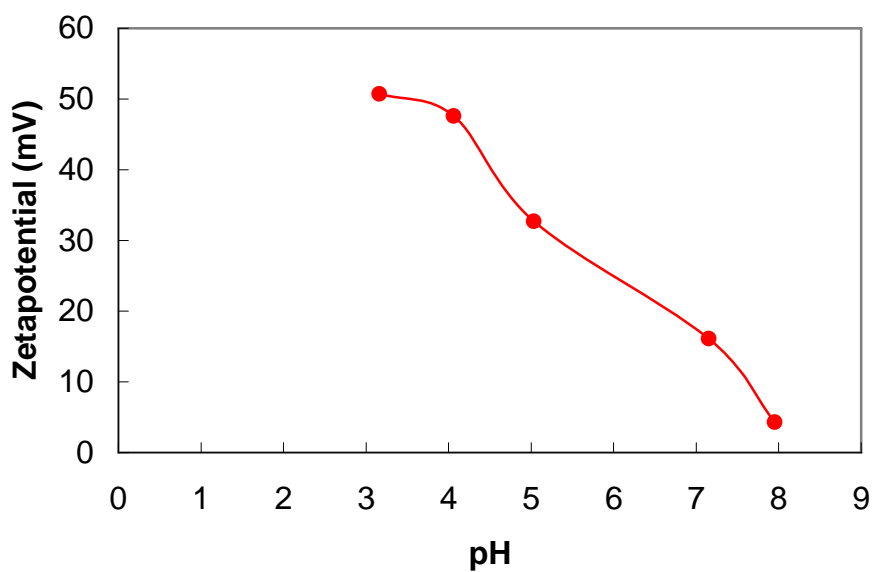


Figure 6.6. pH dependence of the ζ -potential of MCS particles measured in a 1 mM NaCl solution at 25 °C.

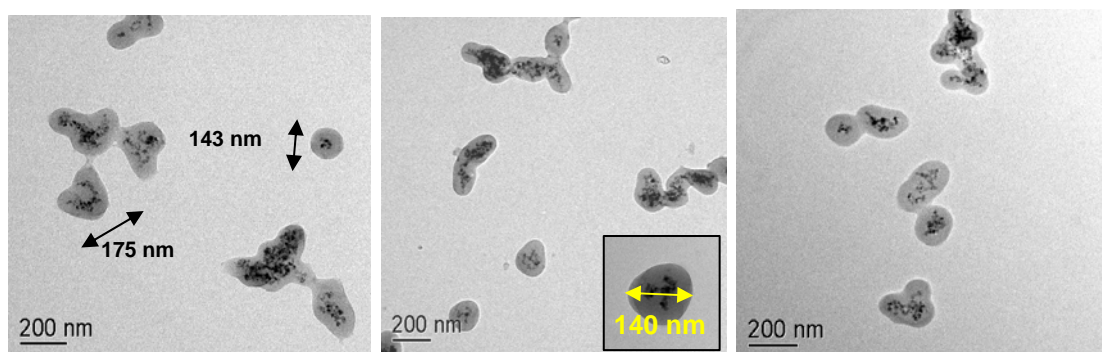


Figure 6.7. TEM images of MCS particles.

6.3.2 Purification of as-prepared single-walled carbon nanotubes (*AP-SWNTs*)

AP-SWNTs were prepared with a modified arc-discharge apparatus using Ni/Y as the catalyst.^{167,168} Since it is known that carbon nanotubes have a poor dispersing ability in aqueous solutions because of their hydrophobic phenylene rings, the *AP-SWNTs* were thus dispersed in acetone with the help of a homogenizer, prior to TEM characterization. Figure 6.8 shows the TEM images of *AP-SWNTs*, which clearly reveal the SWNTs bundles with diameters ranging from 15 to 50 nm. Furthermore, a lot of amorphous carbons and metal oxide nanoparticles were entrapped by the SWNTs.

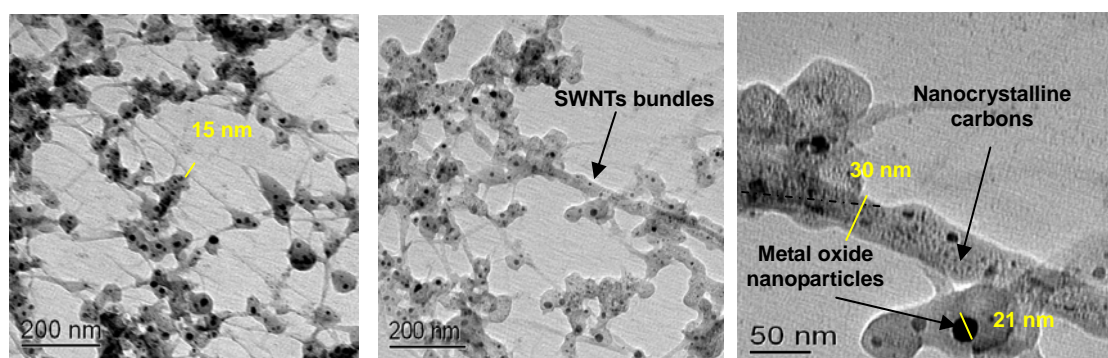


Figure 6.8. TEM images of *AP-SWNTs*.

Figure 6.9 shows the TGA thermogram of *AP-SWNTs* in an attempt to determine the composition of *AP-SWNTs*. There was a significant weight loss (70 %) after 310

°C, which was attributed to the decomposition of amorphous carbon matrices and SWNTs.¹⁶⁷ The remaining weight (30 %) after 480 °C was due to the presence of metal oxide residues.¹⁶⁷ Based on the TGA results, it was found that *AP*-SWNTs contained 70 % of carbonaceous materials (including SWNTs, nanocrystalline carbons and amorphous carbons) and 30 % of metal oxide nanoparticles. These values were close to the values reported by Lv *et al.*¹⁶⁷

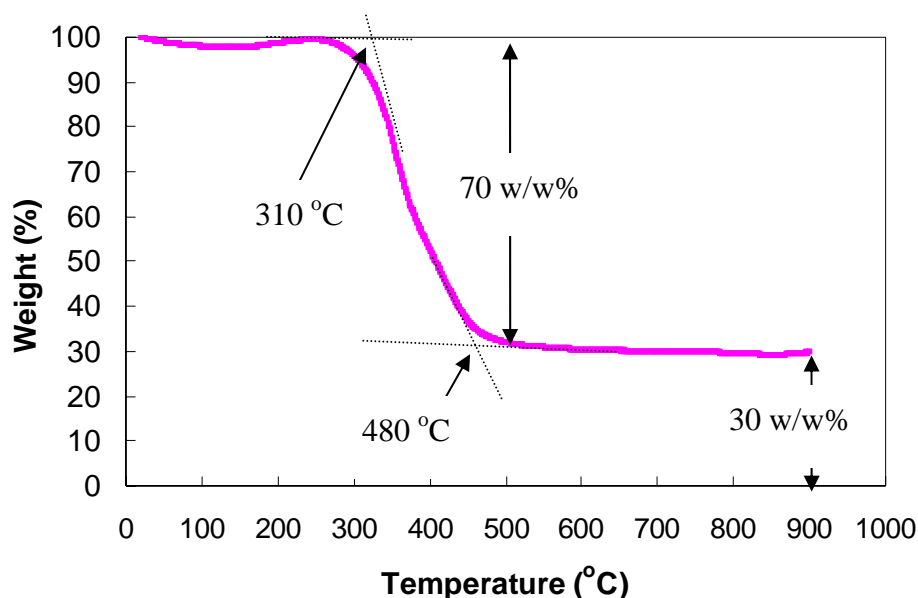


Figure 6.9. TGA thermogram of *AP*-SWNTs (using a heating rate of 2 °C/min under a mixture of 20 % of O₂ and 80 % of N₂ atmosphere).

In order to remove the metal oxide residues from the *AP*-SWNTs, and functionalize the tube end of SWNTs, *AP*-SWNTs were treated with a HNO₃ solution (3 M) under reflux for 16 h, followed by repeated washing of the acid-refluxed *AP*-SWNTs using successive centrifugation, decantation and re-dispersion cycle.^{167,169}

The purified acid-refluxed materials were dispersed in water, and stored for further use. Figure 6.10 shows the TEM images of the purified acid-refluxed materials (or acid-treated SWNTs). Although the SWNTs still form bundles, and are encased within the mat by a relatively thick and uniform carbonaceous matrix, a large portion of metal oxide nanoparticles (i.e. the black spots) seems to have been removed via the acid treatment.

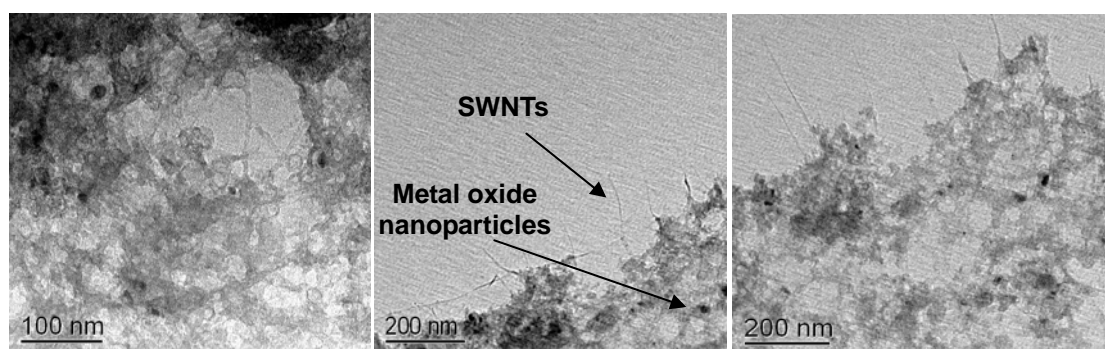


Figure 6.10. TEM images of purified acid-refluxed AP-SWNTs (or acid-treated SWNTs).

Analyses of the acid-treated SWNTs using TGA (Figure 6.11 b) showed that there are three weight losses. The initial weight loss (10 %) at 100 °C was due to the water evaporation; while the second weight loss (22 %) from 100 to 480 °C was due to the removal of amorphous carbon and its surface functional groups. An additional weight loss (63 %) after 480 °C might be attributed to the decomposition of SWNTs [Dillon *et al.* 1999]. The remaining weight (5 %) after 560 °C was attributed to the

metal oxide residues. Based on the TGA results, it was found that the purified acid-treated SWNTs now contained 24.5 % of amorphous carbonaceous materials, 70 % of SWNTs, and 5.5 % of metal oxide residues. Compared with *AP*-SWNTs (Figure 6.11 a), the content of metal oxides in the acid-treated SWNTs decreased from 30 to 5.5 %, indicating that 82 % of metal oxides had been removed through the acid-reflux treatment. Furthermore, the surface of acid-treated SWNTs is more hygroscopic than that of *AP*-SWNTs, which may be due to the presence of carboxyl, aldehyde, and other oxygen-containing functional groups on the surface of carbonaceous materials.¹⁶⁹

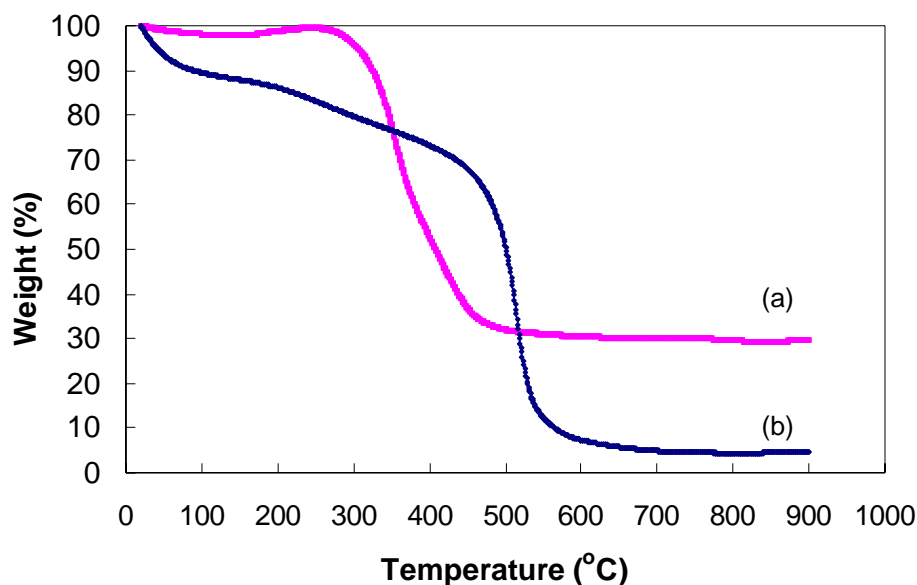


Figure 6.11. TGA thermogram of (a) *AP*-SWNTs, and (b) acid-treated SWNTs (Both TGA measurements were performed using a heating rate of 2 °C/min under a mixture of 20 % of O₂ and 80 % of N₂ atmosphere).

Figure 6.12 shows the ζ -potential analyses of the acid-treated SWNTs as a function of pH at 25 °C. The negative ζ -potential of the materials increased from -10 to -15 mV as the pH increased from 3.5 to 8.0. This effect was probably attributed to the de-protonation of the carboxylic acid groups generated during acid treatment process.

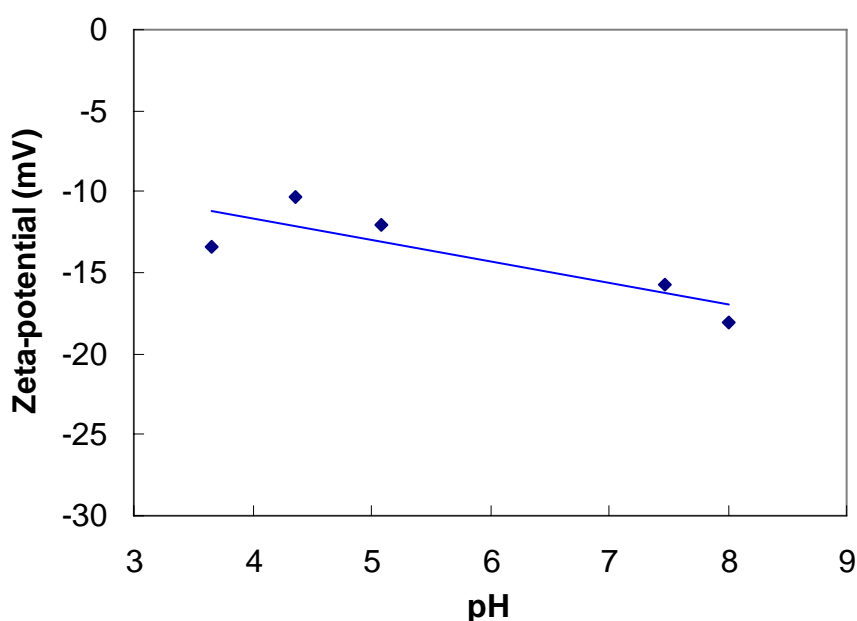


Figure 6.12. pH dependence of the ζ -potential of acid-treated SWNTs measured in a 1 mM NaCl solution at 25 °C.

The presence of carboxylic acid groups on the surface of carbonaceous materials was further confirmed by FT-IR analyses (Figure 6.13). The spectrum of acid-treated SWNTs showed three characteristic peaks. The absorption bands between 1500 and 1600 cm^{-1} were characteristic of phenylene stretching of carbon nanotubes and

amorphous carbon matrixes,¹⁷⁰ while the weak absorption bands between 1650 and 1750 cm^{-1} were characteristic of the carbonyl stretching of carboxylate groups.¹⁷⁰ The strong bands between 3000 to 3800 cm^{-1} indicated the OH stretching of carboxylic acids. These results suggest that the carboxylic acid groups ($-\text{COOHs}$) were produced on the carbonaceous materials. In summary, the acid treatment process not only removes most of the metal oxide residues, but also produces carboxylic acid groups on the surface of carbonaceous materials, including the tube end of SWNTs and the surface of amorphous carbon.

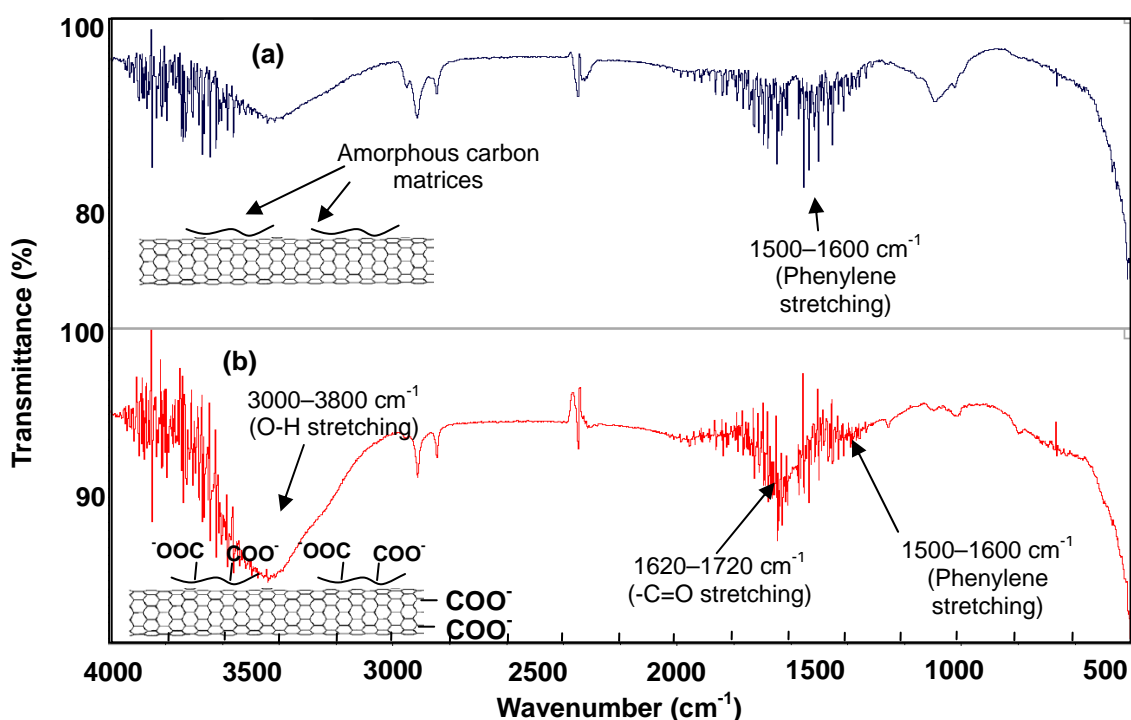
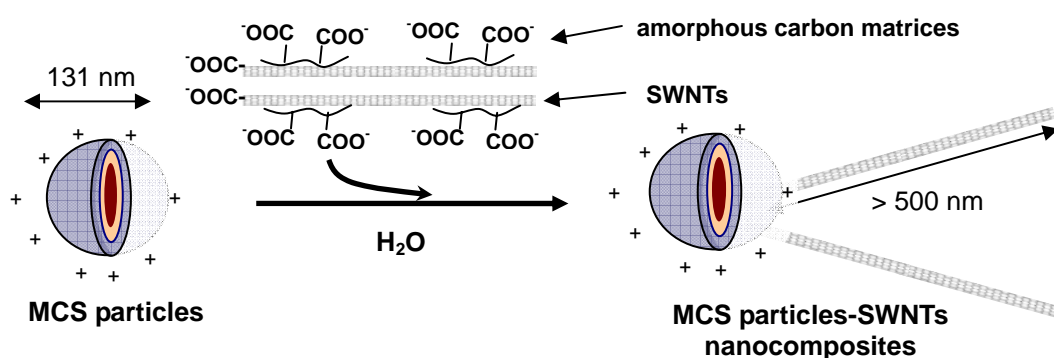


Figure 6.13. FT-IR spectra of (a) AP-SWNTs and (b) acid-treated SWNTs.

6.3.3 Formation of MCS particles-SWNTs nanocomposites

Formation of MCS particles-SWNTs nanocomposites was based on the electrostatic complexation between positively charged MCS particle dispersion and negatively charged acid-treated SWNTs, as illustrated in Scheme 6.2. Thus, surface charges of MCS particles play a major role in controlling the complexation and colloidal stability of the resulting nanocomposites. Since the positive charges of MCS particle surfaces decrease upon complexation of both negatively charged SWNTs and amorphous carbons, the particles are expected to become less stable, as the content of the acid-treated SWNTs increases. Thus, a study was carried out to determine the effect of complex stability of the SWNTs on MCS particles.



Scheme 6.2.Preparation of MCS particles-SWNTs nanocomposites.

6.3.3.1 Effect of weight ratio of MCS particles to acid-treated SWNTs

Figure 6.14 shows the ζ -potential of MCS particles-SWNTs nanocomposites as a function of weight percentage of acid-treated SWNTs at pH 5.0 in a 1 mM NaCl solution at 25 °C. The positive ζ -potential of these nanocomposites decreases, reaches the isoelectric point, and finally becomes negative as the SWNTs content increases from 1 to 20 %. These results confirm the electrostatic complexation between negatively charged SWNTs and/or amorphous carbons and positively charged MCS particles. Furthermore, the result indicates that the nanocomposites may become unstable and form aggregates when the acid-treated SWNTs content in the nanocomposites is higher than 10 w/w%, because of their low ζ -potentials ($< +10$ mV).

6.3.3.2 Effect of pH

To increase the SWNTs loading on MCS particles with good colloidal stability, the pH of the particle and the SWNTs dispersions were adjusted from pH 5.0 to 4.3 and 3.0, respectively, prior to complexation (Figure 6.14). These results showed that the ζ -potential values of the obtained nanocomposites at various acid-treated SWNTs contents (1–20 w/w%) were higher than at pH 5.0. For example, the ζ -potential of the MCS particles(95)-SWNTs(5) nanocomposites increased from +15 mV to +32 mV, as

the pH decreased from pH 5.0 to 4.3. The increase in ζ -potential value is attributed to the higher surface charge densities of MCS particles (ζ -potentials $\sim +40$ mV) at pH 4.3, as compared to their ζ -potential (+30 mV) at pH 5.0. A further decrease of the pH from 4.3 to 3.0 had little influence on their ζ -potentials. Thus, MCS particles and SWNTs complexation at pH 4.0 were used for subsequent studies. The ζ -potential measurement also suggested that SWNTs loading on MCS particles below 10 w/w% could give stable nanocomposites with ζ -potential higher than +20 mV.

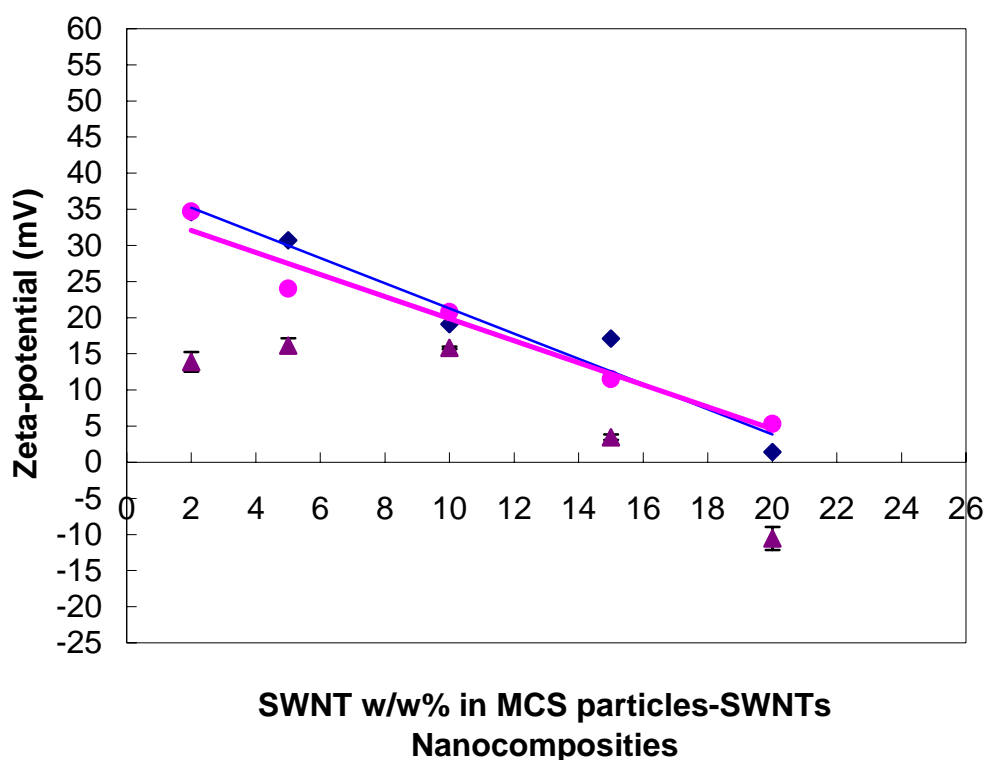


Figure 6.14. ζ -potentials of MCS particles-SWNTs nanocomposites prepared at different pHs: (●) pH 3; (◆) pH 4.3; (▲) pH 5.0.

6.3.4 Morphologies of MCS particles-SWNTs nanocomposites

Figure 6.15 (a–c) shows the TEM images of the MCS particles-SWNTs nanocomposites with different weight ratio of MCS particles to acid-treated SWNTs (95 : 5; 90 : 10; 85 : 15). The SWNTs formed bridges between MCS particles, where the SWNTs bundles had diameters ranging from 15 to 30 nm. Formation of this end-to-end attachment is probably attributed to the electrostatic interactions between the negatively charged nanotube ends and positively charged MCS particles. Since the tube ends of carbon nanotubes usually contain metal catalysts, and have a greater curvature with defective structures (i.e. pentagon instead of hexagonal), the nanotube ends are more susceptible to oxidization to form –COOH groups than the side wall when subjected to the nitric acid reflux treatment.¹⁷¹

Figure 6.15 (a–c) show that the presence of MCS particles can significantly prevent the formation of large SWNTs bundles. Formation of these SWNTs bundles is a major challenge in using solution-casting method to disperse SWNTs in a polymer matrix, where SWNTs tend to saturate as low as 2 % and form large aggregates.¹⁷² Figure 6.15 (a–c) also show that the presence of MCS particles was able to separate some amorphous carbons from SWNTs. This observation suggests that the acid-reflux treatment not only oxidizes the tube end of SWNTs, but also

oxidizes the surface of amorphous carbon matrix, which was suggested by Dillon *et*

*al.*¹⁶⁹

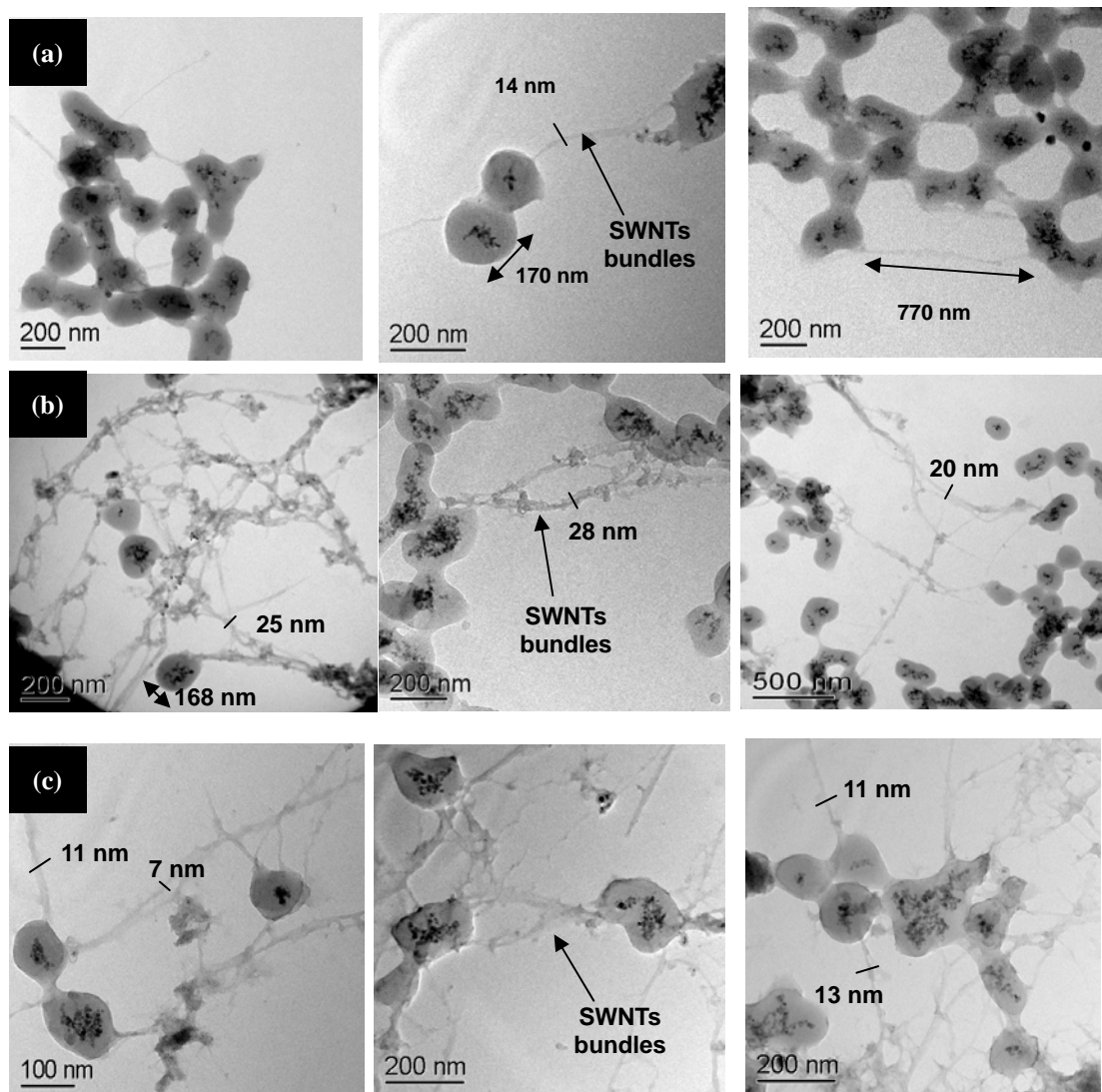


Figure 6.15. TEM images of MCS particles-SWNTs nanocomposites with different MCS particles to SWNTs weight ratios (a) 95 : 5; (b) 90 : 10; (c) 85 : 15.

6.3.5 Film-forming ability of MCS particles and MCS particles-SWNTs nanocomposites

The presence of voids in the electromagnetic interference (EMI) coating materials may cause leakage of electromagnetic radiation and diminish the shielding effectiveness. Thus, the coating materials should possess a good film-forming ability in order to avoid the formation of voids. Since PMMA has a glass transition temperature (T_g) of 105 °C, the film-forming of MCS particles is expected to occur at an annealing temperature higher than its T_g . Thus, the effect of annealing temperatures from 130 to 155 °C on the film-forming ability of MCS particles has been investigated by examining the topologies of MCS particle films using atomic force microscopy (AFM).

Figure 6.16 (a–b) show the AFM topographic images of two MCS films annealed at 130 and 155 °C, respectively. The images clearly revealed that particle deformation occurred at 155 °C, but not at 130 °C. Furthermore, the film annealed at 155 °C showed much less dispersed MCS particles. The roughness of deformed particles (not including the dispersed MCS particles) had an average height of 35 ± 12 nm, as determined by the statistical analyses of the topographic image (Figure 6.16 b). These results suggested that 155 °C was a suitable annealing temperature for good

film-forming of MCS particles.

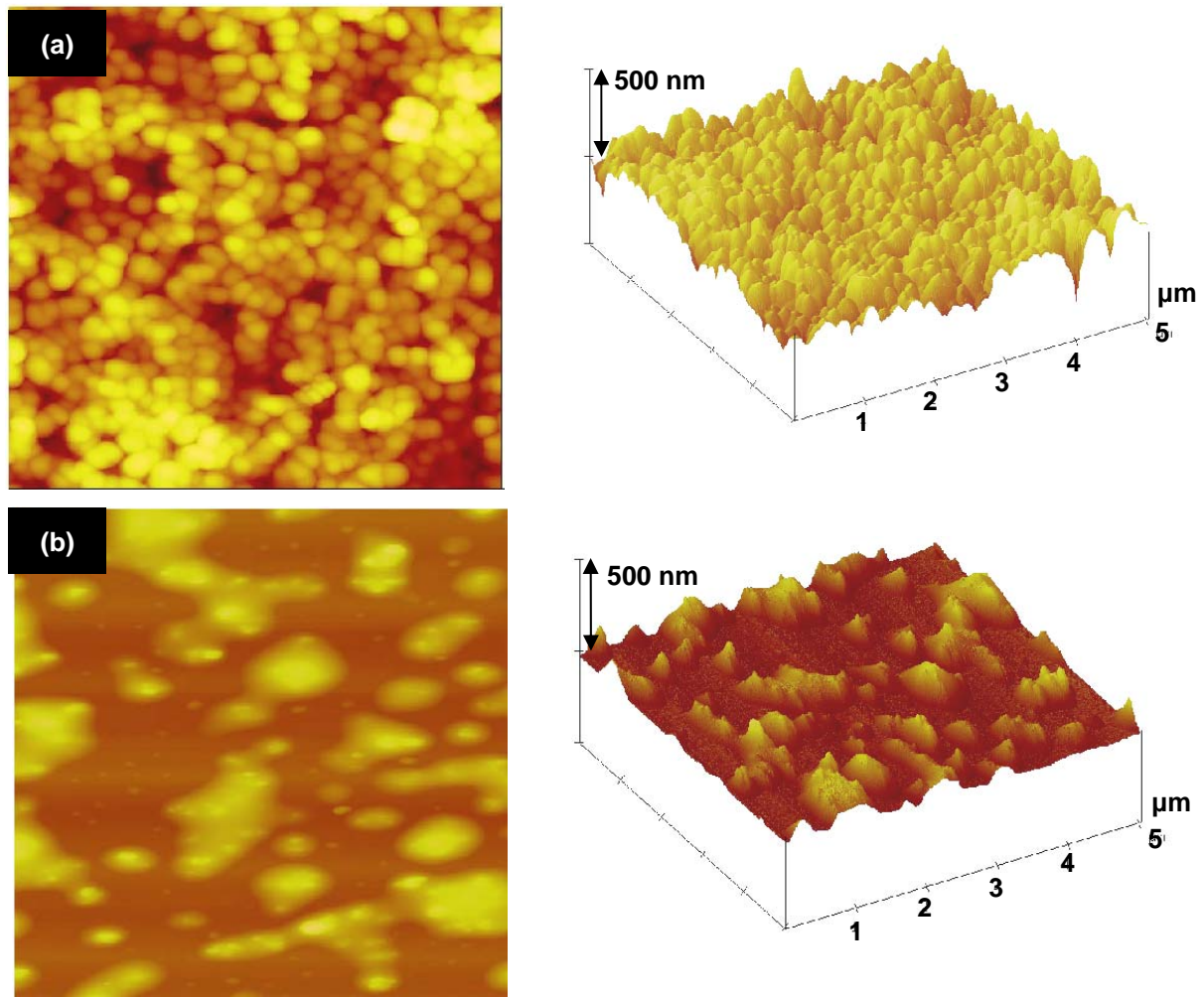


Figure 6.16. Nanocomposite films formed by annealing MCS particle dispersion at 130 °C; (b) 155 °C for 2 h [Left: surface topographic image (5x5 μm); Right: three-dimensional surface topographic image (5x5 μm)].

The MCS film that was annealed at 155 °C was investigated with a magnetic force microscopy (MFM) (Figure 6.17). The circled spots corresponding to the positions of the particles in the topographic image (Figure 6.17 b) are the magnetic signals from the films, and these signals are evenly distributed throughout the films. These results suggest that the well-defined core-shell nanostructure of MCS particles is able to prevent magnetic nanoparticles from severe aggregation in the film during film-forming process, which may have the advantage of providing more uniform absorption of EM radiation.

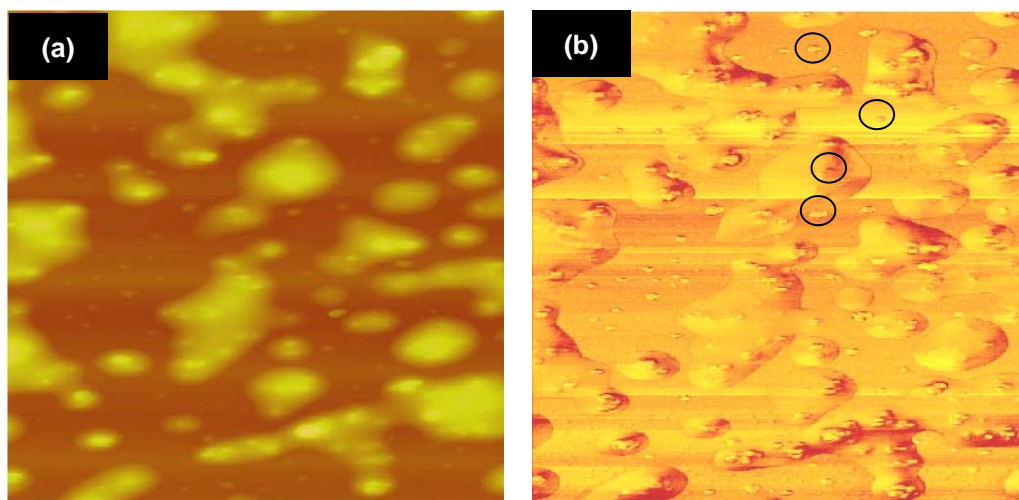


Figure 6.17. Nanocomposite films formed by annealing MCS particle dispersion at 155 °C. (a) Surface topographic image (5x5 μm); (b) Top view of MFM image (5x5 μm).

The film-forming ability of the MCS particles(90)-SWNTs(10) nanocomposites was also examined. Figure 6.18 (a) shows that the AFM topographic image of MCS particles(90)-SWNTs(10) nanocomposites annealed at 155 °C. It is clearly revealed that no individual MCS particles were observed. Instead, the film surface seems to be covered with a thick matrix, which might be attributed to the presence of the amorphous carbon matrices that adsorbed on the surface of MCS particles via electrostatic complexation. The roughness of this nanocomposite film had an average height of 49 ± 11 nm, as determined in the surface image (Figure 6.18 a). This result suggested that the presence of SWNTs had little influence on the film-forming ability of MCS particles; meaning that the MCS particles(90)-SWNTs(10) nanocomposites were able to form a continuous film. Figure 6.18 (b) also shows the MFM image of MCS particles(90)-SWNTs(10) nanocomposite film annealed at 155 °C. The circled magnetic signals in the form of clusters were detected, and these clusters were evenly distributed throughout the film. Formation of these magnetic clusters might be attributed to the decrease in the stability of MCS particles upon complexation with acid-treated SWNTs.

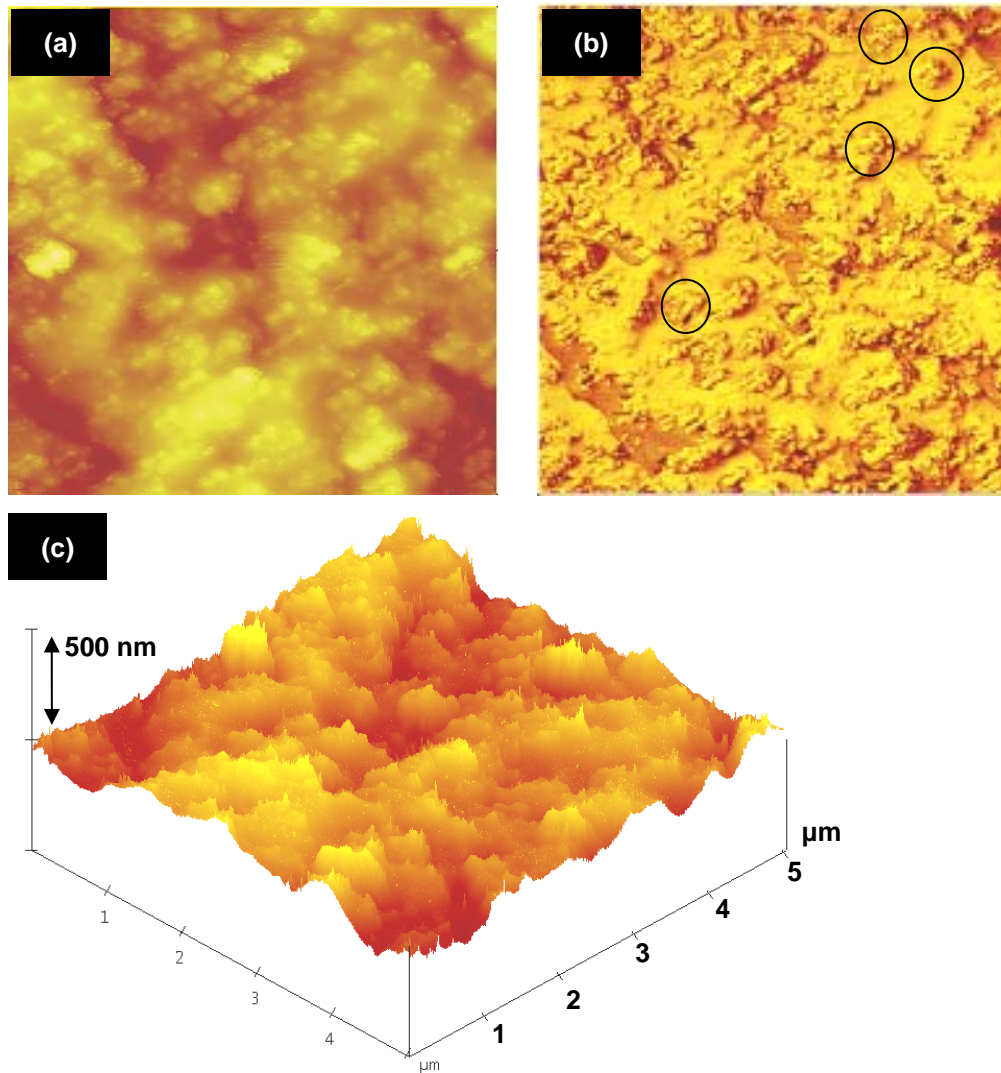


Figure 6.18. Nanocomposite films formed by annealing MCS particles (90)-SWNTs(10) nanocomposites at 155 °C. (a) Surface topographic image (5x5µm); (b) Three-dimensional surface topographic image (5x5µm) and (c) Top view of MFM image (5x5 µm).

To examine the dispersing property of the SWNTs inside MCS film, cross-section field-emission scanning electron microscopy (FE-SEM) images were taken. The MCS particles-SWNTs nanocomposite film was first cut and placed onto a custom-made aluminum holder. As a comparison, MCS film was also prepared and investigated with a FE-SEM. The cross-sectional SEM images of MCS particle film as shown in Figure 6.19 (a) clearly illustrated that MCS particles formed a continuous network. Furthermore, some individual MCS particles and some voids inside the standing film were revealed. This result indicates that particle deformation during the annealing process was not efficient, thus creating some voids in the coating. Inefficient particle deformation might be attributed to the strong charge-charge repulsion (ζ -potential = +33 mV) between MCS particles, which affects the coalescence of MCS particles during the film-forming process.

On the other hand, MCS particles(90)-SWNTs(10) nanocomposites were able to form a continuous film, as seen in Figure 6.19 (b). Furthermore, there were almost no individual MCS particles and voids in the film. Interestingly, a bundle of SWNTs were embedded and spread over the MCS particle film. These results indicate that the presence of SWNTs and amorphous carbons may be able to assist the film-forming of MCS particles. This effect may be due to the decrease of the charge-charge repulsion

between MCS particles upon complexation with the acid-treated SWNTs, facilitating the coalescence of MCS particles to undergo film-forming process.

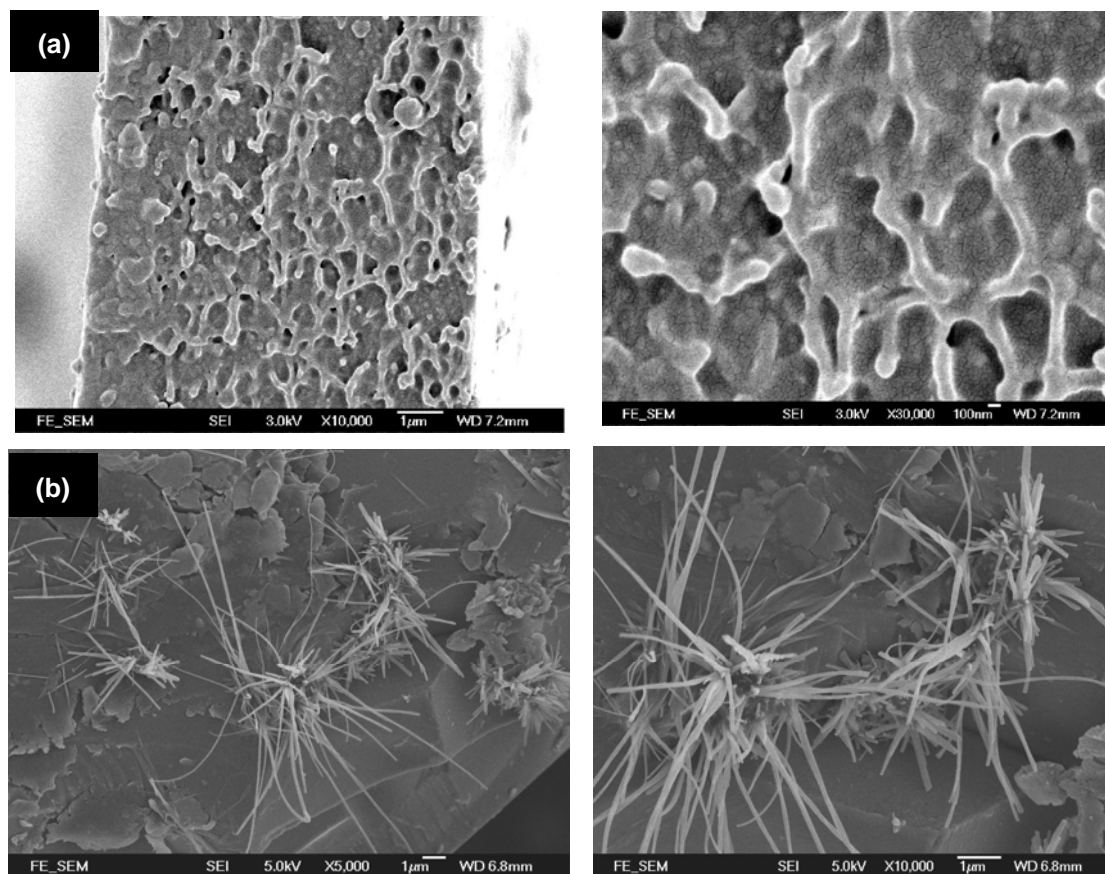


Figure 6.19. FE-SEM images of cross-section of the nanocomposite films formed by (a) MCS particles; (b) MCS particles(90)-SWNTs(10) nanocomposites.

6.3.6 Magnetic properties of MCS particles-SWNTs nanocomposites

Magnetization measurement of MCS particles and MCS particles(90)-SWNTs(10) nanocomposites was studied by applying external magnetic fields from 0 to 5 KOe (Figure 6.20). The result showed that MCS particles exhibited superparamagnetic properties at room temperature, and their saturation magnetization was 3.9 emu/g. However, MCS particles(90)-SWNTs(10) nanocomposites displayed a little hysteresis at room temperature with a remnant magnetization (M_r) of 0.6 emu/g and a coercivity (H_c) of 60 Oe. Their saturation magnetization was 3.7 emu/g. Display of the hysteresis loop may be attributed to the slight aggregation of MCS particles-SWNTs nanocomposites.

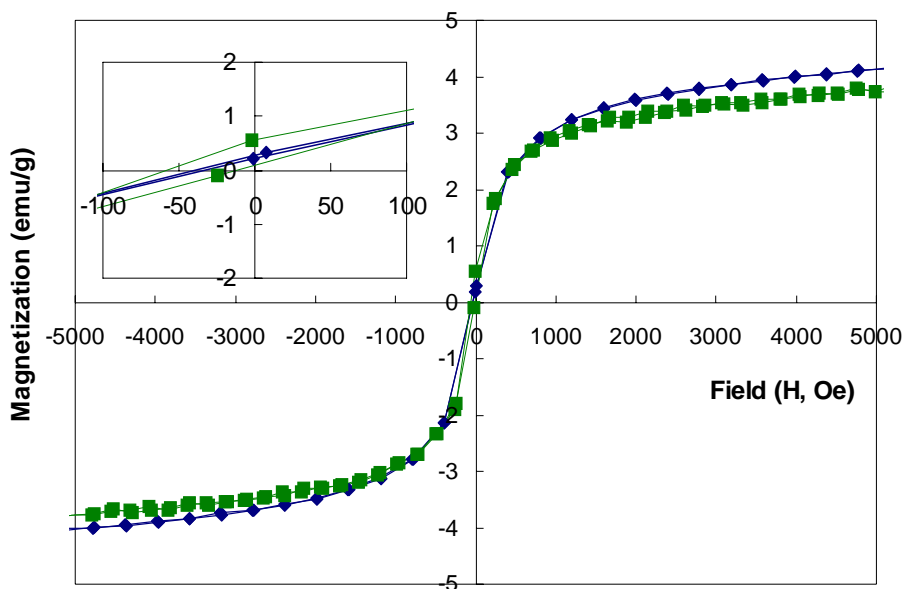


Figure 6.20. Room temperature-magnetization curve of (◆) MCS particles and (■) MCS particles(90)-SWNTs(10) nanocomposites.

6.4 Conclusions

A novel MCS particles-SWNTs nanocomposite as a water-based coating for EMI shielding applications has been developed. Formation of this nanocomposite was achieved via simply mixing the MCS particles with acid-treated SWNTs, where the SWNTs were able to form complexes with the MCS particles. Furthermore, the presence of MCS particles can significantly reduce the formation of large SWNTs aggregates. Such aggregation is a major challenge in using the SWNTs. Other important findings of this study include:

- 1) pH 4.0 was the optimal pH for MCS particles and SWNTs complexation, and the maximum SWNTs loading on MCS particles with a good colloidal stability was 10 w/w%.
- 2) 155 °C was a suitable annealing temperature to produce a continuous MCS film.
- 3) The good film-forming ability of PMMA core and the well-defined core-shell nanostructures of MCS particles allowed good dispersion of the magnetic nanoparticles in the polymer matrix.
- 4) The presence of SWNTs had little influence on the film-forming of MCS particles.

5) MCS particles exhibited superparamagnetic properties at room temperature, and their saturation magnetization was 3.9 emu/g. However, MCS particles(90)-SWNTs(10) nanocomposites displayed a little hysteresis at room temperature. Their saturation magnetization was 3.7 emu/g.

Chapter 7 Conclusions and recommendations for future study

7.1 Synthesis and characterization of magnetic core-shell (MCS) particles

In conclusion, new synthetic methods [*tert*-butyl hydroperoxide (TBHP) and hydrogen peroxide (H_2O_2) system] for the preparation of magnetic core-shell (MCS) particles with average diameters ranging from 100 to 200 nm and narrow size distributions have been developed. The particles had a well-defined core-shell nanostructure that consisted of hydrophobic poly(methyl methacrylate) (PMMA) cores encapsulated with magnetic nanoparticles coated with chitosan shells.

Synthesis and characterization of MCS particles ($\gamma\text{-Fe}_2\text{O}_3$ /PMMA/chitosan) have been studied. Effects of the reaction variables with respect to monomer conversion, particle size and size distribution, grafting percentage of chitosan on MCS particles, encapsulation percentage of $\gamma\text{-Fe}_2\text{O}_3$, nanostructure, as well as morphology have been systemically investigated. The variables are:

- 1) Initiator concentration (0.05–0.4 mM for TBHP; 0.05–1.2 mM for H_2O_2)
- 2) Monomer concentration (1.2–3.6 % MMA)
- 3) MPS- Fe_2O_3 concentration (0.2–0.6 % for TBHP system; 0.4–0.8 % for H_2O_2 system)

- 4) Reaction temperature (60–80 °C for H₂O₂ system)
- 5) Types of surface-modified magnetic nanoparticles (o-Fe₂O₃, c-Fe₂O₃ and MPS-Fe₂O₃)
- 6) Types of initiators (TBHP and H₂O₂)
- 7) Types of water-soluble polymers containing amino groups [chitosan, Polyethylenimine (PEI), Poly(vinyl amine) (PVAm), cellulase and casein]
- 8) Types of vinyl monomers [*n*-butyl acrylate (*n*-BA) and *N*-isopropyl acrylamide (NIPAM)]

Important features of this method are summarized as follows:

- 1) Well-defined core-shell particles containing magnetic nanoparticles inside the core can be produced in the absence of surfactants and in aqueous solution.
- 2) This method is also able to allow making MCS particles with multi-functional properties such as tunable glass transition temperature and thermo-responsiveness by varying the core compositions and materials. Thus, these new materials could be extremely useful in a wide range of applications.

7.2 Application of MCS particles

Application of these novel core-shell particles as a water-based coating has been exploited. MCS particles were used to form stable nanocomposites with single-walled carbon nanotubes (SWNTs) for electromagnetic interference (EMI) shielding. Loading efficiency of SWNTs on MCS particles was evaluated. The results showed that the maximum loading of SWNTs on the particles with good colloidal stability was 10 w/w%. Morphological observation showed that the SWNTs formed a bridge between MCS particles, in which the presence of MCS particles was able to prevent the formation of large SWNTs bundles. The well-defined core-shell nanostructure of MCS particles was able to prevent magnetic nanoparticles from severe aggregation in the film during film-forming process. The MCS particles-SWNTs nanocomposites were able to form a continuous film on a glass substrate at 155 °C. Magnetization study showed that this nanocomposite film possessed a good magnetic responsiveness. Exploration of this novel type of nanocomposite for EMI shielding applications is in progress.

7.3 Recommendations for future study

7.3.1 Synthesis of MCS particles

Work is now in progress to increase the amount of iron oxide encapsulated and chitosan being grafted onto the MCS particles. An attempt to avoid the precipitation of reaction mixture due to the formation of hydrophobic PMMA-coated iron oxide composites will be made. Further studies of two multi-functional core-shell particles, including magnetic/PBA-PMMA/chitosan core-shell particles and magnetic/PNIPAM/chitosan microgels will also be conducted. Finally, encapsulation of other types of magnetic nanoparticles (e.g. Nickel and Cobalt) into the core-shell particles will be investigated.

7.3.2 Application of MCS particles

Exploration of the use of multi-functional core-shell (MCS particles-SWNTs) nanocomposites as a water-based coating for electromagnetic interference (EMI) shielding application is currently being undertaken. Other applications of using MCS particles for immobilization of inorganic catalysts and bio-catalysts will also be explored.

Appendix

Table A-1. Magnetization units and conversions.	257
Table A-2. Types of electromagnetic interference shielding materials	258
Figure A-1. Calibration curve of MPS solution at 203.5 nm.	260
A-1. Determination of the viscosity average molecular weight (M_v) of chitosan using dilute solution viscosity measurement	261
A-2. $^1\text{H-NMR}$ spectrum of chitosan and determination of the degree of deacetylation of chitosan	262
B-1. Determination of the composition of MCS particles (TBHP system)	264
B-2. Determination of the composition of MCS particles (H_2O_2 system)	266
B-3. Determination of the composition of MCS particles (120906-1)	268
C-1. Introduction to magnetic domain theory	270

Table A-1. Magnetization units and conversions.^{Scholten} A is ampere, cm is centimeter, m is meter, emu is electromagnetic unit, G is gauss, Oe is oersted, $\mu_0 = 4\pi \times 10^{-7}$ newton/ampere² is the permeability of free space.

Quantity	Symbol	cgs unit	SI-1 unit	cgs equiv.	SI-2 unit	cgs equiv.	SI-3 unit	cgs equiv.
Field strength	H	Oe G emu	A/m	$4\pi 10^{-3}$ Oe	A/m	$4\pi 10^{-3}$ Oe	T	10^4 Oe
Induction = total flux density	B	G Emu	T	10^4 G	T	10^4 G	T	10^4 G
Magnetization $= \frac{\text{dipole moment}}{\text{volume}}$	I J M	Emu/cm ³ emu G	T	$10^4/4\pi$ G	kA/m	1 G	k A/m	1 G
Magnetization = flux density due to the material	4π I M	G	T	10^4 G				
Mass-magnetization	σ I M	G cm ³ /g emu/g emu cm ³ /g emu	Wb m/kg	$10^7/4\pi$ emu/g	A m ² /kg	1 emu/g	A m ² /kg	1 emu/g
Dipole moment	M	G cm ³ erg/Oe emu	Wb m	$10^{10}/4\pi$ emu/g	A m ²	1 kG cm ³	A m ²	1 kG cm ³
Field equation		$B = H + 4\pi M$ $B = H + M$	$B = \mu_0 H + M$		$B = \mu_0 (H + M)$		$B = H + \mu_0 M$	

Notes: the 4π factor originates from the unit field created by a unit polar on the surface of a sphere of 1 cm radius, which enclosed the pole with a surface area of $4\pi r^2$.

^{Scholten} Scholten, P. C. *J. Magn. Magn. Mater.* 1995, 149, 57.

Table A-2. Types of EMI shielding materials.

Types of EMI shielding materials	Filler's	Advantages	Disadvantages	Example	EMI (dB) ^a
Metal sheet	Metal	(1) High conducting (2) High magnetic permeability	(1) Bulky and heavy (2) Poor processability (3) Poor wear or scratch resistance (4) Poor durability (i.e. corrosion)		
Cement matrix composites	Metal or carbon filaments	(1) Good processability (2) good wear or scratch resistance (3) less expensive	(1) Poor durability (i.e. corrosion) (2) High density (i.e. Heavy)	Cement-Carbon filaments (0.1 μ m, 1.5 v/v%)	40
Polymer-matrix composites	Metal	(1) Good processability (i.e. moldability) (2) Low density (i.e. Light) (3) High magnetic permeability	(1) Poor durability (i.e. corrosion) (2) High density (i.e. Heavy)	Al flakes (20 v/v%)-PES Steel fibers (20 v/v%)-PES Ni particles (9.4 v/v%)-PES Ni filaments (7 v/v%)-PES	26 42 23 58
	Conducting polymers	(1) Conducting (2) Light (3) Good resistance to corrosion	(1) Poor processability (2) Poor mechanical properties	PPy-Ag(37%)-PET composites [Hong et al. 2001] ^{Hong} PPy-AgPd-PET composites [Lee et al. 2002] ^{Lee et al.}	29–33 (50 MHz–1.5 GHz) 80 (1MHz–1.5 GHz)

^{Hong} Hong, Y.K.; Lee, C.Y.; Jeong, C.K.; Sim, J.H.; Kim, K.; Joo, J.; Kim, M.S.; Lee, J.Y.; Jeong, S.H.; Byun, S.W. Electromagnetic interference shielding characteristics of fabric complexes coated with conductive polypyrrole and thermally evaporated Ag, *Curr. Appl. Phys.* 2001, 1, 439.

^{Lee et al.} Lee, C. Y.; Lee, D. E.; Jeong, C. K.; Hong, Y. K.; Shim, J. H.; Joo, J.; Kim, M. S.; Lee, J. Y.; Jeong, S. H.; Byun, S. W.; Zang, D. S.; Yang, H. G. Electromagnetic interference shielding by using conductive polypyrrole and metal compound coated on fabrics, *Polym. Adv. Tech.* 2002, 13, 577.

Types of EMI shielding materials	Filler's	Advantages	Disadvantages	Example	EMI (dB) ^a
Polymer-matrix composites	Carbon nanostructured materials	(1) Highly conducting (2) Light (3) Good resistance to corrosion	(1) Expensive (2) Poor processability	Ni/carbon fibers(95w/w%)-ABS [Huang and Mo 2002] ^{Huang}	50
				carbon fibers(40 w/w%)/PVA	0.5–4.8

Polyethersulfone (PES); Poly(ethylene terephthalate) (PET); Polyrrole (PPy); Acrylonitrile-butadiene-styrene (ABS); Poly(vinyl alcohol) (PVA); Poly(urea urethane) (PUU); Multi-walled carbon nanotubes (MWNT); ^aThe EMI shielding effectiveness (SE) of a material is defined as $SE (dB) = -10 \log(P_t/P_0)$, where P_t and P_0 are the transmitted and incident electromagnetic power.

^{Huang} Huang, C. Y.; Mo, W. W. The effect of attached fragments on dense layer of electroless Ni/P deposition on the electromagnetic interference shielding effectiveness of carbon fibre/acrylonitrile-butadiene-styrene composites, *Surface and Coatings Tech.* **2002**, *154*, 55.

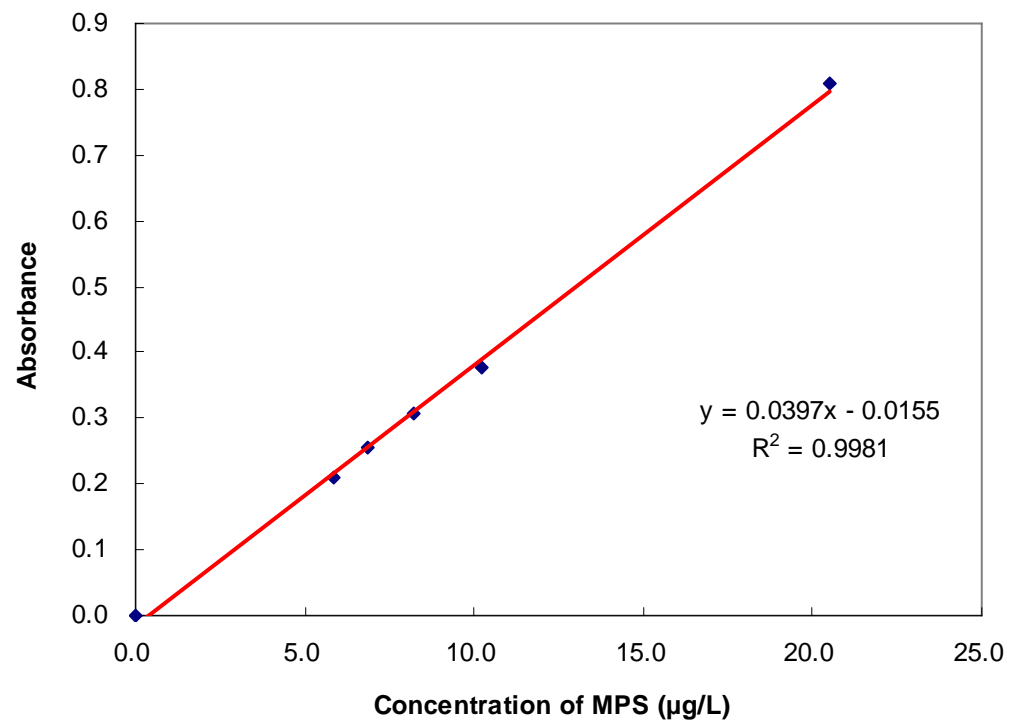


Figure A-1. Calibration curve of MPS solution at 203.5 nm.

**Determination of the viscosity average molecular weight (M_v) of chitosan
using a dilute solution viscosity measurement**

The viscosity average molecular weight (M_v) of chitosan samples was calculated by Mark-Houwink equation $[\eta] = KM^a$ where $K = 0.076$ and $a = 0.76$ [Rinaudo *et al.* 1999].¹ The viscosity of the chitosan in a buffer solution containing 0.3 M acetic acid (HOAc) and 0.2 M sodium acetate (NaOAc) was measured using a Cannon-Ubbelohde viscometer. The efflux time of the solution in a constant temperature bath at 25 ± 0.1 °C was recorded. The mean of the six replicates was taken for the calculation of M_v . Results are calculated and plotted in Figure A-2. The M_v of chitosan based on the calculation was 80404.

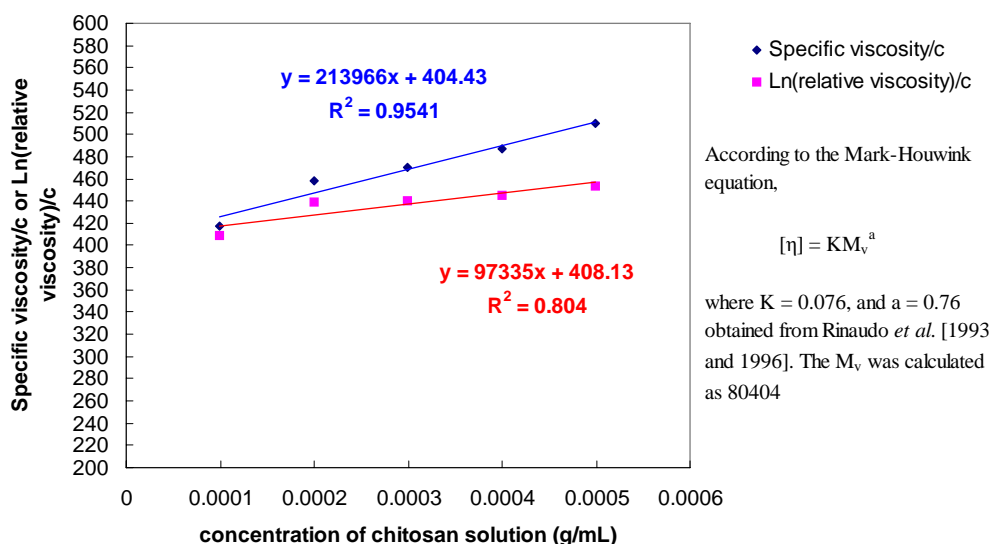


Figure A-2. A plot of specific and relative viscosity of chitosan against chitosan concentration (chitosan dissolved in 0.3 M HOAc/0.2 M NaOAc).

1. (a) Roberts, George A.F. and Domszy, Julian G. "Determination of the viscometric constants for chitosan". *Int. J. Biol. Macromol.* **1982**, 4, 374. (b) Rinaudo, M.; Pavlov G. and Desbrieres, J. "Influence of acetic acid concentration on the solubilization of chitosan". *Polymer* **1999**, 40, 7029.

¹H-NMR spectrum of chitosan and determination of the degree of deacetylation of chitosan²

The degree of deacetylation (DDA) was evaluated from equation (1) by using the integral intensity of methyl carbon (I_{CH_3}) from *N*-acetyl group, and the sum of integral intensities, $I_{\text{H}_2\text{-H}_6}$ of H-2 proton of glucosamine residue, and H-3, H-4, H-5, H-6, H-6' protons of the hexosamine residue (*N*-acetyl-glucosamine and glucosamine). The DDAs of chitosan (Adlrich) was determined as 74 %.

$$\text{DDA (\%)} = \left\{ 1 - \left(\frac{1}{3} I_{\text{CH}_3} / \frac{1}{6} I_{\text{H}_2\text{-H}_6} \right) \right\} \times 100 \text{ ----- (1)}$$

-
2. (a) Hirai, A.; Odani, H.; Nakajima, A. "Determination of Degree of Deacetylation of Chitosan by ¹H NMR Spectroscopy". *Polym. Bull.* **1991**, 26, 87. (b) Rinaudo, M.; Dung, P. L.; Gey C. and Milas, M. "Substituent distribution on *O*, *N*-carboxymethylchitosans by ¹H and ¹³C n.m.r." *Int. J. Biol. Macromol.* **1992**, 14, 122.

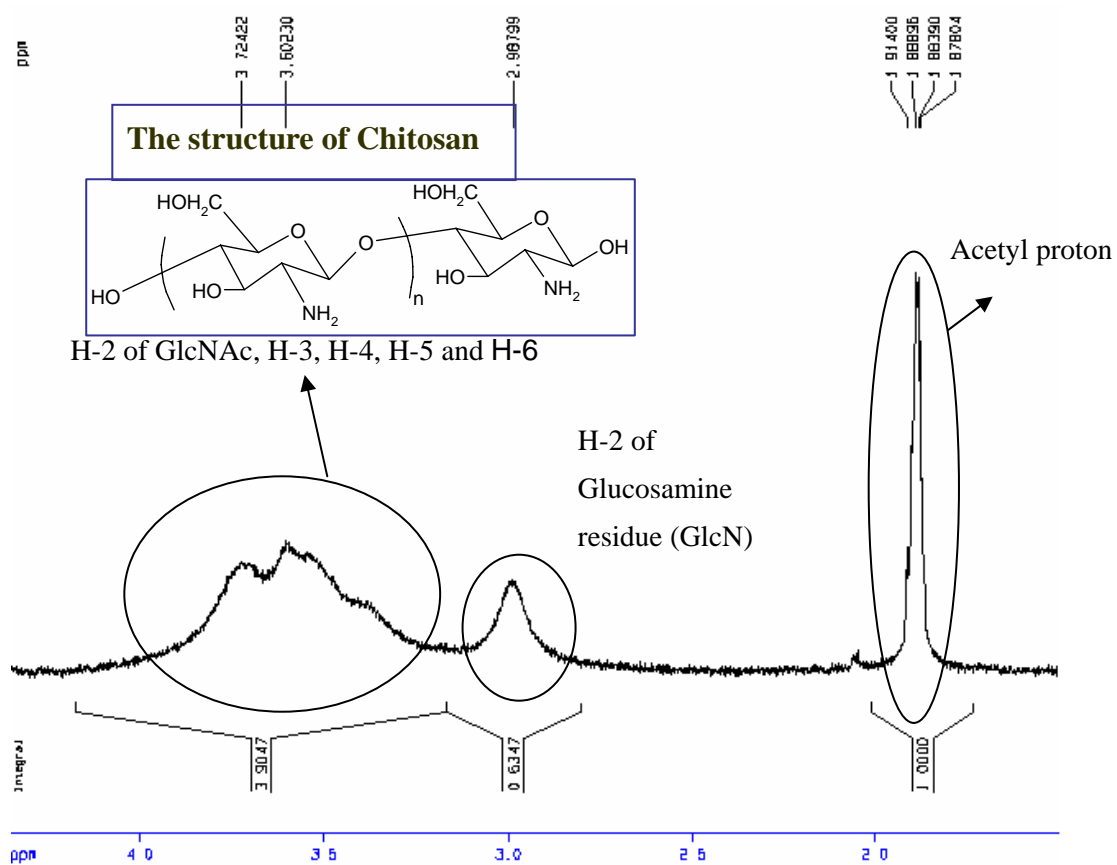


Figure A-3. 400 MHz ^1H -NMR spectrum of chitosan (Aldrich medium M_v), in $\text{CD}_3\text{COOD}/\text{D}_2\text{O}$ solvent (provided by Dr. Leung Man Fai).

B-1. Determination of the compositions of MCS particles (TBHP system)

Sample code: 220305/060505

Recipe: Chitosan (CTS):MMA:MPS-Fe₂O₃ = 2.5:6:1 (w/w/w); solid content =
3.8 %; charged weight (W_i) = 0.95 g

Result obtained after copolymerization:

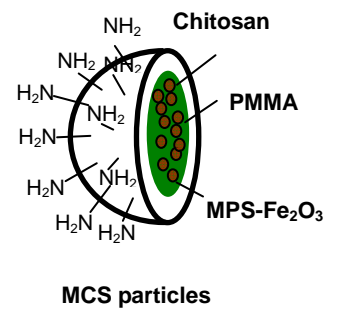
Final weight of MCS particles (W_f) obtained = 0.818 g

MMA conversion = 78 %

precipitate percentage (ppt%) = 33 %

CTS% graft = 38 %

γ-Fe₂O₃ % encapsulated = 8.4 % (8 %)



Determination of the weight of purified MCS particles obtained after copolymerization:

Assume a little amount of chitosan was grafted onto the PMMA-coated

MPS-Fe₂O₃ aggregates

Weight of unpurified MCS particle dispersion obtained (W_{MCS_P})

$$= W_f - (W_i \times \text{ppt}\%)$$

$$= (0.818 \text{ g}) - (0.95 \text{ g} \times 33 \%)$$

$$= 0.5045 \text{ g}$$

Weight of purified MCS particle dispersion ($W_{\text{p-MCSP}}$)

$$= W_{\text{MCSP}} - (\text{weight of chitosan initially added})(\text{un-reacted chitosan})$$

$$= (0.5045 \text{ g}) - ((0.25)(62 \%))$$

$$= 0.3495 \text{ g}$$

Determination of the weight percentage of CTS in purified MCS particles:

$$\text{Weight of CTS on purified MCSP} = (0.25 \text{ g})(38 \%) = 0.095 \text{ g}$$

$$\text{CTS\% in p-MCSP} = \frac{0.095\text{g}}{0.3495\text{g}} \times 100\% = 27 \%$$

Determination of the weight percentage of PMMA in purified MCS particles:

$$\text{Weight of PMMA \%} = 100 \% - \text{CTS \%} - \gamma\text{-Fe}_2\text{O}_3 \%$$

$$= 100\% - 27 \% - 8 \%$$

$$= 65 \%$$

B-2. Determination of the compositions of

MCS particles (H_2O_2 system)

Sample code: 160306-2

Recipe: Chitosan (CTS):MMA:MPS- Fe_2O_3 = 2.5:6:1 (w/w/w); solid content =

3.8 %; charged weight (W_i) = 0.95 g

Result obtained after copolymerization:

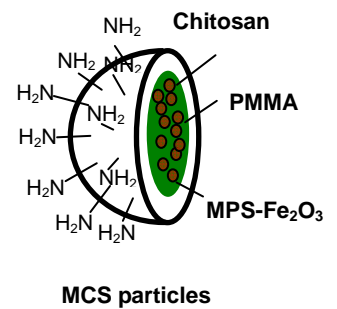
Final weight of MCS particles (W_f) obtained = 0.902 g

MMA conversion = 92 %

precipitate percentage (ppt%) = 19 %

CTS% graft = 33 %

γ - Fe_2O_3 % encapsulated = 7.0 %



Determination of the weight of purified MCS particles obtained after copolymerization:

Assume a little amount of chitosan was grafted onto the PMMA-coated

MPS- Fe_2O_3 aggregates

Weight of unpurified MCS particle dispersion obtained (W_{MCSP})

$$= W_f - (W_i \times \text{ppt}\%)$$

$$= (0.902 \text{ g}) - (0.95 \text{ g} \times 19 \%)$$

$$= 0.7215 \text{ g}$$

Weight of purified MCS particle dispersion ($W_{\text{p-MCSP}}$)

$$= W_{\text{MCSP}} - (\text{weight of chitosan initially added})(\text{un-reacted chitosan})$$

$$= (0.7215 \text{ g}) - ((0.25)(67 \%))$$

$$= 0.554 \text{ g}$$

Determination of the weight percentage of CTS in purified MCS particles:

$$\text{Weight of CTS on purified MCSP} = (0.25 \text{ g})(33 \%) = 0.0825 \text{ g}$$

$$\text{CTS\% in p-MCSP} = \frac{0.0825\text{g}}{0.554\text{g}} \times 100\% = 15 \%$$

Determination of the weight percentage of PMMA in purified MCS particles:

$$\text{Weight of PMMA \%} = 100 \% - \text{CTS \%} - \gamma\text{-Fe}_2\text{O}_3 \%$$

$$= 100\% - 15 \% - 7 \%$$

$$= 78 \%$$

B-3. Determination of the compositions of

MCS particles (120906-1)

Sample code: 120906-1

Recipe: Chitosan (CTS):MMA:MPS-Fe₂O₃ = 2.5:4:1 (w/w/w); solid content = 3

%; charged weight (W_i) = 0.75 g

Result obtained after copolymerization:

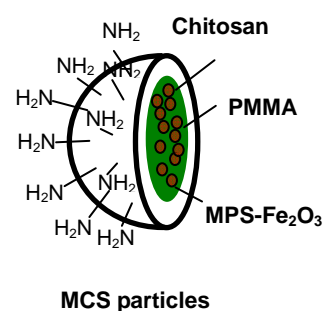
Final weight of MCS particles (W_f) obtained = 0.67 g

MMA conversion = 80 %

precipitate percentage (ppt%) = 17 %

CTS% graft = 40 %

γ-Fe₂O₃ % encapsulated = 16 %



Determination of the weight of purified MCS particles obtained after copolymerization:

Assume a little amount of chitosan was grafted onto the PMMA-coated

MPS-Fe₂O₃ aggregates

Weight of unpurified MCS particle dispersion obtained (W_{MCS_P})

$$= W_f - (W_i \times \text{ppt}\%)$$

$$= (0.67 \text{ g}) - (0.75 \text{ g} \times 17 \%)$$

$$= 0.5425 \text{ g}$$

Weight of purified MCS particle dispersion ($W_{\text{p-MCSP}}$)

$$= W_{\text{MCSP}} - (\text{weight of chitosan initially added})(\text{un-reacted chitosan})$$

$$= (0.5425 \text{ g}) - ((0.25)(60 \%))$$

$$= 0.3925 \text{ g}$$

Determination of the weight percentage of CTS in purified MCS particles:

$$\text{Weight of CTS on purified MCSP} = (0.25 \text{ g})(40 \%) = 0.1 \text{ g}$$

$$\text{CTS\% in p-MCSP} = \frac{0.1 \text{ g}}{0.3925 \text{ g}} \times 100\% = 25 \%$$

Determination of the weight percentage of PMMA in purified MCS particles:

$$\text{Weight of PMMA \%} = 100 \% - \text{CTS \%} - \gamma\text{-Fe}_2\text{O}_3 \%$$

$$= 100\% - 25 \% - 16 \%$$

$$= 59 \%$$

Introduction to Magnetic domains (Weiss domains)

In the early 1900, weiss developed a theory which is so-called “magnetic domain theory” to describe this phenomena.³ He proposed that *bulk* ferromagnetic or ferrimagnetic materials are subdivided into different regions (i.e. domains). Each domain represents the net magnetic moment of a particular magnetism, in which the domains have different orientations of magnetic moments (Figure C-1 a).

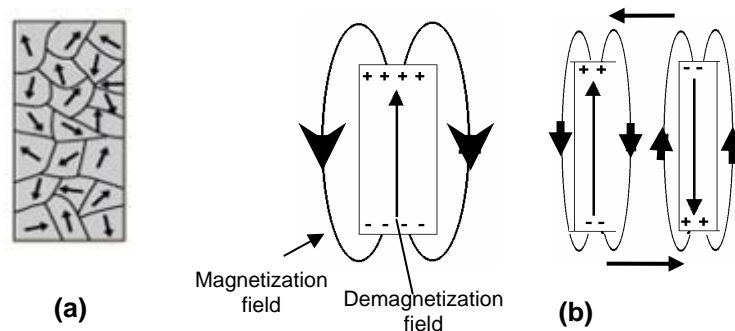


Figure C-1. Illustration of (a) magnetic domains and (b) driving force for the formation of magnetic domains.

The driving force for formation of magnetic domains is to minimize the field energy of a magnetized material. In a magnetized material, magnetic field is generated around the domain, which induces electrical charges on the boundary of the domain as shown in Figure C-1 (b). These flows of charges create the

³ Rosensweig, R. E. *Ferrohydrodynamics*, Cambridge University Press, Cambridge, 1985.

demagnetization field against the magnetization field. The energy associated with the surface charge distribution is called magnetostatic energy. Splitting a single-domain into two domains where their magnetic fields are in an opposite direction, can reduce magnetostatic energy by half. Formation of two domains brings (+) and (-) charges closer together, thus decreasing the *spatial extent of the demagnetization field*. However, the subdivision of magnetic domains is unable to continue indefinitely because the transition region between domains (i.e. a domain wall) requires energy to be produced and maintained. The width of a domain wall depends on the balance between magnetocrystalline and exchange energy. Eventually, an equilibrium number of domains is reached for a given particle size. The size of a domain is approximately from 0.05 to 0.5 μm .⁴

1.1 Magnetic anisotropy

Magnetic anisotropy is the dependence of magnetic properties of a material. The common types of anisotropy are (1) magnetocrystalline anisotropy, (2) shape anisotropy, (3) exchange anisotropy, (4) stress anisotropy, and (5) externally induced anisotropy.⁴ The most common types of anisotropy observed in magnetic materials are magnetocrystalline, shape and exchange anisotropy.

⁴ Dunlop, D. J. *Science* 1972, 176, 41

Magnetic anisotropy is the energy associated with the alignment of magnetic moments in a single crystal from the easy (i.e. preferred direction) to the hard direction (i.e. magnetized direction) (Figure C-2).

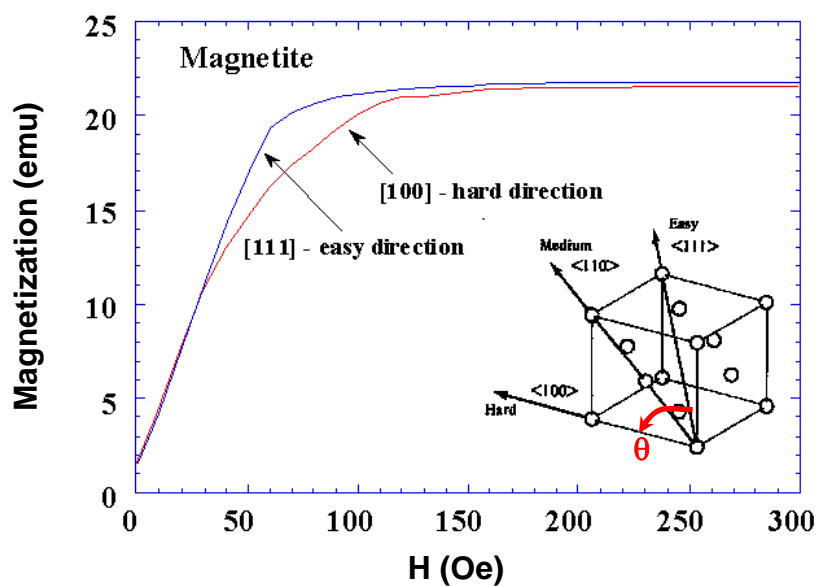


Figure C-2. A magnetization curve for magnetite. (<111> is the preferred direction of magnetization, <110> is the intermediate direction, and <100> is the hard direction of magnetization)

According to the Stoner-Wohlfarth theory, the magnetic anisotropy (E_A) can often be modeled as uniaxial in character and represented by its simplest form (Equation 1.1):

$$E_A = KV\sin^2\theta \quad (1.1)$$

where K is the effective uniaxial anisotropy energy per unit volume (which is a function of five anisotropies), V is the volume of the nanoparticle, and θ is the

angle between the magnetization direction and the easy axis of the nanoparticle.

1.1.1 Magnetocrystalline anisotropy

Magnetocrystalline anisotropy is the energy barrier for crystallographic orientation of magnetic domains from $\langle 111 \rangle$ to $\langle 100 \rangle$. The energy barrier between easy and hard direction arises from spin-orbit coupling, but is independent on particle shape.⁴ Figure C-3 shows the existence of a wide domain wall causes high magnetocrystalline anisotropy because the spins within the wall are no longer aligned along an easy axis of magnetization, while a thin domain wall results in low magnetocrystalline anisotropy. A polycrystalline sample with no preferred grain orientation has no net magnetocrystalline anisotropy due to averaging over all orientations.⁴ A nonspherical polycrystalline specimen can possess shape anisotropy. A specimen with cylindrical shape is easier to magnetize along the long direction than along the short directions. A symmetric shape, such as a sphere, will have no net shape anisotropy.⁴

⁴ Leslie-Pelecky, D. L.; Rieke, R. D. *Chem. Mater.* 1996, 8, 1770.

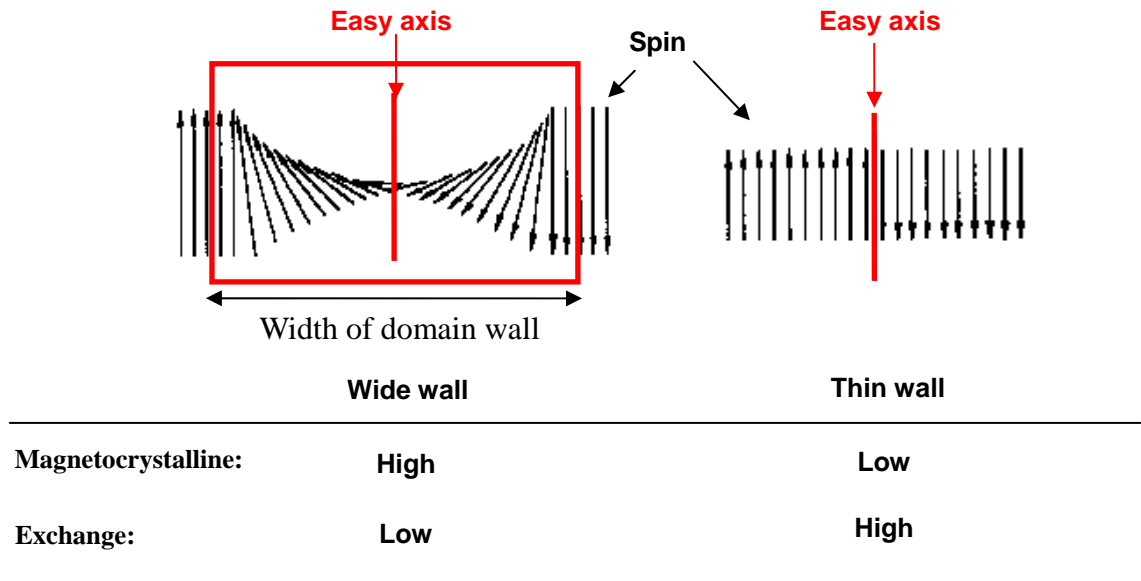


Figure C-3. Illustration of energy balance between magnetocrystalline and exchange anisotropy for the domain wall formation.

1.1.2 Exchange anisotropy

Exchange anisotropy is the energy associated with lining up the magnetic moments. As is shown in Figure C-3, a wide domain wall has low exchange energy because the spins rotate gradually within the domain wall. A thin domain wall has higher exchange energy during the spin rotation because changes in magnetic moment direction can no longer occur through domain wall motion. Therefore, the width of a domain wall depends on the balance between magnetocrystalline and exchange energy.

2.1 Magnetic Properties of single-domain particles

As mentioned earlier, the size of magnetic domains is around 50 to 500 nm.

As the particle size of magnetic materials decreases, the number of magnetic domains per particle also decreases. When the size decreases down to the limit where the domain wall is energetically unfavorable to exist, the size reaches a single-domain size.⁵ Due to the absence of the domain wall, the energy associated with magnetocrystalline anisotropy is low, as discussed in Section 1.1.1. This means that less energy is required to align magnetic moments from easy axis to hard axis when SD particles are placed in an applied magnetic field. Hence, SD particles have lower magnetic susceptibility, compared with multi-domain (MD) particles.⁶

When the field is removed, the orientation of magnetic moments in a single-domain (SD) particle becomes very difficult because high energy is required to overcome the exchange energy related to spin rotation. This means that changes in magnetization direction can no longer occur through domain wall motion but instead require the coherent rotation of magnetic moments. Due to such a high exchange energy, SD particles have much larger coercive forces than MD particles⁴(Figure C-4).

⁵ Wohlfarth, E. P. *J. Magn. Mater.* 1983, 39, 39.

⁶ Blum, E.; Cebers, A.; Maiorov, M. M. *Magnetic Fluids*, Walter de Gruyter, Berlin, 1997.

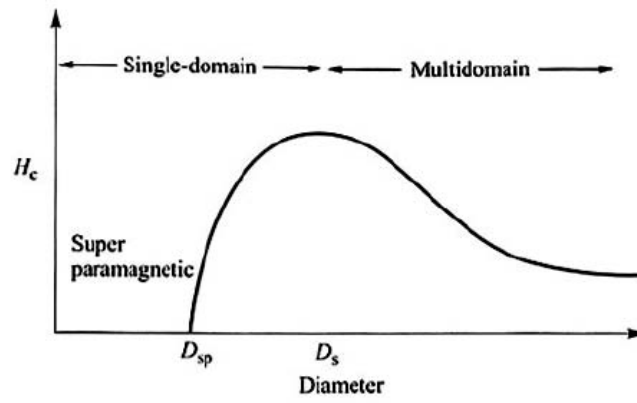


Figure C-4. A correlation of coercivity (H_c) as a function of particle diameter. (D_{sp} is the superparamagnetic size and D_s is the single domain particle size) [Adapted from Sorensen 2001].

References

1. Beiser, A. “*Modern Technical Physics*”, 2 ed., Cummings Publishing Company, Menlo Park, **1973**.
2. Kittel, C. “*Introduction to Solid State Physics*”, Wiley, New York, 1976.
3. Sorensen, C. M. “*Nanoscale Materials in Chemistry*”, John Wiley and Sons, Inc. New York, **2001**, pp. 169.
4. Wohlfarth, E. P. “Magnetic properties of single domain ferromagnetic particles”. *J. Magn. Magn. Mater.* **1983**, 39, 39.
5. Liu, C.; Rondinone, A, J.; Zhang, Z. J. “Synthesis of magnetic spinel ferrite CoFe_2O_4 nanoparticles from ferric salt and characterization of the size-dependent superparamagnetic properties”. *Pure Appl. Chem.* **2000**, 72, 37.
6. Jeong, J.; Lee, S.; Kim, J.; Shin, S. “Magnetic properties of $\gamma\text{-Fe}_2\text{O}_3$ nanoparticles made by coprecipitation method”. *Phys. Stat. Sol. (b)* **2004**, 241, 1593.
7. Huang, H.; Yang, S.; Gu, G. “Preparation of carbon-coated cobalt nanocrystals in a new gas blow arc reactor and their characterization”. *J. Phys. Chem. B* **1998**, 102, 3420.
8. Sun, X.; Gutierrez, A.; Yacaman, M. J.; Dong, X.; Jin, S. “Investigations on magnetic properties and structure for carbon encapsulated nanoparticles of Fe,

- Co, Ni". *Mater. Sci. Eng. A* **2000**, 286, 157.
9. Sun, S. H.; Zeng, H.; Robinson, D. B.; Raoux S.; Rice, P. M.; Wang, S. X.; Li, G. X. "Monodisperse MFe_2O_4 (M = Fe, Co, Mn) nanoparticles". *J. Am. Chem. Soc.* **2004**, 126, 273.
 10. Cornell, R. M.; Schertmann, U. "*Iron oxides in the laboratory: preparation and characterization*", VCH, Weinheim, 2000.
 11. Cornell, R. C.; Schertmann, U. "*The iron oxides: Structure, Properties, Reactions, Occurrence and Uses*", VCH Publishers, Weinheim, 2003.
 12. Massart, R. "Preparation of aqueous magnetic liquids in alkaline and acidic media". *IEEE Trans. Magn.* **1981**, 17, 1247
 13. Bacri, J.; Perzynski, R.; Salin, D.; Cabuil, V.; Massart, R. "Ionic ferrofluids: a crossing of chemistry and physics" *J. Magn. Magn. Mater.* **1990**, 85, 27.
 14. Wooding, A.; Kilner, M.; Lambrick, D. B. "Studies of the double surfactant layer stabilization of water-based magnetic fluids" *J. Colloid Interf. Sci.* **1991**, 144, 236.
 15. Yu, S.; Chow G. M. "Carboxyl group ($-CO_2H$) functionalized ferrimagnetic iron oxide nanoparticles for potential bio-applications" *J. Mater. Chem.* **2004**, 14, 2781.
 16. Tourinho, F. A.; Franck, R.; Massart, R.; Perzynski, R. *Prog. Colloid. Polym.*

Sci. **1989**, 79,128.

17. Hafeli, U.; Schütt, W.; Teller, J.; Zborowski, M. “*Scientific and Clinical Applications of Magnetic Carriers*” **1997**, Plenum Press, New York and London, Part A.
18. Molday, R .S. “*Cell Separation, Methods and Selected Applications*” **3**, Academic Press, NY, **1984**, P. 237–248.
19. Ugelstad, J.; Berge, A.; Ellingsen, T.; Schmid, R.; Nilsen, T. N.; Moerk, P. C.; Stenstad, P.; Hornes, E.; Olsvik, O. “Preparation and application of new monosized polymer particles” *Progress in Polymer Science* **1992**, 17(1), 87-161.
20. Freeman, M. W.; Arrot, A.; Watson, J. H. L. “Magnetism in medicine” *J. Appl. Phys.* **1960**, 31, 404.
21. Gupta, P. K.; Hung, C. T. “*Microspheres and Regional Cancer Therapy: Magnetically Controlled Targeted Chemotherapy*” Chapter 4.
22. Langer, R. “New method of drug delivery” *Science* **1990**, 249,1527.
23. Gao, H.; Wang, J. Y.; Shen, X, Z.; Den, Y. H.; Zhang, W. “Preparation of magnetic poly(butylcyanoacrylate) nanospheres encapsulated with aclacinomycin A and its effect on gastric tumor” *World J. Gastroenterol* **2004**, 10, 2010.

24. Kato, T. "Encapsulated drugs in targeted cancer therapy, in Bruck S D (Ed.), *Controlled Drug Delivery*" **1982**, v.2, CRC Press Boca Raton, FL, 189.
25. Widder, K. J.; Morris, R. M. "Tumor remission in yoshida sarcoma-bearing rats by selective targeting of magnetic albumin microspheres containing doxorubicin". *Proc. Natl. Acad. Sci. USA* **1981**, 78(1), 579.
26. Kiwada, H.; Sato, J.; Yamada, S.; Kato, Y. *Chem. Pharm. Bull.* **1986**, 34, 4253.
27. Ito, R.; Machida, Y.; Sannan, T.; Nagai, T. "Magnetic granules: a novel system for specific drug delivery to esophageal mucosa in oral administration". *Int. J. Pharm.* **1990**, 61, 109.
28. Alexiou, C.; Arnold, W.; Klein, R. J.; Parak, F. G.; Hulin, P.; Bergemann, C. "Locoregional cancer treatment with magnetic drug targeting". *Canc. Res.* **2000**, 60, 6641.
29. Nobuto, H.; Sugita, T.; Kubo, T.; Shimose, S.; Yasunaga, Y.; Murakami, T.; Ochi, M. "Evaluation of systemic chemotherapy with magnetic liposomal doxorubicin and a dipole external electromagnet". *Int. J. Cancer.* **2004**, 109, 627.
30. Moroz, P.; Jones, S. K.; Gary, B. N. *Int. J. Hyperthermia* **2002**, 18, 267.
31. Gupta, A. K.; Gupta, M. "Synthesis and surface engineering of iron oxide

- nanoparticles for biomedical applications”. *Biomaterials* **2005**, 26, 3995.
32. Hiergeist, R.; Andra, W.; Buske, N.; Hergt, R.; Hilger, I.; Richter, U.; Kaiser, W. “Application of magnetite ferrofluids for hyperthermia”. *J. Magn. Magn. Mater.* **1999**, 201, 420.
33. Gilchrist, R. K.; Medal, R.; Shorey, W. D.; Hanselman, R. C.; Parrott, J. C.; Taylor, C. B. *Ann. Surg.* **1957**, 146, 596.
34. Jordan, A.; Scholz, R.; Wust, P.; Fahling, H.; Felix, R. “Magnetic fluid hyperthermia (MFH): cancer treatment with AC magnetic field induced excitation of biocompatible superparamagnetic nanoparticles”. *J. Magn. Magn. Mater.* **1999**, 201, 413.
35. Chan, D. C. F.; Kirpotin, D. B.; Bunn, P. A. “Synthesis and evaluation of colloidal magnetic iron oxides for the site-specific radiofrequency-induced hyperthermia of cancer”. *J. Magn. Magn. Mater.* **1993**, 122, 374.
36. Rosensweig, R. E. “Heating magnetic fluid with alternating magnetic field”. *J. Magn. Magn. Mater.* **2002**, 252, 370.
37. (a) Tartaj, P.; Morales, M. P.; Veintemillas-Verdaguer, S. González-Carreño, T.; Serna, C. J. “The preparation of magnetic nanoparticles for applications in biomedicine”. *J. Phys. D. Appl. Phys.* **2003**, 36, R182. (b) Morales, M. P.; Veintemillas-Verdaguer, S.; Montero, M. I.; Serna, C. J.; Roig, A.; Casas,

- Ll ; Martinez, B.; Sandiumenge, F. "Surface and internal spin canting in γ -Fe₂O₃ nanoparticles" *Chem. Mater.* **1999**, *11*, 3058.
38. Coroiu, I. "Relaxivities of different superparamagnetic particles for application in NMR tomography". *J. Magn. Magn. Mater.* **1999**, *201*, 449.
39. Louie, A. Y.; Hüber, M.M.; Ahrens, E. T.; Rothbächer, U.; Moats, R.; Jacobs, R. E.; Fraser, S.E.; Meade, T.J. "In vivo visualization of gene expression using magnetic resonance imaging". *Nature Biotechnology* **2000**, *18*, 321.
40. Babes, L.; Denzot, B., Tanguy, G., Le Jeune, J. J.; Jallet, P. "Synthesis of iron oxide nanoparticles used as MRI contrast agents: a parametric study". *J. Colloid. Interface Sci.* **1999**, *212*, 474.
41. Lawaczeck, R.; Bauer, H.; Frenzel, T.; Hasegawa, M.; Ito, Y.; Kito, K.; Miwa, N.; Tsutsui, H.; Vogler, H.; Weinmann, H. J. *Acta Radiol.* **1997**, *38*, 584.
42. Pankhurst, Q. A.; Connolly, J.; Jones, S. K.; Dobson, J. "Applications of magnetic nanoparticles in biomedicine". *J. Phys. D. Appl. Phys.* **2003**, *36*, R167.
43. Berry, C. C; Curtis, A. S. G. "Functionalisation of magnetic nanoparticles for applications in biomedicine". *J Phys D: Appl Phys* **2003**, *36*, R198.
44. Bonnemain, B. "Superparamagnetic agents in magnetic resonance imaging: physicochemical characteristics and clinical applications. A review" *J. Drug*

Target. **1998**, 6, 167.

45. (a) Chung, D. D. L. "Materials for electromagnetic interference shielding". *J. Mater. Eng. Performance* **2000**, 9, 350; (b) Chung, D. D. L. "Electromagnetic interference shielding effectiveness of carbon materials". *Carbon* **2001**, 39, 279.
46. Tang, B. Z.; Geng, Y.; Lam, J. W. Y.; Li B.; Jing, X.; Wang, X.; Wang, F.; Pakhomov, A. B.; Zhang, X. X. "Processible nanostructured materials with electrical conductivity and magnetic susceptibility: preparation and properties of maghemite/polyaniline nanocomposite films". *Chem. Mater.* **1999**, 11, 1581.
47. Nguyen, T.; Diaz, A. "A novel method for the preparation of magnetic nanoparticles in a polypyrrole powder". *Adv. Mater.* **1994**, 6, 858.
48. Bidan, G.; Jarjays, O.; Fruchart, J. M.; Hannecart, E. "New nanocomposites based on "tailor dressed" magnetic particles in a polypyrrole matrix". *Adv. Mater.* **1994**, 6, 152.
49. Wan, M.; Li, W. "A composite of polyaniline with both conducting and ferromagnetic functions". *J. Polym. Sci. Polym. Chem.* **1997**, 35, 2129.
50. Ray, K.; Moskowitz, R. "Commercial applications of ferrofluids". *J. Magn. Mater.* **1990**, 85, 233.
51. Hamley, I. W. "Nanotechnology with Soft Materials". *Angew. Chem. Int. Ed.*

2003, 42, 1692.

52. Tourinho, F. A.; Franck, R.; Massart, R. "Aqueous ferrofluids based on manganese and cobalt ferrites" *J. Mater. Sci.* **1990**, 25, 3294.
53. Fauconnier, N.; Bee, A.; Roger, J.; Pons, J. N. "Adsorption of gluconic and citric acids on maghemite particles in aqueous medium" *Prog. Colloid Polym. Sci.* **1996**, 100, 212.
54. Wu, K. T.; Kuo, P. C.; Yao, Y. D.; Tsai, E. H. "Magnetic and optical properties of Fe₃O₄ nanoparticle ferrofluids prepared by coprecipitation technique". *IEEE Transactions on Magnetics* **2001**, 37, 2651.
55. Yee, C.; Kataby, G.; Ulman, A.; Prozorov, T.; White, H.; King, A.; Rafailovich, M.; Sokolov, J.; Gedanken, A. "Self-assembled monolayers of alkanesulfonic and -phosphonic acids on amorphous iron oxide nanoparticles". *Langmuir* **1999**, 15, 7111
56. Van, Ewijk, G. A.; Vroege, G. J.; Philipse, A. P. "Convenient preparation methods for magnetic colloids". *J. Magn. Magn. Mater.* **1991**, 201, 31.
57. Deng, Y. H.; Wang, C. C.; Hu, J. H.; Yang, W. L.; Fu, S. K. "Investigation of formation of silica-coated magnetite nanoparticles via sol-gel approach" *Colloids and Surface A. Physiochem. Eng. Aspects.* **2005**, 262, 87.
58. Burugapalli, K.; Koul, V.; Dinda, A. K. "Effect of composition of

interpenetrating polymer network hydrogels based on poly(acrylic acid) and gelatin on tissue response: A quantitative in vivo study". *J. Biomed. Mater. Res.* **2004**, 68A, 210.

59. Zhang, Y.; Kohler, N.; Zhang, M. "Surface modification of superparamagnetic magnetite nanoparticles and their intracellular uptake". *Biomaterials* **2002**, 23, 1553.
60. Gupta, A. K.; Curtis, A. S. G. "Surface modified superparamagnetic nanoparticles for drug delivery: interaction studies with human fibroblasts in culture". *J. Mater. Sci. Mater. Med.* **2004**, 15, 493.
61. Shan, G. B.; Xing, J. M.; Luo, M. F.; Liu, H. Z.; Chen, J. Y. "Immobilization of pseudomonas delafieldii with magnetic polyvinyl alcohol beads and its application in biodesulfurization". *Biotechnol. Lett.* **2003**, 25, 1977.
62. Honda, H.; Kawabe, A.; Shinkai, M.; Kobayashi, T. "Recovery of recombinant escherichia coli by chitosan-conjugated magnetite". *Biochem. Eng. J.* **1999**, 3, 157.
63. Chang, Y. C.; Chen, D. H. "Preparation and adsorption properties of monodisperse chitosan-bound Fe₃O₄ magnetic nanoparticles for removal of Cu(II) ions". *J. Colloid Interface Sci.* **2005**, 283, 446.
64. Bergemann, C.; Müller-Schulte, D.; Oster, J.; Brassard, L.; Lübke, A. S.

- “Magnetic ion-exchange nano- and microparticles for medical, biochemical and molecular biological applications”. *J. Magn. Magn. Mater.* **1999**, *194*, 45.
65. Berry, C. C.; Wells, S.; Charles, S.; Curtis, A. S. G. “Dextran and albumin derivatised iron oxide nanoparticles: influence on fibroblasts in vitro”. *Biomaterials* **2003**, *24*, 4551.
66. Weissleder, R.; Bogdanov, A.; Neuweltb, E. A.; Papisov, M. “Long-circulating iron oxides for MR imaging”. *Adv. Drug. Del. Rev.* **1995**, *16*, 321.
67. Bulte, J. M.; Vymazal, J.; Brooks, R. A.; Pierpaoli, C.; Frank, J. A. “Frequency dependence of MR relaxation times II. Iron oxides”. *J. Magn. Reson. Imaging* **1993**, *3*, 641.
68. Pileni, M. P. “Reverse micelles as microreactors”. *J. Phys. Chem.* **1993**, *97*, 6961.
69. López-Quintela, M. A.; Rivas, J. “Chemical reactions in microemulsions: a powerful method to obtain ultra-fine particles”. *J. Colloid. Interface Sci.* **1993**, *158*, 446.
70. Feltin, N.; Pileni, M. P. “New Technique for Synthesizing Iron Ferrite Magnetic Nanosized Particles”. *Langmuir* **1997**, *13*, 3927.

71. Lee, Y.; Lee, J.; Bae, C. J.; Park, J. Noh, H.; Park, J.; Hyeon, T. "Large-scale synthesis of uniform and crystalline magnetite nanoparticles using reverse micelles as nanoreactors under reflux conditions". *Adv. Funct. Mater.* **2005**, *15*, 503.
72. Lee, K. M.; Sorensen, C. M.; Klabunde, K. J.; Hadjipanayis, G. C. "Synthesis and characterization of stable colloidal Fe₃O₄ particles in water-in-oil microemulsions". *IEEE Transactions on Magnetics* **1992**, *28*, 3180.
73. Dresco, P. A.; Zaitsev, V. S.; Gambino, R. J.; Chu, B. "Preparation and properties of magnetite and polymer magnetite nanoparticles" *Langmuir* **1999**, *15*, 1945.
74. O'Connor, C. J.; Seip, C.; Sangregorio, C.; Carpenter, E.; Li, S.; Irvin, G.; John, V. T. "Nanophase magnetic materials: synthesis and properties" *Molecular Crystals and Liquid Crystals* **1999**, *335*, 1135.
75. Yaacob, I.; Nunes, A. C.; Bose, A.; Shah, D. O. "Synthesis and characterization of magnetic nanoparticles in spontaneously generated vesicles" *J. Colloid Interface Sci.* **1994**, *168*, 289.
76. Carpenter, E. E. "Iron nanoparticles as potential magnetic carriers" *J. Magn. Mater.* **2001**, *225*, 17.
77. Liz, L.; Lopez-Quintela, M. A.; Mira, J.; Rivas, J. "Preparation of colloidal

- Fe₃O₄ ultrafine particles in microemulsions” *J. Mater. Sci.* **1994**, *29*, 3797.
78. Rockenberger, J.; Scher, E. C. Alivisatos, A. P. “A new nonhydrolytic single-precursor approach to surfactant-capped nanocrystals of transition metal oxides” *J. Am. Chem. Soc.* **1999**, *121*, 11595.
79. Hyeon, T.; Lee, S. S.; Park, J.; Chung, Y.; Na, H. B. “Synthesis of highly crystalline and monodisperse maghemite nanocrystallites without a size-selection process” *J. Am. Chem. Soc.* **2001**, *123*, 12798.
80. Sun, S.; Zeng, H. “Size-controlled synthesis of magnetite nanoparticles” *J. Am. Chem. Soc.* **2002**, *124*, 8204.
81. Park, J.; Lee, E.; Hwang, N.; Kang, M.; Kim, S. C.; Hwang, Y.; Park, J.; Noh, H.; Kim, J.; Park, J.; Hyeon, T. “One-nanometer-scale size-controlled synthesis of monodisperse magnetic iron oxide nanoparticles” *Angew. Chem. Int. Ed.* **2005**, *44*, 2872.
82. Bourgeat-Lami, E.; Lang J. “Encapsulation of inorganic particles by dispersion polymerization in polar media: 1. silica nanoparticles encapsulated by polystyrene” *J. Colloid Interface Sci.* **1998**, *197*, 293.
83. Ugelstad, J.; Stenstad, P.; Kilass, L.; Prestvik, W. S.; Herje, R.; Bererge, A.; Hornes, E. “Monodisperse magnetic polymer particles. New biochemical and biomedical applications” *Blood Purif.* **1993**, *11*, 349.

84. Denkbas, E. B.; Kilicay, E.; Birlikseven, C.; Ozturk, E. "Magnetic chitosan microspheres: preparation and characterization" *React. & Funct. Polym.* **2002**, *50*, 225.
85. Gupta, P. K.; Hung, T. C.; Lam, F. C.; Perrier, D. G. "Albumin microspheres. III. Synthesis and characterization of microspheres containing adriamycin and magnetite" *Int. J. Pharm.* **1988**, *43* 167.
86. Chatterjee, J.; Haik, Y.; Chen, C. *US patent*, **2003**, 6,989,196.
87. Hassen, E. E.; Parish, R. C.; Gallo, J. M. "Optimized formulation of magnetic chitosan microspheres containing the anticancer agent" Oxantrazole *Pharm. Res.* **1992**, *9*, 390.
88. Rorrer, G. L.; Hsien, T.; Way, J. D. "Synthesis of porous-magnetic chitosan beads for removal of cadmium ions from wastewater" *Ind. Eng. Chem. Res.* **1993**, *32*, 2170.
89. Honda, H; Kawabe, A.; Shinkai, M.; Kobayashi, T. "Development of Chitosan-Conjugated Magnetite for Magnetic Cell Separation" *J. Fermant. Bioeng.* **1998**, *86*, 191.
90. Müller-Schulte, D.; Brunner, D. "Novel magnetic microspheres on the basis of poly(vinyl alcohol) as affinity medium for quantitative detection of glycated haemoglobin" *J. Chromatogr. A.* **1995**, *711*, 53.

91. Fendler, J. H. “*Nanoparticles and Nanostructured Films: Preparation, Characterization and Application*” **1998**, Weinheim, Wiley-VCH.
92. Ulman, A. “*An Introduction to Ultrathin Organic Films: From Langmuir-Blodgett to Self-assembly*” **1991**, Boston: Academic.
93. Caruso, F.; Susa, A. S.; Giersig, M.; Möhwald, H. “Magnetic core-shell particles: preparation of magnetite multilayers on polymer latex microspheres” *Adv. Mater.* **1999**, *11*, 950.
94. Sauzedde. F.; Elaissari. A.; Pichot. C. “Hydrophilic magnetic polymer latexes.
1. Adsorption of magnetic iron oxide nanoparticles onto various cationic latexes” *Colloid Polym. Sci.* **1999**, *277*, 846.
95. Sauzedde. F.; Elaissari. A.; Pichot. C. “Hydrophilic magnetic polymer latexes.
2. Encapsulation of adsorbed iron oxide nanoparticles” *Colloid Polym. Sci.*, **1999**, *277*, 1041.
96. Deng, Y. H.; Yang, W.; Wang, C.; Fu, S. K. “A novel approach for preparation of thermoresponsive polymer magnetic microspheres with core-shell structure” *Adv. Mater.* **2003**, *15*, 1729.
97. Zaitsev, V. S.; Filimonov, D. S.; Presnyakov, I. A.; Gambino, R. J.; Chu, B. “Physical and chemical properties of magnetite and magnetite-polymer nanoparticles and their colloidal dispersions” *J. Colloid Interface Sci.* **1999**,

212, 49.

98. Gu, S.; Shiratori, T.; Konno, M. "Synthesis of monodisperse, magnetic latex particles with polystyrene core" *Colloid Polym. Sci.* **2003**, 281, 1076.
99. Daniel, J. C.; Schuppiser, J. L.; Tricot, M. *US Patent* **1982**, 4358388.
100. Charmot, D; Vidil, C. *US Patent* **1994**, 5356713.
101. Wormuth, K. "Superparamagnetic latex via inverse emulsion polymerization" *J. Colloid. Interface Sci.* **2001**, 241, 366.
102. Ugelstad, J.; El-Aasser, M. S.; Vanderhoff, J. W. "Emulsion polymerization. Initiation of polymerization in monomer droplets" *J. Polym. Sci., Polym. Lett. Ed.* **1973**, 11, 503.
103. Tiarks, F.; Landfester, K.; Antonietti, M. "Encapsulation of carbon black by miniemulsion polymerization" *Macromol. Chem. Phys.* **2001**, 202, 51.
104. Bechthold, N.; Tiarks, F.; Willert, M.; Landfester, K.; Antonietti, M. "Miniemulsion polymerization: applications and new materials" *Macromol. Symp.* **2000**, 151 549.
105. Pamírez, L. P.; Landfester, K. "Magnetic polystyrene nanoparticles with a high magnetite content obtained by miniemulsion processes" *Macromol. Chem. Phys.* **2003**, 204, 22.
106. Xu, Z.Z.; Wang, C.C.; Yang, W.L.; Deng, Y.H.; Fu, S.K. "Encapsulation of

- nanosized magnetic iron oxide by polyacrylamide via inverse miniemulsion polymerization” *J. Magn. Magn. Mater.* **2004**, 277, 136.
107. Chen, C.; Liao, W. and Tsai, G. “Antibacterial effects of *N*-sulfonated and *N*-sulfobenzoyl chitosan and application to oyster preservation” *J. Food Protect.* **1998**, 61, 1124.
108. Shahidi, F.; Arachchi, J. K. V.; Jeon, Y. J. “Food applications of chitin and chitosans” *Trends Food Sci. Tech.* **1999**, 10, 37.
109. (a) Li, Pei; Zhu, Junmin; Sunintaboon, Panya; Harris, Frank W. “New route to amphiphilic core-shell polymer nanospheres: graft copolymerization of methyl methacrylate from water-soluble polymer chains containing amino groups” *Langmuir* **2002**, 18, 8641. (b) Li, Pei; Zhu, Jun Min; Harris, Frank W. “Amphiphilic core-shell latexes” *U.S. Patent* **2003**, 6573313.
110. (a) Dahneke, B. E. “*Measurement of Suspended Particles by Quasi-Elastic Light Scattering*”, John Wiley & Sons, **1983**, pp. 119–236. (b) <http://www.malvern.co.uk/home/index.html>.
111. Zhao, S.; Kee, D. K.; Kim C. W.; Cha G. G.; Kim, Y. H.; Kang, Y. S. “Synthesis of magnetic nanoparticles of Fe_3O_4 and CoFe_2O_4 and their surface modification by surfactant adsorption” *Bull. Korean Chem. Soc.* **2006**, 27, 237.

112. Li, M.; Schnablegger, H.; Mann, S. "Coupled synthesis and self-assembly of nanoparticles to give structures with controlled organization" *Nature* **1999**, *402*, 393.
113. Lin-Vien, D.; et al. "*The Handbook of IR and Raman Characteristic Frequencies of Organic Molecules*" Academic Press: New York, **1991**, pp. 137.
114. Alcántara, R.; Lavela, P.; Tirado, J. L. "Lithium-Nickel Citrate Precursors for the Preparation of LiNiO₂ Insertion Electrodes" *Chem. Mater.* **1997**, *9*, 2145.
115. Huignard, A.; Buissette, V.; Laurent, G.; Gacoin, T.; Boilot J. P. "Synthesis and Characterizations of YVO₄: Eu Colloids" *Chem. Mater.* **2002**, *14*, 2264.
116. Stöber, W.; Fink, A.; Bohn, E. "Controlled growth of monodisperse silica spheres in the micron size range" *J. Colloid Interf. Sci.* 1968, *26*, 62.
117. Wright, J. D. "*Sol-Gel Materials: Chemistry and Applications*", Australia: Gordon and Breach Science Publishers, 2001, Chapter 2.
118. Badley, R. D.; Ford, W. T.; McEnroe, F. J.; Assink, R. A. "Surface modification of colloidal silica" *Langmuir* **1990**, *6*, 792.
119. Wei, Y.; Wang, W.; Yang, D.; Tang L. "Synthesis of water-soluble polyacrylics modified silica sol-gel materials" *Chem. Mater.* **1994**, *6*, 1737.
120. Gao, Z; Yu, J. "Grafting of dendritic polyethers onto nanometre silica

- surface” *J. Mater. Sci.* **2002**, *12*, 468.
121. Badley, R. D.; Ford, W. T.; McEnroe, F. J.; Assink, R. A. “Surface modified colloidal silica”. **1990**, *6*, 792.
122. Fei, B.; Lu, H.; Xin, J. H. “One-step preparation of organosilica@chitosan crosslinked nanospheres”. *Polymer* **2006**, *47*, 947.
123. Zhu, J. M.; Tang, A.; Law, L. P.; Feng, M.; Ho, K. M.; Lee, D. K. L.; Harris, F. W.; Li, P. “Amphiphilic Core-Shell Nanoparticles with Poly(ethylenimine) Shells as Potential Gene Delivery Carriers”. *Bioconjugate Chemistry* **2005**, *16*, 139.
124. Feng, Min; Lee, Daniel; Li, Pei. “Intracellular uptake and release of poly(ethyleneimine)-co-poly(methyl methacrylate) nanoparticle/pDNA complexes for gene delivery” *International Journal of Pharmaceutics* **2006**, *311*, 209.
125. (a) Ye, Weijun; Leung, Man Fai; Xin, John; Kwong, Tsz Leung; Lee, Daniel Kam Len; Li, Pei. “Novel core-shell particles with poly(n-butyl acrylate) cores and chitosan shells as an antibacterial coating for textiles” *Polymer* **2005**, *46*, 10538. (b) Xin, John Haozhong; Li, Pei; Ye, Weijun. “Polymer latex emulsion containing chitosan core-shell particles for use as textile's antibacterial finishing agents” *U.S. Patent pending*; (c) Ye, Weijun; Xin, John

- H.; Li, Pei; Lee, Kam-Len Daniel; Kwong, Tsz-Leung. "Durable antibacterial finish on cotton fabric by using chitosan-based polymeric core-shell particles" *Journal of Applied Polymer Science* **2006**, *102*, 1787.
126. Hirai, A.; Odani, H.; Nakajima, A. "Determination of degree of deacetylation of chitosan by proton NMR spectroscopy" *Polym. Bull.* **1991**, *26*, 87.
127. Laukkanen, A.; Wiedmer, S. K.; Varjo, S.; Riekkola, M. L.; Tenhu, H. "Stability and thermosensitive properties of various poly(*N*-vinylcaprolactam) microgels" *Colloid Polym. Sci.* **2002**, *280*, 65.
128. Kataokaa, K.; Haradaa, A.; Nagasaki, Y. "Block copolymer micelles for drug delivery: design, characterization and biological significance" *Adv. Drug. Del. Rev.* **2001**, *47*, 113.
129. Bourgeat-Lami, E.; Tissot, I.; Lefebvre, F. "Synthesis and Characterization of SiOH-Functionalized Polymer latexes using methacryloxy propyl trimethoxysilane in emulsion polymerization" *Macromolecules* **2002**, *35*, 6185.
130. Yang, Y. Dan, Y. "Preparation of PMMA/SiO₂ composite particles via emulsion polymerization", *Colloid. Polym. Sci.* **2003**, *281*, 794.
131. Peterson, J. D.; Vyazovkin, S.; Wight, C. A. "Kinetic study of stabilizing effect of oxygen on thermal degradation of poly(methyl methacrylate)" *J.*

Phys. Chem. B **1999**, *103*, 8087.

132. Kittur, F. S.; Prashanth, H.; Sankar, K. U.; Tharanathan, R. N. "Characterization of chitin, chitosan and their carboxymethyl derivatives by differential scanning calorimetry" *Carbohydrate Polym.* **2002**, *49*, 185.
133. Maxwell, I. A.; Morrison, B. R.; Napper, D. H.; Gilbert, R. G. "Entry of free radicals into latex particles in emulsion polymerization" *Macromolecules* **1991**, *24*, 1629.
134. (a) Rizzardo, E.; Solomon, D. H. "Acid-induced free-radical decomposition of hydroperoxides: polymerization of methyl methacrylate with tert-butyl hydroperoxide and sulfuric acid" *J. Macromol. Sci. Chem.* **1980**, *A14*, 33. (b) Sharma, R. K.; Misra, B. N. "Grafting onto wool. XVIII. Graft copolymerization of methyl methacrylate onto wool fiber in the presence of tertiary butyl hydroperoxide-mineral acid as initiator" *J. Macromol. Sci. Chem.* **1983**, *A20*, 225.
135. Lindquist, G. M.; Stratton, R. A. "The role of polyelectrolyte charge density and molecular weight on the adsorption and flocculation of colloidal silica with polyethylenimine" *J. Colloid Interface Sci.* **1976**, *55*, 45.
136. (a) Hurst, P. L.; Nielsen, J.; Sullivan, P. A.; Shepherd, M. G. "Purification and properties of a cellulase from *Aspergillus niger*" *Biochem. J.* **1977**, *165*,

- 33.(b) Hurst, P. L.; Sullivan, P. A.; Shepherd, M. G. "Chemical modification of a cellulase from *Aspergillus niger*" *Biochem. J.* **1977**, *167*, 549. (c) <http://www.ebi.ac.uk/thornton-srv/databases/cgi-bin/pdbsum/GetPage.pl?pdbcode=1ks4>.
137. (a) Zhu, Junmin; Li, Pei. "Synthesis and characterization of poly(methyl methacrylate)/casein nanoparticles with a well-defined core-shell structure" *Journal of Polymer Science, Part A: Polymer Chemistry* **2003**, *41*, 3346. (b) <http://www.foodsci.uoguelph.ca/deicon/casein.html>.
138. Chern, C. S.; Lee, C. K.; Ho, C. C. "Colloidal stability of chitosan-modified-poly(methyl methacrylate) latex particles" **1999**, *277*, 507.
139. Santra, S.; Tapeç, R.; Theodoropoulou, N.; Dobson, J.; Hebard, A.; Tan, W. H. "Synthesis and characterization of silica-coated iron oxide nanoparticles in microemulsion: The effect of nonionic surfactants" *Langmuir* **2001**, *17*, 2900-2906.
140. Betancourt-Galindo, R.; Saldívar, R.; Rodríguez-Fernández, O.S.; Ramos-de Valle, L. F. "Preparation and characterization of magnetic latexes using styrene monomer" *Polym. Bull.* **2004**, *51*, 395.
141. Gu, S.; Onishi, J.; Kobayashi, Y.; Nagao, D.; Konno, M. "Preparation and colloidal stability of monodisperse magnetic polymer particles" *J. Colloid*

- Interf. Sci.* **2005**, 289, 419.
142. (a) Moad, G.; Solomon, D. H. “*The Chemistry of Radical Polymerization*”. Boston (Elsevier), **2006**, pp. 96. (b) Clark, J. H. “*Applications of Hydrogen Peroxide and Derivatives*”. Cambridge (Royal Society of Chemistry), **1999**, pp. 21.
143. Goodwin, J. W.; Ottewill, R. H.; Pelton, R. Vianello, G.; Yates, D. E. “Control of particle size in the formation of polymer latexes” *The British Polym. J.* **1978**, 10, 173.
144. Okaya, T.; Kikuchi, K.; Suzuki, A.; Ohara, C. “Thermosensitive poly(methyl methacrylate) emulsion prepared in the presence of poly(vinyl alcohol) with a cloud point as a protective colloid” *Colloid Polym. Sci.* **2004**, 283, 111.
145. Gilbert, R. “*Emulsion Polymerization: A Mechanistic Approach*” **1995**, Academic Press, Chapter 4.
146. Pelton, R.; Chibante, P. “Preparation of aqueous latices with *N*-isopropylacrylamide” *Colloids Surf.* **1986**, 20, 247; (b) Pelton, R. “Temperature-sensitive aqueous microgels” *Adv. Colloid Interface Sci.* **2000**, 85, 1.
147. Sauer, M; Streich, D.; Meier, W. “pH-sensitive nanocontainers” *Adv. Mater.* **2001**, 13, 1649.

148. Ibarz, G.; Dahne, L.; Donath, E.; Möhwald, H. “Smart micro- and nanocontainers for storage, transport, and release” *Adv. Mater.* **2001**, *13*, 1324.
149. Brandrup, J.; Immergut, E. H. “*Polymer handbook*”. New York : Wiley, c1989.
150. Yang, Y.; Gupta, M. C.; Dudley, K. L.; Lawrence, R. W. “Novel carbon nanotube-polystyrene foam composites for electromagnetic interference shielding” *Nano. Lett.* **2005**, *5*, 2131.
151. Baughman, R. H.; Cui, C. X.; Zakhidov, A. A.; Iqbal, Z.; Barisci, J. N.; Spinks, G. M.; Wallace, G. G.; Mazzoldi, A.; De Rossi, D.; Rinzler, A. G.; Jaschinski, O.; Roth, S.; Kertesz, M. “carbon nanotube actuators” *Science* **1999**, *284*, 1340.
152. Dresselhaus, M. S. “Applied physics Nanotube antennas” *Nature* **2004**, *432*, 959.
153. Zhang, M.; Fang, S. L.; Zakhidov, A. A.; Lee, S. B.; Aliev, A. E.; Williams, C. D.; Atkinson, K. R.; Baughman, R. H. “Strong, transparent, multifunctional, carbon nanotube sheets” *Science* **2005**, *309*, 1215.
154. Bryning, M. B.; Islam, M. F.; Kikkawa, J. M.; Yodh, A. G. “Very low conductivity threshold in bulk isotropic single-walled carbon

- nanotubes-epoxy composites” *Adv. Mater.* **2005**, *17*, 1186.
155. Moniruzzaman M.; Winey, K. I. “Polymer nanocomposites containing carbon nanotubes” *Macromolecules* **2006**, *39*, 5194.
156. Li, N.; Huang, Y.; Du, F.; He, X.; Lin, X.; Gao, H.; Ma, Y.; Li, F.; Chen, Y.; Eklund, P. C. “Electromagnetic interference (EMI) shielding of single-walled carbon nanotube epoxy composites”. *Nano. Lett.* **2006**, *6*, 1141.
157. Hong, Y.K.; Lee, C.Y.; Jeong, C.K.; Sim, J.H.; Kim, K.; Joo, J.; Kim, M.S.; Lee, J.Y.; Jeong, S.H.; Byun, S.W. “Electromagnetic interference shielding characteristics of fabric complexes coated with conductive polypyrrole and thermally evaporated Ag”. *Curr. Appl. Phys.* **2001**, *1*, 439.
158. Lee, C. Y.; Lee, D. E.; Jeong, C. K.; Hong, Y. K.; Shim, J. H.; Joo, J.; Kim, M. S.; Lee, J. Y.; Jeong, S. H.; Byun, S. W.; Zang, D. S.; Yang, H. G. “Electromagnetic interference shielding by using conductive polypyrrole and metal compound coated on fabrics” *Polym. Adv. Tech.* **2002**, *13*, 577.
159. Huang, C. Y.; Mo, W. W. “The effect of attached fragments on dense layer of electroless Ni/P deposition on the electromagnetic interference shielding effectiveness of carbon fibre/acrylonitrile–butadiene–styrene composites” *Surface and Coatings Tech.* **2002**, *154*, 55.
160. Jin, L.; Bower, C.; Zhou, O. “Alignment of carbon nanotubes in a polymer

- matrix by mechanical stretching” *Appl. Phys. Lett.* **1998**, *73*, 1197.
161. Shaffer, M. S. P.; Windle, A. H. “Fabrication and characterization of carbon nanotube/poly(vinyl alcohol) composites” *Adv. Mater.* **1999**, *11*, 937.
162. Qian, D.; Dickey, E. C.; Andrews, R.; Rantell, T. “Load transfer and deformation mechanisms in carbon nanotube-polystyrene composites” *Appl. Phys. Lett.* **2000**, *76*, 2868.
163. McCarthy, B.; Coleman, J. N.; Czerw, R.; Dalton, A. B.; Panhius, M.; Maiti, A.; Drury, A.; Bernier, P.; Nagy, J. B.; Lahr, B.; Byrne, H. J.; Carroll, D. L.; Blau, W. J. “A microscopic and spectroscopic study of interactions between carbon nanotubes and a conjugated polymer” *J. Phys. Chem. B* **2002**, *106*, 2210.
164. Grimes, C.A.; Mungle, C.; Kouzoudis, D.; Fang, S.; Eklund, P.C. “The 500 MHz to 5.50 GHz complex permittivity spectra of single-wall carbon nanotube-loaded polymer composites”. *Chem. Phys. Lett.* **2000**, *319*, 460.
165. Barraza, H. J.; Pompeo, F.; Rear, E. A.; Resasco, D. E. “SWNT-filled thermoplastic and elastomeric composites prepared by miniemulsion polymerization”. *Nano. Lett.* **2002**, *2*, 797.
166. Kim, H. M.; Kim, K.; Lee, C. Y.; Joo, J.; Cho, S. J.; Yoon, H. S.; Pejakovic, D. A.; Yoo, J. W.; Epstein, A. J. “Electrical conductivity and electromagnetic

- interference shielding of multiwalled carbon nanotube composites containing Fe catalyst”. *Appl. Phys. Lett.* **2004**, *84*, 589.
167. Lv, X.; Du, F.; Ma, Y.; Wu, Q.; Chen, Y. “Synthesis of high quality single-walled carbon nanotubes at large scale by electric arc using metal compounds” *Carbon* **2005**, *43*, 2020.
168. Du, F.; Ma, Y.; Lv, X.; Huang, Y.; Li, F.; Chen, Y. “The synthesis of single-walled carbon nanotubes with controlled length and bundle size using the electric arc method” *Carbon* **2006**, *44*, 1327.
169. Dillon, A. C.; Gennett, T.; Jones, K. M.; Alleman, J. L.; Parilla, P. A.; Heben, M. J. A “Simple and complete purification of single-walled carbon nanotube materials” *Adv. Mater.* **1999**, *11*, 1354.
170. Ge, J.; Zhang, D.; Li, Q.; Hou, H.; Graham, M. J.; Dai, L.; Harris, F. W.; Cheng, S. Z. D. “Multiwalled carbon nanotubes with chemically grafted polyetherimides” *J. Am. Chem. Soc.* **2005**, *127*, 9984.
171. Meyyappan, M. “*Carbon Nanotubes: Science and Applications*”, CRC press (2005), P. 20.
172. McCarthy, B.; Coleman, J. N.; Czerw, R.; Dalton, A. B.; in het Panhuis, M.; Maiti, A.; Drury, A.; Bernier, P.; Nagy, J. B.; Lahr, B.; Byrne, H. J.; Carroll,

D. L.; Blau, W. J. *J. Phys. Chem. B.* **2002**, *106*, 2210.